

**Laser pulse excited electrons and spins in ferromagnetic
heterostructures**

I n a u g u r a l d i s s e r t a t i o n

zur

Erlangung des akademischen Grades eines

Doktors der Naturwissenschaften (Dr. rer. nat.)

der

Mathematisch-Naturwissenschaftlichen Fakultät

der

Ernst-Moritz-Arndt-Universität Greifswald

vorgelegt von

Ulrike Martens

geboren am 02.06.1986

in Stralsund

Greifswald, 27. Dezember 2017

Dekan: Prof. Dr. Werner Weitschies

1. Gutachter: Prof. Dr. Markus Münzenberg

2. Gutachter: PD Dr. Hans Werner Schumacher

Tag der Promotion: 29.03.2018

Dedicated to Willy Buchin

Content

1. Introduction	- 1 -
1.1 Tunnel magnetoresistance	- 5 -
1.1.1 Phenomenological description.....	- 6 -
1.1.2 Coherent tunneling.....	- 7 -
1.2 Tunnel magneto-Seebeck effect.....	- 11 -
1.2.1 Origin of the tunnel magneto-Seebeck effect.....	- 12 -
1.2.2 CoFe/MgO/CoFe junctions	- 15 -
1.2.3 Methods to create temperature gradients	- 18 -
1.2.4 Temperature profile simulations	- 20 -
1.3 Nernst effects & Ultrafast spin currents.....	- 22 -
1.3.1 Anomalous and planar Nernst effect.....	- 22 -
1.3.2 From spin currents to THz emission.....	- 24 -
2. Materials & Methods.....	- 29 -
2.1 Sample fabrication	- 29 -
2.2 Electrical access to the sample and sample design.....	- 31 -
2.3 Experimental setup	- 33 -
2.4 Lateral heat maps	- 35 -
3. Results/Publications in summary	- 37 -
3.1 Investigations enabled by lateral heat maps - Articles I+II.....	- 37 -
3.2 Ways to control the tunnel magneto-Seebeck effect - Articles III-V	- 46 -
3.3 The development of Terahertz emitters based on metallic heterostructures – Article VI.....	- 48 -
4. Conclusion & Outlook	- 51 -
References	- 55 -

5. Cumulative thesis articles	- 61 -
Author contributions	- 61 -
5.1 Pumping laser excited spins through MgO barriers (Thesis article I).....	- 65 -
5.2 Anomalous Nernst effect on the nanometer scale: exploring three-dimensional temperature gradients in magnetic tunnel junctions (Thesis article II)	- 75 -
5.3 Large magneto-Seebeck effect in magnetic tunnel junctions with half-metallic Heusler electrodes (Thesis article III).....	- 91 -
5.4 Comparison of laser induced and intrinsic tunnel magneto-Seebeck effect in CoFeB/MgAl ₂ O ₄ and CoFeB/MgO magnetic tunnel junctions (Thesis article IV)	- 113 -
5.5 Enhancement of thermovoltage and tunnel magneto-Seebeck effect in CoFeB based magnetic tunnel junctions by variation of the MgAl ₂ O ₄ and MgO barrier thickness (Thesis article V)	- 121 -
5.6 Efficient metallic spintronic emitters of ultrabroadband terahertz radiation (Thesis article VI)	- 131 -

1. Introduction

Modern electronics development and material research focus on continuous device down-scaling as well as the reduction of energy consumption. In light of this goals, a new promising research field combining the interplay of charge, heat and spin currents in nanoscale devices called spin caloritronics emerged [1–3].

The studied effects are possible candidates to provide new read-out mechanisms for memories and sensors by making use of waste heat in electronics. The latter aspect is important in terms of energy efficiency, which means the conversion of an existing input energy to a developable output that is in addition cost-efficient.

In 1821, Thomas Johann Seebeck established [4] the basis for caloritronics research with the observation of an electrical current generated in a closed circuit of two different metals generated by a temperature gradient. Pioneering work connecting thermoelectric effects with spin-dependent transport was added by Johnson and Silsbee [5]. In 2008, the report of a new effect called spin Seebeck effect [6] caught considerable attention. All those investigations guided to the wide-ranging and exciting research field of spin caloritronics.

The work presented in the following chapters focusses on spin-dependent caloritronic effects in magnetic tunnel junctions (MTJs). These devices consist of two ferromagnetic layers separated by a thin insulating barrier, which acts as spin filter for the charge carriers travelling between the electrodes. In dependence on the driving force, two different effects are present in an MTJ.

The first one is the tunnel-magneto resistance effect (TMR). Here a small applied voltage acts as driving force. This effect defines the change of the resistance depending on the magnetic alignment of the electrodes and was first described by Julliere [7] in 1975. MTJs are well-studied in focus of the TMR. Effect ratios of several hundred percent are reached at room temperature, with a record of 604 % for CoFeB/MgO/CoFeB MTJs [8], which is mainly attributed to the MgO barrier providing coherent tunneling conditions [9, 10]. Today, TMR devices are used as readout mechanism in magnetic random access memories (MRAMs) [11] and read heads of hard disc drives (HDDs).

In addition, these nanopatterned pillars exhibit a second property, which is the occurrence of the spin caloritronic analogon to the TMR called the tunnel magneto-Seebeck effect (TMS). This effect was theoretically predicted by Czerner *et al.* [12] in 2011. Shortly after,

the TMS was experimentally observed in our work group by Walter *et al.* [13] and almost simultaneously by Liebing *et al.* [14] for CoFeB/MgO/CoFeB MTJs. The great benefit of such thermomagnetic effects is that they do not need external power in form of an external voltage, but can be run by temperature gradients induced by waste heat. A thermovoltage is generated that depends the magnetic orientation of the electrodes since the Seebeck coefficient changes during the transition from parallel to antiparallel alignment. Nevertheless, in recent research the TMR effect was mainly in focus, since the TMS effect is quite recently explored and so far provides relatively low signals and effect ratios for the mainly studied CoFeB/MgO/CoFeB junctions.

The aim of this thesis is in the first instance to further extend the knowledge of spin caloritronic effects in MTJs induced and controlled by optical heating. For this purpose, the thermally generated voltages are investigated under various aspects. First, the influence of the heating procedure is examined, showing the impact of different temperature distributions on the TMS effect as well as the occurrence of additional thermomagnetic effects. Then, the materials used for the barrier and the electrodes in the devices are replaced to study the corresponding properties. These investigations are performed with in-plane magnetized MTJs.

Another important aim of this work was the development of new terahertz emitter. A recent study reveals how magnetic heterostructures influence the THz spin currents injected by femtosecond laser pulses [15]. This builds the basis for the development of new terahertz emitters and guides to our new investigations. In this context, our conventional electrode material CoFeB is used for the design of new THz emitters. THz radiation is highly interesting for imaging and spectroscopy revealing deeper insight in material properties for numerous applications [16] such as in view of biomedical applications [17] and the analysis and identification of drugs and other dangerous substances [18]. These investigations are as well integrated in this thesis.

This thesis is divided as follows: In the first part, the TMR is introduced as one of the major effect observed in MTJs. This effect serves as an indicator for the device quality and functionality. The second part summarizes the spin caloritronic effect that is also present and unique for MTJs – the tunnel-magneto Seebeck effect including a selection of recent investigations in this field. Here, the origin of this effect and the standard composition of the MTJs CoFeB/MgO/CoFeB is introduced. The different methods to generate temperature gradients across the layer stack of an MTJ are presented. Afterwards, the access to the temperature across the layer stack is discussed.

In the following section, additional effects based on temperature gradients are described. Here, the Nernst effects are briefly introduced since they are potentially present due to the variation of the temperature profile within the MTJs in our TMS measurements.

In addition, the spin-dependent Seebeck effect and the spin Seebeck effect are presented which play a key role for the development of THz emitters attributed to the characteristics of our CoFeB layers.

The Materials & Methods chapter deals with the sample fabrication, especially of MTJs as well as with the device layout. The electrical and optical setup for the TMR and TMS measurements is described in detail. Furthermore, the extended measurement method which results from ongoing setup development is introduced.

The subsequent chapter provides a brief conclusion of the included manuscripts and additional results that are not yet published. Consequently, the results are summarized and an outlook for future investigations is given in the Conclusion & Outlook chapter. In the last chapter, the peer reviewed manuscripts which are the main part of this thesis together with the corresponding author contributions are reprinted.

1.1 Tunnel magnetoresistance

Magnetic tunnel junctions (MTJs) consist of two ferromagnets separated by a thin insulating barrier. The electric resistance R of such a device depends on the magnetic configuration of both magnetic electrodes. The well-established spintronic effect based on the underlying resistance change is the tunnel magnetoresistance effect (TMR). A tunneling current is driven by an external bias voltage and enables to determine the resistance of the device. The TMR ratio is defined as:

$$\text{TMR} = \frac{R_{\text{ap}} - R_{\text{p}}}{R_{\text{p}}}, \quad (1.1)$$

Where p denotes the parallel and ap the antiparallel magnetization alignment of the electrodes. Figure 1 depicts one example TMR curve for an applied bias voltage of 10 mV of a pseudo spin-valve MTJ. The arrows indicate the magnetic alignment of the electrodes. For high external magnetic fields both electrode magnetizations are aligned parallel to each other and R_{p} is much smaller than R_{ap} for the antiparallel alignment. When the external field $\mu_0 H$ is swept from high fields and reversed, first one electrode magnetization switches due to the lower anisotropy and a smaller coercive field. In the ap alignment R increases and

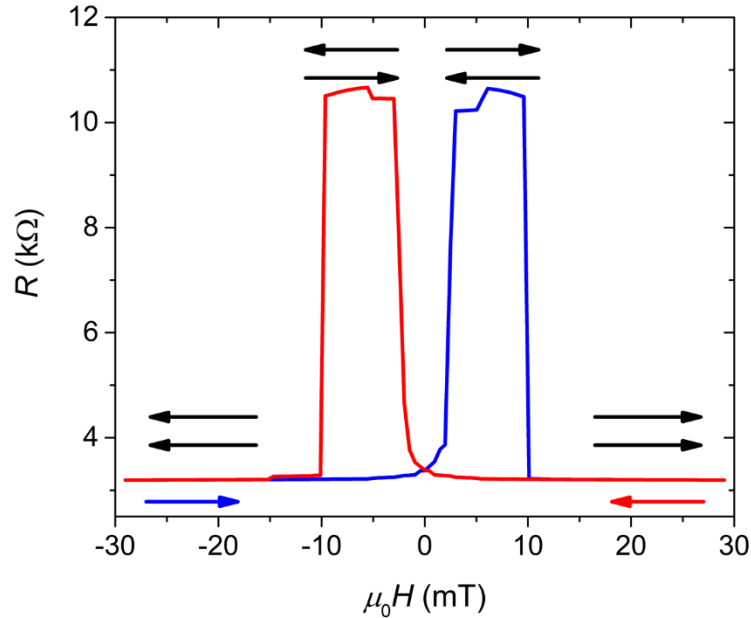


Figure 1: Example TMR curve of a pseudo spin-valve MTJ. The alignment of the electrodes is indicated by the black arrows for the parallel as well as for the antiparallel state. The blue and red arrow denote the switching direction of the applied magnetic field.

shows a plateau until the applied field is high enough to switch the other electrodes magnetization restoring the p magnetization state with a low R_p again. Through the existence of two free electrode magnetizations, two parallel and antiparallel orientations are observable. In accordance to equation (1.1), the TMR ratio using the example TMR curve of figure 1 is calculated to $\approx 230\%$.

1.1.1 Phenomenological description

In 1975, Julliere first investigated Fe/GeO/Co tunnel junctions and observed a TMR ratio of 14 % at low temperatures (4.2 K) [7]. He argued that the states of high and low resistances stem from the spin-polarization in the electrodes and thus this effect originates from spin-polarized electron tunneling through the barrier. From his observations he developed a model, assuming that the tunneling current for each spin direction is proportional to the density of states (DOS) at the Fermi level of the tunneling electrodes. In addition, Slonczewski [19] developed a more detailed explanation of the theory by considering the density of states at both electrodes in combination with a rectangular potential barrier in which the amplitude of the applied voltage decays as relevant for this behavior.

The scenario depicting this simple two-current theory is shown in figure 2 for both magnetization alignments. Since an applied voltage shifts the electrochemical potential of one electrode in relation to the other, electrons can tunnel into unoccupied states of the same spin identity. In the parallel alignment the tunneling probability is high. Here, in the energy interval between the electrochemical potentials of the electrodes a large number of majority spins (spin up) are present in the first electrode which travel to a large number of unoccupied

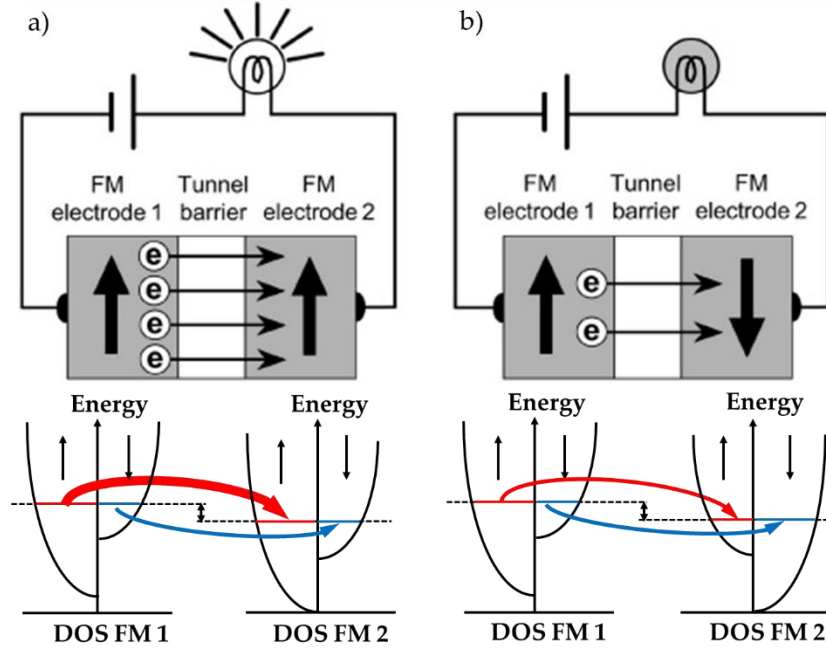


Figure 2: Simplified depiction of the TMR with (a) parallel magnetization alignment of the electrodes and (b) antiparallel magnetization alignment. The DOS at the Fermi energy for the majority-spin and minority-spin bands are indicated for the first ferromagnet (FM1) and the second ferromagnet (FM2), respectively. (Taken and adapted from reference [22])

states of the same spin identity in the final second electrode. The number of minority spins (spin down) is smaller, thus contributing less to the tunneling current. In the antiparallel magnetization configuration, in one electrode the spin states are reversed [20]. This results in a limited tunneling since in this configuration only a small number of either initial or final states is available. Thus, the resulting current in the parallel magnetization state is higher than in the antiparallel state resulting in different resistances for the individual electrode magnetization alignments. This model will be further extended in the TMS section in order to sketch the differences between the TMR and the TMS effect.

1.1.2 Coherent tunneling

One main factor that constitutes a tunnel junction is the barrier material. The composition and quality of this component sets the conditions for spin tunneling and acts in this function as spin filter. In 2001, Butler *et al.* [9] and Mathon & Umerski [10] predicted independently several thousand percent TMR ratios for Fe/MgO/Fe junctions. This high values originates from the symmetry filtering effect referred to as coherent tunneling. Nevertheless, up to now

such high theoretically calculated TMR ratios are not confirmed by experiments at room temperature.

The following section focusses on CoFe/MgO/CoFe MTJs because this corresponds to the mainly used devices in our investigations. The subsequent annealing of the deposited CoFeB/MgO/CoFeB sample results in the diffusion of boron into the adjacent Ta layers. In fact, the resulting MTJ consists mainly of CoFe/MgO/CoFe.

MTJs with CoFe electrodes and MgO barrier have been intensively studied as spintronic devices since this MTJs exhibit the required crystallographic symmetry and are easy to prepare by sputter deposition with the essential surface and interface quality [21, 22]. These devices provide high TMR ratios of several hundred percent. Ikeda *et al.* [8] reached an experimental value of 604 % at room temperature which is attributed to the crystalline structure of the MgO barrier resulting in coherent tunneling. From band structure calculations of CoFe/MgO/CoFe it is shown that there exist different tunneling probabilities in the majority and minority spin channel [20]. The tunneling process perpendicular to the interfaces is indicated in figure 3. In the parallel alignment of the electrodes, the dominant tunneling proceeds from the initial majority to the final majority channel. This means, the Bloch states with identical symmetry are available in the second electrode and the tunneling process is mainly limited by the decay rate. The slowest decay rate is observed for the Δ_1 state. Thus, this Bloch-state from the initial electrode with Δ_1 symmetry can efficiently

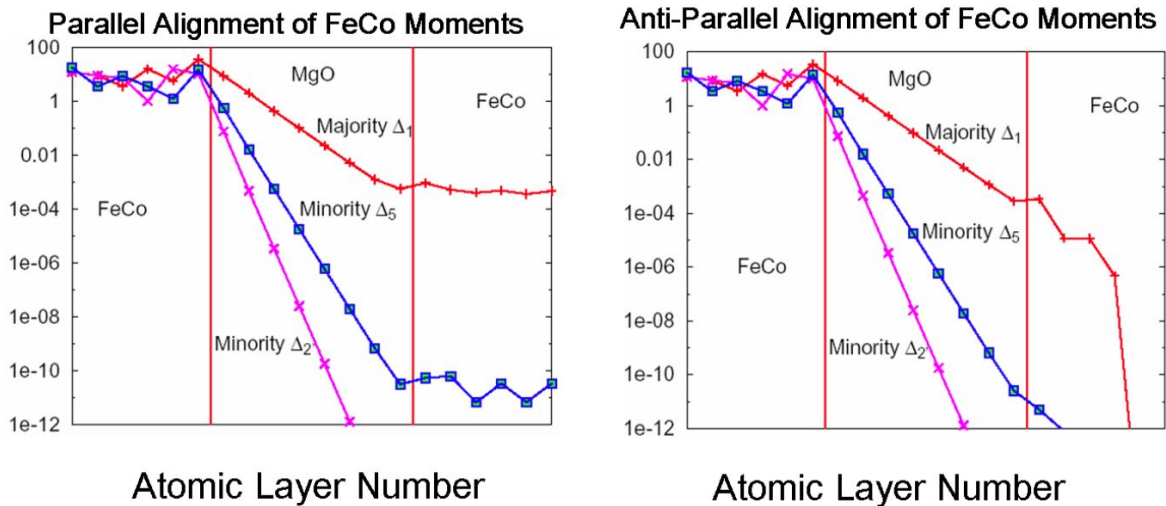


Figure 3: Electron tunneling perpendicular to the interface in an FeCo–MgO–FeCo MTJ indicated for the individual symmetries. On the left for parallel magnetization alignment of the electrodes and on the right for antiparallel magnetization alignment. Taken from reference [20].

couple to the equivalent state in the barrier and the final electrode. The minority spin bands Δ_5 and Δ_2 show a fast decay and therefore contribute much less to the tunneling. As mentioned in the previous section, the spin identities in the antiparallel alignment are reversed for one electrode. Since the Δ_1 state is absent in the minority channel, here the conductance is suppressed resulting in a fast decay in the second electrode [9]. In conclusion, the MgO barrier acts efficiently as a symmetry filter and the tunneling is dominated by the Δ_1 majority channel. In Co, Fe and CoFe the Δ_1 states are highly spin polarized and based on this explanation of coherent tunneling, the resistances for both electrode alignments strongly differ and thus result in high TMR ratios.

Since amorphous barrier materials have no preferred crystal symmetry all present orbital symmetries couple equally well to the states of the barrier and thus the spin polarization does not affect the tunneling. Therefore, the TMR ratio is drastically reduced. This is referred to as incoherent tunneling. Figure 4 represents a schematic depiction comparing the coherent and incoherent tunneling process in an MTJ.

A detailed description of these phenomena can be found in references [20, 22].

The deposition of high-quality nanometer-thin oxide films without pinholes requires optimized fabrication conditions. Here it has to be mentioned that in addition to the barrier itself also the interfaces to the electrodes are very important to enable coherent tunneling. The electrodes have to be ultra-smooth to provide the basis for the barrier layer. The crystal structure can be influenced by impurities from the interdiffusion or migration of other atoms to the structure originating from the fabrication process [23, 24]. In this regard, a factor that

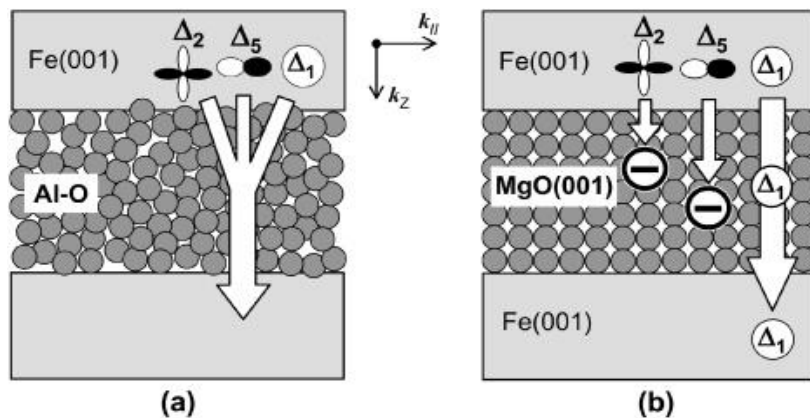


Figure 4: Simplified depiction of the electron tunneling process through (a) an amorphous alumina barrier and (b) a crystalline MgO (001) barrier, taken from reference [22].

notably influences the quality of the device is the annealing temperature. Annealing is important for the crystallization of the amorphous CoFeB alloy [22, 23]. This fact is again mentioned in the sample fabrication section.

The TMR effect depicts the spin-dependent tunneling process and serves in our experiments as an indicator for the surface smoothness as well as the junction quality and functionality.

1.2 Tunnel magneto-Seebeck effect

The tunnel magneto-Seebeck effect (TMS) also referred to as magneto-thermoelectric power (MTEP) or tunneling magnetothermopower (TMTP) is the expansion of the classical charge Seebeck effect by adding a magnetization component for the special case of MTJs. The Seebeck effect was discovered in 1821 by Thomas Johann Seebeck and pictures the generation of a voltage in metals or semiconductors caused by a temperature gradient ∇T [4, 25]. The generated voltage scales linearly with the temperature difference ΔT between the measurement points and the Seebeck coefficient S . Thus, this phenomenon can be simply expressed as:

$$V = -S \cdot \Delta T. \quad (2.1)$$

The TMS expresses the change of the Seebeck coefficients S_p, S_{ap} of a magnetic tunnel junction due to the switching of the electrodes magnetization between the parallel (p) and antiparallel (ap) alignment. This effect is experimentally detected by applying a temperature gradient across the layer stack and tracing the generated thermovoltage depending on a changing applied magnetic field. The TMS ratio is defined as:

$$\text{TMS} = \frac{S_p - S_{ap}}{\min(|S_p|, |S_{ap}|)} \triangleq \frac{V_{ap} - V_p}{\min(|V_{ap}|, |V_p|)}, \quad (2.2)$$

where V is the Seebeck voltage for the p and ap state, respectively.

An example TMS measurement curve is depicted in figure 5. The electrodes exhibit the same switching behavior in dependence on the applied magnetic field compared to TMR measurements (see figure 1).

This effect was first experimentally studied by Walter *et al.* [13] and almost simultaneously by Liebing *et al.* [14], whereas the method to create the temperature gradient across the layer stack of the MTJ was different. Similar to the method utilized in the present thesis, Walter *et al.* used laser heating, while Liebing *et al.* treated the device by Joule heating with an additional heater line on top of the MTJ.

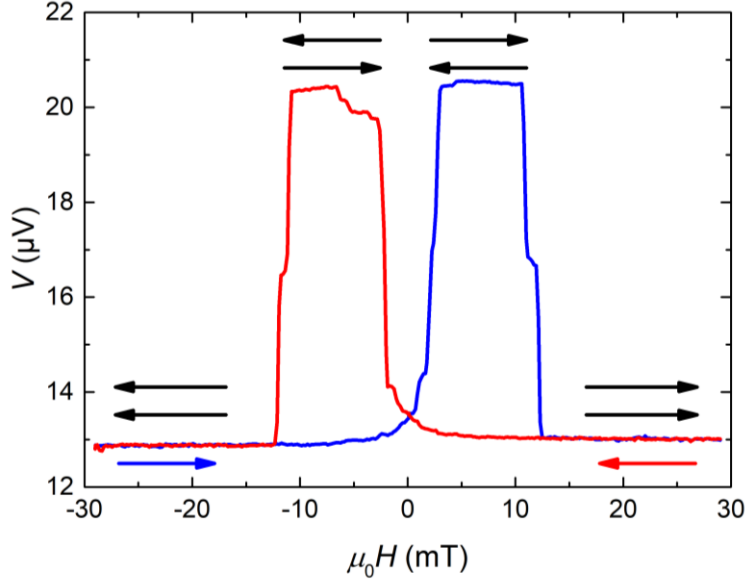


Figure 5: Example TMS curve of a pseudo spin-valve MTJ. The alignment of the electrodes is indicated by the black arrows for the parallel as well as for the antiparallel state. The blue and red arrow denote the switching direction of the applied magnetic field.

1.2.1 Origin of the tunnel magneto-Seebeck effect

The theory group of Christian Heiliger predicted the TMS in 2011 [12] with ratios of up to several 1000 % and pointed out the strong nonlinear temperature dependence for MgO-based MTJs with CoFe electrodes. This effect originates from the different asymmetries of the density of states (DOS) at the Fermi level for both spin channels resulting in different Seebeck coefficients for the p and ap state.

With the assumption of a one-dimensional transport through the barrier the TMS can be derived from irreversible thermodynamic transport equations [26]. Since spin caloritronic phenomena are characterized by the flow of heat and charge transport the TMS can be expressed in terms of the specific transport coefficients for particles $-J_N$ (note, the negative sign is attributed to the negative charge of the electrons) and heat J_Q , which depend on the electrochemical potential μ and ∇T :

$$\begin{pmatrix} -J_N \\ J_Q \end{pmatrix} = \begin{pmatrix} L_0 & \frac{1}{T} L_1 \\ L_1 & \frac{1}{T} L_2 \end{pmatrix} \begin{pmatrix} \nabla \mu \\ \nabla T \end{pmatrix} \quad (2.3)$$

With the moments L_n . If we consider a particle transport in the form of electrons, then also a charge transport is present. This is given as:

$$J_N = L_0 \nabla \mu + \frac{1}{T} L_1 \nabla T. \quad (2.4)$$

In the case of $J_N = 0$ the resistance is high, and the particles accumulate on one side. Then equation (2.4) can be solved for $\nabla \mu$:

$$\nabla \mu = -\frac{1}{T} \frac{L_1}{L_0} \nabla T.$$

Since the electrochemical potential per unit charge is given by $(1/e)\nabla \mu$ the formula can be transformed to:

$$\xRightarrow{J_N=0} \frac{1}{e} \nabla \mu = V = -\frac{1}{eT} \frac{L_1}{L_0} \nabla T = S \nabla T, \quad (2.5)$$

where $S = \frac{1}{eT} \frac{L_1}{L_0}$ denotes the Seebeck coefficient. The conductance G is defined for a homogenous isothermal system as the density of electric current eJ_N per unit potential gradient $\left(\frac{1}{e}\right) \nabla \mu$.

$$G \equiv -\frac{eJ_N}{\frac{1}{e} \nabla \mu} \quad \text{for } \nabla T = 0. \quad (2.6)$$

Related to equation (2.3) by setting $\nabla T = 0$ leads to the expression:

$$\xRightarrow{\nabla T=0} eJ_N = e^2 L_0 \frac{1}{e} \nabla \mu = G \frac{1}{e} \nabla \mu. \quad (2.7)$$

The conductance is given by:

$$G = e^2 L_0. \quad (2.8)$$

The moments L_n can be expressed in terms of the Landauer-Büttiker formalism and are integrals of the transmission function $T_t(E)$, the electron energy E above Fermi level and the change of the Fermi distribution function $(-\partial_E f(E, \mu, T))$. Thus, the formula can be written as [12]:

$$L_n = \frac{2}{h} \int T_t(E) (E - \mu)^n (-\partial_E f(E, \mu, T)) dE, \quad (2.9)$$

where the factor 2 accounts for the spin degeneracy, h is the Planck constant, f the Fermi distribution function in dependence on the E , μ and T . The moments are derived from band

structure calculations in accordance to the electronic structure to calculate the transmission function.

Walter *et al.* [13] showed the dependence of both effects, the TMR and TMS, on the energy symmetries in the transmission function and depicted the differences between them. The transport coefficients are both calculated from the transmission function $T_t(E)$, but the integral values are different. The conductance G is determined via:

$$G = \frac{e^2}{h} \int T_t(E) (-\partial_E f(E, \mu, T)) dE. \quad (2.10)$$

The Seebeck coefficients are calculated as derivative of the product of the spin-dependent transmission function $T_t(E)$ and occupation function $\partial_E f(E, \mu, T)$:

$$S = - \frac{\int T_t(E) (E - \mu) (-\partial_E f(E, \mu, T)) dE}{eT \int T_t(E) (-\partial_E f(E, \mu, T)) dE}. \quad (2.11)$$

Here, it has to be highlighted that the Seebeck coefficient is the geometric center of this function. In this context, we can assume two different cases, depicted in figure 6. In these graphs, the transmission function is sketched in light colors for the p and ap state, respectively. For a high TMR ratio the transmission probability for the electrons at the Fermi level needs to be different for both states. This requirement is fulfilled in both cases in figure 6. Here, the transmission in the parallel state is high and in the antiparallel state strongly reduced. The Seebeck coefficients are illustrated by the orange lines. For the first configuration we expect a high TMS ratio given by the strong asymmetry of the Seebeck coefficients positioned around the Fermi energy. In the second, the Seebeck coefficients are symmetric positioned at the same energy E and thus no TMS is expected.

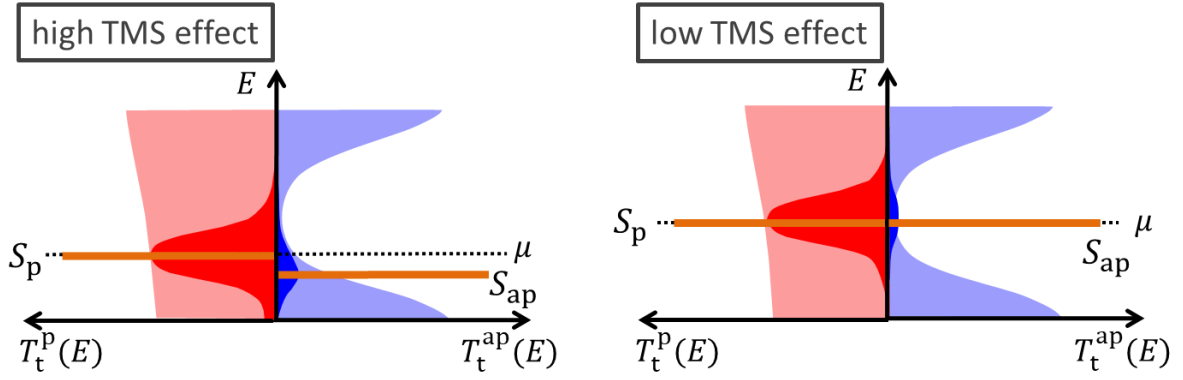


Figure 6: The transmission function of MTJs as origin of TMR and TMS, illustrating the differences in accordance to the spin-dependent tunneling channels and the influence of asymmetries. The darker color shows $T_t(E)(-\partial_E f(E, \mu, T))$ and the resulting Seebeck coefficients S_p, S_{ap} as geometric centers marked by an orange line for p and ap magnetization state, respectively. Taken and adapted from reference [13]

This depiction clearly shows that TMR and TMS are not directly connected and therefore strong differences within the effect ratios are possible. However, a high TMR is a necessary condition for a high TMS, because it is a measure not only for suitable TMR material, but also for a good sample quality. Those requirements are realized within CoFeB/MgO/CoFeB junctions.

1.2.2 CoFe/MgO/CoFe junctions

The TMS in CoFe/MgO/CoFe MTJs is strongly influenced by the design of the utilized components. Heiliger *et al.* [27] showed the strong dependence of TMS on the composition of the CoFe electrodes in *ab initio* studies. In brief, small differences in the alloy composition can change the value and sign of the effect due to a complex change in the transmission function. Additionally, there is a second factor to consider, namely the barrier thickness as shown in this study for a barrier of 6 and 10 monolayers (ML), respectively. One monolayer MgO is equal to a thickness of 0.21 nm.

A giant effect for ultrathin MgO based junctions was reported by Teixeira [28] with an intrinsic TMS ratio of up to -1189 % for a device with a 0.85 nm-thick MgO barrier (~ 4 ML). They observed a sign change of the TMS at 1.35 nm MgO thickness (~ 6 ML). Here, it has to be pointed out that with decreasing barrier thickness the probability for pinholes increases and thus the probability for intact barriers decreases. Their results are highly questionable

due to their used method to determine the TMS. This point is extended discussed in reference [29].

A dominant factor also influencing the Seebeck coefficients and thus the TMS is the composition of the interface between the CoFe electrodes and the MgO barrier [13, 30]. The atoms terminating the CoFe electrode strongly influence these values and the resulting TMS ratio. Walter *et al.* [13] and Czerner *et al.* [30] studied the impact within ab initio calculations based on density functional theory. In the first study concerning the atoms populating the interface between electrodes and tunnel barrier an ordered alloy with 50 % Co and 50 % Fe as terminating atoms at the ten-monolayer (10 ML) thick MgO barrier is pointed out. The Seebeck coefficients S_p and S_{ap} as well as the TMS ratio are determined in dependence on temperature. The results reveal a sign change of the TMS ratio at 400 K from negative to positive values with increasing temperature. The influence of the atoms terminating the interface is more extendedly studied by Czerner *et al.* [30]. This investigation is highlighted in figure 7 and 8. Figure 7 depicts three different possible interface termination scenarios with in the first case Fe as terminating atoms, second Co and third one Co and one Fe terminated electrode. In figure 8 the corresponding Seebeck coefficients S_p and S_{ap} as well as the resulting TMS ratios are displayed in dependence on the temperature. The TMS ratio for all shown designs is positive for a barrier thickness of 6 monolayers and 10 monolayers, respectively. In contrast, the first experimentally observed TMS effect with an MgO barrier of 10 monolayers reveals a relatively small ratio of -8.8 % [13]. Furthermore, it is shown that the TMS ratio for Fe terminated junctions strongly decreases with increasing barrier thickness. Nevertheless, in experiments a mixed termination at the interface is more realistic.

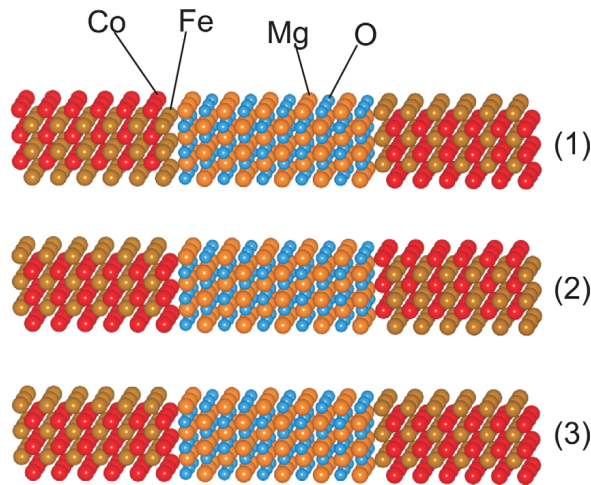


Figure 7: Illustration of different termination scenarios at the interface of CoFe and the MgO barrier with (1) CoFe/MgO/FeCo, (2) FeCo/MgO/CoFe and (3) FeCo/MgO/FeCo, taken from reference [30].

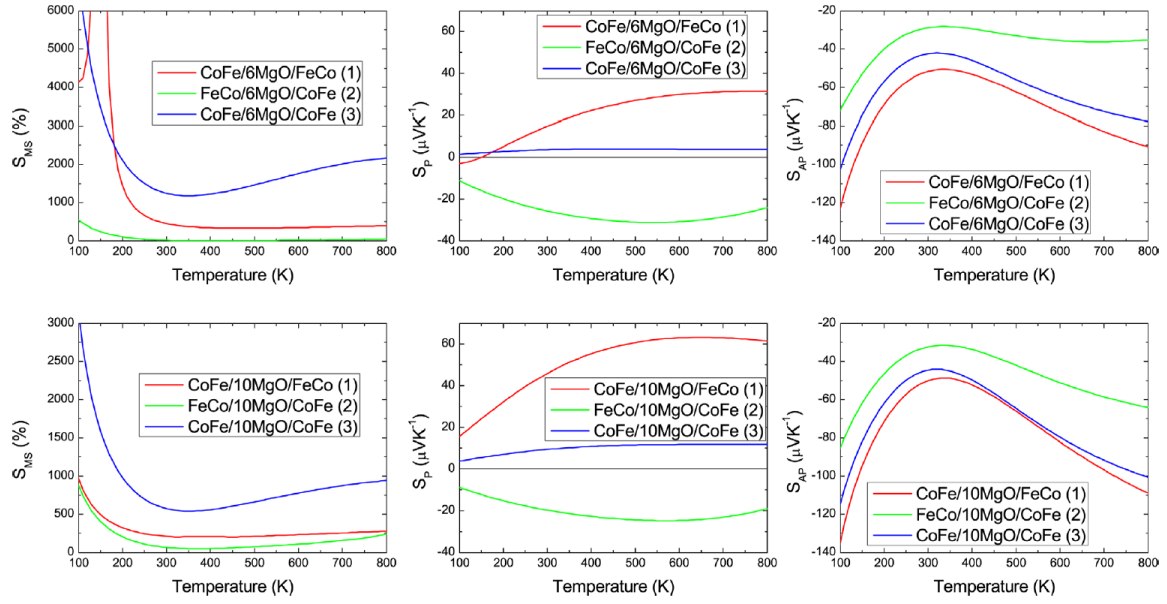


Figure 8: TMS ratio (here S_{MS} , left column) and the corresponding Seebeck coefficients S for p (middle column) and ap (right column) magnetization alignment as a function of temperature calculated for a MgO barrier thickness of 6 monolayers (top) and 10 monolayers, respectively. Here the numbering equates to the termination scenarios in figure 7. Taken from reference [30].

Coherent tunneling also depends on the barrier structure. Oxygen vacancies influence the coherent tunneling due to incoherent tunneling contribution [31]. The impact of these defects at the film interface is theoretically studied by Wang *et al.* [32] for different thicknesses of the MgO barrier. They reported that with an increasing degree of oxygen vacancies, the Seebeck coefficients are greatly affected for $Co_{0.5}Fe_{0.5}$ and the resulting TMS ratio is decreasing from large positive values even to negative values. Furthermore, they pointed out, that their results for 9 monolayers MgO with 7 % oxygen vacancies matches with the results experimentally obtained by Walter *et al.* [13].

All those studies reveal, that there is a great spectrum of relevant parameters affecting the Seebeck coefficients and thus the TMS that need to be controlled. Besides the key role of temperature, the electrode composition, the interface design and barrier thickness are pointed out as influencing factors concerning the engineering of high quality devices that lead to significant TMS ratios. With regards to these conditions, the experimental investigations on CoFeB/MgO/CoFeB junctions reveal slightly different results.

Despite a large number of studies concerning MgO based barrier systems, also other MTJ-material systems have been investigated. In 2012, Lin *et al.* [33] reported a ‘giant’ TMS for amorphous alumina (Al_2O_3) barriers in combination with $Co_{90}Fe_{10}$ electrodes. In comparison to the observations of Liebing *et al.* [34] for MgO barriers where the tunnel thermocurrent

shows the same switching behavior as the TMR and TMS, here only a constant value for the thermocurrent appears independent of the applied magnetic field. The TMS ratio Lin *et al.* obtained by laser heating is similar to the TMR ratio in those MTJs with around 40 %. The generated thermovoltage is high with up to 1 mV compared to the signals achieved with MgO barriers which are in the μV -range. Because of this, Al_2O_3 appeared to be a promising material for practical applications. Nevertheless, this high signal in the mV-regime has not been reproduced until now. The TMS for this kind of barrier reaches ratios of up to 12 % in theory [35]. In 2016, the group of Mangin argued that this high previously experimentally observed effect in alumina-based junctions can be attributed to artifacts described in reference [36]. This gives also an explanation for the anomalous thermocurrent behavior. In addition, I had the opportunity to perform TMR and TMS measurements on MTJs with Al_2O_3 barrier. Here, the effect ratios for the TMR were comparable to those reported by Lin *et al.* with around 40 %, and in contrast to this, the TMS ratio was around 6 %. In addition, the observed thermovoltages were much lower with less than 20 μV and did not reach the millivolt-range.

1.2.3 Methods to create temperature gradients

As mentioned in the previous section different methods are established to create temperature gradients across MTJs. The first method performed by Liebing *et al.* is extrinsic Joule-heating [14, 34]. Schematic pictures of the measurement configuration (a) and the MTJ stack (b) are depicted in figure 9. Here, an injected current I_{heat} through the heater line (HL)

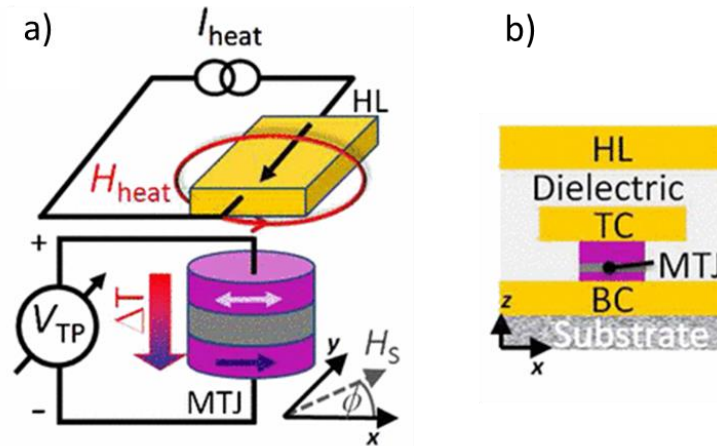


Figure 9: (a) Experimental setup used by Liebing *et al.* (b) Schematic illustration of the cross section displaying the contact and layer structure, taken from reference [14].

generates the temperature gradient across the subjacent layer stack. The thermovoltage V_{TP} is measured depending on an applied in-plane magnetic field H_S . The schematics in figure 9 illustrate that the heater line is bigger than the underlying MTJ itself, thus a homogenous temperature gradient across the layer stack is expected. The fabrication of MTJ devices with HL requires an additional lithography step. As a consequence, this measurement configuration allows no subsequent alignment of the heating position.

The second method is laser heating as reported firstly by Walter *et al.* [13]. This is the more flexible method to create temperature gradients. The schematic illustration of the setup is sketched in figure 10. In this frame, the modulated laser beam is positioned on the junction surface and the thermovoltage is detected depending on an external magnetic field. The MTJ is covered by a gold pad which acts as heat absorber and additionally, enables electrical access by contact bonding. This method of laser heating allows strong variations through manual positioning. However, an exact positioning of the laser spot on the MTJ is inevitable to create a defined out-of-plane temperature gradient across the layer stack [37, 38]. The application of a camera in the setup is supporting the positioning procedure. First position-dependent measurements are reported in reference [37] also displaying the temporal evolution of the voltage signal corresponding to the laser modulation in a rectangular shape. The resulting data is depicted in figure 11. Here, it is shown that the signal is just attributed to the junction and at maximum by placing the laser spot on the center of the MTJ (blue line in figure 11). Heating the vicinity of the junction results in drastically reduced themovoltages

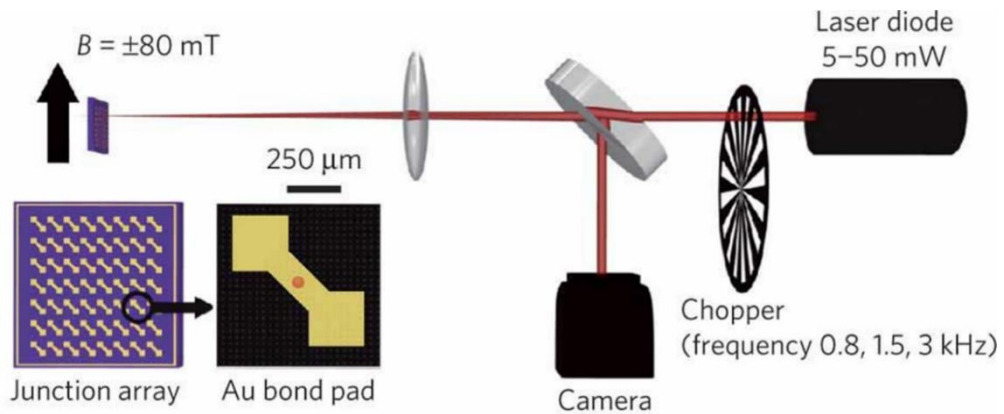


Figure 10: Schematic illustration of the measurement setup using laser heating together with a depiction of the junction design used by Walter *et al.* [13].

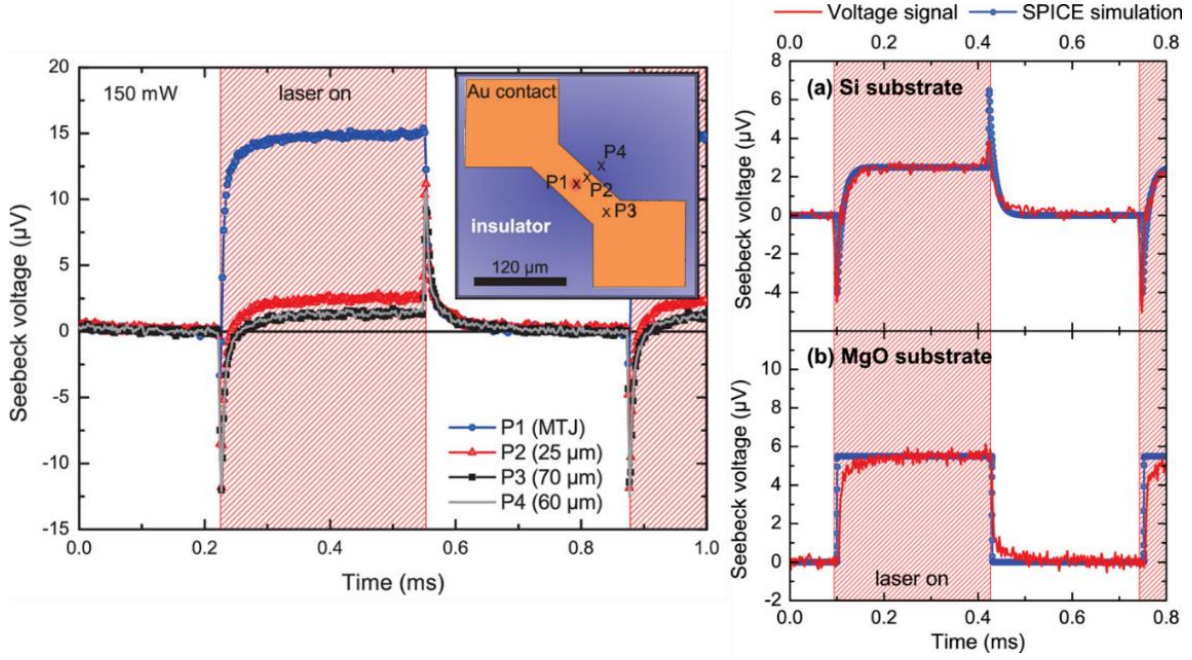


Figure 11: The left graph shows the temporal evolution of the thermovoltage signal in laser assisted TMS measurements as well as the signal achieved by heating different positions of the bondpad. On the right side: Substrate-dependent measurements displaying the electrical capacitance resulting from the Si substrate (a) in comparison to MgO substrate (b), taken from reference [37].

which is indicated by the red, black and grey lines. This clearly points out the importance of the exact positioning. In addition, it is depicted in figure 11 (a) (on the right) that additional voltage signals arise due to the capacitive effect of the Si substrate. By using MgO substrates this incoupling signal vanishes, resulting in a rectangular signal shape. Also the group of Mangin [36] reported the generation of a photovoltage by using Si substrates. This has to be considered in TMS measurements by monitoring the temporal evolution of the signals to avoid misleading results.

Laser heating is the method to create a temperature gradient utilized in the frame of this thesis. In addition to several preliminary works [13, 29, 37, 39], this method offers extensive possibilities to create and control the temperature profiles across the layer stack and in the layer planes.

1.2.4 Temperature profile simulations

The main challenge in TMS studies is the access to the generated temperatures and their gradients, especially within such thin barrier dimensions of a few nanometers. Until now, no experimental access has been realized. The only way is indirect through finite element

simulations (COMSOL). Within this research field this is a common method to estimate the temperature profile within the investigated nano-sized tunnel junctions [13, 14, 29, 37, 40, 41].

The main issue of these calculations lies in the thermal conductivity parameters of the barrier material. In general, for COMSOL simulations a value for the thermal conductivity κ_{MTJ} is chosen which is between that for bulk MgO and thin film MgO. The values deviate by one order of magnitude [42, 43]. It is also shown that the thermal conductivity is significantly dependent on the oxygen vacancies at the film interfaces [32]. Zhang *et al.* [42] studied the impact of phonons on the thermal conductance of the whole MTJ and state that the thermal conductivity is lower than the thin films value. Furthermore, in recent experimental studies it is confirmed that the thermal interface resistance dominates and thus the thermal conductivity of the MgO barrier itself is lower than previously suggested [43].

Recently, Böhnert *et al.* [44] prepared MTJ devices with resistance thermometers on top and bottom contacts and determined the temperature difference across the sample. The experimentally determined temperature difference differs from the temperature profile of the MTJ pillar itself since thermal resistances at the interfaces contribute to the measured values and the temperature was measured over additional adjacent layers. This new approach is a step forward to the temperature profile determination. Nevertheless, it confirms again that the experimental approach is very challenging and that there is still no method available to measure an accurate temperature difference over such short length scales in the nanometer-range. Gaining access to the temperature difference at the barrier is still the main challenge in this research field.

1.3 Nernst effects & Ultrafast spin currents

Besides the described unique effects in MTJs, the TMR and TMS, the optimized setup allows to fully control temperature gradient directions in three dimensions and the generation of effects that are not solely attributed to MTJs and so far have only been observed in simple macroscopic and mesoscopic structures. Some of the emerging effects are hard to separate in direct measurements because of similar characteristics, for instance the same measurement configuration. The following part guides through spin caloritronic effects that are potentially present within our studies.

Furthermore, CoFeB is a powerful material for spintronic applications due to the material-specific high spin polarization of 65 % [45] and the possibility to grow smooth layers making it a first choice material for spin-polarized transport processes. In this section, the additional spin caloric effects which are related to CoFeB films are described.

1.3.1 Anomalous and planar Nernst effect

The Nernst effects are very interesting since laser heating enables a strong variation of temperature gradients which consequently result in the occurrence of this effects. In the following, the geometries of the Nernst effects are briefly outlined to enable a direct comparison to the TMS measurement configuration.

The Nernst effects are based on the transport of charge carriers driven by a temperature gradient and the interaction with the magnetization. The anomalous Nernst effect (ANE) defines the electric force E_{ANE} perpendicular to the temperature gradient ∇T and the magnetization M : $E_{\text{ANE}} \propto \nabla T \times M$. As given by the definition, the ANE exhibits a sign change with magnetization reversal. Commonly this effect is measured in in-plane magnetized samples and an out-of-plane applied temperature gradient which is depicted in figure 12a. The ANE is verified in several studies contributing to the thermovoltage signal [46–50]. For example, Meier *et al.* [46] studied the angular dependence of the ANE with respect to the temperature gradient and the magnetization. The investigators identified the ANE through the agreement of their results with the cross product definition as well as due to the conductivity of their studied NiFe_2O_4 film in dependence on the temperature.

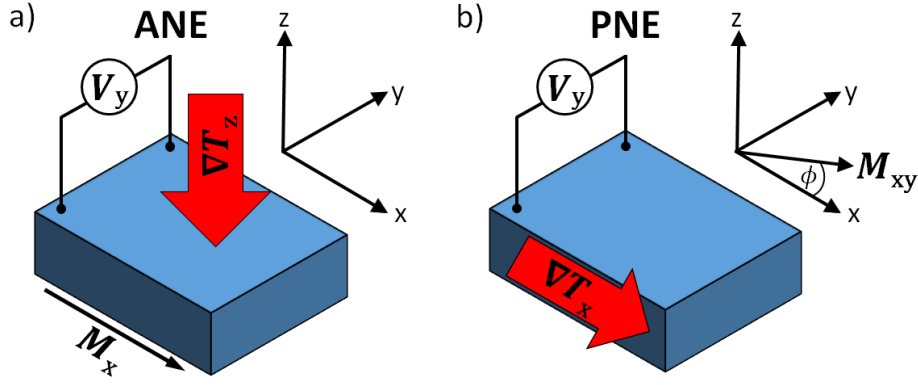


Figure 12: Schematic representation of (a) the anomalous Nernst effect ANE and (b) the planar Nernst effect PNE configuration.

When both, M and ∇T are oriented in the film plane, the voltage generated in this plane is referred to as the planar Nernst effect (PNE) [51, 52]. Figure 12b depicts the voltage measurement along the y-axis and perpendicular to the applied temperature gradient ∇T (x-axis) with an in-plane magnetization M . The voltage caused by the PNE can be expressed as: $V_{\text{PNE}} \propto |M|^2 \sin(\phi) \cos(\phi) |\nabla T_x|$, where ϕ denotes the angle between M and ∇T [53]. The PNE is reported for Ni and Ni₈₀Fe₂₀ thin films deposited on silicon nitride membranes [54]. This kind of substrate is chosen to exclude bulk properties, which otherwise influence the formation of ∇T . The researchers identified the effect due to the angular dependence and the opposite sign of the voltage signal by reversing the direction of ∇T . The PNE is also observed by Schmid *et al.* [55] for Py films on MgO and GaAs substrates as well as on silicon nitride membranes and furthermore by Meier *et al.* [53] on MgO and sapphire substrates.

The upgrade of the TMS measurement setup that is realized as one important part of this thesis enables the very sensitive detection of the ANE in MTJs. The corresponding investigations present the verification of the ANE via lateral heat maps and the angular dependence of the arising thermovoltages.

1.3.2 From spin currents to THz emission

In 1987, Johnson and Silsbee [5] published their studies on spin transport generated by temperature gradients originating from the spin polarization of the conduction electrons. This effect is named spin-dependent Seebeck effect (SDSE). Slachter *et al.* [56] experimentally achieved thermal spin injection through a ferromagnetic/non-magnetic metal (FM/NM) junction generated by a heat current. Since the transport properties are different for minority and majority spins individual conductivities and Seebeck coefficients are defined for each spin kind. By applying a temperature gradient heat current flows through the ferromagnet and a spin current is generated determined by the spin-dependent Seebeck coefficient. Due to the strict change of spin current by passing from the ferromagnet to the adjacent nonmagnet a spin accumulation is detected at the interface.

The spin Seebeck effect (SSE) is also driven by a temperature gradient but it defines a collective process of spins. The name originates from its discovery when the underlying mechanism has not been fully understood. Uchida *et al.* [6] were the first who reported this effect in 2008. They studied a permalloy (Py) layer covered with Pt stripes at the edges of this mm-thick film. The in-plane temperature gradient is applied parallel to the film magnetization M . At the ends of the Pt strip a voltage is measured perpendicular to the temperature gradient. This arrangement is referred to as the transverse configuration and is schematically depicted in figure 13b. The temperature gradient applied to the ferromagnet leads to a pure spin current that is subsequently injected to the adjacent nonmagnetic metal with high spin-orbit coupling. That means the Pt stripe in reference [6] acts as a detection

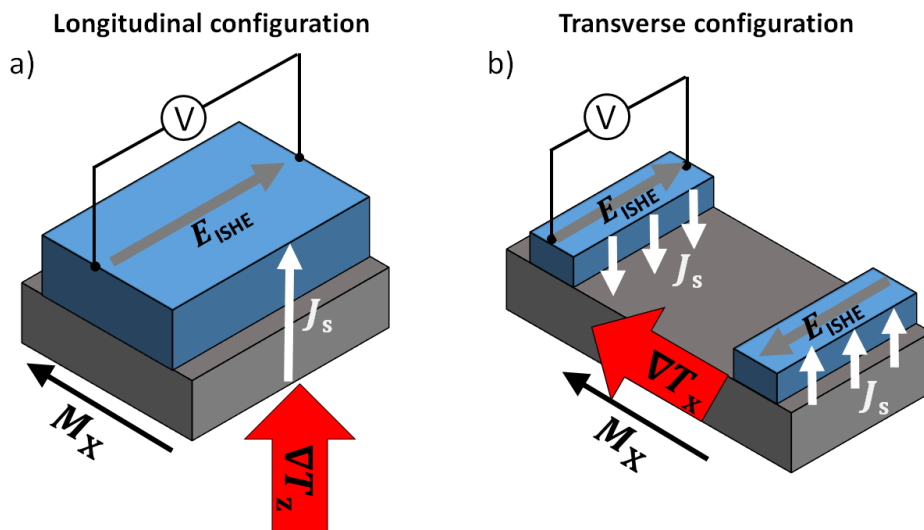


Figure 13: Depiction of the spin Seebeck effect SSE in (a) the longitudinal and (b) transverse configuration, respectively.

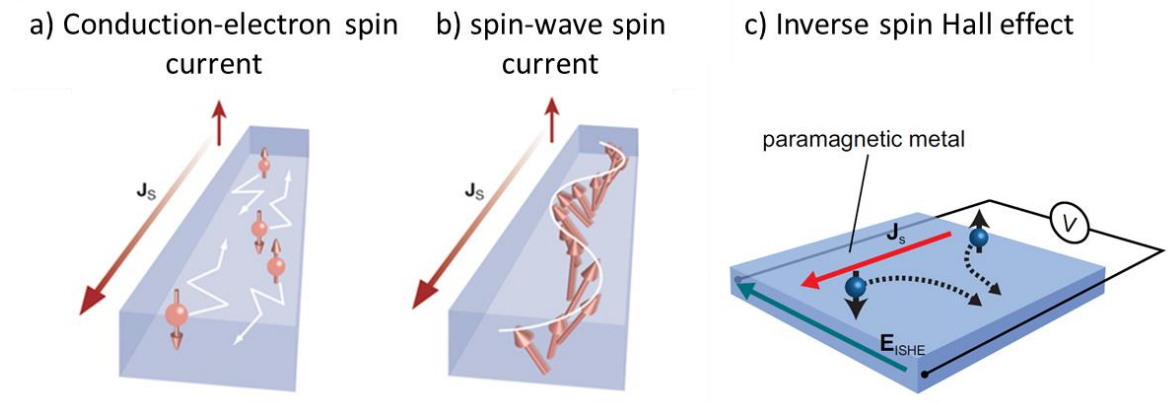


Figure 14: Depiction of the two types of spin currents: (a) conduction-electron spin current and (b) spin-wave spin current (taken from reference [63]). (c) Schematic of ISHE, (taken from reference [64]).

layer. Due to the inverse spin Hall effect (ISHE) [57–59] the spin current J_s is transformed into a transverse electric voltage in result of spin-dependent scattering to opposite sides, schematically depicted in figure 14c. In this way the generated electric field can be defined as follows [60]:

$$E_{\text{ISHE}} = (\theta_{\text{SH}}\rho)J_s \times \sigma \quad (3.1)$$

where θ_{SH} is the spin Hall angle, ρ the electrical resistivity of the normal metal and σ the spin polarization vector.

The occurrence of the SSE was also reported for ferromagnetic semiconductors [61] and insulators [60] in this configuration. Furthermore, the researchers detected this effect in the longitudinal configuration (figure 13a) by using $\text{Y}_3\text{Fe}_5\text{O}_{12}$ (YIG), a ferrimagnetic insulator [62].

In conclusion, they demonstrated the generation of a spin voltage over such macroscopic length scales not limited by the spin diffusion length and even in insulators in which the energy bandgap limits the electron excitation. Hence, the results show that this effect is different from the scenario described by Johnson and Silsbee. For instance, Kajiwara *et al.* [63] pointed out that spin currents can either be initiated by conduction electrons or spin waves as depicted in figure 14a/b. In this regard, the SSE can be explained as an effect that originates from the collective spin excitation interacting with phonons as spin waves.

Despite the first reports of the SSE in the transverse configuration (TSSE), in several other experiments the effect could not be identified [53, 55, 64, 65]. Although, PNE and TSSE are detectable in the same measurement geometry only the PNE contributed to the thermovoltage signal [53–55].

However, the SSE in the longitudinal configuration (LSSE) was measured by several groups [66–68] in different materials. In addition, this effect can be overlain by the ANE due to the same measurement configuration (see figure 12a and 13a for comparison).

For detailed information about the SSE in the longitudinal geometry I refer to the reviews of Uchida *et al.* [69] and Adachi *et al.* [70].

The combination of SDSE and SSE builds the basis for the design of THz emitters composed of CoFeB and NM materials with different spin Hall angles.

Recently, Kampfrath *et al.* [15] demonstrated in theory as well as experimentally the generation of femtosecond spin currents in magnetic heterostructures. A femtosecond pump pulse excites the spins in the ferromagnetic Fe layer. Since the majority spins own a much higher velocity than the minority spins a spin-polarized current is injected to the adjacent NM capping layer. Two different NM layers are tested, one with high electron mobility (Au) and one with a rather low electron mobility (Ru) resulting in different transport dynamics. Due to the much higher band velocity of the *sp*-states in Au, the electrons just stay short before back-reflection into the Fe layer. This is in contrast to Ru where the electrons will occupy the *d*-bands with rather low velocity. Thus, by using Ru as cap layer the transport of the electrons is much slower and an enhanced spin accumulation is predicted. The relaxation occurs by spin flips together with spin waves generation. Taking advantage of ISHE the generated spin current is converted in an ultrafast charge current. In result, a THz pulse is generated. The principle of THz pulse generation is depicted in figure 15. The experimental

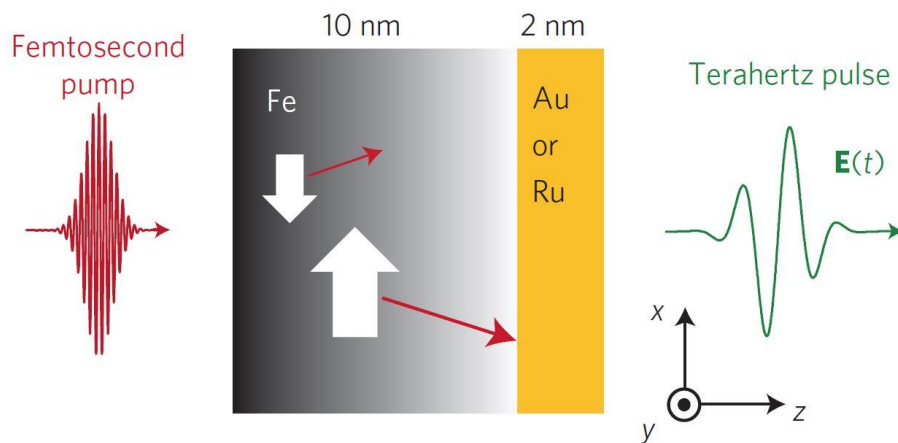


Figure 15: Scheme of THz generation. A femtosecond pump pulse excites the spins in the ferromagnetic Fe layer. The majority spins (big arrow) are much faster injected to the adjacent capping layer. The resulting electron transport dynamics lead to a THz electromagnetic pulse. (M is oriented in the y -axis). Taken from reference [15].

results agree with the theoretical model demonstrating the strong influence of the magnetic heterostructure design. Due to the faster dynamics, the Fe/Au sample covers a wider emission spectra of 0.3 to ~ 20 THz compared to Fe/Ru with emission in the frequency range of 0.3 to ~ 4 THz. In addition, a sign change of the THz waveform is observed for the Fe/Au film. Furthermore, the samples also reveal an unequal dependence of the THz emission on the pump pulse energy. The THz energy for Fe/Ru saturates at a fluence of $\sim 1 \text{ mJ cm}^{-2}$, while the THz energy for the Fe/Au sample scales linearly with the pump fluence.

The results presented by Kampfrath *et al.* serve as a basis for the design of highly efficient THz emitter. Our investigations concerning this topic are described in the included thesis manuscript: 'Efficient metallic spintronic emitters of ultrabroadband terahertz radiation'.

2. Materials & Methods

This chapter contains the information of the sample fabrication and preparation with focus on the MTJs since the heterostructures for THz emitters are fabricated with the same deposition procedure but without additional patterning.

In detail, a description of the layer deposition in our homebuilt ultrahigh-vacuum (UHV) chamber which was further developed over the last years and the design of the device for electrical connection in the measurement setup is given. In the subsequent part, the measurement equipment is described highlighting the improvements added in the course of this thesis after the first observation of the TMS by Walter *et al.* [13] and the relocation of this setup from Göttingen to Greifswald. All TMS and TMR measurements included in the integrated manuscripts are performed by myself or under my supervision in the described setup.

2.1 Sample fabrication

The samples produced in Greifswald consist of CoFeB-based electrodes with a thin MgO barrier and are fabricated in a home built UHV system with a base pressure of 5×10^{-10} mbar. This setup was improved step by step over the last two decades with focus on the MTJ fabrication.

As substrate material MgO (100) was chosen to avoid interfering conductance effects from semiconducting substrates as described in reference [37]. The $\text{Co}_{20}\text{Fe}_{60}\text{B}_{20}$ electrodes (EDX and XPS analysis: Co:Fe 0.32:0.68) and the Ta buffer layer are fabricated by magnetron sputtering using 2 inch targets. The MgO barrier is e-beam evaporated in a separate adjacent chamber without exposing the sample to ambient conditions. The O_2 partial pressure is controlled for each sample barrier and kept constant within one series of samples via an implemented HIDEN mass detector. On top of the film stack, a Ru capping layer is deposited by electron-beam evaporation to prevent oxidation of the underlying layers. The sample stacks are *ex situ* annealed in an applied in-plane magnetic field of 300 mT at a temperature

of 450°C for one hour in a separate high vacuum chamber. During this procedure, the amorphous CoFeB electrodes crystalize around the MgO layer and the B diffuses into the Ta layers. The Boron in the sputtering target is necessary for ultrasmooth amorphous layers. In this case, the Ta layers are good B sinks for both CoFe electrodes [23, 71, 72]. The final samples provide the necessary requirements for coherent tunneling described in chapter 1. The deposition and annealing process is followed by two lithography steps. First, elliptical MTJs are patterned by electron-beam lithography and then ion-beam etched. For this purpose, the sample is coated with a negative resist (AR-N 7520-18 at 5000 rpm for 30 s, bake-out 2 min at 80 °C on hot plate), that is afterwards exposed with a Zeiss Leo 1530 scanning electron microscope (SEM) equipped with a high precision interferometer sample positioning stage and a Raith lithography unit. Note, that the ellipses are orientated with the long axis parallel to the direction of the magnetic field applied during the annealing procedure. After the exposure, the unexposed resist and the underlying layers are removed by Ar ion etching until only the MTJ pillars and the bottom layer remain. This procedure is controlled by a secondary ion mass spectrometer (SIMS). Finally, Ta₂O₅ (150 nm) as isolating material between individual MTJs is sputtered and subsequently, the residual resist and markers are removed from the sample in an ultrasonic bath of 1-methyl-2-pyrrolidinone. This procedure is followed by the deposition of a 5-nm-thick Ta adhesion layer and a 70-nm-thick Au layer on top of the MTJ pillars. In the second lithography step, the Au layer is patterned to enable individual contacting of the MTJs. In this regard, the sample is again covered by a negative resist which is consequently exposed in a pattern by e-beam lithography which in result builds the Au contact pads. This procedure is again followed by Ar ion etching until the conducting material vanishes and the Ta₂O₅ appears. Afterwards, the remaining resist and markers are removed. The complete sample stack consists of Au 70 nm/ Ta 5 nm/ Ru 3 nm/ Ta 5 nm/ CoFeB 5.4 nm/ MgO 2.1 nm/ CoFeB 2.5 nm/ Ta 10 nm/ MgO substrate.

2.2 Electrical access to the sample and sample design

The sample is electrically accessible in the experimental setup by implementation into a ceramic IC bond socket with 24 pins (NTK, IDK24F1-6099AAL). The individual MTJs are connected to the pins by ball-wedge bonding with a 25 μm -wide Au wire using the HB10 tpt wire bonder. Here, the parameters have to be carefully adapted in order to achieve a good adhesion between sample and gold wire and to avoid the destruction of the junction by mechanical stress. The Ta layer beneath the CoFeB electrode acts as the bottom contact and is identical for all MTJs. The receptacle for the bond socket is positioned in between the pole shoes of the electromagnet in the experimental setup.

The MTJs are sensitive to electric breakdown. For this reason, the laboratory is equipped with electrostatic discharge (ESD) accessories, e.g. antistatic chairs, electrical grounding wristbands for the experimenter and insulating mattings especially for the wire bonding process. The bonded sample is transported in ESD sample boxes.

The investigated samples are partly fabricated in Greifswald and in Bielefeld. A comparison of the samples is listed in table 1. They differ in the electrode composition due to the used sputtering target material. The samples produced in Bielefeld consist of one antiferromagnetically pinned electrode. This means the magnetization of one electrode is constantly fixed within the magnetization field strength of our measurement setup. In this case, only one parallel and one antiparallel alignment of the electrodes is possible. This kind of devices are more applicable for memory devices in comparison to pseudo spin-valves because they provide a wider range of the antiparallel magnetization state. Despite these benefits the disadvantage lies here in the possibility of Mn and Ru diffusion into adjacent layers [24] that can limit the effect ratios.

Table 1: Comparison of the samples fabricated in Greifswald and Bielefeld.

	Greifswald samples	Bielefeld samples
layer stack	pseudo-spin valves	*
electrode composition	$\text{Co}_{20}\text{Fe}_{60}\text{B}_{20}$ (Co:Fe 0.32:0.68)	$\text{Co}_{40}\text{Fe}_{40}\text{B}_{20}$ Co_2FeSi , Co_2FeAl
barrier material	MgO electron-beam evaporated	MgO, MAO sputtered
substrate material	MgO (100)	MgO (100)

* one electrode is antiferromagnetically coupled by use of an additional MnIr layer

The next parameter that differs for the samples produced in Bielefeld and Greifswald is the process of the barrier deposition. While we use electron-beam evaporation for MgO the MTJs fabricated in Bielefeld are sputtered.

The samples consisting of Heusler electrodes as well as the samples with MAO barrier are fabricated in Bielefeld. The detailed sample fabrication process is described in reference [73] for the Heusler samples and the fabrication of devices with MAO barrier in reference [29]. The same sample layout is preferred for all samples allowing the electrical connection via wire-bonding. The single bondpads are organized in columns and rows to detect them in the experimental setup. The size of the Au bondpads is adapted to cover the MTJ and prevent heating from below and to the size of the ball-bond. The used sample design is depicted in figure 16. The microscopic picture (fig. 16b) illustrates a group of four bondpads with MTJs of different size, while the bottom right junction is connected via wire-bonding.

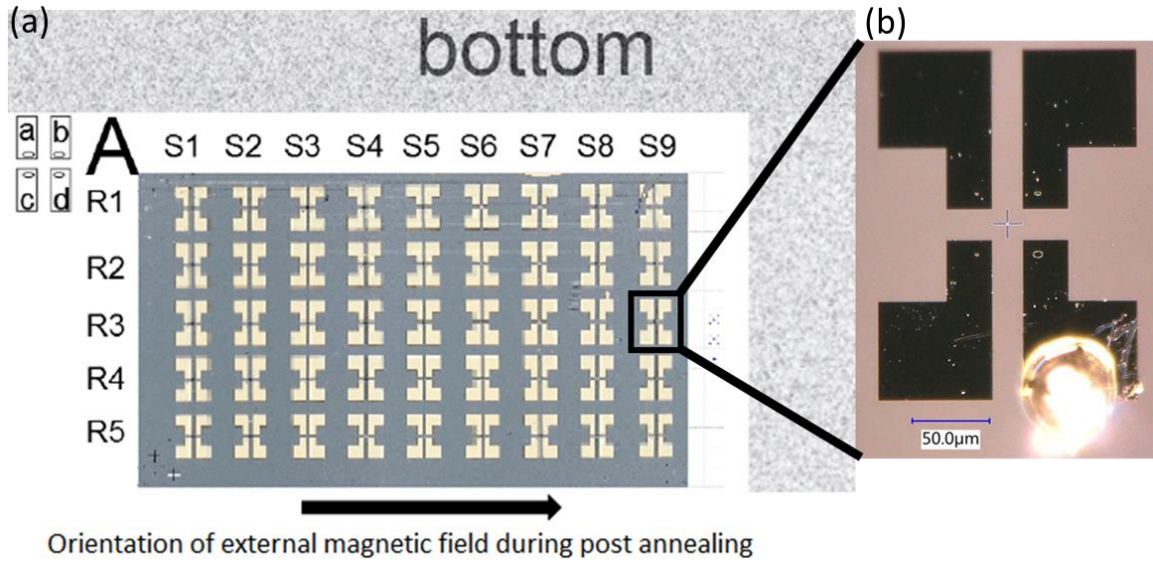


Figure 16: (a) Schematic depiction of the sample layout together with a microscopic picture of the sample. The MTJs are quadripartite arranged. The annealing magnetization field is aligned in the long axis of the subsequent patterned ellipses. (b) Microscope picture of a wire-bonded MTJ.

2.3 Experimental setup

In this section, the experimental setup that is specifically designed and optimized for the TMS measurements is described in detail. All samples are measured in the setup established in Greifswald that has been continuously improved as a central aspect of this thesis.

Because of the small measurement signals in the μV -range and the sensitivity of the devices, the setup needs a separate optical table to avoid in-coupling signals of adjacent experiments. For the same reason the controlling and measuring electronics are connected to separate power stations and the electrical grounding is realized in a star-layout. In addition, the sample holder is electrically isolated from the electromagnet. The sample itself is very sensitive to voltage peaks that arise while the connected measurement electronics are exchanged for different experiments and thus a circuit breaker is integrated to avoid such sample damaging signals by shortening the top contacts and bond contacts during this procedure. Consequently, it is necessary for the experimenter to wear ESD shoes and an electrical grounding wristband.

The temperature gradient across the layer stack of the tunnel junction is generated optically using a laser diode (TOPTICA ibeam smart) with a wavelength of 638 nm and a tunable power range of 1 mW to 150 mW. The laser diode is modulated by a waveform generator (Agilent, 33500B series) in a square wave at a frequency adapted to the impedances of the samples between a few Hz up to the kHz range, which is also used as modulation frequency for the lock-in amplifier.

The laser spot diameter can be adjusted between 2 μm and 8 μm full-width at half-maximum by varying the distance between the microscope objective (NIKON, primary magnification 20x, working distance 20.5 mm, numerical aperture 0.35) and the sample. Thus, the maximum power density applied to the sample with a minimized spot size equates to $\leq 47.75 \text{ mW } \mu\text{m}^{-2}$. The position of the laser spot on the sample is controlled by a CCD camera with a confocal microscope arrangement. For an exact characterization of the beam width, the knife edge method [74] is used. For this purpose, a photodiode is implemented, collecting the reflected light of a sharp edge. The reflection of the gold pad differs from that of the insulator surface and thus the diode voltage changes depending on the position of the laser spot. Moving the laser beam over a well-defined edge from the Au bondpad to the insulator the diode signal is measured. From this curve the beam width is determined from the error function fit.

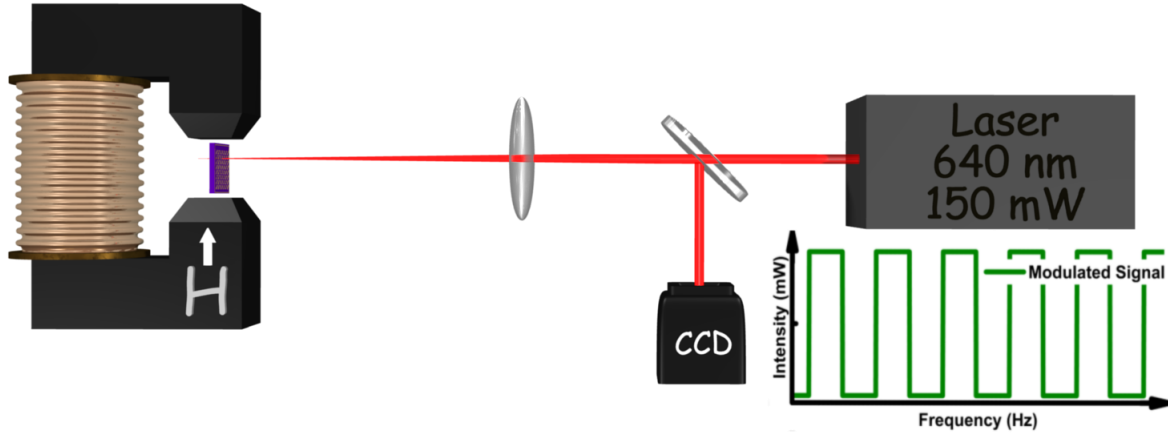


Figure 17: Schematic illustration of the main components building the TMS measurement setup.

For magnetization dependent measurements, the sample is placed in between two pole shoes of an electromagnet (max. 40 mT) on a ceramic IC bond socket. On this unit linear stages with motorized actuators are implemented to enable the defined movement in x- (horizontal), y- (vertical) and z-direction and thus an exact positioning of the laser beam on the sample surface. Thus, automated position dependent measurements of the thermovoltage versus the magnetization direction are possible.

In the first instance, the setup is designed to determine the TMS. Besides this, the junction functionality can be confirmed by recording TMR curves in between the TMS measurements. Therefore, the setup is equipped with a Keithley 2400 sourcemeter in constant voltage mode to record the current with a bias voltage of 10 mV. From the resistance versus magnetic field data the TMR ratio of the MTJ according to equation (1.1) is determined.

Furthermore, for the determination of the TMS effect a voltage preamplifier in DC mode with a gain of 60 dB (factor 1000) and a bandwidth of 100 kHz is incorporated. Subsequently, the thermovoltage is detected with a lock-in amplifier (Stanford Research Systems SR830) that is locked to the modulation frequency of the laser diode. To observe the temporal evolution and phase of the generated voltage signal an oscilloscope is implemented in the setup monitoring the diode signal of the reflected light, the modulation frequency of the laser and the lock-in signal. The saturation of the voltage signal is observed and thus, the appropriate modulation frequency can be chosen. All measurements are performed at an ambient temperature of 295 K. A simplified illustration of the measurement setup is given in figure 17.

2.4 Lateral heat maps

In addition to the conventional use with a laser spot adapted to the junction size and a central positioning on the junction resulting in homogenous temperature gradients, throughout this work this setup has been upgraded to enable the creation of temperature gradients in three dimensions. In this regard, motorized actuators have been implemented. The flexibility of the laser spot positioning allows a precise positioning on the junction center and enables the systematical analysis of lateral heating effects through a wide-ranging variation of the created temperature gradients. The related investigations are realized through lateral heat maps which experimental procedure is schematically shown in figure 18a.

The motorized actuators with a step size of $\geq 0.2 \mu\text{m}$ together with new linear stages allow a very precise laser positioning in all three dimensions. The z-axis defines the direction in line with the focusing objective and the sample (see figure 18b). Thus, through the controlled variation of the distance between objective and the sample surface the laser spot size on the sample can be adapted. An exact positioning allows a minimum spot size diameter of $2 \mu\text{m}$ (FWHM) which is the best size for the lateral heat maps. In addition, linear stages with motorized actuators are integrated on the sample holder for the horizontal and vertical movement (x- and y-axis) of the sample with respect to the laser beam.

To create a huge variation of temperature gradients on the MTJ also the junction size must be adapted. Therefore, the junction needs to be bigger than the laser spot size. In our investigation we use elliptical junctions with dimensions of $6 \times 4 \mu\text{m}$ in diameter. An area of $30 \times 30 \mu\text{m}^2$ is scanned. In this procedure, first the MTJ is located with the use of the camera. Subsequently, the exact alignment is done by maximizing the generated voltage signal with the movement in the x- and y-axis of the sample in steps of $0.2 \mu\text{m}$. From this point the heating laser spot is moved $15 \mu\text{m}$ left and $15 \mu\text{m}$ up (see figure 18a). This is the starting point for the measurements. Here, the first TMS measurement is done. Afterwards, the laser spot is moved in $1 \mu\text{m}$ steps while at every single position the generated thermovoltage is measured. The sample is scanned line by line starting with horizontal movement from the highest left point (1;1) and ends up with the lowest right point (30;30) as indicated in figure 18a. Within the framework of this procedure, the resulting pattern consists of 30×30 points and thus 900 individual measurements are performed on a single MTJ and beyond. The performance of those systematic measurements leads to a strong variation of the created temperature profiles within MTJs together with a high spatial

resolution. The analysis of the data reveals a map of thermovoltages generated on the measured area. For example, the extracted V_p and V_{ap} data for one 2-dimensional scan are illustrated in three-dimensional surface plots in figure 18c and d, respectively. Here, the position of the MTJ is determined by a Gaussian surface fit and centered in the graphs displaying the extracted data for a sample area of $20 \times 20 \mu\text{m}^2$.

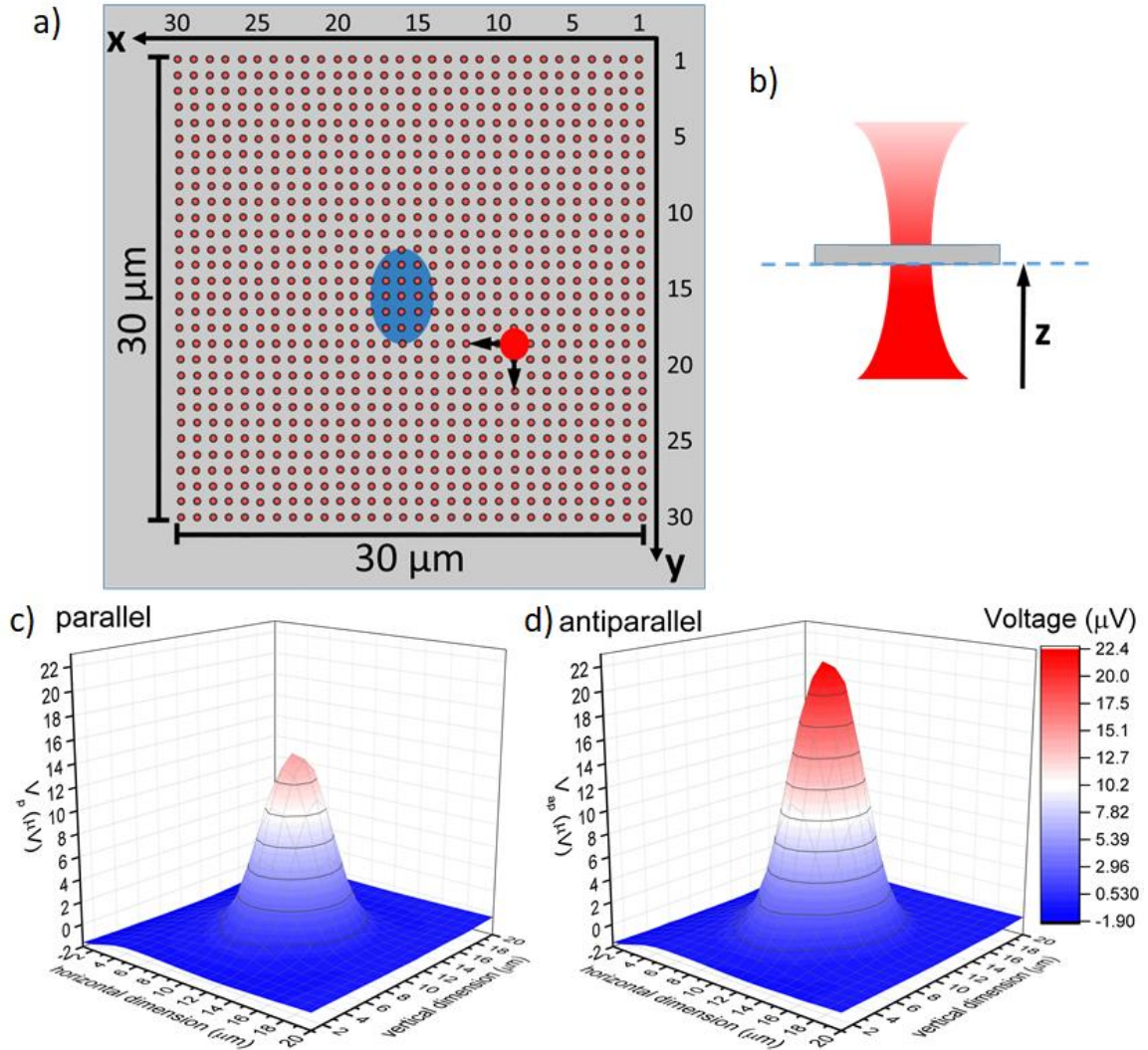


Figure 18: (a) Schematic depiction of the experimental procedure for lateral heat maps over an area of $30 \times 30 \mu\text{m}^2$. The MTJ is indicated in blue. The pattern formed by the small red dots illustrates the different positions for the measurements. The laser spot is indicated by the red point with arrows which show the movement of the heating position. (b) Illustration of the z-dimension. The distance between focusing objective and sample surface defines the laser spot size. (c) and (d): extracted V_p and V_{ap} data in a three-dimensional surface plot for an area of $20 \times 20 \mu\text{m}^2$, respectively.

3. Results/Publications in summary

The improvements of the TMS measurement setup described in the Material & Methods section and realized in the frame of this thesis allow a highly flexible variation of the temperature profile applied to the MTJ. The building of lateral heat maps from systematical measurements leads to the investigations described in the following sections.

Furthermore, TMS measurements are performed with different MTJ compositions. In this regard, half-metallic Heusler compounds are used as one electrode. Another possibility is to replace the MgO barrier. This is done by employing MgAl_2O_4 barriers in combination with CoFeB electrodes. Moreover, the barrier thicknesses for MAO as well as for MgO are varied to study the influence on the TMR and TMS effect. These investigations are described and summarized in the second section of this chapter. All of the reported TMS measurements are realized at the Greifswald setup.

An additional goal of this thesis is the development of new THz emitter. This is done in a collaboration with the Fritz-Haber-Institute Berlin. A main part of the used devices in this studies were produced in Greifswald. In consequence, I have fabricated more than 40 samples contributing to this research. The related investigations are summarized in the last section.

3.1 Investigations enabled by lateral heat maps - Articles I+II

In the manuscript “Pumping laser excited spins through MgO barriers”, we report a systematical study investigating the influence of the size, position and intensity of the laser spot on the generated thermovoltages as well as the resulting TMS effect in MTJs.

In this regard, we determined TMS ratios from 55 % to 65 %, from Seebeck voltages generated through homogenous heating of the layer stack which remain constant within the variation of the applied power density. The laser spot size is a critical parameter to obtain specific TMS ratios. Measurements with heating areas bigger than the MTJ itself reveal an influence of edge effects. The generated thermovoltages are drastically reduced and even cross zero and change sign. This leads to calculated TMS ratios which exceed 1000 %.

A further aspect of this publication is the first systematical study of thermovoltages generated over large MTJ areas using a high spatial resolution. For this purpose, the minimized heating laser spot is automatically moved to different positions across the MTJ and beyond. The recorded lateral heat maps mirror the thermovoltages that are created by varying heat distributions within the studied device. Consequently, the sensitivity of the thermally induced spin transport to the change of temperature gradients is depicted. This extended technique, to automatically heat different areas and record TMS hysteresis loops permits us to investigate the origin of the arising voltages and track down the shape and direction of the temperature gradients. Hence, misleading results due to the heating of the MTJ edges and thus the creation of lateral temperature gradients are depicted. In fact, those effects have to be considered for the determination of the Seebeck coefficients. With respect to this aspect, also discrepancies in comparison to theoretical calculated values could be interpreted.

These new insights are of great importance for future investigations of spin transport and excitation in magnetic materials, and of great general interest as a system for thermally induced data readout for future magnetic storage applications. Furthermore, we built a new basis to compare the calculated Seebeck coefficients with experimentally obtained data.

In the second thesis article “Anomalous Nernst effect on the nanometer scale: exploring three-dimensional temperature gradients in magnetic tunnel junctions”, we employ the TMS setup together with the performance of lateral heat maps to extend the knowledge and analyze the contribution of thermal effects generated by in-plane temperature gradients.

The change in the thermovoltage signal being different to general TMS curves is discussed. Within this investigation we identified the ANE contributing to the TMS signal, resulting in an asymmetry of the voltage signal for the two parallel magnetization states observable by the usage of pseudo spin-valves. So far, experiments verifying the ANE have been performed on thin films [46, 48–50, 53, 55, 75, 76], micrometer sized hallbar geometries [47, 77, 78] with bulk like properties and very recently in nanowires [79, 80]. Here, we report the first observation of this thermomagnetic effect in such a configuration and in addition within MTJs. While the detection is performed out-of-plane within the nm-length scale, the temperature gradient expands in-plane on the μm -scale. The determined Nernst coefficient for CoFeB is $K_N \approx 1.6 \cdot 10^{-8} \frac{\text{V}}{\text{T}\cdot\text{K}}$ which is lower than previously reported ANE coefficients [47, 79, 81, 82]. This points out the high sensitivity of our ANE detection method.

The temperature distribution within the MTJs achieved by our laser heating method is derived from finite element simulations (COMSOL) and supports our results.

In the following, additional analyses are displayed which are not yet published. This experiments are carried out to study the influence of the rotation of the magnetization vector. For this purpose, the MTJ is rotated in the external field. Since the anisotropy plays a role, it is investigated first. In this regard independent experiments are carried out to determine the in-plane anisotropy of the examined MTJs.

First, static hysteresis measurements are performed conducted on the magnetic layers after annealing, but before structuring elliptic MTJs. Here, the crystalline anisotropy, which is dominant is already formed. The results of the magneto-optical Kerr-effect (MOKE) measurement are presented in figure 19. The sample is rotated with respect to the applied magnetic field $\mu_0 H$. For the anisotropy analysis, the MOKE signal (black) needs to be decomposed into the linear, longitudinal effect, LMOKE part (blue) and the quadratic effect, QMOKE part (red). The decomposition is done following the procedure described in reference [83]. The QMOKE contribution originates from magnetization components perpendicular to the plane of incidence. In the present LMOKE setup, QMOKE contributions can occur if the magnetization is still pointing in the sample plane, but divergent to the external field. The data in figure 19 represents weak QMOKE contributions at the rotational angles of 135° and 315° . Here, the QMOKE signal increases and shows delta like peaks in the vicinity of the coercive field, where the magnetization is rotated and changes sign quite abruptly. The broadening of the peaks can be attributed to the angle precision during manual sample positioning. Both angles, 0° and 180° as well as 90° and 270° show QMOKE contributions of different sign but similar amplitude. This indicates the

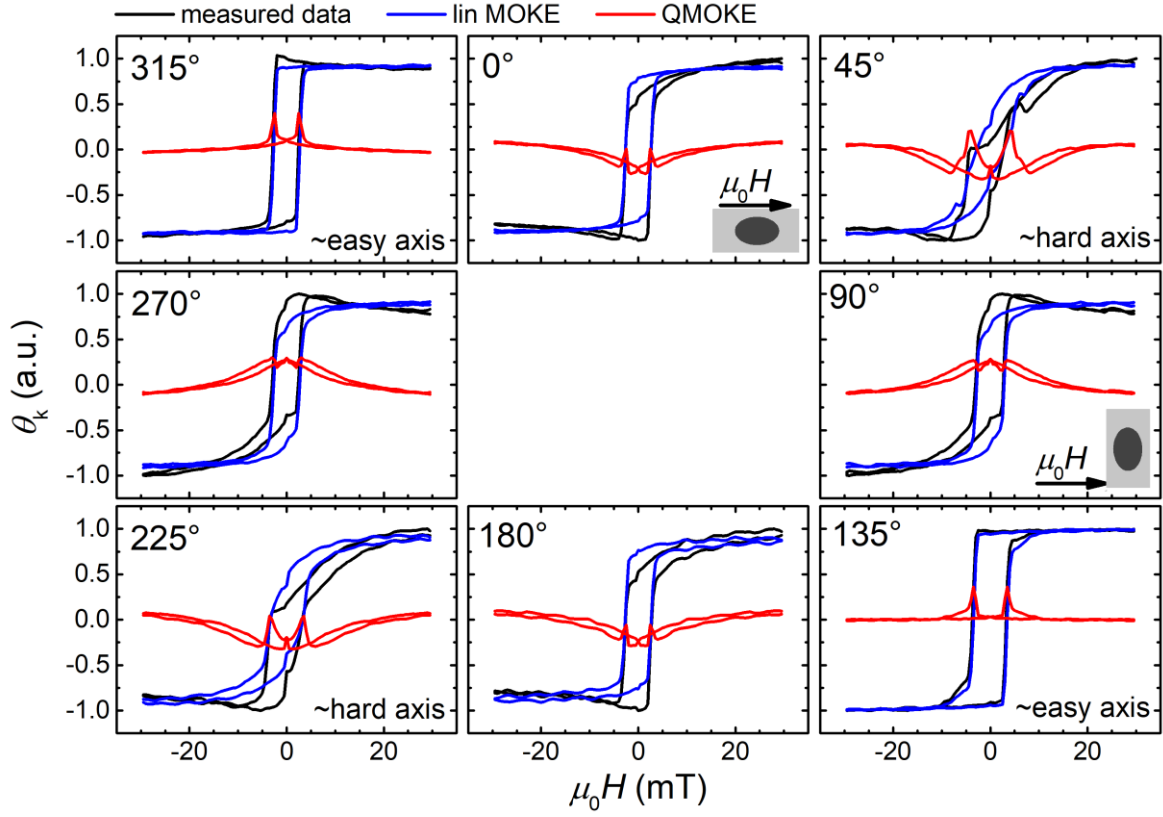


Figure 19: Hysteresis MOKE measurements (black curves) for different rotation angles with respect to the external field. The alignment of the afterward structured ellipses is indicated for 0° and 90° , respectively. The blue/red curves show the linear/quadratic contribution to the MOKE signal. The easy and hard magnetization axes are identified from the quadratic part according to the discussion in the text.

same deflection of the external field to the easy axis but different directions. The strongest QMOKE contribution is observed for the 45° and 225° rotation angles. In conclusion, the easy axis of magnetization is identified within a sample rotation of 135° and 315° , while the hard axis corresponds to a rotation of 45° and 225° . That means, due to crystalline anisotropy, the layers exhibit an uniaxial magnetic anisotropy along the crystallographic (001) direction of the MgO substrate or along the 45° direction in our coordinate system.

In addition, the TMR is measured with the MTJ aligned at different rotation angles ϕ_E in respect to $\mu_0 H$ (see figure 20). The geometries correspond to the alignments in figure 19. The graphs are grouped by colors for the same ellipse orientation with respect to the $\mu_0 H$ direction, but different sign. All groups show characteristics that enable the deduction of the magnetization easy axis. The low TMR ratios and broad regions of antiparallel magnetization alignment with suppressed change of resistance R as $\mu_0 H$ is increased, measured at $\phi_E = 45^\circ$ and $\phi_E = 225^\circ$ (dark yellow) suggest a maximum deflection of the magnetization easy axis in relation to the external field. Whereas, the high TMR ratio, the

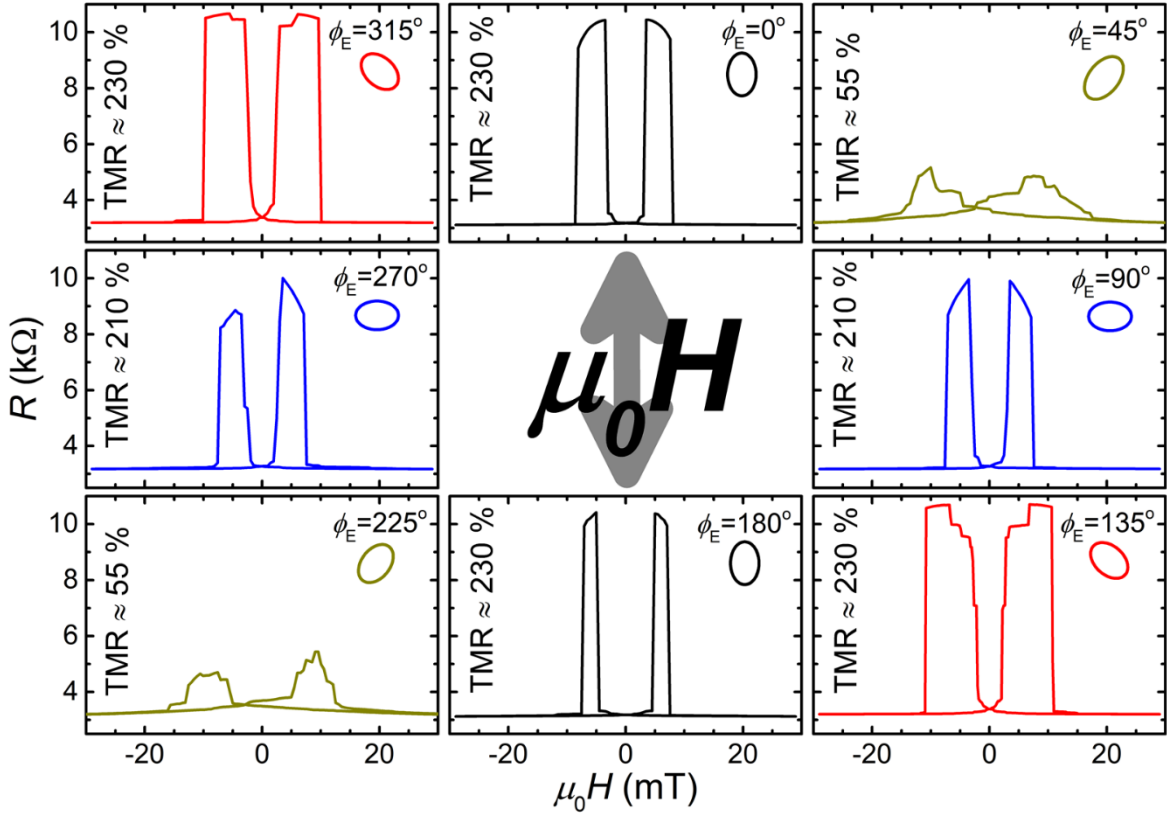


Figure 20: TMR measurements for MTJs rotated in an external field $\mu_0 H$ of constant direction. Note, that the plots with the same orientation of the MTJ to $\mu_0 H$ but different sign are grouped by the same colors. The MTJs are rotated by the angle ϕ_E . At $\phi_E = 45^\circ$ and $\phi_E = 225^\circ$ (dark yellow), the TMR is small and the antiparallel region is stretched. At $\phi_E = 0^\circ, 180^\circ$ (black), $\phi_E = 90^\circ, 270^\circ$ (blue) the TMR ratios are high, but the regions for antiparallel alignment are narrow and display sharpened pillars. At $\phi_E = 135^\circ$ and $\phi_E = 315^\circ$ (red) the MTJs show a broader region of antiparallel alignment with formation of defined plateaus, however they show jumps.

steep increase of R and the well-defined plateaus in the high R region suggest an alignment close to the easy magnetization axis. The steps visible in the plateaus illustrate a slight deviation of the easy axis that is given by the accuracy in the measurement setup. Measurements at the angles $\phi_E = 0^\circ, \phi_E = 180^\circ$ (black) and $\phi_E = 90^\circ, \phi_E = 270^\circ$ (blue) also show high TMR ratios, but the plateaus at high R show a slope. These slopes indicate a deviation of the easy magnetization axis, at which the magnetization aligns slowly with increasing external field amplitude. That means, the magnetization easy axis is oriented at an 45° clock wise rotation angle to the designated y-axis. This agrees with the conclusions from the MOKE measurements.

Finally, the ANE is measured at different ellipse rotation angles in relation to the applied magnetic field $\mu_0 H$, which is constantly kept in the y-axis as depicted in figure 21. For this purpose, furthermore lateral heat maps are recorded. The ΔV_{ANE} values are extracted in

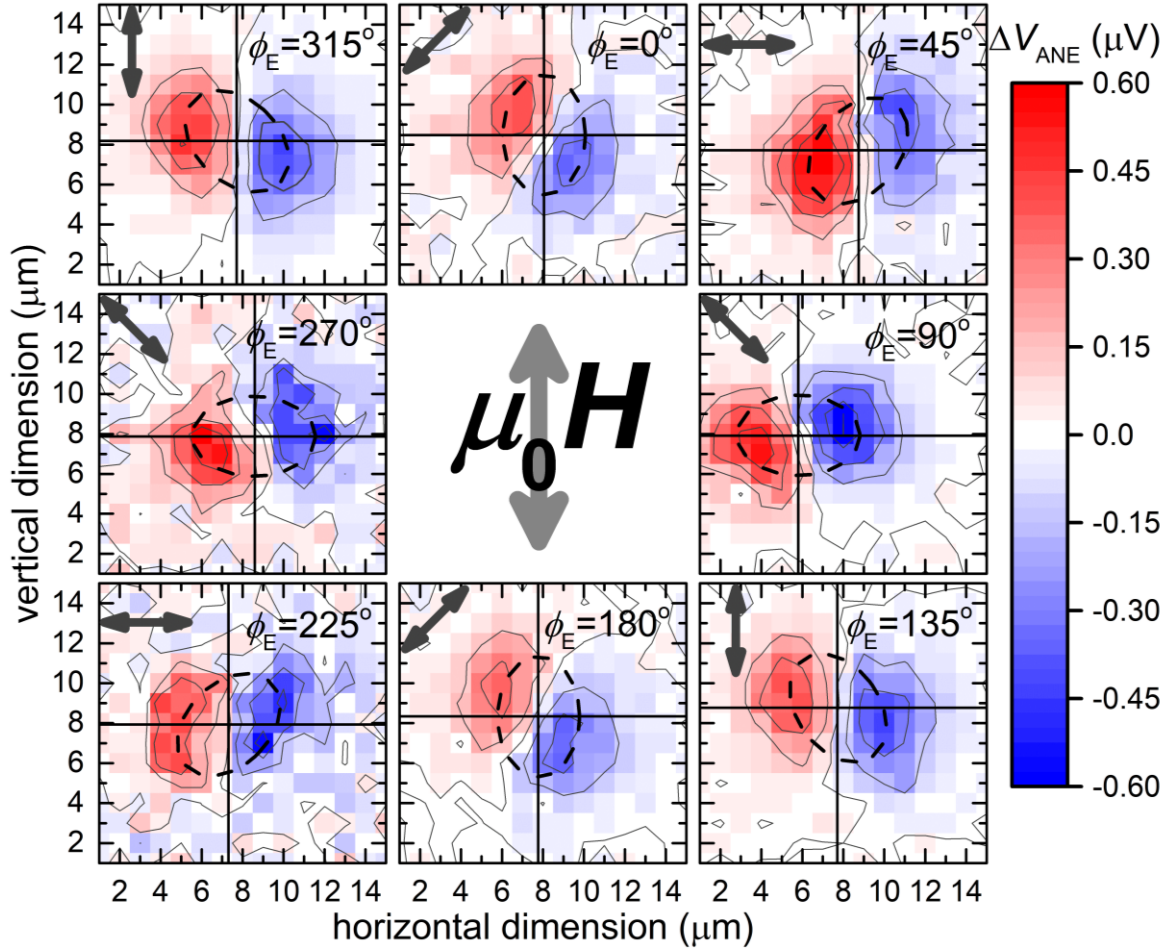


Figure 21: The extracted ΔV_{ANE} values for a full rotation ϕ_E of the elliptic MTJ (indicated by the dashed lines) in respect to the external field $\mu_0 H$ in steps of 45° . Note that due to experimental constraint, the MTJ center cannot be positioned in the center of the plot for every rotational degree.

accordance to the procedure of the manuscript “Anomalous Nernst effect on the nanometer scale: exploring three-dimensional temperature gradients in magnetic tunnel junctions”. Figure 21 displays the results in false color plots. Each graph exhibits an opposing pair pattern of ΔV_{ANE} elevation (red) and decrease (blue) separated by a transient borderline section. The patterns angular alignment changes, when the MTJ is rotated by ϕ_E . This is done in steps of 45° for a full rotation. For enhanced view, the dashed ellipses indicate the MTJ location in each graph of figure 21, and the dark grey arrows indicate the determined magnetization easy axis, identified by the previous measurements. The transient borderline aligns with the indicated magnetization easy axis, except for the MTJ orientations with $\phi_E = 45^\circ$ and $\phi_E = 225^\circ$, where the easy axis is oriented perpendicular to $\mu_0 H$. Due to anisotropy effects, at $|\mu_0 H| = 30$ mT the magnetization is still aligned with its preferred direction along the uniaxial magnetic anisotropy (UMA) axis, although both CoFeB electrodes magnetization are aligned parallel. That leads to the rotation of the characteristic pattern in

the graphs. The MTJs center are determined from a Gaussian fit of the extracted voltage signal, then the dotted ellipse lines are placed to determine the location. Subsequently, the ΔV_{ANE} values are extracted along this contour. The results are plotted in a false color plot in figure 22 with two profile plots. The top plot shows ΔV_{ANE} extracted at an angle of $\phi_E = 315^\circ$ position for a varying angle of the applied temperature gradient ϕ_{VT} , whereas the right profile plot shows the values extracted at $\phi_{VT} = 120^\circ$. The top profile shows a sine behavior without any phase shift. This is expected, because for this MTJ positioning, the magnetization easy axis is aligned parallel to $\mu_0 H$. The side profile shows a symmetrical profile around the $\phi_E = 180^\circ$ ellipse orientation. This is expected, because a rotation by more than 180° leads to the same orientation in the interplay between the magnetization and the temperature gradient. The phase shifts are analyzed by fitting:

$$\Delta V_{ANE} = A \cdot \sin(\phi_{VT} - \phi_0) + V_0$$

to the extracted ΔV_{ANE} for each ϕ_E . The results are presented in figure 23. A is the maximum signal amplitude, ϕ_0 the phase shift and V_0 is the offset. The maximum amplitudes A lie usually around $\sim 0.4 \mu V$ and do not show any significant variation with the MTJ orientation. The offset is $\sim 0 \mu V$ without any significant aberrations. The phase shift ϕ_0 ranges from -45° for $\phi_E = 0^\circ$ and $\phi_E = 180^\circ$ to $\phi_0 = 20^\circ$ for $\phi_E = 90^\circ$ and $\phi_E = 270^\circ$. The smaller positive shifts for the latter two MTJ position angles can be explained by considering the interplay of anisotropy contributions. In this case the shape anisotropy is an influencing factor. For temperature gradient angles $60^\circ \leq \phi_{VT} \leq 90^\circ$ and $240^\circ \leq \phi_{VT} \leq 270^\circ$, the voltages exhibit almost constant levels for a full rotation of ϕ_E , the former are positive, the latter negative.

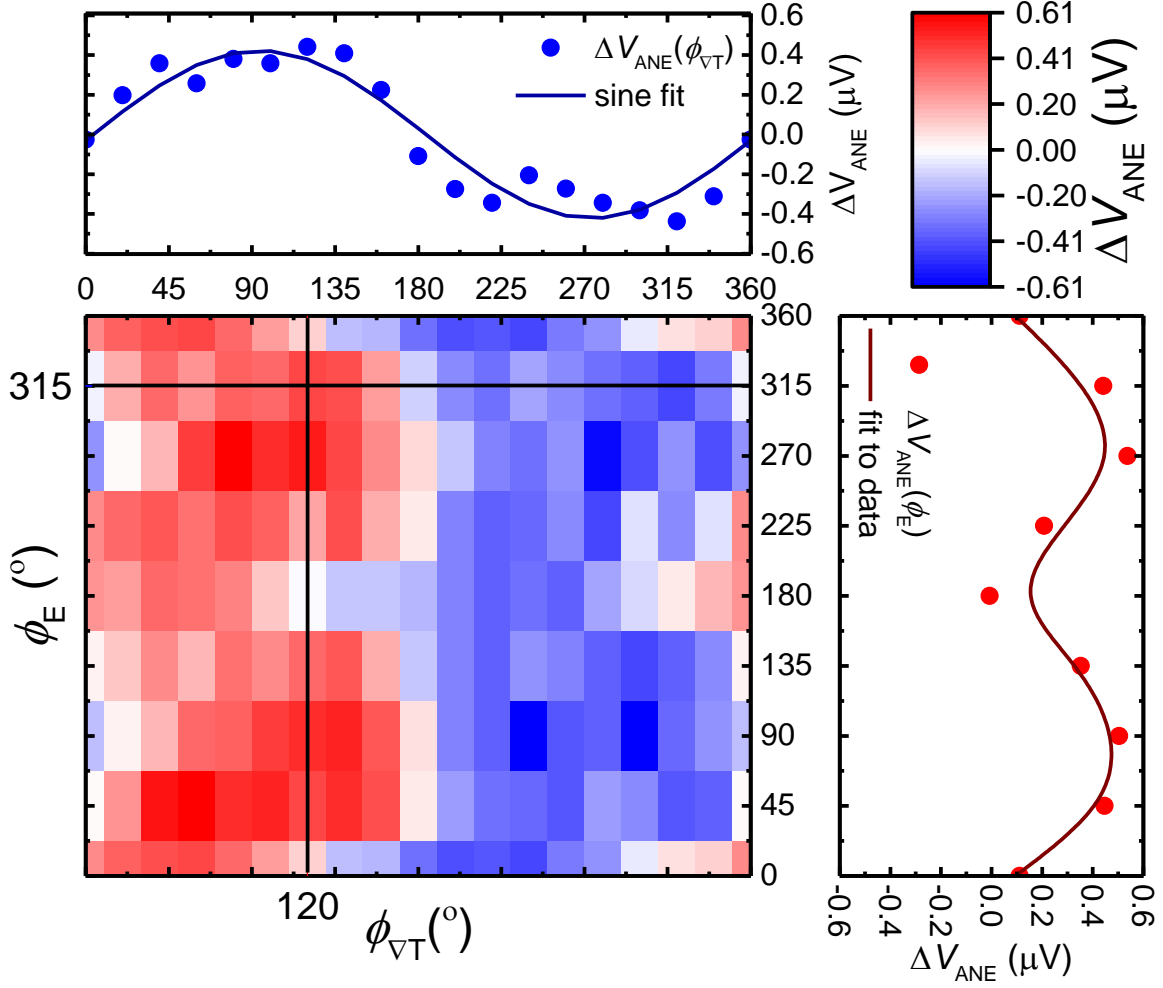


Figure 22: ΔV_{ANE} values extracted from data shown in figure 21. For each MTJ rotation ϕ_E , the values are extracted along the ellipse contour and thus plotted in respect to the temperature gradient angle ϕ_{VT} . The starting point is at the top position, so that at $\phi_{VT} = 0$, $\phi_{VT} \parallel \mu_0 H$. The top profile shows ΔV_{ANE} data points with respect to ϕ_{VT} , exemplary for $\phi_E = 315^\circ$, when $\mu_0 H$ is applied along the easy magnetization axis. The right profile plot along the $\phi_{VT} = 120^\circ$ line shows the extracted ΔV_{ANE} values plotted against ϕ_E . In both plots, the fitted lines are guides to the eye.

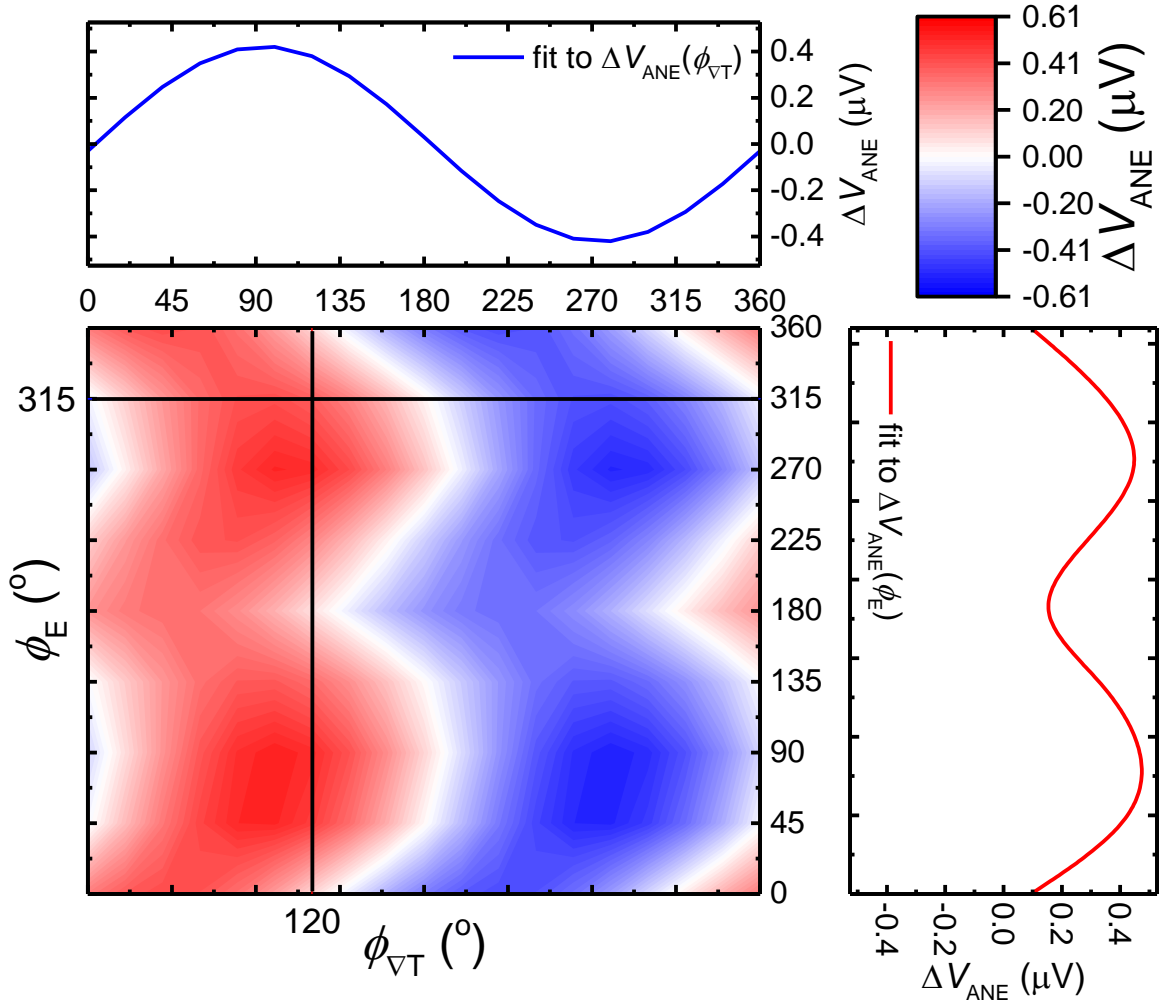


Figure 23: Sine fits to the data shown in figure 22 with exemplary profile plots at the same position as in figure 22.

This analysis results open new possibilities for MTJ applications additional to data storage. Making use of the interplay between temperature distribution and magnetization properties voltage generation can be controlled at desired locations. This allows the design of new logic devices in the μm -range that can be operated by energy harvesting using waste heat that is available in almost all conventional microelectronic devices. Further applications are precise thermometers, that do not only measure the local temperature, but also the direction of the temperature gradient, which opens new ways to monitor densely stacked electronics and, for example, detecting malfunctioning components directly inside a microchip, by the microchip itself.

3.2 Ways to control the tunnel magneto-Seebeck effect - Articles III-V

MTJs are well-studied devices in focus of the high TMR ratios they exhibit. Thus, they can be produced in high quality and are already commercially available as part of MRAMs. In this context MTJs are the building blocks for modern spintronics. In contrast to the TMR, the TMS ratio obtained in MTJs with CoFe electrodes is relatively low with ratios of only several 10 %. In addition, the observed thermovoltages are in the μV -range. For this order of magnitude, the devices are inapplicable for technical implementation. Therefore, the challenge is to enhance this effect in terms of thermovoltage as well as effect ratio.

As pointed out in the introduction the TMS for CoFeB/MgO/CoFeB junctions can be affected by adapting the composition of the CoFeB alloy. Also, the fabrication of these devices with respect to the design of the interfaces requires adjustment.

Böhnke *et al.* [39] already demonstrated that the effect ratio can be tuned by applying a bias voltage. In this way the relative position of the Fermi level is shifted and the experimentally observed so-called bTMS ratio reached values of $\approx -3000\%$. However, our investigations are based on the temperature gradient as one and only driving force.

Another way to influence the asymmetry of the DOS and the temperature distribution is given by choosing different electrode and/or barrier materials. So far, MgO and Al_2O_3 are the best studied barrier materials together with CoFe-based electrodes in TMS devices. Within the following publications we expand this field. On one hand, we use half-metallic Heusler compounds as one electrode instead of CoFeB and in the second we use MgAl_2O_4 as barrier material. The results are summarized in the subsequent paragraphs.

In the publication “Large magneto-Seebeck effect in magnetic tunnel junctions with half-metallic Heusler electrodes” we present half-metallic Heusler compounds namely Co_2FeAl and Co_2FeSi as promising material to enhance both, the effect ratio as well as the generated voltage signal. We introduce a model based on the DOS which illustrates the spin-dependent thermoelectric transport and identifies the great potential of the half-metallic Heusler compounds. This model is confirmed by our experiments. First, we investigate tunnel junctions, in which we replace one electrode of the conventional CoFeB/MgO/CoFeB junctions by Co_2FeAl and Co_2FeSi . In the second step, we compare the results to CoFeB/MgO/CoFeB junctions. The investigation reveals that the effect ratio and the voltage signal are enlarged within the new sample system. The TMS is substantially increased with

ratios up to -93% by utilizing Heusler electrodes and the thermovoltages are enhanced up to $-664\text{ }\mu\text{V}$. Compared to the results for CoFeB/MgO/CoFeB the TMS is twice as high, while the TMR is halved. Furthermore, the sign of the Seebeck coefficients and TMS ratio are reversed compared to the commonly used layer stack. Overall, the results fit very well to our theoretical model. In addition, it shows that TMR and TMS are independent, while both depend on the DOS.

The TMS measurements with different heating powers show only small variations of the effect ratio. This is an additional benefit for applications. Besides, our introduced model allows the prediction of thermoelectric and spin caloritronic properties of a material simply by considering the DOS. Hence, a quick screening for optimum materials is possible.

Another way to study the TMS effect is to replace the MgO barrier by a MgAl_2O_4 (MAO) barrier, which has not been done so far. This material seems to be of great potential because MAO provides similar to MgO a Δ_1 spin filtering effect [84] and in addition in comparison to MgO (lattice mismatch $\sim 3\%$) a decreased lattice mismatch of less than 1% to Fe [85]. In the manuscript “Comparison of laser induced and intrinsic tunnel magneto-Seebeck effect in CoFeB/ MgAl_2O_4 and CoFeB/MgO magnetic tunnel junctions” the two different methods of temperature gradient generation, laser and intrinsic heating, regarding the TMS measurement results are compared. The results differ in value and sign. With MAO-barriers we obtain TMR ratios of 34% and TMS ratios by laser heating of 3.3% , while the TMS for MgO barriers reaches 23% and the TMR is improved to 200% . The relatively low TMR ratio of MAO based MTJs leads to the assumption that coherent tunneling is not present within MAO-based devices. Thus, the Brinkman model [86], which deals with the I/V-characteristics is a good approximation. The analysis of the I/V curves indicates the disagreement to the intrinsic TMS model proposed by Zhang *et al.* [87] in which a symmetric linear behavior is suggested. The results of laser heating and intrinsic heating are not directly comparable. Within this investigation, we are able to provide an alternative explanation of the observed symmetric contributions in contrast to the intrinsic TMS model. We state that the symmetric contribution is only attributed to the barrier asymmetry. This new insight is a significant step towards the understanding of the TMS concerning different heating methods and of great interest for the development of thermally driven devices.

Within the study “Enhancement of thermovoltage and tunnel magneto-Seebeck effect in CoFeB based magnetic tunnel junctions by variation of the MgAl_2O_4 and MgO barrier thickness” we concentrate on both, the MgAl_2O_4 (MAO) and the MgO-based MTJs. Here, a

systematical variation of the barrier thickness is done in order to investigate the influence of this parameter on the generated thermovoltages as well as on the TMS. This is the first detailed barrier thickness study for these devices in general.

The investigated samples consist of $\text{Co}_{40}\text{Fe}_{40}\text{B}_{20}$ -alloy electrodes and are fabricated at the Bielefeld University. The measurements are performed in our home-built TMS setup in Greifswald. The results reveal a maximum TMS ratio with a barrier thickness of 2.6 nm for both materials with 8 % for an MAO-based MTJ and 28 % for an MgO-based MTJ. Note, that this is in contrast to the samples prepared in Greifswald with other CoFeB composition and e-beam evaporated barrier, where no effect is observable with such high thicknesses. In this study, we also employ the Brinkman model to calculate the MAO barrier parameters.

MAO as barrier material provides much higher generated thermovoltages of more than 350 μV compared to the devices with MgO barrier with 80 μV . In addition, finite element simulations for heat transfer (COMSOL Multiphysics) provide the thermal distribution within the MTJs. In result the corresponding Seebeck coefficient are estimated: $S_p(\text{MAO}) = -59 \mu\text{V/K}$ vs. $S_p(\text{MgO}) = -18 \mu\text{V/K}$. This outcome shows the great potential of MAO barriers concerning the application in future spin caloritronic experiments and devices. Principally the importance of TMS studies with other barrier materials and barrier thicknesses is indicated.

3.3 The development of Terahertz emitters based on metallic heterostructures – Article VI

In this investigation, we present the application of photoinduced spin transport and the inverse spin Hall effect (ISHE) to construct new spintronic THz emitters.

In this regard, several devices (in particular about 40 on my own, in Greifswald) are prepared to find and optimize the best THz emitter in close collaboration with Tobias Kampfrath and co-workers from the Fritz-Haber-Institute in Berlin. The step-by-step improvement of the samples resulted in the publication with the name “Efficient metallic spintronic emitters of ultrabroadband terahertz radiation” and is summarized in the next section.

Terahertz radiation covers the frequency range between 0.3 and 30 THz in the electromagnetic spectrum and has a huge potential for applications e.g. imaging and quality control suitable for instance in the analysis of food and pharmaceuticals. The investigated

devices are simple bilayer heterostructure systems composed of one in-plane magnetized ferromagnetic and one nonmagnetic film.

By applying a femtosecond pump-pulse, electrons in the metal are excited and a spin current is injected into the adjacent nonmagnetic layer. The generated spin current is transformed into a transversal charge current by ISHE. It is a result of spin orbit coupling that electrons are deflected under a defined angle in opposite directions with regards to their spin orientations. The generated transversal charge current gives rise to the emission of a terahertz transient.

In our measurement configuration, the THz radiation is linearly polarized (perpendicular to the sample magnetization) and independent of the pump pulse polarization. In addition, the spin current can be reversed by changing the magnetization direction of the external field or by reversing the film order on the substrate. For this purpose, our samples made of $\text{Co}_{20}\text{Fe}_{60}\text{B}_{20}$ and Pt meet all the requirements for developing an efficient terahertz emitter with a large bandwidth. This large bandwidth is attributed to the featureless refractive index of metals [88], which means the conductivity is independent of the frequency and thus the bandwidth is only limited by the pump pulse duration.

Sample parameters are varied to optimize the THz emitter step-by-step. CoFeB in combination with different nonmagnetic materials which have different spin Hall angles are tested. The results are in good agreement with the *ab initio* calculated spin-Hall conductivities (intrinsic contribution) of the used materials.

In the second step, various layer thicknesses are tested while keeping the single layers approximately equally thick. Here, the THz amplitudes are rapidly growing for thinner films. A maximum is found for a 4 nm-thick emitter. This result can be explained by the fact that the films act as a Fabry-Perot cavity. Both, pump echoes on one hand and THz echoes on the other constructively interfere up to a critical thickness.

In the last step, a third layer adjacent to the ferromagnet is added. For the non-magnets W and Pt are used since they provide large spin Hall-angles yet with opposite sign assuming a system in which the current is in sum aligned in the same direction. The corresponding trilayer samples show a doubled THz amplitude confirming this assumption.

In addition, our developed THz emitters are compared to conventional ones. The new spintronic THz emitter provides a wider gapless bandwidth from 1 to 30 THz and also higher amplitudes above 3 THz than up to now used sources.

In summary, we introduced a new spintronic THz emitter that is easy and cost-efficient to prepare, and requires low pump powers. Also, the operation and handling is uncomplicated.

4. Conclusion & Outlook

This thesis reports on thermal excitation of the electron and spin system in ferromagnetic heterostructures via laser heating. The investigation of the corresponding effects requires two fundamentals, high quality samples as well as a highly precise measurement setup. The prepared MTJs exhibit TMR ratios above 200 % ensured by the enhanced electron tunneling of the Δ_1 states. In addition, the bilayer samples for THz emitter are stepwise improved and show a good performance.

All TMS measurements presented in the included publications are performed on my own or under my supervision at our setup in Greifswald. During the course of this thesis, the TMS measurement setup was optimized. The electrical grounding is improved which enables reliably repeatable measurements without destroying the samples. The measurement technique was upgraded and extended to enable an exact positioning of the heating laser spot on the sample as well as to create a large variation of temperature distributions in the MTJ. Systematic position-dependent heating of the device has resulted in new investigations of the TMS and other magnetothermal effects. It is shown that the TMS ratio is highly sensitive to the heating even by the variation of the heated area. These findings demonstrate that the laser spot size has to be adapted to create well-defined out-of-plane temperature gradients which results in a significant TMS effect ratio. In addition, the power density applied to the sample has to be taken into account to make the obtained results for different samples comparable.

Furthermore, within these studies a new effect present in MTJs was detected and identified. Due to the systematical study with variations of the temperature profile we show the presence of the ANE within such short length scales. Our method enables us to create temperature differences over a few μm and the ANE is detected over a nm-distance across the MTJ layer stack. This is the first detection of the ANE in MTJs. In addition, a uniaxial magnetic anisotropy of our MTJs was identified which influences the occurrence of the ANE. The results reveal an additional potential application for MTJs. In this regard, for example defects in complex electronic devices can be located. Further interesting studies in

this scope could determine the influence of the device dimensions and shape on the ANE by replacing the elliptic MTJ with circular or even rectangular ones.

In view of enhanced TMS effect ratios device engineering is a significant factor. The choice of material for the electrodes, barrier, insulator around the MTJs and the substrate material, all those factors strongly affect the characteristics of such devices and lead to diverse results. The knowledge of different material properties for thermovoltage generation is necessary to enhance the effect ratios and in consequence the application of such devices as magnetic sensors and sensors for optical positioning and focusing in the sub micrometer range. In this thesis, it is shown that MgAl_2O_4 has different properties compared to MgO as barrier material even if both exhibit similar tunneling characteristics. Furthermore, a large increase of the TMS effect ratios by the usage of half-metallic Heusler electrodes is obtained. This enhancement was explained within an innovative theoretical model.

There is still a lot of space left for investigations in this special field of MTJ devices and TMS. Nevertheless, a complete theoretical description of the TMS effect is lacking, which leaves room for further analyses. The presented investigations demonstrate the potential applicability of MTJs. However, further studies in material research and device engineering are needed to improve the applicability for this promising devices in the future. For instance, the influence of the barrier thickness should be clearly identified in experiments since it is verified that for devices with MAO and MgO barriers fabricated in Bielefeld the maximum effect ratios are reached with a barrier thickness of 2.6 nm. This is in contrast to the samples prepared in Greifswald, which do not show any effect with such `thick` barriers. This could be attributed to the deposition process because the tunneling barriers are prepared by sputter deposition in Bielefeld and by electron-beam evaporation in Greifswald. The sputtering technique involves much higher energies and thus the atoms arriving at the substrate are characterized by higher velocities which results in the incorporation of this atoms in adjacent layers and in result the films are less smooth. Thus, one of the next steps should focus on the thickness dependence of the e-beam evaporated barriers in combination with our CoFeB composition.

In addition, MTJs with different CoFeB alloys prepared under the same conditions could verify the theoretical investigations by the group of Christian Heiliger [27], where the Co and Fe compositions were systematically varied. This study reveals a strong influence of the composition.

With the improved setup all these studies are feasible.

In addition, I recommend to perform finite element simulations for the thermal transfer in MTJs with different substrate materials and insulating materials adjacent to the MTJs. Already, our first studies implicate strong variations of the temperature profile by choice of these materials.

Also in the scope of this thesis was the design of new THz emitter. In order to fabricate high quality emitters, I have prepared more than 40 samples based on a step-by-step improvement of the devices. These improvements included the testing of different substrates and film material combinations as well as thickness variations. The resulting THz emitters exhibit a high efficiency and are acting as figure of merit in further studies [89]. Following the procedure of these investigations, other heterostructures may be identified as a basis for new emitters. Furthermore, in our work group efforts are made to apply the developed bilayers in combination with nanostructured lenses on a glass fiber of a commercially available THz spectrometer. That should result in a miniaturized high energy density device covering a broader range of emission. In addition to the easy preparation, the laser can be focused even more tightly, which should result in a better energy efficiency, since the THz emission scales with the pump power. Consequently, a large pump power system would not be necessary, and the whole THz arrangement is easily applicable for every laboratory. Another point in this view is that THz emission can be generated with the use of MTJs. In this regard, materials with adapted spin Hall angles have to be chosen. As deducted from previous results, CoFeB serves as efficient component of THz emitters. Recent investigations reported the enhanced THz emission of annealed devices [90] which fits to the materials and fabrication processes of our studied MTJ devices. Thus, MTJs are possible candidates to produce new THz emitters. By using MgO as barrier the spin polarization can be tuned. In addition, it should be possible to adjust the barrier thickness to realize a phase shift in a way that circular polarized THz radiation is created.

In conclusion, the results presented within the scope of this thesis shed more light on spin caloritronic effects based on laser excitation and provide new insights which build the basis for future research.

References

- [1] Bauer G E W, Saitoh E and van Wees B J 2012 Spin caloritronics *Nat. Mater.* **11** 391–9
- [2] Yu H, Brechet S D and Ansermet J-P 2017 Spin caloritronics, origin and outlook *Phys. Lett. A* **381** 825–37
- [3] Boona S R, Myers R C and Heremans J P 2014 Spin caloritronics *Energy Environ. Sci.* **7** 885
- [4] Seebeck T J 1822-1823 Magnetische Polarisation der Metalle und Erze durch Temperaturdifferenz *Abhandlung der Königlich Preussischen Akademie der Wissenschaften zu Berlin* 265–375
- [5] Johnson M and Silsbee R H 1987 Thermodynamic analysis of interfacial transport and of the thermomagnetolectric system *Phys. Rev. B* **35** 4959–72
- [6] Uchida K, Takahashi S, Harii K, Ieda J, Koshibae W, Ando K, Maekawa S and Saitoh E 2008 Observation of the spin Seebeck effect *Nature* **455** 778–81
- [7] Julliere M 1975 Tunneling between ferromagnetic films *Phys. Lett. A* **54** 225–6
- [8] Ikeda S, Hayakawa J, Ashizawa Y, Lee Y M, Miura K, Hasegawa H, Tsunoda M, Matsukura F and Ohno H 2008 Tunnel magnetoresistance of 604% at 300 K by suppression of Ta diffusion in CoFeB/MgO/CoFeB pseudo-spin-valves annealed at high temperature *Appl. Phys. Lett.* **93** 82508
- [9] Butler W H, Zhang X-G, Schulthess T C and MacLaren J M 2001 Spin-dependent tunneling conductance of Fe|MgO|Fe sandwiches *Phys. Rev. B* **63** 54416
- [10] Mathon J and Umerski A 2001 Theory of tunneling magnetoresistance of an epitaxial Fe/MgO/Fe(001) junction *Phys. Rev. B* **63** 220403
- [11] Bhatti S, Sbiaa R, Hirohata A, Ohno H, Fukami S and Piramanayagam S N 2017 Spintronics based random access memory: A review *Mater. Today* **20** 530–48
- [12] Czerner M, Bachmann M and Heiliger C 2011 Spin caloritronics in magnetic tunnel junctions: *Ab initio* studies *Phys. Rev. B* **83** 132405
- [13] Walter M *et al* 2011 Seebeck effect in magnetic tunnel junctions *Nat. Mater.* **10** 742–6
- [14] Liebing N, Serrano-Guisan S, Rott K, Reiss G, Langer J, Ocker B and Schumacher H W 2011 Tunneling magnetothermopower in magnetic tunnel junction nanopillars *Phys. Rev. Lett.* **107** 177201
- [15] Kampfrath T *et al* 2013 Terahertz spin current pulses controlled by magnetic heterostructures *Nat. Nanotechnol.* **8** 256–60
- [16] Pawar A Y, Sonawane D D, Erande K B and Derle D V 2013 Terahertz technology and its applications *Drug Invention Today* **5** 157–63
- [17] Yang X, Zhao X, Yang K, Liu Y, Liu Y, Fu W and Luo Y 2016 Biomedical Applications of Terahertz Spectroscopy and Imaging *Trends Biotechnol.* **34** 810–24

-
- [18] Davies A G, Burnett A D, Fan W, Linfield E H and Cunningham J E 2008 Terahertz spectroscopy of explosives and drugs *Mater. Today* **11** 18–26
 - [19] Slonczewski J C 1989 Conductance and exchange coupling of two ferromagnets separated by a tunneling barrier *Phys. Rev. B* **39** 6995–7002
 - [20] Butler W H 2008 Tunneling magnetoresistance from a symmetry filtering effect *Sci. Technol. Adv. Mater.* **9** 14106
 - [21] Djayaprawira D D, Tsunekawa K, Nagai M, Maehara H, Yamagata S, Watanabe N, Yuasa S, Suzuki Y and Ando K 2005 230% room-temperature magnetoresistance in CoFeB/MgO/CoFeB magnetic tunnel junctions *Appl. Phys. Lett.* **86** 92502
 - [22] Yuasa S and Djayaprawira D D 2007 Giant tunnel magnetoresistance in magnetic tunnel junctions with a crystalline MgO(0 0 1) barrier *J. Phys. D: Appl. Phys.* **40** R337–R354
 - [23] Wang Z, Saito M, McKenna K P, Fukami S, Sato H, Ikeda S, Ohno H and Ikuhara Y 2016 Atomic-Scale Structure and Local Chemistry of CoFeB-MgO Magnetic Tunnel Junctions *Nano Lett.* **16** 1530–6
 - [24] Hayakawa J, Ikeda S, Lee Y M, Matsukura F and Ohno H 2006 Effect of high annealing temperature on giant tunnel magnetoresistance ratio of CoFeB/MgO/CoFeB magnetic tunnel junctions *Appl. Phys. Lett.* **89** 232510
 - [25] Münzenberg M and Thomas A 2012 Heiße Elektronik *Phys. Unserer Zeit* **43** 288–95
 - [26] Callen H B 1960 *Thermodynamics: An Introduction to the Physical Theories of Equilibrium Thermostatics and Irreversible Thermodynamics* (New York/London: JOHN WILEY & SONS, INC.)
 - [27] Heiliger C, Franz C and Czerner M 2013 *Ab initio* studies of the tunneling magnetoseebeck effect: Influence of magnetic material *Phys. Rev. B* **87** 224412
 - [28] Teixeira J M, Costa J D, Ventura J, Fernandez-Garcia M P, Azevedo J, Araujo J P, Sousa J B, Wisniowski P, Cardoso S and Freitas P P 2013 Giant intrinsic thermomagnetic effects in thin MgO magnetic tunnel junctions *Appl. Phys. Lett.* **102** 212413
 - [29] Huebner T, Boehnke A, Martens U, Thomas A, Schmalhorst J-M, Reiss G, Münzenberg M and Kuschel T 2016 Comparison of laser-induced and intrinsic tunnel magnetoseebeck effect in CoFeB/MgAl₂O₄ and CoFeB/MgO magnetic tunnel junctions *Phys. Rev. B* **93** 224433
 - [30] Czerner M and Heiliger C 2012 Influence of interface termination on the magnetoseebeck effect in MgO based tunnel junctions *J. Appl. Phys.* **111** 07C511
 - [31] Miao G X, Park Y J, Moodera J S, Seibt M, Eilers G and Münzenberg M 2008 Disturbance of tunneling coherence by oxygen vacancy in epitaxial Fe/MgO/Fe magnetic tunnel junctions *Phys. Rev. Lett.* **100** 246803
 - [32] Wang S-Z, Xia K and Bauer G E W 2014 Thermoelectricity and disorder of FeCo/MgO/FeCo magnetic tunnel junctions *Phys. Rev. B* **90** 224406
 - [33] Lin W, Hehn M, Chaput L, Negulescu B, Andrieu S, MONTAIGNE F and Mangin S 2012 Giant spin-dependent thermoelectric effect in magnetic tunnel junctions *Nat. Commun.* **3** 744

-
- [34] Liebing N, Serrano-Guisan S, Krzysteczko P, Rott K, Reiss G, Langer J, Ocker B and Schumacher H W 2013 Tunneling magneto thermocurrent in CoFeB/MgO/CoFeB based magnetic tunnel junctions *Appl. Phys. Lett.* **102** 242413
 - [35] Lopez-Monis C, Matos-Abiague A and Fabian J 2014 Tunneling magnetothermopower in magnetic tunnel junctions *Phys. Rev. B* **89** 54419
 - [36] Xu Y, Lin W, Petit-Watelot S, Hehn M, Rinnert H, Lu Y, Montaigne F, Lacour D, Andrieu S and Mangin S 2016 Origins of large light induced voltage in magnetic tunnel junctions grown on semiconductor substrates *J. Appl. Phys.* **119** 23907
 - [37] Boehnke A, Walter M, Roschewsky N, Eggebrecht T, Drewello V, Rott K, Münzenberg M, Thomas A and Reiss G 2013 Time-resolved measurement of the tunnel magneto-Seebeck effect in a single magnetic tunnel junction *Rev. Sci. Instrum.* **84** 63905
 - [38] Martens U, Walowski J, Schumann T, Mansurova M, Boehnke A, Huebner T, Reiss G, Thomas A and Münzenberg M 2017 Pumping laser excited spins through MgO barriers *J. Phys. D: Appl. Phys.* **50** 144003
 - [39] Boehnke A *et al* 2015 On/off switching of bit readout in bias-enhanced tunnel magneto-Seebeck effect *Sci. Rep.* **5** 8945
 - [40] Liebing N, Serrano-Guisan S, Rott K, Reiss G, Langer J, Ocker B and Schumacher H W 2012 Determination of spin-dependent Seebeck coefficients of CoFeB/MgO/CoFeB magnetic tunnel junction nanopillars *J. Appl. Phys.* **111** 07C520
 - [41] Shan J, Dejene F K, Leutenantsmeyer J C, Flipse J, Münzenberg M and van Wees B J 2015 Comparison of the magneto-Peltier and magneto-Seebeck effects in magnetic tunnel junctions *Phys. Rev. B* **92** 20414
 - [42] Zhang J, Bachman M, Czerner M and Heiliger C 2015 Thermal Transport and Nonequilibrium Temperature Drop Across a Magnetic Tunnel Junction *Phys. Rev. Lett.* **115** 37203
 - [43] Böhnert T, Dutra R, Sommer R L, Paz E, Serrano-Guisan S, Ferreira R and Freitas P P 2017 Influence of the thermal interface resistance on the thermovoltage of a magnetic tunnel junction *Phys. Rev. B* **95** 104441
 - [44] Böhnert T, Serrano-Guisan S, Paz E, Lacoste B, Ferreira R and Freitas P P 2017 Magnetic tunnel junctions with integrated thermometers for magnetothermopower measurements *J. Phys.: Condens. Matter* **29** 185303
 - [45] Huang S X, Chen T Y and Chien C L 2008 Spin polarization of amorphous CoFeB determined by point-contact Andreev reflection *Appl. Phys. Lett.* **92** 242509
 - [46] Meier D, Kuschel T, Shen L, Gupta A, Kikkawa T, Uchida K, Saitoh E, Schmalhorst J-M and Reiss G 2013 Thermally driven spin and charge currents in thin NiFe₂O₄/Pt films *Phys. Rev. B* **87** 54421
 - [47] Weiler M *et al* 2012 Local charge and spin currents in magnetothermal landscapes *Phys. Rev. Lett.* **108** 106602
 - [48] Kikkawa T, Uchida K, Daimon S, Shiomi Y, Adachi H, Qiu Z, Hou D, Jin X-F, Maekawa S and Saitoh E 2013 Separation of longitudinal spin Seebeck effect from anomalous

-
- Nernst effect: Determination of origin of transverse thermoelectric voltage in metal/insulator junctions *Phys. Rev. B* **88** 214403
- [49] Wu H, Wang X, Huang L, Qin J Y, Fang C, Zhang X, Wan C H and Han X F 2017 Separation of inverse spin Hall effect and anomalous Nernst effect in ferromagnetic metals *J. Magn. Magn. Mater.* **441** 149–53
- [50] Lee K-D *et al* 2015 Thermoelectric Signal Enhancement by Reconciling the Spin Seebeck and Anomalous Nernst Effects in Ferromagnet/Non-magnet Multilayers *Sci. Rep.* **5** 10249
- [51] Pu Y, Johnston-Halperin E, Awschalom D D and Shi J 2006 Anisotropic thermopower and planar Nernst effect in $\text{Ga}_{1-x}\text{Mn}_x\text{As}$ ferromagnetic semiconductors *Phys. Rev. Lett.* **97** 36601
- [52] Ky V D 1967 Planar Hall and Nernst Effect in Ferromagnetic Metals *phys. stat. sol. (b)* **22** 729–36
- [53] Meier D, Reinhardt D, Schmid M, Back C H, Schmalhorst J-M, Kuschel T and Reiss G 2013 Influence of heat flow directions on Nernst effects in Py/Pt bilayers *Phys. Rev. B* **88** 184425
- [54] Avery A D, Pufall M R and Zink B L 2012 Observation of the planar Nernst effect in permalloy and nickel thin films with in-plane thermal gradients *Phys. Rev. Lett.* **109** 196602
- [55] Schmid M, Srichandan S, Meier D, Kuschel T, Schmalhorst J-M, Vogel M, Reiss G, Strunk C and Back C H 2013 Transverse spin Seebeck effect versus anomalous and planar Nernst effects in Permalloy thin films *Phys. Rev. Lett.* **111** 187201
- [56] Slachter A, Bakker F L, Adam J-P and van Wees B J 2010 Thermally driven spin injection from a ferromagnet into a non-magnetic metal *Nat. Phys.* **6** 879–82
- [57] Saitoh E, Ueda M, Miyajima H and Tatara G 2006 Conversion of spin current into charge current at room temperature: Inverse spin-Hall effect *Appl. Phys. Lett.* **88** 182509
- [58] Jungwirth T, Wunderlich J and Olejník K 2012 Spin Hall effect devices *Nat. Mater.* **11** 382–90
- [59] Sinova J, Valenzuela S O, Wunderlich J, Back C H and Jungwirth T 2015 Spin Hall effects *Rev. Mod. Phys.* **87** 1213–60
- [60] Uchida K *et al* 2010 Spin Seebeck insulator *Nat. Mater.* **9** 894–7
- [61] Jaworski C M, Yang J, Mack S, Awschalom D D, Heremans J P and Myers R C 2010 Observation of the spin-Seebeck effect in a ferromagnetic semiconductor *Nat. Mater.* **9** 898–903
- [62] Uchida K-i, Adachi H, Ota T, Nakayama H, Maekawa S and Saitoh E 2010 Observation of longitudinal spin-Seebeck effect in magnetic insulators *Appl. Phys. Lett.* **97** 172505
- [63] Kajiwarara Y *et al* 2010 Transmission of electrical signals by spin-wave interconversion in a magnetic insulator *Nature* **464** 262–6
- [64] Huang S Y, Wang W G, Lee S F, Kwo J and Chien C L 2011 Intrinsic spin-dependent thermal transport *Phys. Rev. Lett.* **107** 216604

-
- [65] Shestakov A S, Schmid M, Meier D, Kuschel T and Back C H 2015 Dependence of transverse magnetothermoelectric effects on inhomogeneous magnetic fields *Phys. Rev. B* **92** 224425
- [66] Siegel G, Prestgard M C, Teng S and Tiwari A 2014 Robust longitudinal spin-Seebeck effect in Bi-YIG thin films *Sci. Rep.* **4** 4429
- [67] Jin H, Boona S R, Yang Z, Myers R C and Heremans J P 2015 Effect of the magnon dispersion on the longitudinal spin Seebeck effect in yttrium iron garnets *Phys. Rev. B* **92** 609
- [68] Meier D *et al* 2015 Longitudinal spin Seebeck effect contribution in transverse spin Seebeck effect experiments in Pt/YIG and Pt/NFO *Nat. Commun.* **6** 8211
- [69] Uchida K, Ishida M, Kikkawa T, Kirihara A, Murakami T and Saitoh E 2014 Longitudinal spin Seebeck effect: from fundamentals to applications *J. Phys.: Condens. Matter* **26** 343202
- [70] Adachi H, Uchida K-i, Saitoh E and Maekawa S 2013 Theory of the spin Seebeck effect *Rep. Prog. Phys.* **76** 36501
- [71] Schreiber D K, Choi Y-s, Liu Y, Chiaramonti A N, Seidman D N and Petford-Long A K 2011 Effects of elemental distributions on the behavior of MgO-based magnetic tunnel junctions *J. Appl. Phys.* **109** 103909
- [72] Mukherjee S *et al* 2015 Role of boron diffusion in CoFeB/MgO magnetic tunnel junctions *Phys. Rev. B* **91** 85311
- [73] Boehnke A *et al* 2017 Large magneto-Seebeck effect in magnetic tunnel junctions with half-metallic Heusler electrodes *Nat. Commun.* **8** 391
- [74] Khosroffian J M and Garetz B A 1983 Measurement of a Gaussian laser beam diameter through the direct inversion of knife-edge data *Appl. Optics* **22** 3406–10
- [75] Kelekci O, Lee H N, Kim T W and Noh H 2013 Anomalous Nernst Effects of [CoSiB/Pt] Multilayer Films *Journal of Magnetism* **18** 225–9
- [76] Hasegawa K, Mizuguchi M, Sakuraba Y, Kamada T, Kojima T, Kubota T, Mizukami S, Miyazaki T and Takanashi K 2015 Material dependence of anomalous Nernst effect in perpendicularly magnetized ordered-alloy thin films *Appl. Phys. Lett.* **106** 252405
- [77] Bieren A von, Brandl F, Grundler D and Ansermet J-P 2013 Space- and time-resolved Seebeck and Nernst voltages in laser-heated permalloy/gold microstructures *Appl. Phys. Lett.* **102** 52408
- [78] Brandl F and Grundler D 2014 Fabrication and local laser heating of freestanding Ni₈₀Fe₂₀ bridges with Pt contacts displaying anisotropic magnetoresistance and anomalous Nernst effect *Appl. Phys. Lett.* **104** 172401
- [79] Wells J, Selezneva E, Krzysteczko P, Hu X, Schumacher H W, Mansell R, Cowburn R, Cuenat A and Kazakova O 2017 Combined anomalous Nernst effect and thermography studies of ultrathin CoFeB/Pt nanowires *AIP Advances* **7** 55904
- [80] Krzysteczko P *et al* 2017 Nanoscale thermoelectrical detection of magnetic domain wall propagation *Phys. Rev. B* **95** 220410

-
- [81] Mizuguchi M, Ohata S, Uchida K-i, Saitoh E and Takanashi K 2012 Anomalous Nernst Effect in an L1₀-Ordered Epitaxial FePt Thin Film *Appl. Phys. Express* **5** 93002
- [82] Sakuraba Y, Hasegawa K, Mizuguchi M, Kubota T, Mizukami S, Miyazaki T and Takanashi K 2013 Anomalous Nernst Effect in L1₀-FePt/MnGa Thermopiles for New Thermoelectric Applications *Appl. Phys. Express* **6** 33003
- [83] Hamrle J, Blomeier S, Gaier O, Hillebrands B, Schneider H, Jakob G, Postava K and Felser C 2007 Huge quadratic magneto-optical Kerr effect and magnetization reversal in the Co₂FeSi Heusler compound *J. Phys. D: Appl. Phys.* **40** 1563–9
- [84] Zhang J, Zhang X-G and Han X F 2012 Spinel oxides: Δ_1 spin-filter barrier for a class of magnetic tunnel junctions *Appl. Phys. Lett.* **100** 222401
- [85] Miura Y, Muramoto S, Abe K and Shirai M 2012 First-principles study of tunneling magnetoresistance in Fe/MgAl₂O₄/Fe(001) magnetic tunnel junctions *Phys. Rev. B* **86** 24426
- [86] Brinkman W F, Dynes R C and Rowell J M 1970 Tunneling Conductance of Asymmetrical Barriers *J. Appl. Phys.* **41** 1915–21
- [87] Zhang Z H *et al* 2012 Seebeck rectification enabled by intrinsic thermoelectrical coupling in magnetic tunneling junctions *Phys. Rev. Lett.* **109** 37206
- [88] Laman N and Grischkowsky D 2008 Terahertz conductivity of thin metal films *Appl. Phys. Lett.* **93** 51105
- [89] Seifert T *et al* 2017 Terahertz Spin Currents and Inverse Spin Hall Effect in Thin-Film Heterostructures Containing Complex Magnetic Compounds *SPIN* **07** 1740010
- [90] Sasaki Y, Suzuki K Z and Mizukami S 2017 Annealing effect on laser pulse-induced THz wave emission in Ta/CoFeB/MgO films *Appl. Phys. Lett.* **111** 102401

5. Cumulative thesis articles

The following chapter includes a selection of manuscripts originated from the last three years of work contributing to the field of spin caloritronics. This delivers an important input to get a deeper insight into the effects based on laser pulse excited electrons and spins in magnetic heterostructures.

Author contributions

Article I: Pumping laser excited spins through MgO barriers

(J. Phys. D: Appl. Phys. 50, 144003 (2017))

U. Martens, J. Walowski, T. Schumann, M. Mansurova, A. Boehnke, T. Huebner, G. Reiss, A. Thomas, M. Münzenberg

U. Martens set up the experiments with contributions of J. Walowski and T. Schumann. U. Martens performed the measurements under supervision of M. Münzenberg. U. Martens and T. Huebner fabricated the samples. U. Martens and J. Walowski analyzed the data and wrote the manuscript. A. Thomas, M. Münzenberg and G. Reiss designed the research approach. All authors discussed the measurements and the manuscript.

Article II: Anomalous Nernst effect on the nanometer scale: exploring three-dimensional temperature gradients in magnetic tunnel junctions

(submitted)

U. Martens, T. Huebner, H. Ulrichs, O. Reimer, T. Kuschel, R. R. Tamming, C.-L. Chang, R. I. Tobey, A. Thomas, M. Münzenberg, J. Walowski

U. Martens, J. Walowski and M. Münzenberg designed and set up the experiments. U. Martens performed the TMS/ANE measurements. U. Martens and T. Huebner prepared the samples. H. Ulrichs carried out the COMSOL simulations, analyzed and discussed the temperature data with U. Martens and J. Walowski. R.R. Tamming, C.-L. Chang and R.I. Tobey performed the magnetization dynamics experiments, analyzed and discussed the anisotropy data with U. Martens and J. Walowski. U.M. and J.W. analyzed the data and discussed the thermal effects with T. Huebner, O. Reimer and T. Kuschel. U.M. and J.W. prepared the manuscript. M. Münzenberg and A. Thomas coordinated the research. All authors discussed the measurements and the manuscript.

Article III: Large magneto-Seebeck effect in magnetic tunnel junctions with half-metallic Heusler electrodes

(Nat. Commun. 8 391, (2017))

A. Boehnke, **U. Martens**, C. Sterwerf, A. Niesen, T. Huebner, M. von der Ehe, M. Meinert, T. Kuschel, A. Thomas, C. Heiliger, M. Münzenberg, G. Reiss

A. Boehnke, U. Martens, T. Huebner, and M. v. d. Ehe set up the experiments and performed the measurements under supervision of T. Kuschel, G. Reiss and M. Münzenberg. A. Boehnke, C. Sterwerf and A. Niesen prepared and characterized the samples. A. Boehnke, C. Heiliger, and G. Reiss developed und discussed the theoretical model. M. Meinert provided the DFT calculations. A. Boehnke wrote the manuscript. A. Thomas, C. Heiliger, M. Münzenberg and G. Reiss designed the research approach. All authors discussed the measurements and the manuscript. [Citation of original manuscript]

Article IV: Comparison of laser-induced and intrinsic tunnel magneto-Seebeck effect in CoFeB/MgAl₂O₄ and CoFeB/MgO magnetic tunnel junctions

(Phys. Rev. B 93, 224433 (2016))

T. Huebner, A. Boehnke, **U. Martens**, A. Thomas, J.-M. Schmalhorst, G. Reiss, M. Münzenberg, T. Kuschel

T. Huebner, A. Boehnke and U. Martens carried out the experiments. T. Huebner and A. Boehnke prepared and characterized the TMR devices. T. Huebner carried out COMSOL simulations and Brinkman analysis. T. Huebner and T. Kuschel developed the model to describe the symmetric contribution with the Brinkman model. A. Thomas and M. Münzenberg designed the research approach. J. Schmalhorst., G. Reiss, M. Münzenberg, T. Kuschel and all authors discussed the experiments and the manuscript.

Article V: Enhancement of thermovoltage and tunnel magneto-Seebeck effect in CoFeB based magnetic tunnel junctions by variation of the MgAl₂O₄ and MgO barrier thickness

(Phys. Rev. B 96, 214435 (2017))

T. Huebner, **U. Martens**, J. Walowski, A. Boehnke, J. Krieff, C. Heiliger, A. Thomas, G. Reiss, T. Kuschel, M. Münzenberg

T. Huebner, U. Martens and J. Walowski carried out the experiments. T. Huebner, J. Krieff and A. Boehnke prepared and characterized the TMR devices. T. Huebner carried out COMSOL simulations. A. Thomas and M. Münzenberg designed the research approach. C. Heiliger, A. Thomas, G. Reiss, T. Kuschel, M. Münzenberg, and all authors discussed the experiments and the manuscript.

Article VI: Efficient metallic spintronic emitters of ultrabroadband terahertz radiation

(Nat. Photonics **10**, 483-488 (2016))

T. Seifert, S. Jaiswal, **U. Martens**, J. Hannegan, L. Braun, P. Maldonado, F. Freimuth, A. Kronenberg, J. Henrizi, I. Radu, E. Beaurepaire, Y. Mokrousov, P. M. Oppeneer, M. Jourdan, G. Jakob, D. Turchinovich, L. M. Hayden, M. Wolf, M. Münzenberg, M. Kläui, T. Kampfrath

T. Kampfrath and T. Seifert conceived the experiments. T. Kampfrath and I. Radu carried out preliminary measurements. S. Jaiswal, U. Martens, A. Kronenberg, J. Henrizi, E. Beaurepaire, M. Jourdan, G. Jakob, M. Münzenberg and M. Kläui fabricated the spintronic emitters and optimized the fabrication process. L. Braun, T. Seifert and T. Kampfrath built the terahertz emission set-up. J. Hannegan and L.M. Hayden fabricated the LAPC electrooptic detectors. T. Seifert performed the terahertz experiments and optical sample characterization. T. Seifert and T. Kampfrath analyzed experimental data with contributions from D. Turchinovich and M. Kläui. T. Kampfrath and T. Seifert developed the analytical terahertz-emitter model with contributions from F. Freimuth and Y. Mokrousov. F. Freimuth and Y. Mokrousov calculated spin-Hall conductivities. P. Maldonado and P.M. Oppeneer conducted calculations of the ultrafast spin transport. T. Kampfrath, T. Seifert, D. Turchinovich., M. Wolf and M. Kläui co-wrote the paper. All authors contributed to discussing the results and writing the paper. [Citation of original manuscript]

Signatures verifying the author contributions:

(Prof. Dr. Markus Münzenberg)

(Ulrike Martens)

5.1 Pumping laser excited spins through MgO barriers (Thesis article I)

Pumping laser excited spins through MgO barriers

Ulrike Martens¹, Jakob Walowski¹, Thomas Schumann¹, Maria Mansurova¹,
Alexander Boehnke², Torsten Huebner², Günter Reiss², Andy Thomas³
and Markus Münzenberg¹

¹ Institut für Physik, Ernst-Moritz-Arndt Universität Greifswald, Felix-Hausdorff-Straße 6, 17489 Greifswald, Germany

² Physics Department, Center for Spinelectronic Materials and Devices, Bielefeld University, Universitätsstraße 25, 33615 Bielefeld, Germany

³ Leibniz Institute for Solid State and Materials Research Dresden (IFW Dresden), Institute for Metallic Materials, Helmholtzstrasse 20, 01069 Dresden, Germany

E-mail: ulrike.martens@uni-greifswald.de

Received 1 November 2016, revised 23 January 2017

Accepted for publication 31 January 2017

Published 9 March 2017



Abstract

We present a study of the tunnel magneto-Seebeck (TMS)⁴ effect in MgO based magnetic tunnel junctions (MTJs). The electrodes consist of CoFeB with in-plane magnetic anisotropy. The temperature gradients which generate a voltage across the MTJs layer stack are created using laser heating. Using this method, the temperature can be controlled on the micrometer length scale: here, we investigate, how both, the TMS voltage and the TMS effect, depend on the size, position and intensity of the applied laser spot. For this study, a large variety of different temperature distributions was created across the junction. We recorded 2D maps of voltages generated by heating in dependence of the laser spot position and the corresponding calculated TMS values. The voltages change in value and sign, from large positive values when heating the MTJ directly in the centre to small values when heating the junction on the edges and even small negative values when heating the sample away from the junction. Those zero crossings lead to very high calculated TMS ratios. Our systematic analysis shows, that the distribution of the temperature gradient is essential, to achieve high voltage signals and reasonable resulting TMS ratios. Furthermore, artefacts on the edges produce misleading results, but also open up further possibilities of more complex heating scenarios for spincaloritronics in spintronic devices.

Keywords: spincaloritronic transport, tunnel magneto-Seebeck effect, laser excitation

(Some figures may appear in colour only in the online journal)

1. Introduction

The demand for new concepts to advance progress in information processing calls for technologies that not solely rely on the electrons charge, but also control the electrons other property, the spin. In the research field of magnonics those concepts are approached by making use of spin-waves [1]. This method opens new aspects for information processing [2, 3].

Gaining control over the excitation and propagation of excited spins is in the focus, both for potential magnetic storage and logic devices. The investigation of spincaloritronic effects is one of the key elements to understand the underlying principles and develop the required techniques. The TMS is defined as the change of the Seebeck coefficients (S_p , S_{ap}) in MTJs regarding the parallel (p) and antiparallel (ap) magnetic configuration of the ferromagnetic electrodes [4–6] while creating a temperature gradient across the layer stack. The resulting temperature difference between the two electrodes leads to the generation of a Seebeck voltage. Because the driving force to

⁴ In other publications this term is also referred to as tunneling magneto thermopower TMTP or the magneto-Seebeck ratio S_{MS} .

generate voltages are temperature gradients, this method also provides the opportunity to recycle waste heat usually generated in electronic spintronic devices. Theoretical *ab initio* calculations show, that the Seebeck coefficients for MTJs in the parallel and antiparallel magnetization alignment vary with the Co and Fe concentration, the MgO barrier thickness and the temperature and can even change sign [7]. This results in large variations of the TMS ratio from -200% up to 1000% in the temperature range between 300 K and 500 K. That means, that for the compositions of Co and Fe in the range around $\text{Co}_{70}\text{Fe}_{30}$ and $\text{Co}_{30}\text{Fe}_{70}$ a sign change in the Seebeck coefficients and rather small values are expected, as reported in [4, 5, 8–12]. The TMS ratios for these concentrations are rather small, ranging around 20%. Usually the experimentally found TMS ratios do not exceed 40% at maximum and can also be negative. Consequently, they are very sensitive to the interface and composition and are difficult to compare. This strong sensitivity in the *ab initio* calculations arises from the fact that multiple bands are crossing at around the Fermi level that contribute to the TMS. Generally, $\text{CoFeB}/\text{MgO}/\text{CoFeB}$ tunnel junctions are well established devices. In 2001, it was predicted that crystalline MgO barrier material provides high tunnel magnetoresistance (TMR) ratios due to the coherent tunneling of fully spin-polarized Δ_1 electrons [13, 14]. The largest reported TMR ratio measured experimentally at room temperature was by Ikeda *et al* with a value of 604% [15]. Furthermore, this class of tunnel junctions is relatively easy to prepare. The material layers can be deposited using sputtering techniques. For patterning optical mask lithography is sufficient. Consequently, the preparation times are rather short. Accordingly, the investigated samples in this work are MgO based pseudo spin valves. The CoFeB electrodes have an in-plane magnetic anisotropy. Generally, two methods are used to generate voltages across layer stacks by creating temperature gradients from top to bottom layer. The first one is by depositing an additional metallic layer on top of the stack and patterning a heater line directly above the MTJ [5, 8, 9]. Precise lithography methods allow the positioning of the heater line exactly on top of the MTJ, enabling full control of the location and direction of the temperature gradient. However, heating and cooling are slower, compared to optical excitations. Besides this, thermal insulation is necessary to avoid unwanted heating of other device regions. Furthermore, once a heater line is deposited, no further adjustments to the size and position can be undertaken. The second method is by using a laser [4, 10, 11, 16]. This approach appears more flexible, because the laser spot and thus the centre of the elevated temperature can be readjusted perpetually. However, for precise positioning of the MTJ with respect to the laser spot, motion steps with resolutions in the sub μm regime are required, considering MTJ and laser spot sizes below 10 μm in diameter. We found, that changes of the laser spot size and its position with respect to the MTJ lead to unwanted effects in the measurement signal. In general, positioning the centre of the laser spot not exactly in the centre of the MTJ, can lead to a smaller Seebeck voltage and even its reversal, resulting in a high TMS because of the vanishing voltage in the denominator in the calculation. That means, the high TMS ratios in

those cases arise at the cost of signal because of a redistribution of the temperature gradients and thus small temperature differences between the electrodes.

Here we present three series of measurements varying the properties of the heating laser beam. In the first series a variation of laser power is presented, which determines the optimum power for thermovoltage generation. In the second series of measurements, the influence of the laser spot size on the thermovoltage and the resulting TMS ratios is investigated. For increasing spot size, we find a drop of the Seebeck voltage, resulting in an increased TMS ratio. Consequently, the third series of measurements demonstrates the influence of systematically moving the laser beam in a square of the size $30\ \mu\text{m} \times 30\ \mu\text{m}$ using steps of 1 μm and recording thermovoltage maps locally. In this third series of measurements the origin of the signal change is identified. In both cases, when varying the spot size as well as when scanning the surface of the sample with the laser spot, the measured Seebeck voltages gain a small amplitude and even change sign, when the MTJ is heated at the edges. Both effects are attributed to the resulting complex lateral temperature gradients direction change, which heats the bottom CoFeB electrode, keeping the top CoFeB electrode at a lower temperature. Furthermore, in-plane temperature gradients inside the MTJs play a significant role and should be investigated but have been difficult to access up to now. The aim of this study is to develop a technique to investigate these effects in more detail.

2. Methods

2.1. Sample fabrication

The films are prepared under ultrahigh-vacuum conditions with a base pressure of 5×10^{-10} mbar on MgO (100) substrates. This kind of substrate is chosen to avoid parasitic effects due to conductance from semiconducting substrates as described in [10]. The $\text{Co}_{20}\text{Fe}_{60}\text{B}_{20}$ electrodes and the Ta buffer layer are fabricated by magnetron sputtering. The MgO barrier is e-beam evaporated in a separate chamber without breaking the vacuum [17]. On top of the film stack, a Ru capping layer is deposited by e-beam evaporation to prevent oxidation of the underlying layers. The sample is *ex situ* annealed under an applied in-plane magnetic field of 300 mT at a temperature of 450 °C for one hour. This procedure results in the crystallization of the amorphous CoFeB electrodes around the MgO layer and the diffusion of B into the Ta layers. The Boron in the sputtering target is necessary for ultrasoft amorphous layers. For crystallization of the Co and Fe atoms around the MgO it has to be removed by solid state epitaxy [18]. In this case, the Ta layers are good B sinks for both CoFe electrodes [19–21]. In the next step elliptical MTJs are patterned by electron beam lithography and subsequently ion-beam etched to conjugate diameters of $6\ \mu\text{m} \times 4\ \mu\text{m}$ with the long axis parallel to the direction of the magnetic field applied during the annealing procedure. Sputtered Ta_2O_5 (150 nm) is used as isolating material between individual MTJs. After this procedure, the resist is removed from the sample and on top a 5 nm-thick Ta adhesion layer and a 70 nm-thick Au contact

layer are deposited. Finally the Au layer is patterned to enable individual contacting of the MTJs and the bottom contact. The sample stack consists of Au 70 nm/Ta 5 nm/Ru 3 nm/Ta 5 nm/CoFeB 5.4 nm/MgO 2.1 nm/CoFeB 2.5 nm/Ta 10 nm/ MgO substrate. A depiction of the layer stack and the structured junction is shown in figure 4(c) (left) and in figure 4(c) (right) the junction is shown embedded into the Au contactpads.

2.2. Experimental setup and measurements

In order to create a temperature gradient across the layer stack, we use a TOPTICA ibeam smart laser diode with a wavelength of 638 nm and $P \leq 150$ mW. The laser can be focused to a diameter $\geq 2 \mu\text{m}$ full-width at half-maximum with a microscope objective (NIKON 20 \times , WD 20.5 mm). The position of the laser spot is controlled by a camera in a confocal microscope arrangement. The schematics of the setup are the same as in [10]. The thermovoltage is detected via a lock-in amplifier. A waveform generator (Agilent, 33500B series) modulates the laser diode with a square wave at a frequency of 77 Hz, which is used as modulation frequency for the lock-in amplifier. The substrate is kept at 295 K, so that the bottom of the layer stack is connected to a constant background temperature of the substrate which is connected to a ceramic IC bond socket. By recording the temporal Seebeck-voltage evolution using an oscilloscope, when the sample is heated repeatedly, the base temperature is monitored. Details are given in [4, 10]. The laser pulse length and frequency can be adjusted by the square wave input signal. To measure magnetization dependent, the sample is situated in between two pole shoes of an electromagnet. Each thermovoltage versus external magnetic field curve is measured ten times and averaged. Linear stages with motorized actuators for the horizontal (x -direction) and vertical (y -direction) movement are implemented to position the laser beam on the sample surface. This function enables us to measure the thermovoltage versus magnetization direction by heating the sample at different positions over a defined area of $30 \mu\text{m} \times 30 \mu\text{m}$ with $\leq 1 \mu\text{m}$ resolution, and additionally perform 2D scans. The laser spot diameter can be varied by adjusting the distance of the sample surface from the focusing objective (z -direction). The knife edge method is used to determine the beam width at the sample surface. In addition, the setup is equipped with a Keithley 2400 Sourcemeter to record TMR curves with a bias voltage of 10 mV to confirm the junction functionality.

2.3. Tunnel-magnetoresistance measurements

The electric resistance of an MTJ depends on the magnetic configuration of both magnetic electrodes. The effect describing the resistance change is the TMR. For parallel magnetization alignment of both electrodes, the resistance is low, for antiparallel alignment, the resistance increases [13, 14]. The TMR effect in the MTJ constitutes the necessary condition for the TMS effect, however, it is not the sufficient condition [4, 7]. Therefore, a high TMR effect does not guarantee a high TMS effect. The TMR ratio is measured before, in between

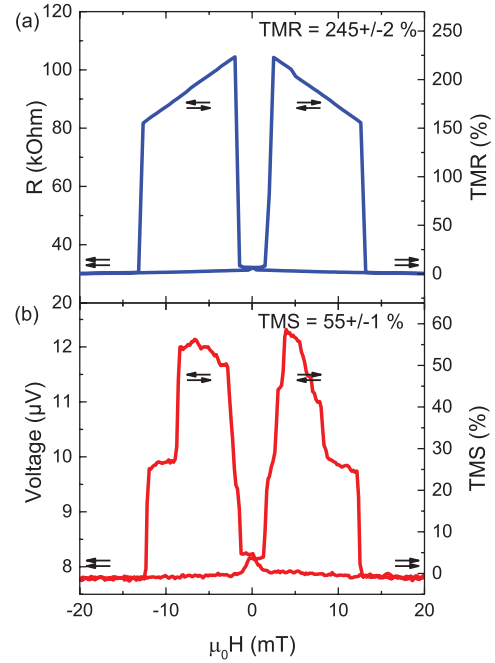


Figure 1. Measurement curves of the (a) TMR effect, by measuring the resistance R of the MTJ and (b) the thermovoltage generated by the temperature gradient against the applied external field $\mu_0 H$. The arrows indicate parallel and antiparallel magnetization alignment of the electrodes, respectively. In the case of the TMR measurement (a), applying a bias voltage of 10 mV, the resistance increase in the antiparallel alignment results in a TMR effect of 245%. In the case of the TMS measurement (b), the thermovoltage also increases in the antiparallel alignment and results in a TMS effect of 55%.

and after the single TMS experiments. Figure 1(a)) shows, an example TMR curve recorded with a bias voltage of 10 mV for the junction investigated in this work. The resistance curve displays a sharp switching between 30 kΩ in the parallel and 104 kΩ in the antiparallel configuration of the ferromagnetic layers, this corresponds to a TMR ratio of 245%. The curve confirms a clear separation of the magnetization states and the effect remains high. The TMR ratio is calculated according to:

$$\text{TMR} = \frac{R_{\text{ap}} - R_{\text{p}}}{R_{\text{p}}}$$

2.4. Tunnel magneto-Seebeck effect measurements

For the TMS measurement the surface of the junction is illuminated by the laser beam thus a thermovoltage is generated. This voltage changes with the magnetization alignment of the magnetic CoFeB electrodes, similar to the resistance in the TMR measurements. A typical TMS effect measurement curve is depicted in figure 1(b)). The external magnetic field is swept beyond the coercive fields of the two CoFeB electrodes. For high external magnetic fields both electrodes are aligned parallel. Here the generated voltage differs from the voltage generated in the region where the magnetization alignment is

antiparallel (indicated by the black arrows). The TMS ratio given on the right in figure 1(b)) is 55%. The TMS ratio was determined using:

$$\text{TMS} = \frac{V_{\text{ap}} - V_{\text{p}}}{\min(|V_{\text{ap}}|, |V_{\text{p}}|)}.$$

3. Results and discussion

3.1. Power dependent TMS measurements

Tuning the laser power, the temperature gradient is increased by depositing more energy in the top electrode and thus raising its temperature, while leaving the bottom electrode at the same base temperature guaranteed by the constant environmental settings of 22 °C. The presented TMS measurements are performed with 10 mW, 25 mW and in 25 mW steps up to 150 mW laser power. The MTJ is heated in the centre to obtain the highest possible voltage that can be generated for each applied laser power. For the adjustment of the centre position, the laser power is set to 150 mW and the voltage signal is maximized by positioning the laser spot on the MTJ. Both, the position and the size of 2.2 μm (FWHM) of the laser spot remain unchanged throughout all measurements in this set. The measurements are performed setting the laser power randomly to avoid systematic errors in the following order: 100 mW, 50 mW, 10 mW, 25 mW, 75 mW, 150 mW, 125 mW. For each setting the TMS is measured ten times and averaged. The extracted Seebeck voltages for the parallel and antiparallel magnetization alignment of both CoFeB electrodes versus the applied laser power are shown in figure 2 (left scale). On one hand the voltages for both orientations are increasing linearly with the laser power, the linear increase is indicated by the red and black dashed lines, which are not fits to the data, but guides to the eye. In the parallel state values up to 7.6 μV are achieved and in the antiparallel state up to 12.3 μV at 150 mW laser power. On the other hand, the calculated TMS values depicted in figure 2 (right scale) as a function of laser power, remain at a constant rate between 65% and 55%, as indicated by the blue dashed line as a guide to the eye. This indicates, that effects heating the MTJs surroundings at high laser powers in the given range are not present. High laser power focused to one spot and centred on top of the junction creates a temperature gradient with a high temperature difference between the top and bottom electrodes. Because the power dependent measurements show the highest voltage signal for 150 mW, all further measurements are performed by keeping the laser power at this value.

3.2. Laser spot size dependent TMS measurements

For a further investigation the heat gradient is varied, by increasing the laser spot size d on the tunnel junction element of 6 $\mu\text{m} \times 4 \mu\text{m}$. The first step of the procedure is to place the sample into the focal point of the objective. Here, the spot size is 2.7 μm . Moving the sample away from the objective in z -direction, the spot size increases to 6.7 μm . The

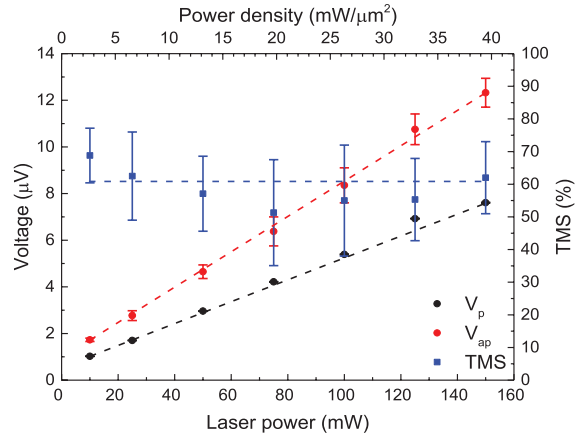


Figure 2. The extracted voltages for the parallel magnetization alignment V_p (black dots) and the antiparallel magnetization alignment (red dots) of the CoFeB electrodes (left scale). The resulting TMS ratio is calculated from the voltages (blue squares, right scale). Both quantities are plotted as functions of the laser power and the corresponding power density applied for heating. All depicted lines are guides to the eye.

spot size for each z -position of the sample is determined using the knife edge method, by moving the sample horizontally in x -direction and recording the signal change of the reflected light at the edge of the Au contact pad and the Ta_2O_5 insulator. The spot size is calculated from the recorded data according to [22], the laser beam profile is circular. In order to heat the MTJ directly on top and to create a temperature difference preferably only within the MTJ, a spot size smaller than the actual MTJ is chosen. Increasing the spot size, also a temperature difference is created in the surroundings of the MTJ. The extracted thermovoltages for the parallel magnetization alignment V_p , the antiparallel magnetization alignment V_{ap} and the voltage difference $|V_{ap} - V_p|$ are plotted in figure 3 (left scale). The calculated TMS is plotted in figure 3 (right scale). The voltage decreases for both magnetization alignments proportional to $1/d^2$, since this is also the factor by which the laser fluence is reduced when the laser spot diameter increases. Additionally, for spot sizes, that exceed the MTJ dimensions, V_p becomes even negative. There are two effects leading to small thermovoltages. The first is, that with increasing the laser spot size, the power density and with it the energy density deposited at the sample surface decreases. This leads to a lower temperature rise in the top CoFeB electrode in respect to the bottom electrode, because the energy is distributed over a larger in-plane area, and thus generating a smaller thermovoltage. The second is in the case of the sample design used here. We assume that the Ta_2O_5 layer is transparent for the incoming photons, which are transmitted through the Au layer to the bottom Ta layer [23]. However, the intensity transmitted through the Au and top Ta layer is below 1%, considering the thickness of 70 nm. This would transport less than 1 mW of the laser power to the bottom layers, which is not enough to generate a thermovoltage across the MTJ. Besides this, theoretical simulations of the Seebeck coefficients do not show a

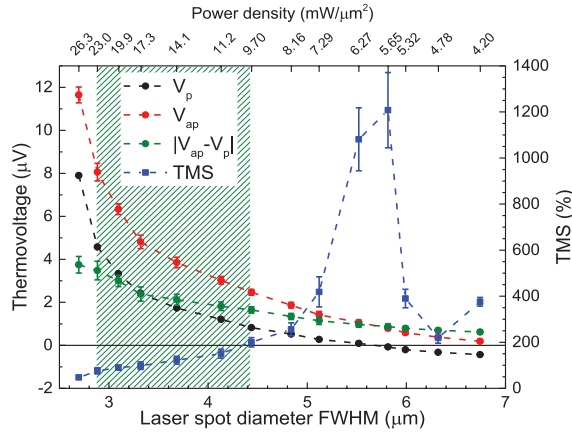


Figure 3. Dependence of measured thermovoltages and TMS ratios on the laser spot diameter for an elliptically shaped MTJ ($6\ \mu\text{m} \times 4\ \mu\text{m}$) with a laser power of 150 mW. The left scale shows the extracted voltages for the parallel magnetization alignment V_p (black dots), the antiparallel magnetization alignment V_{ap} (red dots) and the difference $|V_{ap} - V_p|$. The right scale shows the TMS ratio calculated from the measured voltages. All data is plotted as a function of the laser spot size variation (bottom) and the corresponding power density (top). The green shaded area displays the range with most homogenous heating, resulting in a well-defined out-of-plane temperature gradient. Here the diameter is adapted to the size of the given MTJ.

sign change in the temperature regions above 300 K, even in view of variations in the Co and Fe compositions of the electrodes [7]. However, looking at the patterned MTJ structures at the edges, like it was investigated in [18], the etching process does not homogeneously remove the material, shaping straight pillars, but instead, the bottom electrode becomes broad. At the interface of the pillar and the Ta_2O_5 insulator, the energy can be passed on to the bottom CoFeB electrode, raising its temperature and, thus, reversing the temperature gradient inside the MTJ. The calculated TMS ratios increase from around 50% to above 1300% to the point, where V_p changes sign. The drastic increase of the TMS ratio in this region is caused by the rapid decrease of V_p , with increasing laser spot size, that is stronger than the decrease of $|V_{ap} - V_p|$. Also, too small laser spot sizes will lead to unwanted in-plane temperature gradients within the MTJ. In figure 3, the green area represents the spot size range that is best adapted to the junction size. It has to be noted that for the present sample layout of MTJs, pattern structure and oxide used for electric isolation, those in-plane effects are most prominent. Although a sign change of the thermovoltage is not always observed, it shows that homogenous heating of the whole MTJ is crucial to obtain reliable values of the thermovoltage and the TMS ratio.

3.3. 2D scan of the magnetic tunnel junction

In order to deepen the understanding of the effects observed and confirm the conclusions made, position dependent laser spot measurements are performed. For this set of measurements, the laser spot size is set to $2.6\ \mu\text{m}$. This ensured a small

heating area and high Seebeck voltages when heating the junction in the centre. To define the scanning area, the laser spot was positioned in the centre of the MTJ. Then the MTJ was moved $15\ \mu\text{m}$ in both, the x - and the y -direction. From that point, the MTJ was moved in $1\ \mu\text{m}$ steps a distance of $30\ \mu\text{m}$ in both directions towards the MTJ, recording the magnetization dependent Seebeck voltages like shown in figure 1(b) at each point. The extracted voltages for the parallel (figure 5(a)) and the antiparallel (figure 5(b)) magnetization alignment are plotted in 3D graphs. Two dimensions are used to depict the scanned area (x - and y -direction). The third dimension (z -scale) displays the recorded values. Additionally the same data is depicted zoomed in in a false colour plot (figures 5(c) and (d)). The figures demonstrate, that the generated voltage decreases exponentially, as the laser spot is moved away from the centre of the MTJ. In close vicinity of the MTJ, when the laser beam is not striking it anymore, the measured voltage becomes negative, before the signal goes to 0, at larger distance about $15\ \mu\text{m}$ away from the junction centre. The false colour plots show a further analysis, from which the position and the shape of the MTJ can be reconstructed, by fitting a 2D Gaussian function to the data. The fits reveal a rotation of the MTJs long axis of $\sim 10^\circ$ from the vertical position, which is reasonable, considering inaccuracies when installing the sample in the setup. Further, the FWHM dimensions of the fits have dimensions of $3.9\ \mu\text{m}$ and $4.6\ \mu\text{m}$ for the short axis and $4.7\ \mu\text{m}$ and $6.1\ \mu\text{m}$ for the long axis. Those are the dimensions of the junction. This confirms, that the best signal can only be achieved, when heating the junction in the centre. Altogether, the voltages, extracted for the parallel and antiparallel magnetization alignment, indicate, which parameters need to be satisfied in order to achieve high signals. First, the voltage increases linearly with the laser intensity applied. Second, the laser power needs to be focused to the highest energy density. Third, the MTJ needs to be heated by the laser beam in the centre. The calculated TMS ratios from the extracted voltages for the parallel and antiparallel magnetization alignment are plotted in figure 6. The results are similar to those discussed in section 3.2. In both cases, when heating the vicinity of the MTJ, the measured voltages decrease and even change their sign, the TMS ratio increases and reaches values up to 6000%.

The cross-section along the horizontal 0 line from figure 5(c) is presented in figure 4(a), the thermovoltages V_p , moving the laser beam across the centre of the MTJ along the short axis. The voltage values are given by the red dots connected to the x -axis by drop lines. The grey area at the bottom of the graph represents the Ta_2O_5 with the MTJ layer stack in between. For a clarification of the sample structure a sketch of the MTJ layer stack enlarged, and embedded into the Au and Ta contact pads is depicted in figure 4(c). The Gaussian curve indicating the heat distribution across the layer stack and its in-plane expansion is drawn into the plot to illustrate the direction of the incoming laser beam onto the sample and the resulting perpendicular temperature gradient from the top to the bottom layer. The data clearly states, that the largest temperature difference between the top and the bottom layer in the junction is achieved, when the laser

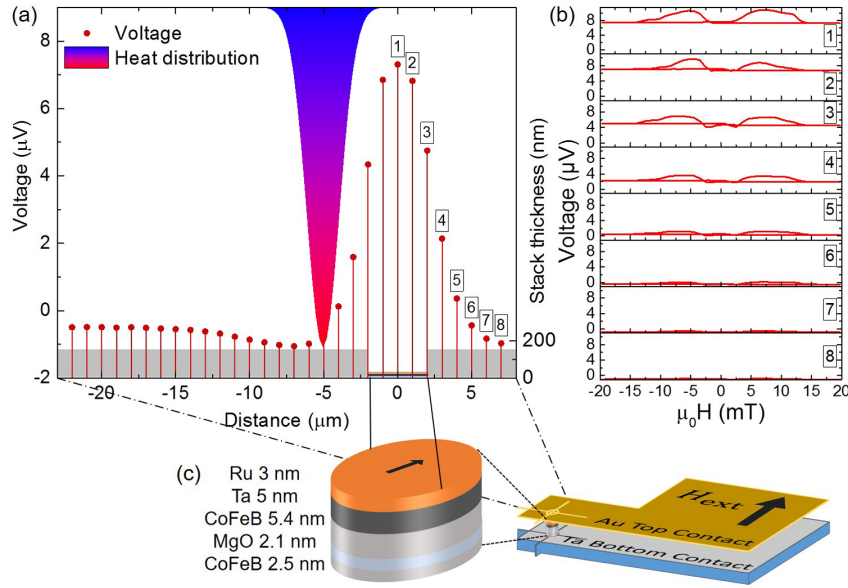


Figure 4. (a) Cross-section of the voltages recorded along the centre of the MTJs short axis, taken from the horizontal 0-line in figure 5(a) (left scale). The grey shaded area at the bottom represents a cross-section of the sample (150 nm Ta_2O_5) with the MTJ layer stack in between. The thickness is indicated on the right scale. The blue-red Gaussian function indicates the vertical heat gradient. The voltages numbered 1–8 are extracted from measurement curves in (b). (c) The structure of the pure MTJ is sketched on the left. The MTJ is embedded in the Au and Ta contacts. The blue layer underneath represents the substrate. The arrows show the direction of the external field.

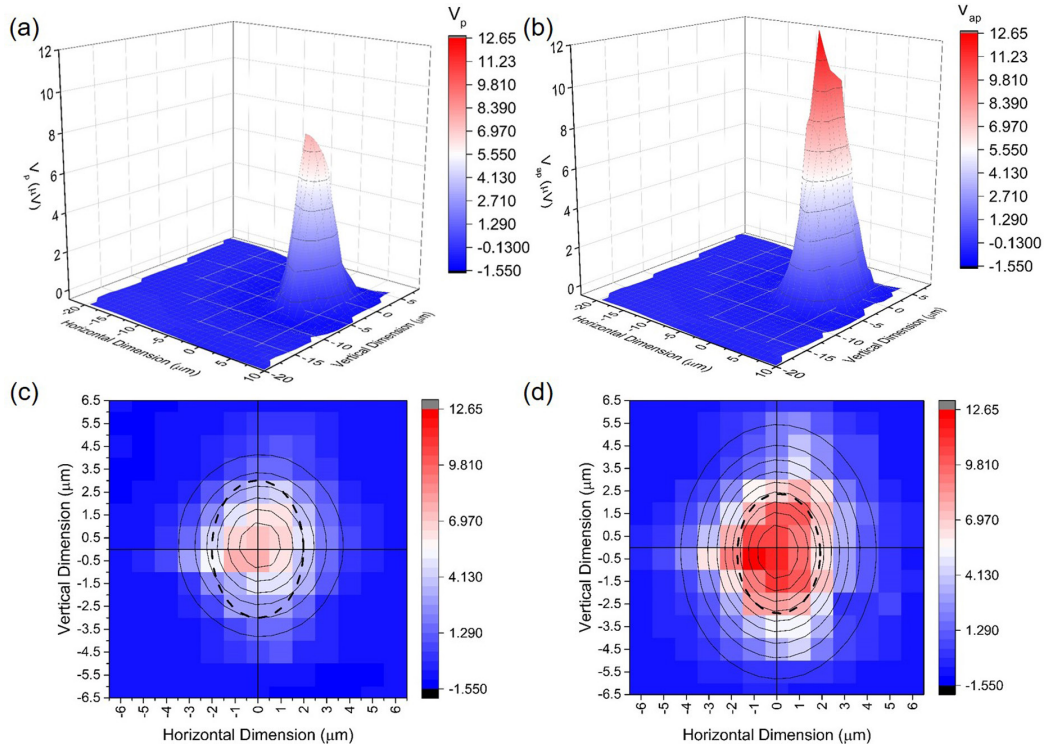


Figure 5. The extracted thermovoltages for the (a) parallel V_p and (b) antiparallel V_{ap} magnetization alignment as a function of the laser spot position (0 position is the centre of the MTJ). The false colour plots in (c) and (d) show the sections of V_p and V_{ap} respectively centred on the voltage peaks. In addition, both graphs contain 2D Gaussian function fits to the data, outlining the decrease of the signal from the centre to the edge. The dashed centred ellipse has the dimensions of the MTJ ($6 \mu\text{m} \times 4 \mu\text{m}$).

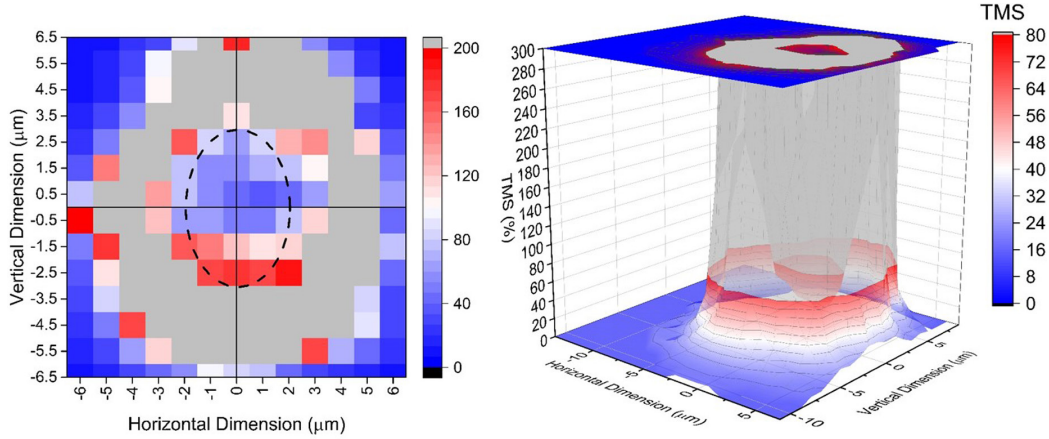


Figure 6. The TMS ratio calculated from the data depicted in the 2D scan (0 position is the centre of the MTJ). On the left, the false colour plot shows the region centred on the MTJ, marked by the dashed ellipse. The grey area depicts TMS ratios larger than 200%. The 3D surface plot illustrates the centre, where the MTJ is located with moderate TMS ratios around 50%–70%.

spot is positioned in the centre of the MTJ. Accordingly, the highest thermovoltages are generated, positioning the laser beam within $2.5 \mu\text{m}$ distance from the centre of the MTJ. At distances more than $8 \mu\text{m}$ away from the centre of the MTJ, the temperature remains largely unaffected. Considering the optical properties [23–25] of Ta_2O_5 , our first interpretation of the sign change is that the heat is transported through the Ta_2O_5 layer to the Ta bottom contact layer, which is distributed throughout the whole sample and as a result only the temperature of the bottom CoFeB layer increases. However, as stated in section 3.2, the laser power transmitted through the Au layer does not exceed 1%. Taking into account the low thermal conductivity and high heat capacity of Ta_2O_5 [26, 27], the heat is not conducted to the bottom Ta layer, which could pass it on to the bottom CoFeB electrode. This confirms the interface between the pillar stack and the Ta_2O_5 as the only channel to transport the heat to the bottom CoFeB electrode, which because of the irregularities remaining from the patterning process leads to a reversal of the temperature gradient. Because the in-plane distance is one order of magnitude larger than the layer stack thickness, the temperature difference is low. This leads to only a very small negative voltage. When positioning the laser spot $2 \mu\text{m}$ away from the MTJs edge, the voltage is small, but the calculated TMS ratio reaches values higher than 1000%. In this region, the layer stack is heated laterally, resulting in an elevated temperature, but only to a small temperature gradient and thus a small voltage is generated. To visualize this, figure 4(b)) shows the thermovoltage measurement curves numbered 1–8, from which the voltages in figure 4(a)) were extracted. Those curves show clearly, how the difference between the voltage in the parallel and antiparallel magnetization alignment decreases, when the laser is moved over the sample surface. In addition, it is also clearly visible, how the signal altogether decreases. These small signals give rise to the disproportionate increase in the calculated TMS ratios.

4. Conclusion

In this work, we have systematically varied the laser beam parameters to demonstrate effects of the lateral profile for the created temperature gradient in an MTJ layer stack and its influence on the generated thermovoltage and the corresponding TMS ratio. For the type of junction and oxide used for electric isolation we find that the best results are obtained, when the laser beam is situated directly above the centre of the MTJ and its diameter are smaller and equal to the junction size. That concludes, that for those laser spot sizes edge heating effects are minimized, reducing the in-plane created temperature gradients, leading to most homogeneous heating in the direction across the layer stack. The apparently high TMS ratios arise from lateral temperature gradients, which lead to elevated temperatures, but only small temperature gradients. These are mirrored in the small measurement signals leading to large TMS values. The thermovoltage maps show that a controlled temperature gradient has to be applied to avoid misinterpretations of the TMS effect. These effects of spot size and spot positioning are especially important if a sign change is observed in the lateral voltage maps. Furthermore, this shows an additional aspect, when comparing the data to theoretical simulations of the Seebeck coefficients. Here not only the temperature difference, that so far is only accessible through heat transfer simulations, but also the sensitivity of the thermovoltage signal in respect to the created temperature profiles can cause fluctuations in the calculated Seebeck coefficients. However, it also shows that the TMS in nanoscale spintronic devices allows much more variation of voltage and thermal landscapes in spin caloritronic devices on the micrometer scale. Concerning the current state of electronics, where devices are operated on signals in the magnitude of 1 V, the generated thermovoltages in the range of microvolts are still too low to implement this procedure and read information stored in MTJs. However, variations of other parameters, like

e.g. the junction size have not been addressed in a comparable systematic study so far. Already the variation of the tunnel barrier by replacing MgO with MAO or AlO can change the thermovoltage by up to one order of magnitude [12, 16]. This leaves a lot of room for investigation and improvement in the future.

Acknowledgments

This work was funded by the German Research Foundation (DFG) through the priority program ‘SpinCaT’ (SPP 1538).

References

- [1] Krawczyk M and Grundler D 2014 Review and prospects of magnonic crystals and devices with reprogrammable band structure *J. Phys.: Condens. Matter* **26** 123202
- [2] Lenk B, Ulrichs H, Garbs F and Münzenberg M 2011 The building blocks of magnonics *Phys. Rep.* **507** 107–36
- [3] Chumak A V, Serga A A and Hillebrands B 2014 Magnon transistor for all-magnon data processing *Nat. Commun.* **5** 4700
- [4] Walter M et al 2011 Seebeck effect in magnetic tunnel junctions *Nat. Mater.* **10** 742–6
- [5] Liebing N, Serrano-Guisan S, Rott K, Reiss G, Langer J, Ocker B and Schumacher H W 2011 Tunneling magnetothermopower in magnetic tunnel junction nanopillars *Phys. Rev. Lett.* **107** 177201
- [6] Czerner M, Bachmann M and Heiliger C 2011 Spin caloritronics in magnetic tunnel junctions: *ab initio* studies *Phys. Rev. B* **83** 132405
- [7] Heiliger C, Franz C and Czerner M 2013 *Ab initio* studies of the tunneling magneto-Seebeck effect: influence of magnetic material *Phys. Rev. B* **87** 224412
- [8] Liebing N, Serrano-Guisan S, Rott K, Reiss G, Langer J, Ocker B and Schumacher H W 2012 Determination of spin-dependent Seebeck coefficients of CoFeB/MgO/CoFeB magnetic tunnel junction nanopillars *J. Appl. Phys.* **111** 07C520
- [9] Liebing N, Serrano-Guisan S, Krzysteczko P, Rott K, Reiss G, Langer J, Ocker B and Schumacher H W 2013 Tunneling magneto thermocurrent in CoFeB/MgO/CoFeB based magnetic tunnel junctions *Appl. Phys. Lett.* **102** 242413
- [10] Boehnke A, Walter M, Roschewsky N, Eggebrecht T, Drewello V, Rott K, Münzenberg M, Thomas A and Reiss G 2013 Time-resolved measurement of the tunnel magneto-Seebeck effect in a single magnetic tunnel junction *Rev. Sci. Instrum.* **84** 63905
- [11] Boehnke A et al 2015 On/off switching of bit readout in bias-enhanced tunnel magneto-Seebeck effect *Sci. Rep.* **5** 8945
- [12] Huebner T, Boehnke A, Martens U, Thomas A, Schmalhorst J-M, Reiss G, Münzenberg M and Kuschel T 2016 Comparison of laser-induced and intrinsic tunnel magneto-Seebeck effect in CoFeB/MgAl₂O₃ and CoFeB/MgO magnetic tunnel junctions *Phys. Rev. B* **93** 224433
- [13] Butler W H, Zhang X-G, Schulthess T C and MacLaren J M 2001 Spin-dependent tunneling conductance of Fe/MgO/Fe sandwiches *Phys. Rev. B* **63** 54416
- [14] Mathon J and Umerski A 2001 Theory of tunneling magnetoresistance of an epitaxial Fe/MgO/Fe(001) junction *Phys. Rev. B* **63** 220403
- [15] Ikeda S, Hayakawa J, Ashizawa Y, Lee Y M, Miura K, Hasegawa H, Tsunoda M, Matsukura F and Ohno H 2008 Tunnel magnetoresistance of 604% at 300 K by suppression of Ta diffusion in CoFeB/MgO/CoFeB pseudo-spin-valves annealed at high temperature *Appl. Phys. Lett.* **93** 82508
- [16] Lin W, Hehn M, Chaput L, Negulescu B, Andrieu S, Montaigne F and Mangin S 2012 Giant spin-dependent thermoelectric effect in magnetic tunnel junctions *Nat. Commun.* **3** 744
- [17] Yuasa S, Nagahama T, Fukushima A, Suzuki Y and Ando K 2004 Giant room-temperature magnetoresistance in single-crystal Fe/MgO/Fe magnetic tunnel junctions *Nat. Mater.* **3** 868–71
- [18] Leutenantsmeyer J C et al 2015 Spin-transfer torque switching at ultra low current densities *Mater. Trans.* **56** 1323–6
- [19] Schreiber D K, Choi Y-s, Liu Y, Chiamonti A N, Seidman D N and Petford-Long A K 2011 Effects of elemental distributions on the behavior of MgO-based magnetic tunnel junctions *J. Appl. Phys.* **109** 103909
- [20] Mukherjee S et al 2015 Role of boron diffusion in CoFeB/MgO magnetic tunnel junctions *Phys. Rev. B* **91** 85311
- [21] Wang Z, Saito M, McKenna K P, Fukami S, Sato H, Ikeda S, Ohno H and Ikuhara Y 2016 Atomic-scale structure and local chemistry of CoFeB-MgO magnetic tunnel junctions *Nano Lett.* **16** 1530–6
- [22] Khosrofian J M and Garetz B A 1983 Measurement of a Gaussian laser beam diameter through the direct inversion of knife-edge data *Appl. Opt.* **22** 3406–10
- [23] Babeva T, Atanasova E and Koprinarova J 2005 Optical characteristics of thin rf sputtered Ta₂O₅ layers *Phys. Status Solidi a* **202** 330–6
- [24] Bright T J, Watjen J I, Zhang Z M, Muratore C, Voevodin A A, Koukis D I, Tanner D B and Arenas D J 2013 Infrared optical properties of amorphous and nanocrystalline Ta₂O₅ thin films *J. Appl. Phys.* **114** 83515
- [25] Chandra S V J, Reddy P S, Rao G M and Uthanna S 2007 Effect of postdeposition annealing on the structural, electrical, and optical properties of DC magnetron sputtered Ta₂O₅ films *Res. Lett. Mater. Sci.* **2007** 1–5
- [26] Jacob K T, Shekhar C and Waseda Y 2009 An update on the thermodynamics of Ta₂O₅ *J. Chem. Thermodyn.* **41** 748–53
- [27] Wu Z L, Reichling M, Hu X Q, Balasubramanian K and Guenther K H 1993 Absorption and thermal conductivity of oxide thin films measured by photothermal displacement and reflectance methods *Appl. Opt.* **32** 5660–5

5.2 Anomalous Nernst effect on the nanometer scale: exploring three-dimensional temperature gradients in magnetic tunnel junctions (Thesis article II)

Anomalous Nernst effect on the nanometer scale: Exploring three-dimensional temperature gradients in magnetic tunnel junctions

Ulrike Martens¹, Torsten Huebner², Henning Ulrichs³, Oliver Reimer², Timo Kuschel²,
Ronnie R Tamming⁴, Chia-Lin Chang⁴, Raanan I Tobey⁴, Andy Thomas⁵, Markus
Münzenberg¹, Jakob Walowski¹

1 Institut für Physik, Ernst-Moritz-Arndt Universität Greifswald, Felix-Hausdorff-Straße 6, 17489
Greifswald, Germany

2 Center for Spinelectronic Materials and Devices, Physics Department, Bielefeld University,
Universitätsstraße 25, 33615 Bielefeld, Germany

3 I. Physikalisches Institut, Georg-August-Universität Göttingen, Friedrich-Hund-Platz 1, 37077
Göttingen, Germany

4 Optical Condensed Matter Physics, Zernike Institute for Advanced Materials, University of
Groningen, Nijenborgh 4, 9747 AG Groningen, The Netherlands

5 Leibniz Institute for Solid State and Materials Research Dresden (IFW Dresden), Institute for
Metallic Materials, Helmholtzstrasse 20, 01069 Dresden, Germany

E-Mail: jakob.walowski@uni-greifswald.de, ulrike.martens@uni-greifswald.de

Abstract. Localized laser heating creates temperature gradients in all directions and thus leads to three-dimensional electron flux in metallic materials. Temperature gradients in combination with material magnetization generate thermomagnetic voltages. The interplay between these direction-dependent temperature gradients and the magnetization along with their control enable to manipulate the generated voltages, e.g. in magnetic nanodevices. We identify the anomalous Nernst effect (ANE) generated on a nanometer length scale by micrometer sized temperature gradients in magnetic tunnel junctions (MTJs). In a systematic study, we extract the ANE by analyzing the influence of in-plane temperature gradients on the tunnel magneto-Seebeck effect (TMS) in three dimensional devices. To investigate these effects, we utilize in-plane magnetized MTJs based on CoFeB electrodes with an MgO tunnel barrier. Due to our measurement configuration, there is no necessity to disentangle the ANE from the spin Seebeck effect in inverse spin-Hall measurements. The temperature gradients are created by a tightly focused laser spot. The spatial extent of the measured effects is defined by the MTJ size, while the spatial resolution is given by the laser spot size and the step size of its lateral translation. This method is highly sensitive to low voltages and yields an ANE coefficient of $K_N \approx 1.6 \cdot 10^{-8} \frac{V}{TK}$ for CoFeB. In general, TMS investigations in MTJs are motivated by the usage of otherwise wasted heat in magnetic memory devices for read/write operations. Here, the additionally generated ANE effect allows to expand the MTJs' functionality from simple memory storage to nonvolatile logic devices and opens new application fields such as direction dependent temperature sensing with the potential for further downscaling.

1. Introduction

Spin-dependent thermally driven transport phenomena have the potential to expand the functionality of today's conventional electronics. A dream of spintronic researchers has been to improve not solely the devices speed, but also enhance power management. This can be accomplished by employing additional energy conversion mechanisms usually available in semiconductor based integrated circuitry in the form of waste heat. The emerging field of spin caloritronics takes advantage of spin electronic devices in combination with thermal effects. This research field stands at the frontier between thermal transport and spin physics [1–3]. Magnetic tunnel junctions (MTJs) are one great testbed for spin caloritronic application devices. Originally, they were developed for storage capacity enhancement by the use of the tunnel magnetoresistance effect (TMR) [4]. However, their properties can be directly translated to spin caloritronics, when an electric potential as a driving force is replaced by temperature gradients. The thermal method generate voltage and read out information from MTJs employing temperature gradients utilizes the tunnel magneto-Seebeck effect (TMS). When a temperature gradient is applied across a layer stack of two magnetic electrodes separated by an insulating barrier, the generated voltage V differs, depending on whether the electrodes' magnetizations are aligned parallel (p) or antiparallel (ap). The microscopic origin together with theoretical predictions of the TMS for multiple CoFe compositions with MgO barriers is given in reference [5, 6] and is calculated by:

$$\text{TMS} = \frac{V_{\text{ap}} - V_{\text{p}}}{\min(|V_{\text{ap}}|, |V_{\text{p}}|)}. \quad (1)$$

The TMS effect has been observed and analyzed for various combinations of barrier and electrode materials, showing thermovoltages in the μV range for MgO [7–13] and MgAl_2O_4 [14, 15], and reaching the mV range for Heusler based MTJs [16]. All examined material configurations result in specific TMS ratios. While MgAl_2O_4 exhibits ratios below 10%, MgO reaches values up to 60% [15] and for electrode combinations CoFeB/MgO/Heusler even ratios of approximately 100% are reported. Meanwhile, the thermal voltage amplitudes approach the order of magnitude that could be used in commercial electronics. Besides this, other effects e.g. the Onsager reciprocal effect, the tunnel Peltier effect has been realized experimentally [17].

Two preconditions are required to unambiguously achieve enhanced Seebeck voltages in the MTJ's parallel and antiparallel state, V_{p} and V_{ap} , [9, 11]. One must apply a large temperature gradient that across the junction and the whole junction area needs to be heated homogeneously. As a consequence, using all-optical laser heating, the spot size needs to be adapted to the junction size and positioned centrally in order to create a well-defined temperature gradient across both electrodes and generate reliable voltages [11]. Temperature gradients deviating from the out-of-plane direction, for example temperature inhomogeneities in the sample plane, lead to additional thermoelectric effects that influence the total Seebeck voltages. In this study we focus on effects generated by these in-plane temperature gradients.

There are three thermomagnetic effects that come into question when considering ferromagnetic metal materials whose temperature gradient ∇T and the magnetization M are aligned in the same plane. The first two are the anisotropic magneto thermopower (AMTP) $E_{\text{AMTP}} \propto \nabla T \cdot \cos(\phi_{\nabla T}) M^2 \cdot \cos(2\phi_M)$ and the planar Nernst effect (PNE) $E_{\text{PNE}} \propto \nabla T \cdot \sin(\phi_{\nabla T}) \cdot M^2 \cdot \sin(2\phi_M)$. The angles $\phi_{\nabla T}$ and ϕ_M express the direction of ∇T and M with respect to the direction of voltage measurement. The third is the anomalous Nernst effect (ANE), $E_{\text{ANE}} \propto \nabla T \times M \propto \nabla T \cdot$

$M \cdot \sin(\phi)$. The angle ϕ denotes the angle between the magnetization M and the temperature gradient ∇T . In the first two configurations, the generated electric fields E_{AMTP} and E_{PNE} are both coplanar with ∇T and M [18], while in the last case, the voltage is orthogonal to both, ∇T and M . The former two effects are quadratic in M , which means, that magnetization reversal (180° rotation) would not lead to any change in the voltage direction. For the ANE, the resulting electric field is perpendicular to the plane defined by ∇T and the M vector, and in contrast to the former two it exhibits a sign change upon magnetization reversal. In general, ANE experiments are performed with an out-of-plane temperature gradient and the magnetization in the film plane (IM configuration), as published in references [19–28], as well as with in-plane temperature gradients and perpendicular magnetization (PM configuration), see references [24, 29, 30]. In those experiments, usually macroscopic millimeter sized structures and micrometer wide wires are investigated. The voltage is generated on macroscopic length scales ranging from $> 10 \mu\text{m}$ to several millimeters probing predominantly bulk-like properties. In this scope, the ANE measurements in perpendicular magnetized CoFeB nanowires with thicknesses below 1 nm play a special role, because those are the smallest dimensions, in which the ANE has been reported so far. There, the temperature gradients are created on length scales up to 500 nm and the generated voltages are detected on length scales in the micrometer range [31, 32].

In the present study, we utilize an extended TMS measurement configuration to deliberately create in-plane temperature gradients in MTJ electrodes with in-plane magnetization easy axis and detect the underlying thermomagnetic processes on mesoscopic length scales. This is done by the application of complex three-dimensional temperature gradients to drive spin caloritronic effects in the layered device. We exploit a high flexibility to control both, the magnetization and the temperature gradient direction, and measure the voltages in the lithographically structured MTJ. In our experimental configuration the voltage is measured in the out-of-plane direction (defined as z-axis), perpendicular to the applied magnetic field $\mu_0 H$ (defined as y-axis) while the in-plane temperature gradient is rotated in the x-y plane (see figure 1).

We use pseudo-spin valves, because of their most simplistic layer structure and possibility to control the magnetization in both layers of the MTJs. In contrast to exchange biased spin valves, where one magnetic layer is pinned, these devices allow multiple magnetic configurations in the parallel magnetization alignment: With respect to the temperature gradient the magnetization of both ferromagnetic electrodes can be rotated together. We define the thermovoltage measured in the parallel state for direction 1 and 2 as V_{p1} and V_{p2} , as depicted in figure 2. The difference $\Delta V_{\text{ANE}} = V_{\text{p1}} - V_{\text{p2}}$ is employed in the following to disentangle and characterize thermomagnetic effects that arise from in-plane temperature gradients created in the plane of the electrodes.

The structure we use is briefly outlined as follows. First, the sample geometry and layer sequence are sketched to explain temperature distribution within the corresponding geometries and the applied external magnetic fields. The access to temperature gradients and the relevant temperature differences is discussed by finite element simulations using COMSOL. Second, the data extraction procedure is given together with the analysis, from which we conclude the presence of the ANE in our experiments. After that, additional experimental data is presented that identifies the uniaxial magnetic anisotropy present in the investigated samples. In the end, we compare the ANE constant to findings from other experimental techniques and discuss new possible applications for this effect based on micro- and nanoscale MTJ devices.

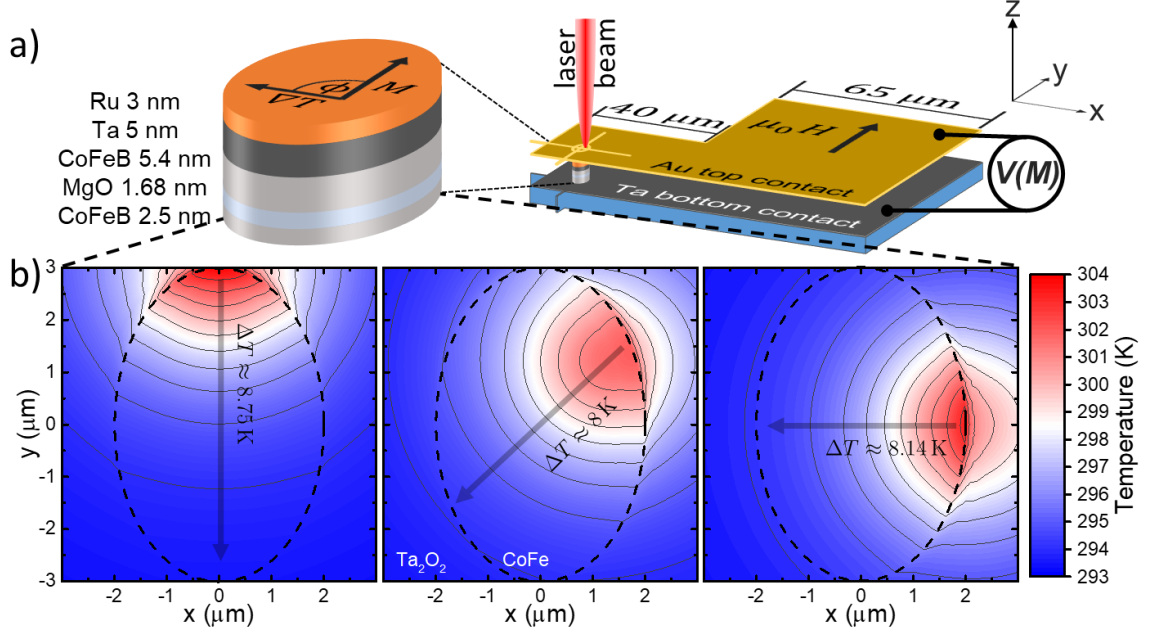


Figure 1 a) Left: The MTJ layer stack with the corresponding thicknesses. The magnetization M , with respect to the in-plane temperature gradient ∇T (black arrows) their relation is given by the in-plane varied angle ϕ . Right: MTJ between the Au top and the Ta bottom contacts. The direction of the incoming laser beam, the external magnetic field $\mu_0 H$ and the thermovoltage measurement configuration are indicated within the coordinate axes. b) False color plots showing the in-plane temperature gradients in the top CoFeB electrode for three heating laser spot positions at the junction edges obtained from COMSOL simulations. The MTJ areas are indicated by the dashed lines. Heating at the end of the long (short) axis results in the main temperature gradient in y-direction (x-direction) as shown in the left (right) graph and is indicated by the black arrows. The middle graph shows the scenario, when the heating laser spot is placed on the edge between both major ellipses axes, resulting in the main temperature gradient at an angle between the two.

2. Temperature distribution

The key feature to analyze spin caloritronic effects in MTJs is the access to temperature distributions on micrometer to nanometer length-scales. TMR junctions provide a rich variety of possibilities to create anisotropic temperature profiles on nm to μm length-scales using position-dependent laser heating. Extending the scanning technique originally developed for the extraction of the preferably pure TMS signal, as introduced in reference [11], allows a systematic temperature gradient variation. The schematic in Figure 1a) depicts this experimental procedure. In general, a centrally positioned laser spot creates a temperature gradient through the layer stack in z-direction that generates a magnetization dependent voltage $V(M)$ which can be varied by sweeping an external magnetic field $\mu_0 H$ applied in y-direction. The MTJ layer stack itself is embedded into Au and Ta contact pads and surrounded by insulating Ta_2O_5 in the x-y-plane. The Au pads thickness is around three times larger than the optical penetration depth $\lambda_{\text{opt}} \approx 15 - 20\text{nm}$, leaving purely thermal excitation in the CoFeB layers. This sample design allows to create and steadily vary temperature gradients in the x-y-plane by moving the laser spot along the surface. The voltage generated at the CoFeB electrodes is measured in z-direction. Due to this configuration the main voltage contribution generated by in-plane temperature gradients stems from the ANE. Both the AMTP and the PNE can be disregarded, because the voltage is generated in the x-y-plane, and only second order processes with amplitudes that are orders of magnitude smaller can contribute to the out-of-plane signal. For the investigation of inhomogeneous laser heating, the setup parameters need additional adjustment. The modulated continuous wave laser spot is focused down to $2\text{ }\mu\text{m}$

in diameter and systematically scanned across the sample within an area of $30 \times 30 \mu\text{m}^2$ in which the elliptically shaped MTJ itself has a dimension of $6 \mu\text{m}$ by $4 \mu\text{m}$. Performing such a 2-dimensional scan, a local heating point is moved over the entire MTJ area, and enables the creation of specifically directed and consistently varied temperature gradients. This allows us to apply complex three-dimensional temperature profiles at will. The situation is discussed in the following example when we place the laser spot at the MTJ's edge.

Figure 1a) (left) shows an enlargement of the elliptically shaped MTJ layer stack. The tunnel junction consists of the CoFeB/MgO/CoFeB stack, the Ta layer is necessary to remove boron during crystallization from the CoFeB/MgO interface and lastly the Ru capping is deposited to prevent oxidation during the ex-situ annealing process and patterning. The in-plane ∇T together with the in-plane M and the angle ϕ are sketched on top of the stack. Note, that during the measurement, the direction of M remains constant, while ∇T is rotated by $\phi = 0^\circ - 360^\circ$. The access to temperature in such small devices is not available experimentally, therefore, three-dimensional finite element simulations using the COMSOL package with the heat transfer module are performed to gain insight into the temperature distribution within the MTJ. The simulations are performed for continuous wave laser heating in equilibrium.

Figure 1b) displays the temperature distribution for three different laser spot positions located at the MTJ edges. The false color plots show the equilibrium temperature distribution inside the top CoFeB electrode which is indicated by the dashed lines. The temperature distribution in the bottom CoFeB shows the same characteristics and is not shown here. However, due to ∇T created in the out-of-plane direction, the overall T is slightly lower. The difference in temperature between top and bottom electrodes ranges from $\Delta T_{\text{top-bottom}} \approx 50 \text{ mK}$ in the vicinity of the laser spot to less than 1 mK at the opposite edge and decreases exponentially. Since the dimensions in the x-y-plane are three orders of magnitude larger, the in-plane temperature differences are larger than those across the layer stack. The temperature gradient directions for each heating scenario are indicated by the gray arrows accompanied by the temperature drop ΔT between both junction edges.

The left plot describes the first scenario, when the laser spot is located at the vertex, then a temperature gradient along the major-axis with a temperature difference $\Delta T \approx 9 \text{ K}$ is created. The right plot illustrates the second scenario, when the laser spot is located at the co-vertex, resulting in a temperature gradient along the minor-axis with $\Delta T \approx 8 \text{ K}$. Finally, the middle plot shows the third heating scenario when the laser spot is located at the edge of the ellipse at a 45° angle between both principal axes. Consequently, this results in a temperature gradient along the MTJ diagonal with $\Delta T \approx 8 \text{ K}$. The slight temperature differences for these extremal cases results from the asymmetry in the MTJ's geometry. A thorough temperature profile analysis reveals that independent of the ∇T angle the in-plane temperature gradient covers equally sized areas of the MTJ. Therefore, we expect the number of electrons involved in the process triggered by the in-plane temperature gradient to remain angle independent.

The largest, most homogeneous area with a high temperature gradient across the layer stack is created when the laser spot is located with its center at least $1.7 \mu\text{m}$ away from the MTJ's edge. When heating within this area, effects from in-plane temperature gradients can be excluded. We conclude that by application of the laser spot at the edge of the tunnel junction, large in-plane gradients can be created that we can rotate by an arbitrary angle in the x-y-plane that dominate the three-dimensional temperature distribution. For a laser spot at the center, the overall x-y-gradient is found to vanish, and we have predominantly a temperature gradient in z-direction.

3. Anomalous Nernst effect

The pseudo spin valves selected in this study allow for the full directional manipulation of the magnetization in both electrodes, because in contrast to conventional MTJ design, none of the magnetic layers is antiferromagnetically pinned. The condition for their antiparallel magnetization alignment is realized by choosing electrodes with different anisotropy strength and thus different coercive fields. In the presented investigation both CoFeB layer differ in thicknesses by around 2 nm to fulfil this criterion. This allows two parallel magnetization alignment configurations of opposite direction.

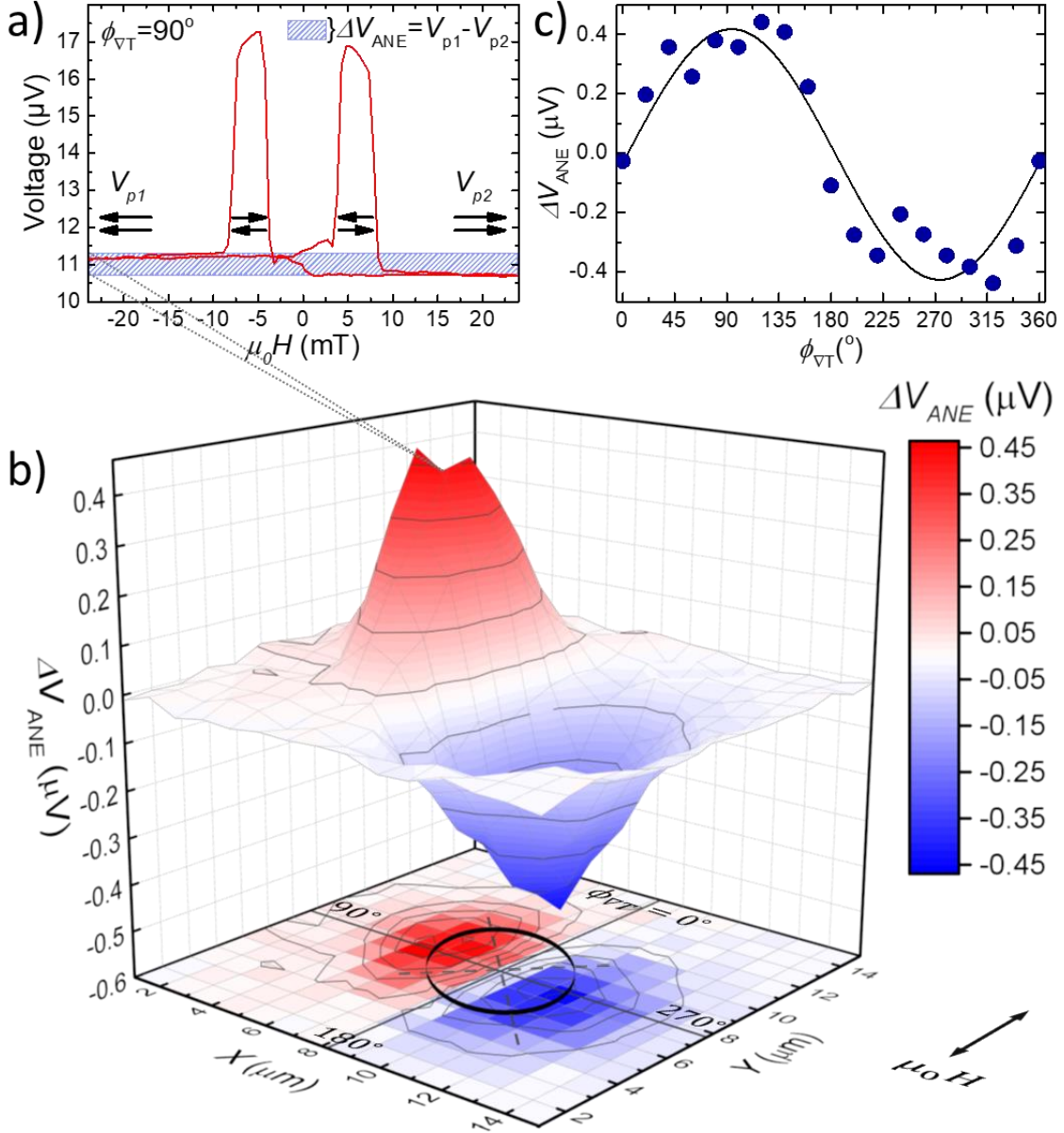


Figure 2 a) Exemplary TMS measurement curve showing the Seebeck voltage vs. the external field (red line). The ranges with parallel and antiparallel magnetization alignment of both electrodes are indicated by the black arrows. The blue area marks the difference ΔV_{ANE} between the voltage measured in parallel magnetization configuration for both directions V_{p1} and V_{p2} . **b)** The extracted ΔV_{ANE} values are plotted vs. the laser position in a three-dimensional surface plot with a false color projection at the bottom. The black ellipse outlines the MTJ area, with the grey cross located along the principal axes. **c)** ΔV_{ANE} values extracted along the ellipses outline plotted against the temperature gradient angle ϕ_{VT} together with the fitted sine curve.

Figure 2 a) shows an example of a Seebeck voltage vs. external field $\mu_0 H$ sweep, recorded while the laser spot is close to the MTJ edge and a pronounced in-plane temperature gradient is generated, $\phi_{\nabla T} = 90^\circ$. The ranges with parallel and antiparallel magnetization alignment are indicated by the black arrows. For large field amplitudes, both electrodes magnetizations align parallel and a different Seebeck voltage is generated than in the antiparallel alignment. From this measurement curve, the TMS ratio is calculated, which results in a ratio of approximately 50 %. This is consistent with the findings reported in reference [11].

The measurement confirms the two possibilities for parallel alignment configuration of opposite direction, V_{p1} for negative $\mu_0 H$ and V_{p2} for positive $\mu_0 H$. Furthermore, the data exhibits a clear shift of V_{p1} with respect to V_{p2} . This voltage shift $\Delta V_{ANE} = V_{p1} - V_{p2}$ is marked by the shaded blue area. We argue that ΔV_{ANE} originates from the in-plane temperature gradient, which affects the voltage in the perpendicular direction for parallel magnetization states of opposite sign. At this point we rule out the PNE and the AMTP. Their quadratic dependence on the magnetization $\sim M^2$ would not result in a difference between V_{p1} and V_{p2} upon magnetization reversal. Conclusively we state that ΔV_{ANE} originates from the ANE.

The laser spot is moved over the sample surface and the in-plane temperature gradient is varied, as analyzed in the previous section from the finite element temperature simulations. From each curve, one ΔV_{ANE} value is extracted and plotted in figure 2 b). In each measurement, the magnetization is reversed together with $\mu_0 H$ along the y-axis, as depicted by the black double arrow next to the graph. Figure 2 b) is divided into two parts.

In the first part, the extracted ΔV_{ANE} values for each heating scenario are illustrated in a three-dimensional surface plot. The spatial position for the ΔV_{ANE} value extracted from figure 2 a) is indicated by the gray dotted lines pointing to figure 2 b). The voltage difference ΔV_{ANE} shows an increase and a decrease with absolute value maxima of around $0.4 \mu V$ showing an inversion symmetry regarding the origin of the coordinate system.

In the second part, the same data is projected at the bottom in a false color plot for a better overview. This depiction includes an outline of the MTJ's elliptical area with both principal axes (dashed dark gray crossed lines). Without loss of generality, the angle $\phi_{\nabla T} = 0^\circ$ is defined along the positive y-axis and parallel to the positive $\mu_0 H$ and the $\phi_{\nabla T}$ rotation is marked in counter clockwise direction. Both extreme values of ΔV_{ANE} are generated when the laser heating spot is located near the MTJ's edge, where the largest in-plane temperature differences are created (compare COMSOL simulations in figure 1) and at $\phi_{\nabla T} = 90^\circ$ and $\phi_{\nabla T} = 270^\circ$. The borderline between the elevation and decrease where $\Delta V_{ANE} \approx 0$ proceeds parallel to $\mu_0 H$ and is perpendicular to the line connecting the extreme ΔV_{ANE} absolute value locations.

As a main result, the ΔV_{ANE} values extracted from the positions marked by the black ellipse outline are plotted versus the temperature gradient angle $\phi_{\nabla T}$ with respect to the $\mu_0 H$ direction is shown in figure 2 c). This two-dimensional plot highlights the ΔV_{ANE} sign change upon in-plane ∇T reversal with respect to the magnetization. This behavior confirms the thermomagnetic origin of the extracted effect. Further analysis of the ΔV_{ANE} signal in figure 2 c) validates the ANE effect generated by in-plane temperature gradients. The extracted data (blue dots) are fitted to the formula given by the ANE cross product definition, when the temperature gradient is rotated by $\phi_{\nabla T}$:

$$\Delta V_{ANE} = A \cdot \sin(\phi_{\nabla T} - \phi_0) + V_0. \quad (2)$$

The extracted fit parameters are $A = (0.42 \pm 0.04) \mu\text{V}$, the maximum ΔV_{ANE} amplitude, $\phi_0 = (4 \pm 5)^\circ$, the phase shift, which expresses the angle between the MTJ's magnetization and ∇T when the temperature gradient is aligned parallel to $\mu_0 H$, and $V_0 = (0.00 \pm 0.026) \mu\text{V}$, the offset voltage.

The small value obtained for ϕ_0 indicates an excellent magnetization easy axis alignment with the external field direction. This also reveals, that when ∇T and M are aligned parallel or antiparallel, $\Delta V_{\text{ANE}} = 0$. This corresponds to the angles $\phi_{\nabla T} = 0^\circ$ and $\phi_{\nabla T} = 180^\circ$, as indicated in the projection in figure 2 b). Both maximum amplitudes are located at $\phi_{\nabla T} = 90^\circ$ and $\phi_{\nabla T} = 270^\circ$, when M and ∇T are perpendicular to each other. In conclusion, our findings are consistent with the cross product definition of the ANE. Besides this, the vanishing offset V_0 confirms the ANEs symmetry with respect to the magnetization direction.

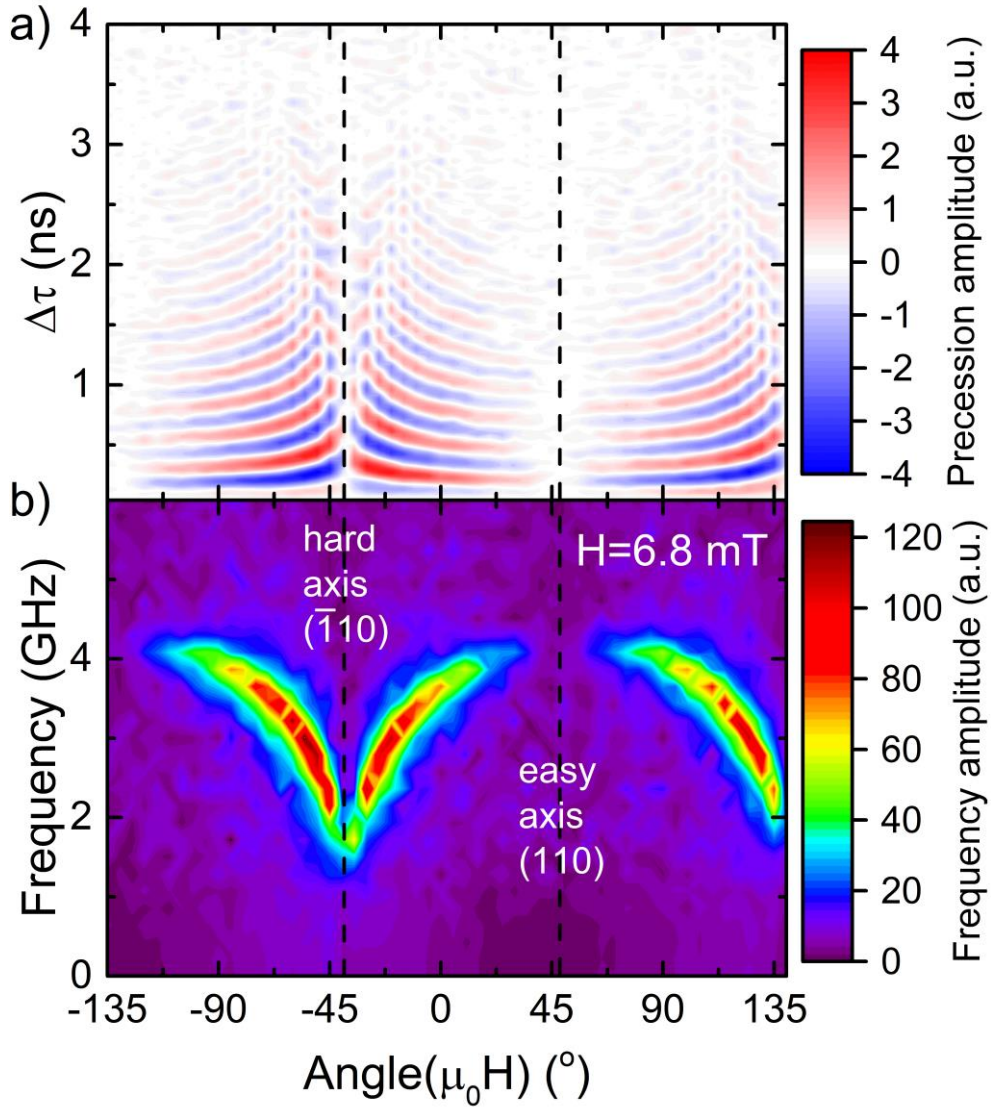


Figure 3 a) Precessional dynamics from all-optical pump-probe experiments recorded for a CoFeB thin film, by rotating the $\mu_0 H = 6.8$ mT in the film plane in steps of 5° . The precession amplitude is coded from negative deflection (blue) to positive deflection (red). b) The precession frequencies extracted by FFT (different color code for a better distinction). The magnetic hard and easy axes are marked by the dashed black lines. The precession frequency increases towards the magnetic easy axis and declines towards the hard axis.

During the course of our measurements, we find that the MTJs possess an in-plane magnetic anisotropy. This is indicated in TMR as well as in MOKE measurements on CoFeB/MgO films. Additional magnetic anisotropy contributions could also influence the characteristics of the ANE effect.

In order to suppress these contributions to the voltage signal generated by in-plane temperature gradients, we first analyze the magnetic anisotropy for CoFeB thin films deposited on MgO substrates in detail. For this purpose, magnetization dynamics experiments, rotating $\mu_0 H$ in the sample plane are performed with an angle resolution of 5° , as depicted in figure 3 a). Here, the precessional dynamics on the nanosecond time scale are plotted vs. the rotation of $\mu_0 H$ in a false color plot, showing the negative/positive precession amplitude in blue/red. Figure 3 b) shows the precession frequencies extracted by fast Fourier transform. The frequency amplitudes are false color coded using a different color scheme for a better distinction. In accordance to the analysis presented in reference [33], we interpret our data as follows. The plot shows a declining precession frequency near the hard axis pointing in the $(\bar{1}10)$ direction and frequency increase when $\mu_0 H$ is rotated towards the easy axis pointing in the (110) direction. The frequency reaches saturation and the amplitude declines in the vicinity of the easy axis, because the applied field amplitude ($\mu_0 H = 6.8$ mT) is sufficient to saturate the sample, but too small to force the magnetization slightly out of the easy axis. This means, CoFeB grown on MgO exhibits a uniaxial magnetic anisotropy (UMA) with the easy axis along the (110) crystalline direction.

Although the MTJ's elliptic shape is aligned with the vertex along the (100) direction, for a 1.5 vertex/co-vertex ratio and a layer thickness in the nanometer range, the calculated demagnetizing fields due to shape anisotropy are approximately 2 mT, using geometrical considerations given in reference [34]. Therefore, solely the magneto-crystalline anisotropy remains as a significant factor leaving the easy axis in the (110) direction. Taking those findings into account, the MTJ is placed with the easy magnetization axis parallel to the applied field $\mu_0 H$ for the ANE measurements.

In addition to this we also exclude contact resistance or bond wire geometry as an origin for this behavior, because repetition of those measurements with the contact wires attached at different angles to the magnetic field as well as at various positions and distances from the MTJ all return the same qualitative and quantitative characteristics (not shown here).

Finally, from these findings, the ANE coefficient can be estimated, considering that the CoFeB saturation magnetization is $M_S \approx 1.6$ T and the in-plane temperature difference $\Delta T \approx 8$ K. The maximum ΔV_{ANE} value needs to be divided by two, because the shift in figure 2 a) influences the voltage measured in both parallel magnetization alignment directions. Starting with a homogeneous heating scenario, where the in-plane $\nabla T \approx 0$, also results in $\Delta V_{ANE} = 0$. However, an in-plane $\nabla T \neq 0$ shifts V_{p1} to higher values, while it shifts V_{p2} to lower values. Thus, the contribution to the ANE is given by $\frac{1}{2} \Delta V_{ANE}$. This results in an anomalous Nernst coefficient of $K_N =$

$\frac{\frac{1}{2} \Delta V_{ANE}}{M_S \cdot \Delta T} \approx 1.6 \cdot 10^{-8} \frac{V}{TK}$. How does this value compare to previously published results? In 2014, Lee et al. determined the anomalous Nernst coefficients in ferromagnet/ non-magnet heterostructures for non-magnet materials with different spin hall angles in the range from $10^{-6} \frac{V}{TK}$ to $10^{-8} \frac{V}{TK}$ [23]. The value found in our detection scheme through magneto-Seebeck measurements, agrees well with the order of magnitude with these values. However, in their measurement the contributions from the ANE and the spin Seebeck effect are difficult to disentangle. A further look into literature reveals that K_N varies between different materials by several orders of magnitude. For instance,

Wells et al. extracted an anomalous Nernst coefficient $K_N = 2.3 \cdot 10^{-6} \frac{\text{V}}{\text{TK}}$ from measurements on perpendicularly (out-of-plane) magnetized amorphous CoFeB nanowires [31]. For FePt, Mizuguchi et al., and later Sakuraba et al. determined an anomalous Nernst coefficient of $\sim 0.5 \cdot 10^{-7} \frac{\text{V}}{\text{TK}}$ [35, 36]. A similar value of $\sim 1.3 \cdot 10^{-7} \frac{\text{V}}{\text{TK}}$ [19] was found by Weiler et al. for Ni. The comparison shows that our experimental method is extremely sensitive. We estimate that even for an anomalous Nernst coefficient as small as $10^{-9} \frac{\text{V}}{\text{TK}}$ a detection would be possible.

4. Conclusion

We investigated how in-plane temperature gradients in single magnetic tunnel junctions enhances or decreases the out-of-plane thermovoltage in TMS measurements. The extracted voltage shows a symmetric characteristic that can be clearly attributed to the anomalous Nernst effect with respect to the uniaxial magnetic anisotropy of the sample. This uniaxial magnetic anisotropy is verified by magnetization dynamics measurements.

Primarily we observe, that the ANE affects only the Seebeck voltage in the parallel magnetization alignment and the ANE voltages are two orders of magnitude smaller compared to the TMS voltages. Therefore, the influence on the overall TMS ratio needs to be considered in the analysis if in-plane temperature gradients are present, even if it is small. Nevertheless, the ANE can be clearly identified and extracted from TMS measurements of pseudo spin valve MTJs.

In the case of MTJs with one antiferromagnetically pinned and one switching electrode, the occurrence of ANE due to inhomogeneous heating and the presence of in-plane temperature gradients will lead to a deviation in the magneto-Seebeck voltage from the real value. However, in this configuration it is not possible to disentangle both contributions.

In our experiments, samples with different MgO barrier thicknesses are measured and show qualitatively similar characteristics. Thus, we can conclude that there is no significant influence of the MgO layer thickness on the ANE contribution.

Within this study, we illustrate the first detection of the anomalous Nernst effect in MTJs on such short length scales also obtaining a high spatial resolution. These results demonstrate very clearly the importance of homogenous laser heating to avoid unintended effects in case of TMS measurements by laser heating. The measurements show a clear dependence of the extracted ANE effect on the angle between the magnetization and the temperature gradient. Together with a proper calibration, and a combination of the investigated effects and technologies enables the construction of a direction dependent thermometer. This thermometer would not only sense the temperature, but also the direction of change. Besides this, the exponential temperature decay in the sample plane together with the sensitivity of this method, leave room for further device miniaturization beyond the micrometer scale.

5. Acknowledgements

The authors gratefully acknowledge financial support by the Deutsche Forschungsgemeinschaft (DFG) within the priority program SpinCaT (SPP 1538).

6. Methods

Sample fabrication

The sample stack of the investigated thin films consists of Au 70 nm/ Ru 3 nm/ Ta 5 nm/ CoFeB 5.4 nm/ MgO 1.68 nm/ CoFeB 2.5 nm/ Ta 10 nm/ MgO (100) substrate. The CoFeB electrodes are fabricated by magnetron sputtering using 2 inch targets with a composition of $\text{Co}_{0.2}\text{Fe}_{0.6}\text{B}_{0.2}$ (analysis Co:Fe 0.32:0.68). In a separate chamber, the MgO barrier is e-beam evaporated without breaking the vacuum. The Ru capping layer is deposited by e-beam evaporation and prevents the underlying layers from oxidation. Ex-situ annealing with applied bias field is performed to crystallize the amorphous CoFeB electrodes and the MgO layer to obtain coherent interfaces and to activate the diffusion of B into the Ta layers [37–39]. Afterwards elliptical MTJs are patterned to a size of $6\ \mu\text{m} \times 4\ \mu\text{m}$ with the long axis parallel to the direction of the magnetic field applied during the annealing by lithography processes. For thermal and electrical isolation, Ta_2O_5 is sputtered in the surroundings of the single MTJs. The Au layer pads on top are necessary to enable electrical contacting. A detailed description of the sample fabrication can be found in reference [11].

Setup

Magneto-Seebeck experiment

For the generation of a temperature gradient across the layer stack, a laser diode (TOPTICA ibeam smart) with a wavelength of 638 nm and a maximum power of 150 mW is used. The laser is focused to a minimum diameter of $\sim 2\ \mu\text{m}$ full-width at half-maximum by utilizing a microscope objective (NIKON 20x, WD 20.5 mm). The generated thermovoltage is detected with a lock-in amplifier. The laser diode is modulated with a square wave at a frequency of 77 Hz, which is used as modulation frequency for the lock-in amplifier. For magnetization-dependent measurements, the sample is placed in between two pole shoes of an electromagnet. The implemented linear stages with motorized actuators for the horizontal (x-direction) and vertical (y-direction) movement enable an exact positioning of the laser beam on the sample surface together with a high spatial resolution of $0.2\ \mu\text{m}$. This setup allows the recording of the generated thermovoltage in z-direction depending on the magnetization direction by heating the sample at different positions over a defined area. In this study, the measured area is adapted to the junction size and in respect to the backlash of the actuators a dimension of $30\ \mu\text{m} \times 30\ \mu\text{m}$ with a resolution of $1\ \mu\text{m}$ is preferred.

Magnetization dynamics

The all-optical pump-probe Faraday configuration uses a 400 nm pump and 800 nm probe beam from a 1 kHz Ti:Sapphire laser system with 120 fs pulse lengths. The pump fluence is $F_{\text{pump}} = 5.7\ \frac{\text{mJ}}{\text{cm}^2}$. The delay can be varied from 0 – 8 ns. The sample is situated in a constant applied magnetic field which can be rotated in the sample plane.

Temperature distribution simulations

The temperature distributions were obtained by finite element modelling with the software package COMSOL version 4.2a, including the heat transfer module. Most values for the necessary material parameters (specific heat c , thermal conductivity κ , density ρ) were taken from reference [7]. For Ta_2O_5 we assumed $c = 135.6\ \frac{\text{J}}{\text{mol}\cdot\text{K}}$, $\kappa = 0.3\ \frac{\text{W}}{\text{m}\cdot\text{K}}$, and $\rho = 8270\ \frac{\text{kg}}{\text{m}^3}$ according to references [40, 41]. In contrast to the work presented in reference [7], here we implemented a fully three-dimensional model of the junction. The laser-heating was taken into account as a

volumetric heating source $H \sim \exp\left(-\frac{z}{\lambda_{opt}} - \frac{2(x-x_0)^2 + (y-y_0)^2}{w^2}\right)$, where $z = 0$ refers to the surface of the top Au electrode.

Authors contributions

U.M., J.W. and M.M. designed and set up the experiments U.M. performed the TMS/ANE measurements. U.M. and T.H. prepared the samples. H.U. performed the COMSOL simulations, analyzed and discussed the temperature data with U.M. and J.W. R.R.T., C.L.C. and R.I.T. performed the magnetization dynamics experiments, analyzed and discussed the anisotropy data with U.M. and J.W. U.M. and J.W. analyzed the data and discussed the thermal effects with T.H., O.R. and T.K. U.M. and J.W. prepared the manuscript. All authors discussed the experiments and the manuscript. M.M. and A.T. coordinated the research.

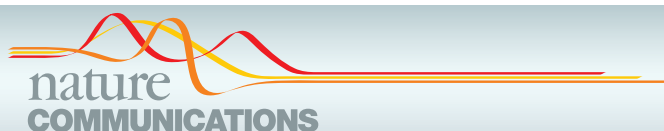
References

- [1] Bauer G E W, Saitoh E and van Wees B J 2012 Spin caloritronics *Nat. Mater.* **11** 391–9
- [2] Yu H, Brechet S D and Ansermet J-P 2017 Spin caloritronics, origin and outlook *Phys. Lett. A* **381** 825–37
- [3] Boona S R, Myers R C and Heremans J P 2014 Spin caloritronics *Energy Environ. Sci.* **7** 885
- [4] Miao G-X, Münzenberg M and Moodera J S 2011 Tunneling path toward spintronics *Reports on Progress in Physics* **74** 36501
- [5] Czerner M, Bachmann M and Heiliger C 2011 Spin caloritronics in magnetic tunnel junctions: Ab initio studies *Phys. Rev. B* **83** 132405
- [6] Heiliger C, Franz C and Czerner M 2013 Ab initio studies of the tunneling magneto-Seebeck effect: Influence of magnetic material *Phys. Rev. B* **87** 224412
- [7] Walter M *et al* 2011 Seebeck effect in magnetic tunnel junctions *Nat. Mater.* **10** 742–6
- [8] Liebing N, Serrano-Guisan S, Rott K, Reiss G, Langer J, Ocker B and Schumacher H W 2011 Tunneling magnetothermopower in magnetic tunnel junction nanopillars *Phys. Rev. Lett.* **107** 177201
- [9] Boehnke A, Walter M, Roschewsky N, Eggebrecht T, Drewello V, Rott K, Münzenberg M, Thomas A and Reiss G 2013 Time-resolved measurement of the tunnel magneto-Seebeck effect in a single magnetic tunnel junction *Rev. Sci. Instrum.* **84** 63905
- [10] Boehnke A *et al* 2015 On/off switching of bit readout in bias-enhanced tunnel magneto-Seebeck effect *Sci. Rep.* **5** 8945
- [11] Martens U, Walowski J, Schumann T, Mansurova M, Boehnke A, Huebner T, Reiss G, Thomas A and Münzenberg M 2017 Pumping laser excited spins through MgO barriers *J. Phys. D: Appl. Phys.* **50** 144003
- [12] Böhnert T, Serrano-Guisan S, Paz E, Lacoste B, Ferreira R and Freitas P P 2017 Magnetic tunnel junctions with integrated thermometers for magnetothermopower measurements *J. Phys.: Condens. Matter* **29** 185303
- [13] Böhnert T, Dutra R, Sommer R L, Paz E, Serrano-Guisan S, Ferreira R and Freitas P P 2017 Influence of the thermal interface resistance on the thermovoltage of a magnetic tunnel junction *Phys. Rev. B* **95** 104441
- [14] Huebner T, Boehnke A, Martens U, Thomas A, Schmalhorst J-M, Reiss G, Münzenberg M and Kuschel T 2016 Comparison of laser-induced and intrinsic tunnel magneto-Seebeck effect in CoFeB/MgAl₂O₄ and CoFeB/MgO magnetic tunnel junctions *Phys. Rev. B* **93** 224433

- [15] Huebner T, Martens U, Walowski J, Boehnke A, Krieff J, Heiliger C, Thomas A, Reiss G, Kuschel T and Münzenberg M 2017 *Enhancement of thermovoltage and tunnel magneto-Seebeck effect in CoFeB based magnetic tunnel junctions by variation of the MgAl₂O₄ and MgO barrier thickness* (arXiv:1706.08287, under review)
- [16] Boehnke A *et al* 2017 Large magneto-Seebeck effect in magnetic tunnel junctions with half-metallic Heusler electrodes *Nat. Commun.* **8** 1626
- [17] Shan J, Dejene F K, Leutenantsmeyer J C, Flipse J, Münzenberg M and van Wees B J 2015 Comparison of the magneto-Peltier and magneto-Seebeck effects in magnetic tunnel junctions *Phys. Rev. B* **92** 20414
- [18] Reimer O *et al* 2017 Quantitative separation of the anisotropic magnetothermopower and planar Nernst effect by the rotation of an in-plane thermal gradient *Scientific reports* **7** 40586
- [19] Weiler M *et al* 2012 Local charge and spin currents in magnetothermal landscapes *Phys. Rev. Lett.* **108** 106602
- [20] Bieren A von, Brandl F, Grundler D and Ansermet J-P 2013 Space- and time-resolved Seebeck and Nernst voltages in laser-heated permalloy/gold microstructures *Appl. Phys. Lett.* **102** 52408
- [21] Brandl F and Grundler D 2014 Fabrication and local laser heating of freestanding Ni 80 Fe 20 bridges with Pt contacts displaying anisotropic magnetoresistance and anomalous Nernst effect *Appl. Phys. Lett.* **104** 172401
- [22] Wu H, Wang X, Huang L, Qin J Y, Fang C, Zhang X, Wan C H and Han X F 2017 Separation of inverse spin Hall effect and anomalous Nernst effect in ferromagnetic metals *Journal of Magnetism and Magnetic Materials* **441** 149–53
- [23] Lee K-D *et al* 2015 Thermoelectric Signal Enhancement by Reconciling the Spin Seebeck and Anomalous Nernst Effects in Ferromagnet/Non-magnet Multilayers *Sci. Rep.* **5** 10249
- [24] Kikkawa T, Uchida K, Daimon S, Shiomi Y, Adachi H, Qiu Z, Hou D, Jin X-F, Maekawa S and Saitoh E 2013 Separation of longitudinal spin Seebeck effect from anomalous Nernst effect: Determination of origin of transverse thermoelectric voltage in metal/insulator junctions *Phys. Rev. B* **88** 214403
- [25] Meier D, Kuschel T, Shen L, Gupta A, Kikkawa T, Uchida K, Saitoh E, Schmalhorst J-M and Reiss G 2013 Thermally driven spin and charge currents in thin NiFe₂O₄/Pt films *Phys. Rev. B* **87** 54421
- [26] Meier D, Reinhardt D, Schmid M, Back C H, Schmalhorst J-M, Kuschel T and Reiss G 2013 Influence of heat flow directions on Nernst effects in Py/Pt bilayers *Phys. Rev. B* **88** 184425
- [27] Schmid M, Srichandan S, Meier D, Kuschel T, Schmalhorst J-M, Vogel M, Reiss G, Strunk C and Back C H 2013 Transverse spin Seebeck effect versus anomalous and planar Nernst effects in Permalloy thin films *Phys. Rev. Lett.* **111** 187201
- [28] Bougiatioti P *et al* 2017 Quantitative Disentanglement of the Spin Seebeck, Proximity-Induced, and Ferromagnetic-Induced Anomalous Nernst Effect in Normal-Metal–Ferromagnet Bilayers *Phys. Rev. Lett.* **119** 227205
- [29] Hasegawa K, Mizuguchi M, Sakuraba Y, Kamada T, Kojima T, Kubota T, Mizukami S, Miyazaki T and Takanashi K 2015 Material dependence of anomalous Nernst effect in perpendicularly magnetized ordered-alloy thin films *Appl. Phys. Lett.* **106** 252405
- [30] Kelekci O, Lee H N, Kim T W and Noh H 2013 Anomalous Nernst Effects of [CoSiB/Pt] Multilayer Films *Journal of Magnetism* **18** 225–9

- [31] Wells J, Selezneva E, Krzysteczko P, Hu X, Schumacher H W, Mansell R, Cowburn R, Cuenat A and Kazakova O 2017 Combined anomalous Nernst effect and thermography studies of ultrathin CoFeB/Pt nanowires *AIP Advances* **7** 55904
- [32] Krzysteczko P *et al* 2017 Nanoscale thermoelectrical detection of magnetic domain wall propagation *Phys. Rev. B* **95** 220410(R)
- [33] Müller G M, Münzenberg M, Miao G-X and Gupta A 2008 Activation of additional energy dissipation processes in the magnetization dynamics of epitaxial chromium dioxide films *Phys. Rev. B* **77** 020412(R)
- [34] Osborn J A 1945 Demagnetizing Factors of the General Ellipsoid *Phys. Rev.* **67** 351–7
- [35] Mizuguchi M, Ohata S, Uchida K-i, Saitoh E and Takanashi K 2012 Anomalous Nernst Effect in an L1₀-Ordered Epitaxial FePt Thin Film *Appl. Phys. Express* **5** 93002
- [36] Sakuraba Y, Hasegawa K, Mizuguchi M, Kubota T, Mizukami S, Miyazaki T and Takanashi K 2013 Anomalous Nernst Effect in L1₀-FePt/MnGa Thermopiles for New Thermoelectric Applications *Appl. Phys. Express* **6** 33003
- [37] Mukherjee S *et al* 2015 Role of boron diffusion in CoFeB/MgO magnetic tunnel junctions *Phys. Rev. B* **91** 85311
- [38] Schreiber D K, Choi Y-s, Liu Y, Chiaramonti A N, Seidman D N and Petford-Long A K 2011 Effects of elemental distributions on the behavior of MgO-based magnetic tunnel junctions *J. Appl. Phys.* **109** 103909
- [39] Wang Z, Saito M, McKenna K P, Fukami S, Sato H, Ikeda S, Ohno H and Ikuhara Y 2016 Atomic-Scale Structure and Local Chemistry of CoFeB-MgO Magnetic Tunnel Junctions *Nano Lett.* **16** 1530–6
- [40] Jacob K T, Shekhar C and Waseda Y 2009 An update on the thermodynamics of Ta₂O₅ *The Journal of Chemical Thermodynamics* **41** 748–53
- [41] Wu Z L, Reichling M, Hu X Q, Balasubramanian K and Guenther K H 1993 Absorption and thermal conductivity of oxide thin films measured by photothermal displacement and reflectance methods *Applied optics* **32** 5660–5

***5.3 Large magneto-Seebeck effect in magnetic tunnel junctions
with half-metallic Heusler electrodes (Thesis article III)***



ARTICLE

DOI: 10.1038/s41467-017-01784-x

OPEN

Large magneto-Seebeck effect in magnetic tunnel junctions with half-metallic Heusler electrodes

Alexander Boehnke¹, Ulrike Martens², Christian Sterwerf¹, Alessia Niesen¹, Torsten Huebner¹, Marvin von der Ehe², Markus Meinert¹, Timo Kuschel^{1,3}, Andy Thomas⁴, Christian Heiliger⁵, Markus Münzenberg² & Günter Reiss¹

Spin caloritronics studies the interplay between charge-, heat- and spin-currents, which are initiated by temperature gradients in magnetic nanostructures. A plethora of new phenomena has been discovered that promises, e.g., to make wasted heat in electronic devices useable or to provide new read-out mechanisms for information. However, only few materials have been studied so far with Seebeck voltages of only some microvolt, which hampers applications. Here, we demonstrate that half-metallic Heusler compounds are hot candidates for enhancing spin-dependent thermoelectric effects. This becomes evident when considering the asymmetry of the spin-split density of electronic states around the Fermi level that determines the spin-dependent thermoelectric transport in magnetic tunnel junctions. We identify Co₂FeAl and Co₂FeSi Heusler compounds as ideal due to their energy gaps in the minority density of states, and demonstrate devices with substantially larger Seebeck voltages and tunnel magneto-Seebeck effect ratios than the commonly used Co-Fe-B-based junctions.

¹ Center for Spinelectronic Materials and Devices, Physics Department, Bielefeld University, Universitätsstr. 25, D-33615 Bielefeld, Germany. ² Institut für Physik, Ernst-Moritz-Arndt-Universität, Felix-Hausdorff-Str. 6, 17489 Greifswald, Germany. ³ Physics of Nanodevices, Zernike Institute for Advanced Materials, University of Groningen, Nijenborgh 4, 9747 AG Groningen, The Netherlands. ⁴ Leibniz Institute for Solid State and Materials Research Dresden (IFW Dresden), Institute for Metallic Materials, Helmholtzstrasse 20, 01069 Dresden, Germany. ⁵ Institut für theoretische Physik, Justus-Liebig-Universität Gießen, Heinrich-Buff-Ring 16, 35392 Gießen, Germany. Correspondence and requests for materials should be addressed to T.K. (email: tkuschel@physik.uni-bielefeld.de) or to G.R. (email: reiss@physik.uni-bielefeld.de)

The search for new materials and phenomena that enable, e.g., energy efficient sensors or memories, is a major driver for research in magnetism. Particularly, the emerging field of spin caloritronics^{1,2} combines spintronics and thermoelectrics, and provides a variety of new effects that might enable waste heat recovery in memory and sensor devices. One of the basic phenomena is the tunnel magneto-Seebeck effect (TMS)^{3,4}, i.e., the change of the Seebeck coefficients of a magnetic tunnel junction (MTJ) when switching between parallel (P) and antiparallel (AP) magnetization alignment. An important benefit of the TMS effect is its occurrence in MTJs. These spintronic devices are available in high quality, facilitating the implementation of the TMS into future electronics. Despite these benefits, only low TMS ratios of a few 10% and Seebeck voltages in the microvolt range have been obtained so far for MTJs with Co-Fe-B or Co-Fe electrodes^{3–11}.

While these types of MTJs form the backbone of modern spintronics, due to their high tunnel magnetoresistance (TMR) effect of several hundred percent¹², they do not provide similarly large TMS ratios. This makes the increase of the TMS a challenging and important task for material research. Furthermore, the connection between the TMR and TMS effects is a fundamental question^{13–15}. It is predicted theoretically that the sizes of the TMR and TMS effects are not directly linked and depend on different features of the density of states (DOS) of the ferromagnetic electrodes. Theory even predicts that large TMS effects can be achieved in MTJs that exhibit no TMR¹⁴. However, an experimental proof has been lacking so far.

In this paper, we show that the TMS is significantly enhanced by replacing conventional Co-Fe-based ferromagnets (FM) by nearly half-metallic (HM) Heusler compounds^{16–22}. We first introduce an approach to describe the thermoelectric transport in an MTJ based on the DOS of the electrode material. This simple model is a powerful tool for identifying the important parameters, e.g., the shape of the DOS and the position of the chemical potential, that a material should possess to enable high Seebeck voltages and high TMS effect ratios. Similar results have been found by *ab initio* calculations^{15,23}. Based on these predictions, we experimentally investigate the two nearly HM Heusler compounds Co₂FeSi and Co₂FeAl, and finally compare the experimental results obtained from the Heusler compound-based MTJs to Co-Fe based MTJs. The results prove a significantly enhanced TMS effect for MTJs with nearly HM Heusler compounds and that the size of the TMR and TMS are not directly correlated.

Results

Theoretical model. For obtaining a basic understanding of the charge transport in an MTJ it is most convenient to examine the electronic DOS of the electrodes and their occupation (Fig. 1a–c). In this picture, a temperature difference ΔT results in different broadenings of the occupations in the hot and cold electrode according to the Fermi-Dirac distribution. This difference in occupation generates diffusion currents between occupied (dark color) and unoccupied states (bright color). Accordingly, above the chemical potential μ electrons travel from the hot to the cold electrode, while below μ electrons travel conversely from the cold to the hot side.

For an MTJ containing two conventional FMs in the free-electron picture ($\text{DOS}(E) \propto \sqrt{E}$, Fig. 1a) these opposing currents are of similar sizes, because a similar number of states is available above and below μ due to the flat DOS ($\partial \text{DOS}(E)/\partial E$ is small) in proximity to μ . Only the tunneling probability is enhanced for electrons at higher energies, causing slightly more electrons to travel above μ than below. Still, the net diffusion across the barrier and, hence, the expected Seebeck voltage $V = -\Delta T$ (S : Seebeck coefficient) is small for this type of MTJ. Since this is

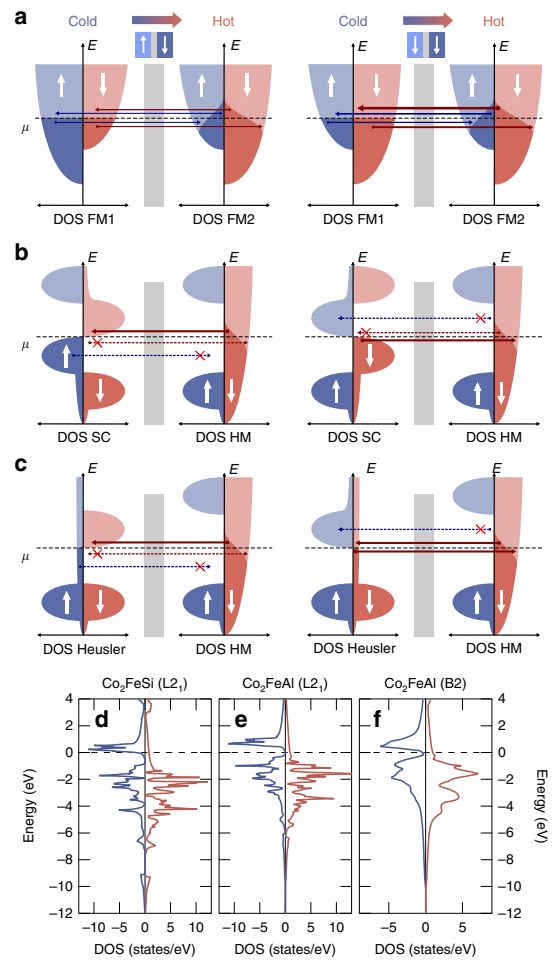


Fig. 1 Influence of the DOS. AP and P state. **a**, FM | FM. Since the individual currents cancel out, the Seebeck effect and TMS ratio are small. **b**, FMSC | HM. In the AP state electrons only travel above μ . In the P state electrons only travel below μ . This is optimal for generating large Seebeck coefficients with opposite sign. **c**, Heusler | HM. In the AP state the transport is similar to the FMSC | HM MTJ. In the P state electrons travel above and below μ . Hence, the Seebeck effect in the P state is small, while it is large in the AP state, leading to a large TMS ratio. **d–f**, The DOS obtained from DFT for Heusler compounds with theoretically predicted high TMS

valid for the P and the AP state of the MTJ, both Seebeck coefficients S_P and S_{AP} have similarly small values. Hence, the TMS ratio

$$\text{TMS} = \frac{S_P - S_{AP}}{\min(|S_P|, |S_{AP}|)} \quad (1)$$

is expected to be small in this type of MTJ.

For increasing the Seebeck effect, one of the diffusion channels above or below μ has to be suppressed. This is achieved by introducing a gap similar to semiconductors (SC). Conventional SCs have already proven to be useful in spin caloritronic applications^{24–26}. In SCs the size and sign of S are defined by the position of μ within the gap. S is positive, if μ is located at the bottom edge of the gap, i.e., a p-type SC, whereas S is negative, if μ is located at the top edge of the gap, i.e., an n-type SC. Hence, for

gaining a large difference between S_P and S_{AP} it is desired to magnetically switch between these two types of SCs. The DOS of a ferromagnetic semiconductor (FMSC) depicted for the left cold electrode in Fig. 1b allows this switching. In the FMSC spin-up electrons (blue) occupy a p-type DOS, while spin-down electrons occupy an n-type DOS. For selecting, which of these electrons contribute to the transport, we choose a HM with a gap in the spin-up states and a metallic DOS for the spin-down electrons as a counter electrode. Since the gap is larger than the thermal activation energy in the hot HM, only the metallic spin-down DOS contributes to the transport, resulting in an n-type like behavior of the junction and, hence, a large positive S . However, when the magnetization of the FMSC is reversed, the spin-down states that contribute to the tunneling process exhibit a p-type like DOS and, hence, we receive a large negative S . Clearly, this would be perfect for reading the two states of the MTJ by the Seebeck voltage.

Since experimentally realizing FMSCs is very challenging, it is desirable to find another more accessible material class that also fulfills the properties of an FMSC | HM MTJ. Heusler compounds are a very promising substitute for the FMSC (Fig. 1c), since some of them, such as Co_2FeSi (Fig. 1d), also reveal an n-type gap in the spin-down DOS. However, they do not possess a p-type gap, but a metallic DOS in the spin-up channel. Thus, when combined with a HM, we only achieve a switching between an n-type like transport in the AP state and a metallic behavior in the P state of the MTJ (Fig. 1c). Our model therefore predicts a large positive Seebeck coefficient, i.e., a negative Seebeck voltage ($V = -\Delta T$), in the AP state and a strongly reduced Seebeck effect in the P state. Hence, we expect that a Heusler | HM MTJ simultaneously provides a high TMS ratio and a large Seebeck voltage in the AP state.

For experimentally realizing this device, we use the Heusler compounds Co_2FeSi and Co_2FeAl in combination with an MgO barrier and a Co-Fe-based counter electrode. Co-Fe on its own is not a HM, but when combined with a crystalline MgO barrier the tunneling process becomes coherent. Under these conditions, the electrons contributing to the tunneling process reveal a HM nature²⁷. For checking the properties of the Heusler compounds Co_2FeSi and Co_2FeAl , we have performed density functional theory (DFT) calculations²¹ of the spin-resolved DOS (Fig. 1d–f). In the minority DOS, Co_2FeSi has a pseudogap right below the chemical potential, while a large number of unoccupied states is found directly above μ . On the contrary, the majority DOS is rather flat around μ . Hence, this DOS perfectly resembles the ideal DOS for a high TMS as sketched in Fig. 1c. Co_2FeAl in the full-Heusler $L2_1$ ordering is predicted to have a pseudogap that is positioned relatively symmetrical around μ (Fig. 1f). Accordingly, a much smaller Seebeck effect is expected. However, Co_2FeAl does not crystallize in the full-Heusler structure, but energetically prefers the less-ordered $B2$ ordering, which results in a less pronounced gap. Additionally, the large number of states above μ is shifted closer towards μ . Thus, similar TMS effects are expected for Co_2FeSi in the $L2_1$ ordering and Co_2FeAl in the $B2$ ordering. Only the absolute Seebeck coefficients are expected to be slightly larger for Co_2FeSi due to the wider gap and larger asymmetry.

To experimentally explore the tunneling properties, we performed tunneling spectroscopy with dI/dV measurements (see Supplementary Note 5 including ref. 28). The data show that none of the used MTJs show a pure parabolic dependence of dI/dV on the voltage V , revealing either coherent tunneling for the CoFeB case or strong deviations of the DOS from an s-like band with $\text{DOS}(E) \propto \sqrt{E}$. Furthermore, X-ray diffraction, atomic force microscopy, and X-ray fluorescence have been used to proof the excellent quality of our samples (see Supplementary Note 2 including ref. 29). Since the structural results, the TMR values,

and the dI/dV curves are quite comparable to earlier work by Mann et al.³⁰, we conclude that our samples have similar half metallic character as shown by inelastic tunneling spectroscopy and ultrafast demagnetization experiments on their samples.

Experimentally determined TMS effects. For experimentally determining the thermoelectric properties of the MTJs, we generate a temperature gradient across the barrier and record the Seebeck voltages for the two magnetic configurations of the MTJ. For heating we use a diode laser (wavelength 635 nm) that is modulated on/off at a frequency of 13 Hz for the high-impedance Heusler MTJs and at 1.5 kHz for the lower-impedance Co-Fe-B MTJs. The beam is focussed on top of a gold transducer placed above the MTJ. The spot size on the transducer is adjusted according to the size of the MTJs to guarantee a homogenous heating. The generated Seebeck voltages are amplified by a high-impedance amplifier and afterward fed into a lock-in amplifier set to voltage mode. Thus, all Seebeck voltages are given as the effective values of the first harmonic of the lock-in amplifier. In a DC experiment the values are expected to be twice as high⁵. For time-dependent investigations, e.g., checking the saturation of the signal, the voltages are recorded with an oscilloscope (see also Supplementary Note 3). We have published a detailed description of the setup used in this work in ref. 5.

TMS in Co_2FeSi MTJs. The first Heusler compound discussed here is Co_2FeSi ³¹. The complete MTJ stack consists of MgO (substrate)/MgO (5)/Cr (5)/ Co_2FeSi (20)/MgO (2)/ $\text{Co}_{70}\text{Fe}_{30}$ (5)/ $\text{Mn}_{83}\text{Ir}_{17}$ (10)/Ru (25), numbers indicate thicknesses in nm (cf. Supplementary Note 1). By e-beam patterning, MTJ pillars are produced, such that the Cr and half of the Co_2FeSi layer remain as bottom lead. After insulating the MTJs with Ta_2O_5 , contact pads consisting of Ta (5)/Au (60) are placed on top of the MTJs to allow electrical contact. Furthermore, these pads assure that the laser is fully absorbed by the Au layer and only the heat is transferred to the functional layers of the MTJ.

Figure 2a displays the Seebeck voltage of a Co_2FeSi MTJ for different heating powers in dependence on an external magnetic field. The characteristic minor-loop of an exchanged-biased MTJ is clearly recognizable. Moreover, the MTJ exhibits a nearly identical switching behavior of the Seebeck voltage and the resistance (Fig. 2b, see also Supplementary Note 3). We further detected the same behavior when directly measuring the Seebeck current (cf. Supplementary Note 4). This is expected, because in the TMS as well as in the TMR effect the spin-dependent transport is altered by changing the magnetization alignment of the FM layers of the MTJ. The Seebeck voltage rises linearly with applied laser power, i.e., enhanced temperature difference across the barrier (Fig. 2c). The largest values reached in our experiments are $V_{AP} \approx -664 \mu\text{V}$ and $V_P \approx -370 \mu\text{V}$ at 150 mW heating power. This yields a TMS ratio of $\sim 80\%$. For lower heating powers the absolute TMS effect ratio is even enhanced, reaching its highest value of $\sim 86\%$ at 10 mW heating power. The base temperatures achieved by the laser heating reach from 300 K at 10 mW to 351 K at 150 mW (cf. Supplementary Note 7 including refs 32–41). This trend shows that large TMS ratios and Seebeck voltages are observed at various heating powers, i.e., different temperature gradients and base temperatures.

To ensure that the spin-dependent thermovoltages are only generated by the MTJ and not by the FM bottom lead, we have forced the MTJ into a dielectric breakdown by applying a bias voltage of 4 V. The MTJ does not show any TMR after this treatment. The subsequently determined Seebeck voltages at unchanged irradiation conditions only reach $-2.2 \mu\text{V}$ at 150 mW heating power. Furthermore, the dependence of the Seebeck

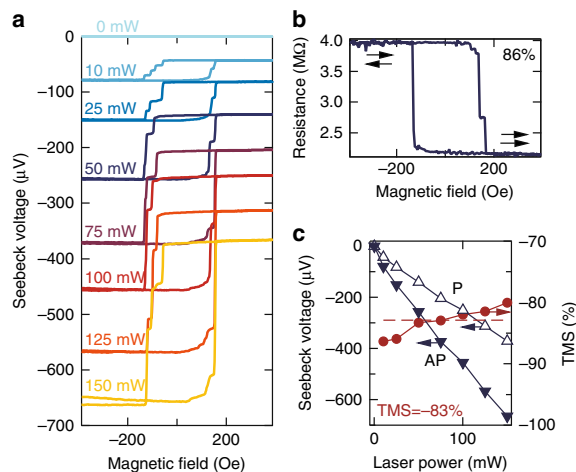


Fig. 2 TMS effect in Co_2FeSi based MTJs. **a**, Seebeck voltage in dependence on magnetic field for different laser powers. **b**, Minor loop of the TMR effect (resistance vs. magnetic field) of the same MTJ without laser heating. **c**, Power dependence of the Seebeck voltage and the TMS ratio extracted from the saturation voltages in **a**. The average TMS effect of the Co_2FeSi based MTJs amounts to -83%

voltage on the external magnetic field vanishes (cf. Supplementary Note 6). Hence, we can fully attribute the high TMS to the intact Heusler based MTJ.

TMS in Co_2FeAl MTJs. The layer stacks for the Co_2FeAl based MTJs consist of MgO (substrate)/ TiN (20)/ Co_2FeAl (10)/ MgO (2)/ $\text{Co}_{40}\text{Fe}_{40}\text{B}_{20}$ (5)/ Ta (3)/ Ru (3)⁴² (cf. Supplementary Note 1). In these samples only the TiN layer serves as a common bottom lead. Accordingly, FM materials only remain in the MTJ pillars. The choice of an insulating substrate and a non-FM lead ensures that a response of the Seebeck effect to an external magnetic field has its origin solely in the MTJ pillars.

Figure 3a displays the Seebeck voltage of a Co_2FeAl MTJ for different heating powers in dependence on an external magnetic field. The characteristic bow-tie shaped switching of a pseudo-spin-valve is clearly recognizable. Again, the MTJ shows a nearly identical switching of the Seebeck voltage and the resistance (Fig. 3b, see also Supplementary Note 3), and the Seebeck voltage rises linearly with applied laser power. Once more, a similar behavior has been observed when directly measuring the Seebeck current (cf. Supplementary Note 4). A TMS of $-93 \pm 2\%$ is found for all applied heating powers, i.e., these Co_2FeAl based MTJs show a nearly constant TMS over a wide range of base temperatures. For the largest heating power of 150 mW, the Seebeck voltages reach $V_{\text{AP}} = -442 \mu\text{V}$ and $V_{\text{P}} = -227 \mu\text{V}$ yielding a switching ratio of nearly -95% .

The small variation of the TMS ratio with laser power in these Co_2FeSi and Co_2FeAl based MTJs indicates a correspondingly small influence of the base temperature. This apparently weak temperature dependence is a favorable property for possible applications of the TMS such as a read-out of the information stored in the magnetic state of the MTJ.

Although we do not expect any influence of the TiN bottom lead on the switching of the Seebeck voltage with magnetic field, we also investigated the Seebeck voltage in the Co_2FeAl based MTJs after dielectric breakdown. Similarly to the Co_2FeSi based MTJs no switching of the Seebeck voltage is observed for the broken MTJs. Moreover, the absolute value of the Seebeck voltage is strongly decreased and even reverses its sign. For a heating

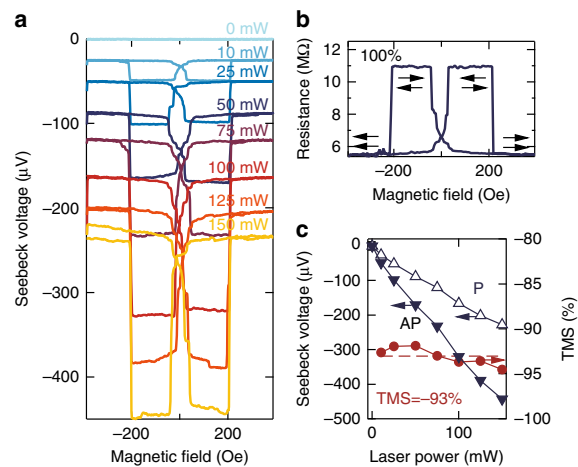


Fig. 3 TMS effect in Co_2FeAl based MTJs. **a** Seebeck voltage in dependence on magnetic field for different laser powers. **b** Major loop of the TMR effect (resistance vs. magnetic field) of the same MTJ without laser heating. **c** Power dependence of the Seebeck voltage and the TMS ratio extracted from the saturation voltages in **a**. The average TMS effect of the Co_2FeAl based MTJs amounts to -93%

power of 150 mW we observe a Seebeck voltage of $15 \mu\text{V}$ in the broken MTJ. This remaining signal is probably generated by an in plane temperature gradient in the TiN .

Comparison to Co-Fe-B MTJs. A direct comparison of Co_2FeAl and $\text{Co}_2\text{Fe}_{54}\text{B}_{20}$ based MTJs makes the benefits of using Heusler compounds for TMS devices obvious (Fig. 4a). The absolute value of the TMS ratio in Co_2FeAl is nearly twice as high as in the Co-Fe-B-based MTJs. However, when comparing the TMR of the two materials we find exactly the opposite (Fig. 4b). The different effect sizes clearly reveal the different influence of the DOS on the two effects, and point out that MTJs with a high TMR do not necessarily generate a high TMS. This has already been predicted theoretically^{13–15}, but a reliable experimental prove had been missing up to now.

The favorable properties of the Heusler compound MTJs become even more clear when comparing multiple MTJs with Co_2FeAl and $\text{Co}_2\text{Fe}_{54}\text{B}_{20}$ electrodes to MTJs containing different Co-Fe-B (Fig. 4c–e) compositions. The Heusler based MTJs do not only show higher TMS ratios of -80 to -120% , they also generate a substantially larger Seebeck voltage of up to $-664 \mu\text{V}$. For the Co-Fe-B-based MTJs this combination of a high Seebeck signal and a high TMS ratio cannot be observed. Although, the MTJs with two $\text{Co}_{26}\text{Fe}_{54}\text{B}_{20}$ electrodes generate TMS ratios of nearly 50% they cannot provide Seebeck voltages of more than $10 \mu\text{V}$. For the $\text{Co}_{40}\text{Fe}_{40}\text{B}_{20}$ the Seebeck voltages are slightly increased and reach up to nearly $50 \mu\text{V}$, but these samples only yield TMS ratios of maximum 10% . These observations for different Co-Fe compositions are consistent with *ab initio* calculations by Heiliger et al.¹⁴. Furthermore, Fig. 4e supports the prediction that the TMS and TMR ratios in MTJs with different DOS, i.e., electrode materials^{13–15}, are not directly correlated. High TMS effects are not observed in the MTJs with the highest TMR. A comparison of the Heusler- to the $\text{Co}_{40}\text{Fe}_{40}\text{B}_{20}$ based MTJs reveals that samples with similar TMR can possess drastically different TMS ratios. However, all MTJs containing Heusler compounds reveal simultaneously large Seebeck voltages and TMS effects, indicating the robustness of the effect size in these MTJs.

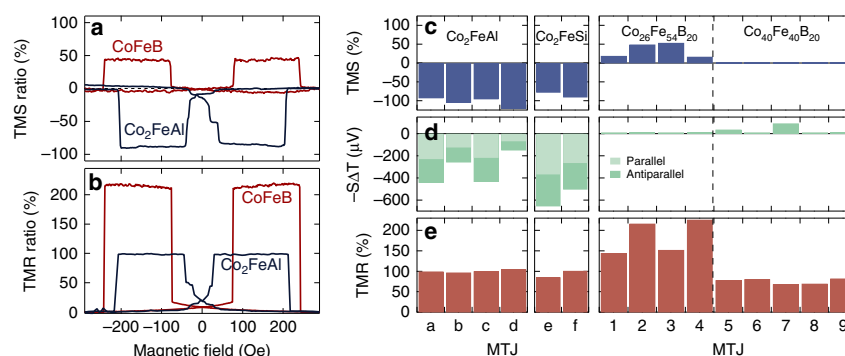


Fig. 4 Comparison of Heusler compound to Co-Fe-B MTJs. **a** The TMS ratios (determined at 150 mW laser power) of Co_2FeAl is twice as high compared to $\text{Co}_{26}\text{Fe}_{54}\text{B}_{20}$ and possesses an inversed sign. **b** For the TMR ratios (at 10 mV bias voltage) of the same MTJs the opposite is found. **c** TMS ratios for various Co_2FeAl and Co_2FeSi based MTJs in comparison to MTJs with two different Co-Fe-B compositions. **d** Corresponding Seebeck-voltages $-\Delta T$ at a laser power of 150 mW in the P and AP configuration of the MTJs. **e** TMR ratio of the MTJs at 10 mV bias. Only the Heusler based MTJs simultaneously exhibit a large Seebeck voltage and high TMS ratio

Table 1 Seebeck coefficients of MTJs with different materials

Materials	$V_P(\mu\text{V})$	$V_{AP}(\mu\text{V})$	$S_P(\mu\text{VK}^{-1})$	$S_{AP}(\mu\text{VK}^{-1})$	TMS
$\text{Co}_{40}\text{Fe}_{40}\text{B}_{20}^a$	90.6	93.2	-750	-770	2.8%
$\text{Co}_{26}\text{Fe}_{54}\text{B}_{20}^b$	6.0	9.0	-545	-818	50%
Co_2FeAl^c	-227	-442	582	1133	-95%
Co_2FeSi^d	-370	-664	948	1703	-80%

The elliptical MTJs have diameters of $2\mu\text{m} \times 1\mu\text{m}$. The Seebeck voltages are obtained at 150 mW laser heating
^a $\text{Co}_{40}\text{Fe}_{40}\text{B}_{20}/\text{MgO}$ 1.5 nm/ $\text{Co}_{40}\text{Fe}_{40}\text{B}_{20}$, for more values see ref. ⁵
^b $\text{Co}_{26}\text{Fe}_{54}\text{B}_{20}/\text{MgO}$ 1.7 nm/ $\text{Co}_{26}\text{Fe}_{54}\text{B}_{20}$, for more values see refs ^{3, 6}
^c $\text{Co}_2\text{FeAl}/\text{MgO}$ 2 nm/ $\text{Co}_{40}\text{Fe}_{40}\text{B}_{20}$
^d $\text{Co}_2\text{FeSi}/\text{MgO}$ 2 nm/ $\text{Co}_{70}\text{Fe}_{30}$

Finally, we estimate the Seebeck coefficients of the MTJs for enabling a quantitative comparison of their properties. As known from literature^{3–6}, the necessary determination of the temperature difference between the upper and the lower electrode of the MTJ is the most challenging aspect. Here, the temperature profile of each sample type is simulated by finite element methods (cf. Supplementary Note 7), and the Seebeck coefficient $S = -V/\Delta T$ is calculated from the Seebeck voltage and the temperature difference between the electrodes (Table 1). Again, a larger value of S is found for the Heusler compound based MTJs. Furthermore, the sign of the Seebeck voltage and coefficient are reversed, when replacing Co-Fe-B by a Heusler compound. We find S_{AP} up to $1703\mu\text{VK}^{-1}$ for the Co_2FeSi based MTJ, while for the Co-Fe-B-based MTJ we only find $-818\mu\text{VK}^{-1}$. Nonetheless, we would like to emphasize that the temperature differences determined by finite element methods can be quite inaccurate. Particularly, the thermal conductivity of the nanometer-thick MgO barrier is a subject discussed in literature^{3, 9, 37, 43}. Hence, the presented Seebeck coefficients (Table 1) can only be compared to values obtained with the same method, e.g., in refs ^{3, 5, 6}, while the absolute values should be considered with great care.

For applications, however, the exact value of the Seebeck coefficient is of secondary interest. A large Seebeck voltage, as well as a high and stable readout contrast between the P and the AP state that can be used for further signal processing are of larger importance. With our direct comparison of Heusler- and Co-Fe-B-based MTJs, we have shown that MTJs based on Heusler compounds are able to provide a favorable combination of TMS ratios between -80 and -120% and large Seebeck voltages of up to $-664\mu\text{V}$.

Conclusion. In conclusion, we have presented an experimental study of the spin-dependent Seebeck effect in Heusler compound based MTJs. Replacing one of the commonly used Co-Fe-B electrodes by a HM Heusler compound largely increases the TMS ratio from several percent up to -120% and simultaneously provides Seebeck voltages of up to $664\mu\text{V}$. These experimental findings can be explained based on the DOS. We have introduced a simple model that allows estimating the thermal diffusion currents, and, hence, the Seebeck coefficients, only from the DOS. This model does not only explain the observed effect sizes, but it is a powerful tool for quickly screening the capability of other materials for providing high TMS based on their DOS, available from material repositories, such as AFLOW.lib⁴⁴. Thus, the more sophisticated and time-consuming *ab initio* studies can be concentrated on the most promising candidate materials. Since the model has already proven its usefulness in our experiments with Heusler compounds, we expect it to be helpful in finding suitable materials for thermoelectric effects and spin caloritronic transport phenomena.

Furthermore, our discovery of a material that enables high TMS ratios paves the way to a large number of new effects. The combination of the high TMS effect, high spin-polarization, and low Gilbert damping⁴⁵ makes these Heusler compound MTJs ideal for investigating the thermal spin transfer torque in MTJs^{46–48}, which is a key ingredient in the design of spin caloritronic memory devices. The high Seebeck effect might also enhance the magneto-Peltier effect that has been investigated in Co-Fe-B-based MTJs⁴⁹. Moreover, our results might also be of interest for the future research on the heat distribution and the resulting effects in magnetic access memory devices (MRAM)^{50, 51}.

Methods

For a detailed explanation of the MTJ preparation, characterization of the MTJs after dielectric breakdown and details on the finite element method simulations please refer to the Supplementary Information and refs ^{5, 31, 42}.

Data availability. The data that support the findings of this study are available from the corresponding author upon request.

Received: 20 January 2017 Accepted: 13 October 2017

Published online: 20 November 2017

References

- Bauer, G. E. W., Saitoh, E. & van Wees, B. J. Spin caloritronics. *Nat. Mater.* **11**, 391–399 (2012).
- Boona, S. R., Myers, R. C. & Heremans, J. P. Spin caloritronics. *Energy Environ. Sci.* **7**, 885–910 (2014).
- Walter, M. et al. Seebeck effect in magnetic tunnel junctions. *Nat. Mater.* **10**, 742–746 (2011).
- Liebing, N. et al. Tunneling magnetothermopower in magnetic tunnel junction nanopillars. *Phys. Rev. Lett.* **107**, 177201 (2011).
- Boehnke, A. et al. Time-resolved measurement of the tunnel magneto-Seebeck effect in a single magnetic tunnel junction. *Rev. Sci. Instrum.* **84**, 063905 (2013).
- Boehnke, A. et al. On/off switching of bit readout in bias-enhanced tunnel magneto-Seebeck effect. *Sci. Rep.* **5**, 8945 (2015).
- Pushp, A. et al. Giant thermal spin-torque-assisted magnetic tunnel junction switching. *Proc. Natl. Acad. Sci. USA* **112**, 6585–6590 (2015).
- Xu, Y. et al. Origins of large light induced voltage in magnetic tunnel junctions grown on semiconductor substrates. *J. Appl. Phys.* **119**, 023907 (2016).
- Huebner, T. et al. Comparison of laser-induced and intrinsic tunnel magneto-Seebeck effect in CoFeB/MgAl₂O₄ and CoFeB/MgO magnetic tunnel junctions. *Phys. Rev. B* **93**, 224433 (2016).
- Böhnert, T. et al. Magnetic tunnel junctions with integrated thermometers for magnetothermopower measurements. *J. Phys. Condens. Matter* **29**, 185303 (2017).
- Böhnert, T. et al. Influence of the thermal interface resistance on the thermovoltage of a magnetic tunnel junction. *Phys. Rev. B* **95**, 104441 (2017).
- Ikeda, S. et al. Tunnel magnetoresistance of 604% at 300 K by suppression of Ta diffusion in CoFeB/MgO/CoFeB pseudo-spin-valves annealed at high temperature. *Appl. Phys. Lett.* **93**, 082508 (2008).
- Czerner, M., Bachmann, M. & Heiliger, C. Spin caloritronics in magnetic tunnel junctions: Ab initio studies. *Phys. Rev. B* **83**, 132405 (2011).
- Heiliger, C., Franz, C. & Czerner, M. Ab initio studies of the tunneling magneto-Seebeck effect: influence of magnetic material. *Phys. Rev. B* **87**, 224412 (2013).
- Bölske, B. & Kratzer, P. Spin-caloric properties of epitaxial Co₂MnSi/MgO/Co₂MnSi magnetic tunnel junctions. *Phys. Rev. B* **92**, 144418 (2015).
- Kandpal, H. C., Fecher, G. H. & Felser, C. Calculated electronic and magnetic properties of the half-metallic, transition metal based Heusler compounds. *J. Phys. D: Appl. Phys.* **40**, 1507–1523 (2007).
- Thomas, A. et al. Evidence for band structure effects in the magnetoresistance of Co-based Heusler compounds. *J. Appl. Phys.* **103**, 023903 (2008).
- Wang, W., Sukegawa, H., Shan, R., Mitani, S. & Inomata, K. Giant tunneling magnetoresistance up to 330% at room temperature in sputter deposited Co₂FeAl/MgO/CoFe magnetic tunnel junctions. *Appl. Phys. Lett.* **95**, 182502 (2009).
- Balke, B. et al. Seebeck coefficients of half-metallic ferromagnets. *Solid State Commun* **150**, 529–532 (2010).
- Schebaum, O. et al. Direct measurement of the spin polarization of Co₂FeAl in combination with MgO tunnel barriers. *J. Appl. Phys.* **107**, 09C717 (2010).
- Meinert, M., Friedrich, C., Reiss, G. & Blügel, S. GW study of the half-metallic Heusler compounds Co₂MnSi and Co₂FeSi. *Phys. Rev. B* **86**, 245115 (2012).
- Meinert, M. et al. Insights into the electronic structure of Co₂FeSi from x-ray magnetic linear dichroism. *Phys. Rev. B* **86**, 054420 (2012).
- Comtesse, D., Geisler, B., Entel, P., Kratzer, P. & Szunyogh, L. First-principles study of spin-dependent thermoelectric properties of half-metallic Heusler thin films between platinum leads. *Phys. Rev. B* **89**, 094410 (2014).
- Jansen, R. Silicon spintronics. *Nat. Mater.* **11**, 400–408 (2012).
- Jeon, K.-R., Saito, H., Yuasa, S. & Jansen, R. Relative strength of thermal and electrical spin currents in a ferromagnetic tunnel contact on a semiconductor. *Phys. Rev. B* **92**, 054403 (2015).
- Le Breton, J.-C., Sharma, S., Saito, H., Yuasa, S. & Jansen, R. Thermal spin current from a ferromagnet to silicon by Seebeck spin tunnelling. *Nature* **475**, 82–85 (2011).
- Butler, W., Zhang, X.-G., Schulthess, T. & MacLaren, J. Spin-dependent tunneling conductance of Fe/MgO/Fe sandwiches. *Phys. Rev. B* **63**, 054416 (2001).
- Brinkman, W. F., Dynes, R. C. & Rowell, J. M. Tunneling conductance of asymmetrical barriers. *J. Appl. Phys.* **41**, 1915–1921 (1970).
- Kato, A. & Tamari, N. Crystal growth of titanium nitride by chemical vapor deposition. *J. Cryst. Growth* **29**, 55–60 (1975).
- Mann, A. et al. Insights into ultrafast demagnetization in pseudogap half-metals. *Phys. Rev. X* **2**, 041008 (2012).
- Sterwerf, C., Meinert, M., Schmalhorst, J.-M. & Reiss, G. High TMR ratio in Co₂FeSi and Fe₂CoSi based magnetic tunnel junctions. *IEEE Trans. Magn.* **49**, 4386–4389 (2013).
- Liebing, N. et al. Determination of spin-dependent Seebeck coefficients of CoFeB/MgO/CoFeB magnetic tunnel junction nanopillars. *J. Appl. Phys.* **111**, 07C520 (2012).
- Papusoi, C., Sousa, R., Herault, J., Prejbeanu, I. L. & Dieny, B. Probing fast heating in magnetic tunnel junction structures with exchange bias. *New J. Phys.* **10**, 103006 (2008).
- Beecher, C., Dinwiddie, R. B., Abeel, A. M. & Lowden, R. A. *The thermal conductivity of silicon nitride with molybdenum disilicide additions* (ed. Tong, T. W.) (Technomic Publishing Company, 1994).
- Zink, B. L., Revaz, B., Cherry, J. J. & Hellman, F. Measurement of thermal conductivity of thin films with a Si-N membrane-based microcalorimeter. *Rev. Sci. Instrum.* **76**, 24901 (2005).
- Zhang, Q. G., Cao, B. Y., Zhang, X., Fujii, M. & Takahashi, K. Influence of grain boundary scattering on the electrical and thermal conductivities of polycrystalline gold nanofilms. *Phys. Rev. B* **74**, 134109 (2006).
- Lee, S. M., Cahill, D. G. & Allen, T. H. Thermal conductivity of sputtered oxide films. *Phys. Rev. B* **52**, 253–257 (1995).
- Bentouaf, A. & Hassan, F. E. H. Structural, electronic, magnetic and thermodynamic properties of full Heusler compound Co₂VSi: Ab initio study. *J. Magn. Magn. Mater.* **381**, 65–69 (2015).
- Shiomi, J., Esfarjani, K. & Chen, G. Thermal conductivity of half-Heusler compounds from first-principles calculations. *Phys. Rev. B* **84**, 104302 (2011).
- Lue, C. S. & Kuo, Y.-K. Thermoelectric properties of the semimetallic Heusler compounds Fe₂V_{1+x}M (M = Al, Ga). *Phys. Rev. B* **66**, 085121 (2002).
- Chase, M. W. Jr. NIST-JANAF Thermochemical Tables, Fourth Edition. *J. Phys. Chem. Ref. Data, Monograph* **9**, 1–1951 (1998).
- Niesen, A. et al. Titanium nitride as a seed layer for Heusler compounds. *J. Appl. Phys.* **118**, 243904 (2015).
- Zhang, J., Bachman, M., Czerner, M. & Heiliger, C. Thermal transport and nonequilibrium temperature drop across a magnetic tunnel junction. *Phys. Rev. Lett.* **115**, 037203 (2015).
- Curtarolo, S. et al. AFLOWLIB.ORG: A distributed materials properties repository from high-throughput ab initio calculations. *Comput. Mater. Sci.* **58**, 227–235 (2012).
- Sterwerf, C. et al. Low Gilbert damping in Co₂FeSi and Fe₂CoSi films. *J. Appl. Phys.* **120**, 083904 (2016).
- Liebing, N., Serrano-Guisan, S., Rott, K., Reiss, G. & Schumacher, H. Noise spectroscopy of CoFeB/MgO/CoFeB magnetic tunnel junctions in the presence of thermal gradients. *J. Magn. Magn. Mater.* **400**, 154–158 (2016).
- Choi, G.-M., Moon, C.-H., Min, B.-C., Lee, K.-J. & Cahill, D. G. Thermal spin-transfer torque driven by the spin-dependent Seebeck effect in metallic spin-valves. *Nat. Phys.* **11**, 576–582 (2015).
- Leutenantsmeyer, J. C. et al. Parameter space for thermal spin-transfer torque. *Spin* **03**, 1350002 (2013).
- Shan, J. et al. Comparison of the magneto-Peltier and magneto-Seebeck effects in magnetic tunnel junctions. *Phys. Rev. B* **92**, 020414 (2015).
- Brataas, A., Kent, A. D. & Ohno, H. Current-induced torques in magnetic materials. *Nat. Mater.* **11**, 372–381 (2012).
- Katine, J. A. & Fullerton, E. E. Device implications of spin-transfer torques. *J. Magn. Magn. Mater.* **320**, 1217–1226 (2008).

Acknowledgements

We gratefully acknowledge financial support by the Deutsche Forschungsgemeinschaft (DFG) within the priority program SpinCaT SPP1538 (RE 1052/24–2, MU 1780/8–2, HE 5922/4–2, KU 3271/1–1, TH 1399/4–2) and the Bundesministerium für Bildung und Forschung (BMBF). Furthermore, we thank Benjamin Geisler for sharing his knowledge about Seebeck effects in half-metallic Heusler compounds.

Author contributions

A.B., U.M., T.H. and M.v.d.E. set up the experiments and performed the measurements under supervision of T.K., G.R. and M.Mü. A.B., C.S. and A.N. prepared and characterized the samples. A.B., C.H. and G.R. developed and discussed the theoretical

model. M.Me. provided the DFT calculations. A.B. wrote the manuscript. A.T., C.H., M.Mü. and G.R. designed the research approach. All authors discussed the measurements and the manuscript.

Additional information

Supplementary Information accompanies this paper at doi:10.1038/s41467-017-01784-x.

Competing interests: The authors declare no competing financial interests.

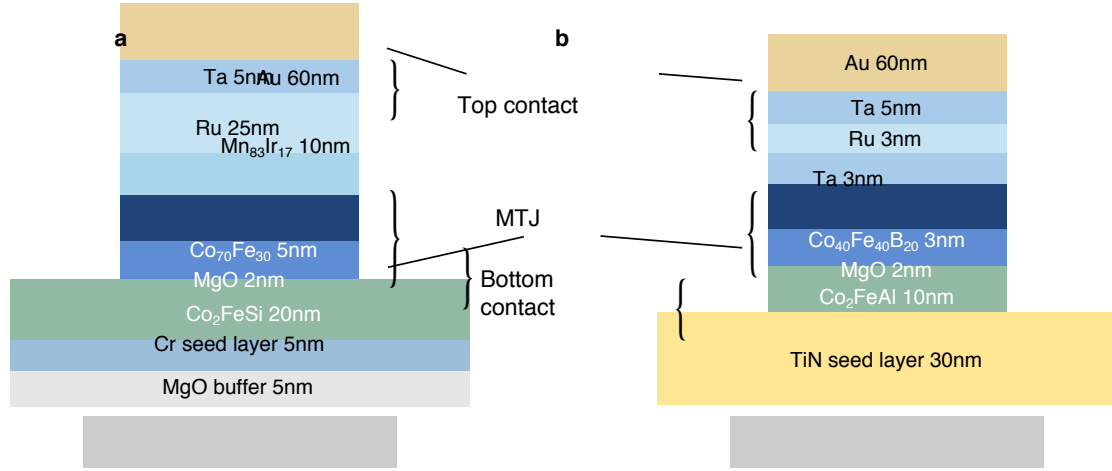
Reprints and permission information is available online at <http://npg.nature.com/reprintsandpermissions/>

Publisher's note: Springer Nature remains neutral with regard to jurisdictional claims in published maps and institutional affiliations.



Open Access This article is licensed under a Creative Commons Attribution 4.0 International License, which permits use, sharing, adaptation, distribution and reproduction in any medium or format, as long as you give appropriate credit to the original author(s) and the source, provide a link to the Creative Commons license, and indicate if changes were made. The images or other third party material in this article are included in the article's Creative Commons license, unless indicated otherwise in a credit line to the material. If material is not included in the article's Creative Commons license and your intended use is not permitted by statutory regulation or exceeds the permitted use, you will need to obtain permission directly from the copyright holder. To view a copy of this license, visit <http://creativecommons.org/licenses/by/4.0/>.

© The Author(s) 2017



Supplementary Figure 1. Heusler based MTJs. **a** Top pinned Co-Fe/MgO/Co₂FeSi MTJs. The Co₂FeSi layer also serves as bottom contact. **b** Co-Fe-B/MgO/Co₂FeSi MTJs. Here, the TiN seed layer provides the bottom contact.

Supplementary Note 1. PREPARATION OF HEUSLER BASED MTJS

The layer stacks for the Co₂FeAl MTJs are produced by magnetron sputtering. The stacks consist of the following layers (thickness in nm) MgO(substrate): / TiN(20) / Co₂FeAl(10) / MgO(2) / Co₄₀Fe₄₀B₂₀(5) / Ta(3) / Ru(3). The TiN seed layer is prepared by reactive sputtering in a BESTEC GmbH sputter deposition chamber with a base pressure of $5 \cdot 10^{-10}$ mbar. The exact process parameters can be found in Reference¹. Afterwards, the sample is transferred to a Leybold CLAB sputtering tool (base pressure 10^{-8} mbar) without vacuum break to deposit the remaining layers at room temperature. We apply RF sputtering from a composite target for the MgO barrier and DC sputtering from composite targets for the Co₂FeAl and the Co₄₀Fe₄₀B₂₀. The Ta and Ru layers are deposited from elementary targets by DC sputtering. After the deposition we annealed the sample *ex situ* in a vacuum furnace ($p \approx 3 \times 10^{-7}$ mbar) at a temperature of 320°C in a magnetic field of 0.65 T for 1 hour.

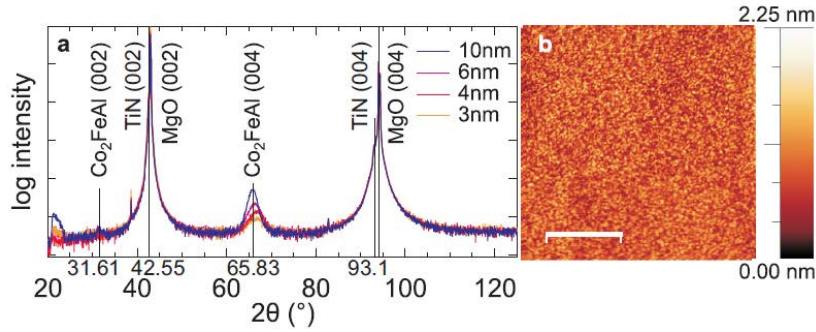
The Co₂FeSi based MTJs are produced according to Reference². The used stacks are identical to the stacks used in that earlier work and are prepared with the same equipment. The annealing is the same as for the Co₂FeAl based MTJs.

After deposition and annealing, elliptically shaped MTJs are patterned by e-beam lithography and subsequent ion-milling. For the Co₂FeAl based MTJs we only use the non-ferromagnetic TiN layer as a bottom lead. For the Co₂FeSi based samples also the Co₂FeSi has to be used as bottom lead for providing sufficiently high conductance. Hence, the cross sections of these two sample types look slightly different after etching (Supplementary Figure 1). For insulation 140 nm of Ta₂O₅ are sputter deposited next to the MTJs, followed by a lift-off procedure. 5 nm of Ta and 60 nm of Au are sputter deposited on top of the MTJs and patterned into contact pads to allow optical access and electrical contact to the MTJs.

Supplementary Note 2. X-RAY INVESTIGATIONS AND TOPOGRAPHY

An extensive study of the quality of the Co₂FeSi films can be found in Reference². These films are produced in the same way as the samples used for the TMS investigations.

For the Co₂FeAl based MTJs, the quality of the buffer layer and the adjacent Co₂FeAl layers is checked by x-ray diffraction (XRD) and atomic force microscopy (AFM) on half MTJ layer stacks prepared in the same way as the complete MTJ stacks (Supplementary Figure 2). The x-ray investigations are performed in a Phillips X'Pert Pro MPD x-ray diffractometer with Cu K_α radiation at a wavelength of 1.5419 Å. The intensity of the diffracted beam is determined with respect to the incident angle 2θ . A full XRD scan covers the interval of $2\theta = 20^\circ - 125^\circ$. The micrographs are obtained in a Bruker Multimode 5 AFM in contact mode.



Supplementary Figure 2. Quality of the TiN/Co₂FeAl/MgO layers. **a** X-ray diffraction data obtained from stacks with different Co₂FeAl thicknesses. The expected diffraction maxima are labeled. **b** Micrograph from an AFM analysis of the layer stack with 10 nm Co₂FeAl with a root-mean-square roughness of 0.25 nm. The scale bar corresponds to a lateral distance of 1.0 μm .

The XRD scans of TiN 30 nm/Co₂FeAl/MgO 2 nm with different Co₂FeAl thicknesses from 3 nm to 10 nm (Supplementary Figure 2a) unveil that the TiN nearly has the same lattice constant as the MgO substrate, since it is only visible as a small shoulder in the MgO peak. The derived lattice constant for the TiN is $(4.25 \pm 0.10) \text{ \AA}$, which is in good agreement with the literature value of 4.24 \AA (see Reference³). The XRD results also suggest that a 10 nm Co₂FeAl layer is the optimum choice for the MTJ stacks, as for this thickness the Co₂FeAl (004) peak perfectly matches the expected value of 65.83° . For the Co₂FeAl, we could find a B2 ordering by detecting the (222) and (444) peaks without finding a (111) peak, as it would be present for the L2₁ ordered Co₂FeAl.

In addition, the composition of the Heusler electrodes is verified by x-ray fluorescence spectroscopy. The used parameters for the co-sputtering of Co₂FeSi result in a film composition of Co_{50.5}Fe_{24.5}Si₂₅. These values are subject to an uncertainty of $\approx 1\%$. Since our setup uses an Al filter, we are not able to check the actual composition of the Co₂FeAl. However, a composite Co₂FeAl target is used and, thus, the final film composition is expected to be close to the target composition.

Furthermore, the micrograph obtained by the AFM investigations (Supplementary Figure 2b) reveals a low roughness of 0.25 nm for the TiN 30 nm/Co₂FeAl 10 nm/MgO 2 nm layers. This low roughness value is crucial for MTJs with a tunnel barrier of high quality that avoids shortening between the two electrodes through pinholes.

Supplementary Note 3. TEMPORAL EVOLUTION AND SWITCHING BEHAVIOR

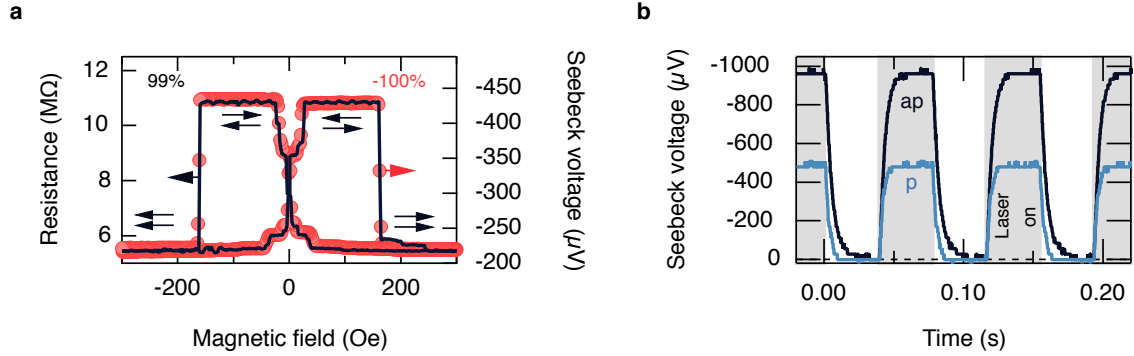
A. Co₂FeAl

Supplementary Figure 3a displays the Seebeck voltage of an elliptically shaped $3 \mu\text{m} \times 1 \mu\text{m}$ sized Co₂FeAl based MTJ under 150 mW laser power at a laser modulation frequency (on/off) of 13 Hz. Since the spot diameter of the laser on top of the MTJ is $\approx 10 \mu\text{m}$, a homogeneous illumination of the MTJ is ensured. A sharp switching of the Seebeck voltage between $-217 \mu\text{V}$ in the P and $-434 \mu\text{V}$ in the AP state of the MTJ is observed. This yields a TMS ratio of -100% . It is noteworthy, that the Seebeck voltage of the Co₂FeAl based MTJs is negative, which is different from the Co-Fe-B MTJs observed by Walter *et al.*⁴, Liebing *et al.*⁵, and Boehnke *et al.*⁶. Furthermore, the generated Seebeck voltages are much higher, than for the Co-Fe-B based MTJs studied with the same laser setup in References^{4,6,7}.

The Seebeck coefficients are calculated from the simulated temperature difference across the MgO barrier of 390 mK (cf. Supplementary Note 7A) and the experimentally determined voltages at a laser power of 150 mW. Seebeck coefficients of $S_P = 556 \mu\text{V/K}$ and $S_{AP} = 1113 \mu\text{V/K}$ are obtained for the P and the AP state, respectively. These values are comparable to the values in Table I obtained from the $2 \mu\text{m} \times 1 \mu\text{m}$ MTJ.

The abrupt changes of the Seebeck voltage occur at the same field values and with the same shape as the switching of the resistance of the MTJ. The similarities are nicely seen when the resistance data is plotted on top of the Seebeck voltage (Supplementary Figure 3a). The resistance, obtained at 10 mV bias voltage, changes between $5.45 \text{ M}\Omega$ in the P state and $10.87 \text{ M}\Omega$ in the AP state, yielding a TMR ratio of 99%.

The similar switching behaviors of the resistance and the Seebeck voltage are an evidences that the reversal of the magnetic orientation of the ferromagnetic electrodes causes the change of the Seebeck voltage. Of course, the



Supplementary Figure 3. Seebeck voltage of a Co_2FeAl based MTJ. **a** The resistance (left axis) at 10 mV bias voltage and the Seebeck voltage (right axis) at 150 mW laser power switch at the same fields, i.e., when the magnetic orientation of the ferromagnetic layers changes between P and AP. **b** Temporal evolution of the Seebeck voltage between laser on/off in the P and AP state.

fundamental origin is the change of the transport coefficients of the MTJ under magnetization reversal (cf. Reference⁸).

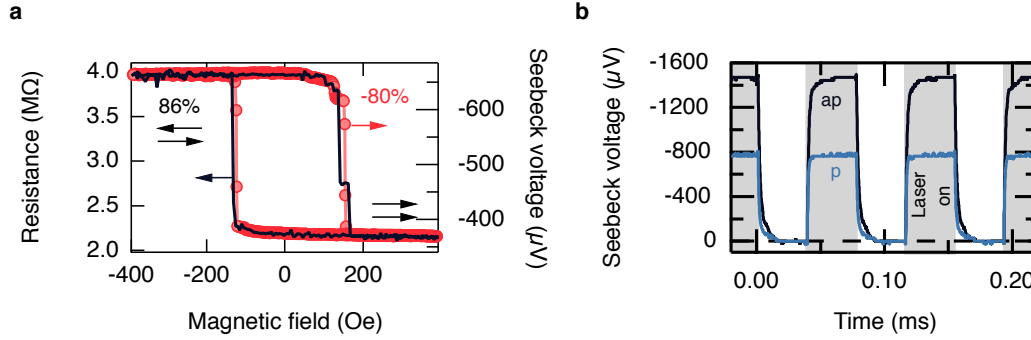
Since a modulated heating source in combination with high-resistive MTJs is used, it is crucial to monitor the temporal evolution of the signal. For the correct detection of the Seebeck voltage by the lock-in amplifier, it is highly important that the Seebeck signal saturates after the laser has been switched on or off. During laser on the voltage has to reach a constant plateau, whereas during laser off it should drop back to zero. The rise and fall times of the signal are dependent on the resistance and capacitance of the MTJ⁶; the higher the resistance, the slower is the saturation. Supplementary Figure 3b displays oscilloscope traces of the Seebeck signal that reveal a saturation of the voltage in the P state after 10 ms and in the AP state after 15 ms when the laser is switched on or off. The increased saturation time in the AP state is attributed to the increased resistance. Accordingly, the modulation of the laser heating with 13 Hz, corresponding to a laser on period of ≈ 38 ms, is slow enough to allow a correct lock-in detection. The higher values of the voltages detected by the scope compared to the lock-in amplifier are due to the difference in the detection techniques. The scope displays the peak-to-peak voltages, whereas the lock-in amplifier displays the root-mean-square value of the first harmonic of the signal⁶. For a conversion to the lock-in-signal, the oscilloscope signal has to be multiplied by a factor of 0.45. As the oscilloscope traces are recorded in the P and AP state of the MTJ, the temporal traces also disclose the difference of the Seebeck voltage between the magnetic states of the MTJ. The TMS ratio obtained from this difference amounts to $\approx -100\%$. Hence, it is of the same size as the TMS ratio obtained from the lock-in measurements in Supplementary Figure 3a. This good agreement is another proof for the reliability of the correct voltage detection by the lock-in technique.

B. Co_2FeSi

The Co_2FeSi MTJs are equipped with an antiferromagnetically pinned top Co-Fe electrode. The pinning prevents the Co-Fe electrode from switching at low external magnetic fields. The higher fields needed to reverse the magnetization of the pinned layer exceed the field provided by the electromagnet in the optical setup⁶. Hence, it is only possible to record minor loops of the MTJs, i.e., reversing the magnetization of the unpinned Co_2FeSi bottom electrode while keeping the magnetization of the Co-Fe electrode constant, and receiving a signal that resembles the hysteresis loop of this layer.

The TMR and TMS loops of an elliptical $2\ \mu\text{m} \times 1\ \mu\text{m}$ Co_2FeSi based MTJ with a 2 nm MgO tunnel barrier and a $\text{Co}_{70}\text{Fe}_{30}$ counter electrode are displayed in Supplementary Figure 4a. The switching of the resistance between 4.00 MΩ in the AP state and 2.15 MΩ in the P state is clearly visible. The resulting TMR ratio amounts to 86%. The Seebeck voltage obtained at the same MTJ with 150 mW laser power exhibits a similar switching behavior as the resistance. It changes at the same fields between $-664\ \mu\text{V}$ in the AP state and $-370\ \mu\text{V}$ in the P state. This change yields a TMS ratio of -80%. Hence, the ratio is only slightly smaller than the values obtained for the Co_2FeAl based MTJs.

Supplementary Figure 4b features the temporal evolution of the Seebeck signal under 150 mW laser radiation with



Supplementary Figure 4. Seebeck voltage of a Co_2FeSi based MTJ. **a** The resistance (left axis) at 10 mV bias voltage and the Seebeck voltage (right axis) at 150 mW laser irradiation switch at the same magnetic fields, i.e., when the magnetization of the Co_2FeSi layer is reversed. **b** Temporal evolution of the Seebeck voltage at 150 mW laser power between laser on/off at a modulation frequency of 13 Hz.

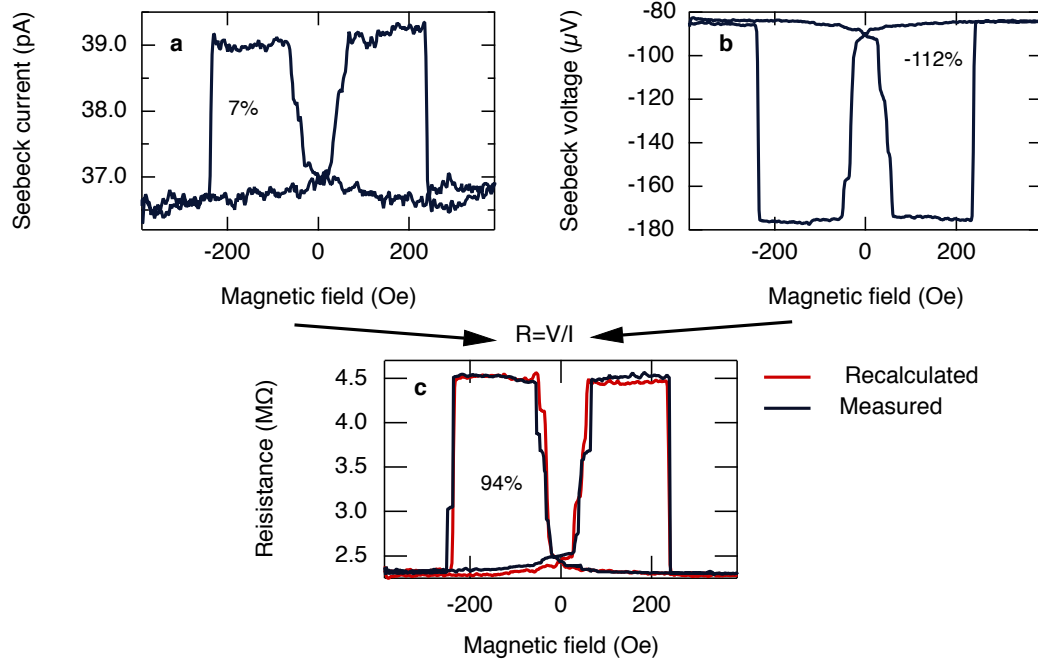
an on/off modulation at a frequency of 13 Hz. The obtained TMS ratio is -92%, which is slightly higher than the value obtained by the lock-in measurement. The peak-to-peak voltages of $\hat{V}_P = -1471 \mu\text{V}$ and $\hat{V}_{AP} = -763 \mu\text{V}$ correspond to root-mean-square voltages of the first harmonic detected by the lock-in-amplifier of $V_P = -661 \mu\text{V}$ and $V_{AP} = -343 \mu\text{V}$. These values are in a similar range as the experimentally obtained lock-in data. Furthermore, the temporal evolution of the Seebeck voltage obtained at the Co_2FeSi based MTJs reveals that the modulation frequency of 13 Hz is slow enough for the Seebeck voltage to reach saturation after the laser is switched on or off. In the P state the increase and decrease of the signal is faster ($\tau_{1/2}^P \approx 0.6 \text{ ms}$) than in the AP state ($\tau_{1/2}^{AP} \approx 1.1 \text{ ms}$) of the MTJ, due to the decreased resistance of the MTJ in the P state. These values correspond to the rise times of the signal from 0% to 50% when the heating is switched on. The 0% to 90% rise times are $\tau_{90\%}^P \approx 1.6 \text{ ms}$ and $\tau_{90\%}^{AP} \approx 3.6 \text{ ms}$.

A similar switching of the Seebeck voltage under varying magnetic field is found for a second elliptical MTJ with a size of $3 \mu\text{m} \times 1 \mu\text{m}$. For this MTJ (MTJ b) the TMS ratio reaches an average of -95%, which is higher than for the previously described MTJ (MTJ a), where the ratio only yields an average of -83% (Supplementary Table 1). A difference is also found in the TMR ratios of the two MTJs. MTJ b has a TMR ratio of 102% whereas MTJ a only produces a TMR ratio of 86%. This observation suggests, that the difference of the TMS ratios is purely based on the less pronounced change of the transport coefficients, i.e., the conductance and the Seebeck coefficient, in MTJ a. Such a behavior is usually evoked by a local variation of the quality of the tunnel barrier. This assumption is supported by the fact that the resistance-area product is decreased for the MTJ with the lower TMR and TMS ratios, indicating the poorer quality of the MgO barrier in MTJ a. A comparison of the most important values is presented in Supplementary Table 1.

Supplementary Table 1. Overview of Co_2FeSi based MTJs. The MTJ with the higher resistance-area product exhibits higher TMR and TMS ratios. The resistance is determined at a bias voltage of 10 mV. The Seebeck voltages are recorded with 150 mW laser power and a spot diameter of $\approx 10 \mu\text{m}$. The TMS ratios are averaged over Seebeck measurements with laser powers between 10 mW to 150 mW.

MTJ	size ($\mu\text{m} \times \mu\text{m}$)	$R_P A$ ($\text{M}\Omega \mu\text{m}^2$)	$R_{AP} A$ ($\text{M}\Omega \mu\text{m}^2$)	TMR	V_P (μV)	V_{AP} (μV)	TMS
a	2×1	3.36	6.28	86%	-370	-664	-83%
b	3×1	3.93	7.94	102%	-263	-503	-95%

The Seebeck coefficients for MTJ a (cf. Supplementary Figure 4 and Supplementary Table 1) are $S_P = 948 \mu\text{V K}^{-1}$ and $S_{AP} = 1703 \mu\text{V K}^{-1}$. For MTJ b the values still reach up to $S_P = 674 \mu\text{V K}^{-1}$ and $S_{AP} = 1290 \mu\text{V K}^{-1}$. These values are even higher than for the Co_2FeAl based MTJs.



Supplementary Figure 5. Seebeck current of Co_2FeAl based MTJ. **a** Seebeck current recorded at 150 mW laser power. **b** Seebeck voltage of the same MTJ under unchanged irradiation conditions. **c** Directly measured resistance at 10 mV bias voltage and recalculated resistance from Seebeck data in **a** and **b**.

Supplementary Note 4. THE SEEBECK CURRENT

Besides the Seebeck voltage, also the Seebeck current of the MTJ is determined. To perform the measurement the heating conditions are not changed, but the lock-in amplifier is directly connected to the MTJ and set to current mode. Derived from Reference⁸, the current in such a measurement is expressed by

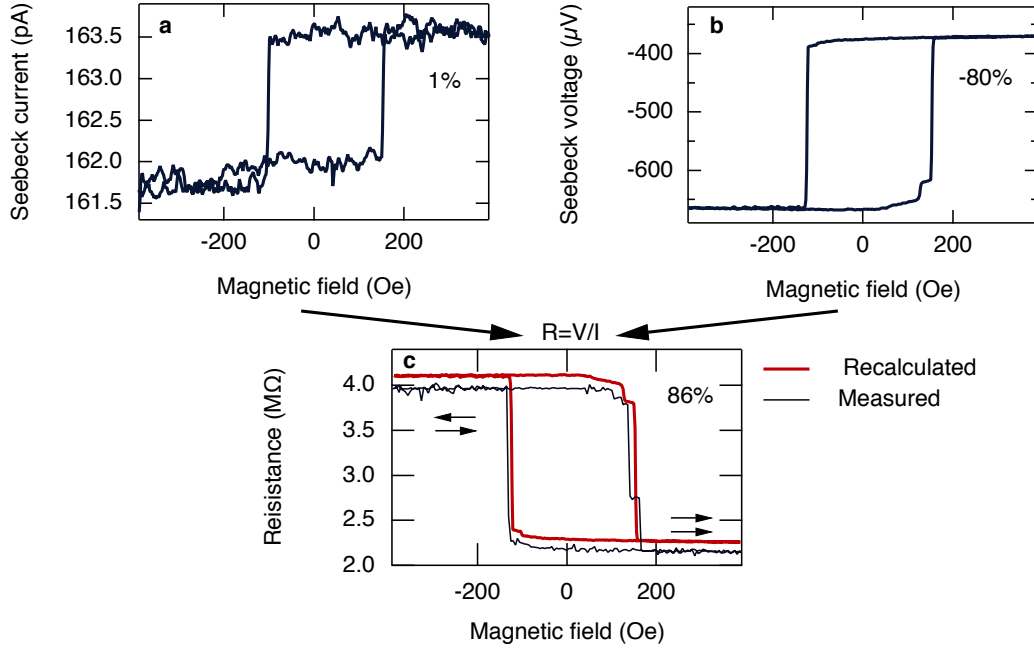
$$I_{P,AP} = \frac{1}{R_{P,AP}} S_{P,AP} \Delta T = \frac{1}{R_{P,AP}} (-V_{P,AP}^{\text{Seebeck}}) \quad (1)$$

$$\Leftrightarrow R_{P,AP} = -\frac{(V_{P,AP}^{\text{Seebeck}})}{I_{P,AP}}. \quad (2)$$

This equations reveal that the Seebeck current depends on the change of the Seebeck coefficients $S_{P,AP}$ and the resistance $R_{P,AP}$ between the P and AP state of the MTJ. After inserting the Seebeck voltage $V = -S\Delta T$ it resembles Ohm's law (Supplementary Equation 2). Thus, the resistance of the MTJ can be recalculated from the independently recorded Seebeck voltage and Seebeck current data.

A. Co_2FeAl

Supplementary Figure 5a depicts the Seebeck current obtained from an elliptical Co_2FeAl based MTJ with diameters of $3 \mu\text{m} \times 1 \mu\text{m}$ at 100 mW laser power. The current is switching between 36.6 pA in the P and 39.3 pA in the AP state, resulting in an effect ratio of approximately 7%. The Seebeck voltage determined at the same MTJ without altering the laser irradiation is displayed in Supplementary Figure 5b. It changes between $-83 \mu\text{V}$ in the P state and $-176 \mu\text{V}$ in the AP state of the MTJ, yielding a TMS ratio of -112%. Recalculating the resistance from the Seebeck



Supplementary Figure 6. Seebeck current of Co_2FeSi base MTJ. **a** Seebeck current recorded at 150 mW. **b** Seebeck voltage of the same MTJ under unchanged irradiation conditions. **c** Directly measured resistance at 10 mV bias voltage and recalculated resistance from Seebeck data in **a** and **b**.

current and the Seebeck voltage data in Supplementary Figure 5a and b, results in a curve that almost perfectly fits the measured resistance displayed in Supplementary Figure 5c.

A similar agreement of the recalculated and measured resistance is also achieved for Seebeck measurements with 150 mW laser power and on a second similarly shaped MTJ with resistances $R_P = 5.4 \text{ M}\Omega$ and $R_{AP} = 10.8 \text{ M}\Omega$. This MTJ reveals a TMR ratio of 100% and a TMS ratio of -97%.

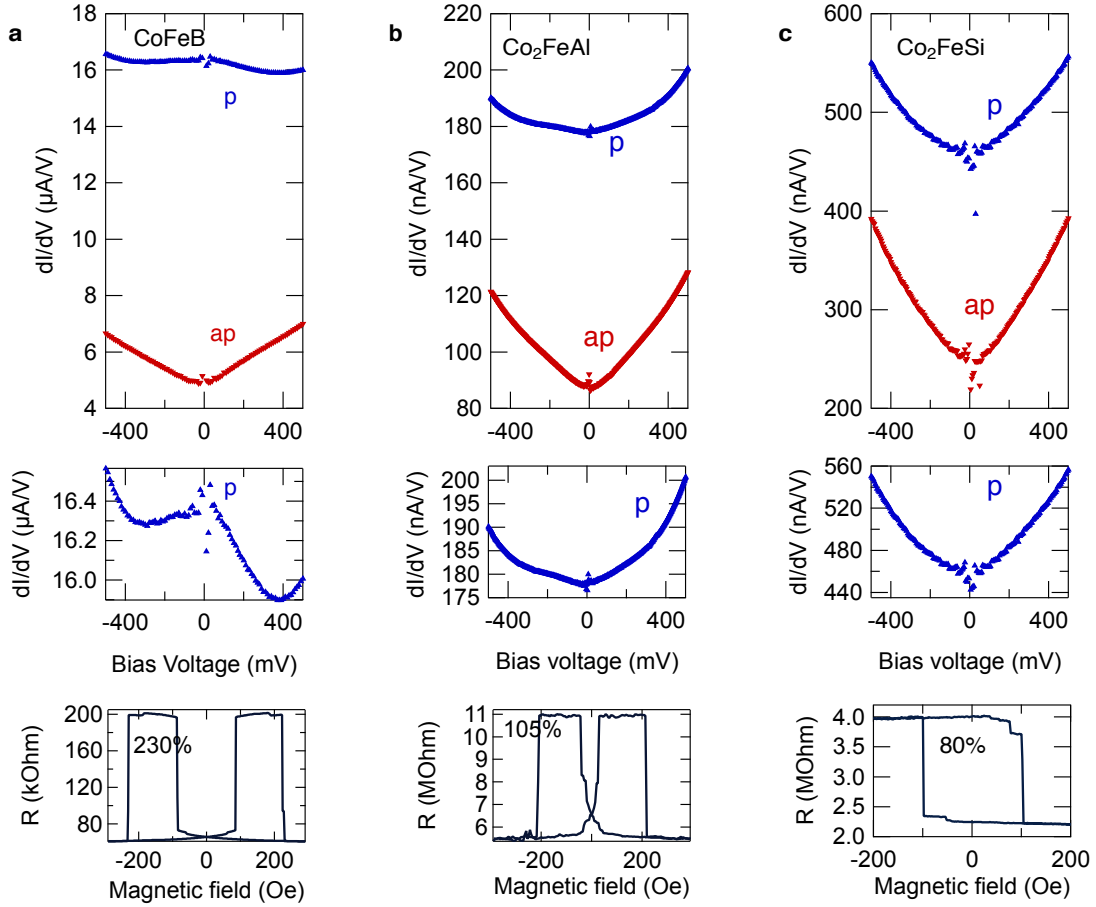
B. Co_2FeSi

Similar to the experiments performed with Co_2FeAl based MTJs, the Seebeck current of the MTJ is determined and the resistance is recalculated by dividing the Seebeck current by the Seebeck voltage. These values are obtained from independent measurements at the same MTJ under unchanged irradiation conditions.

Supplementary Figure 6a displays the switching of the Seebeck current of MTJ a in Supplementary Table 1 (elliptical shape of $2 \mu\text{m} \times 1 \mu\text{m}$). The current resembles the same switching behavior as the resistance and the Seebeck voltage (Supplementary Figure 6b). However, the effect ratio only yields 1%. This is attributed to the similar sizes of the TMR and TMS ratios. According to $I = S/R \cdot \Delta T$, the switching of the Seebeck coefficient S and the resistance R cancel out when the two effects are of similar magnitudes.

Supplementary Figure 6c displays the resistance of the MTJ under varying magnetic field. As before, the difference between the P and AP state of the MTJ is clearly recognizable. Furthermore, the curve of the recalculated resistance from the Seebeck data lies on top of the directly measured resistance, except of a small offset.

As the resistance is correctly recalculated from the Seebeck voltage and current, we draw the conclusion that the Seebeck voltage and current detection of the MTJ are very reliable and reproducible. Independent measurements lead to similar results.

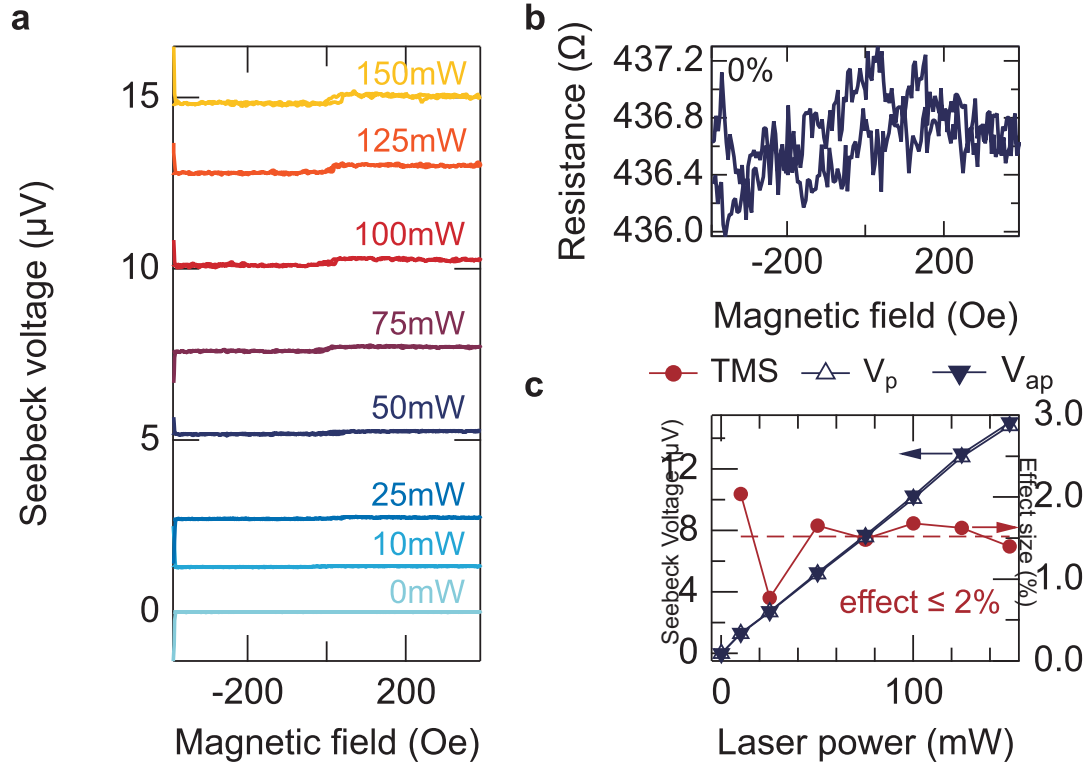


Supplementary Figure 7. Differential conductance. Differential conductance (top) and corresponding TMR effect (bottom) of MTJs containing a Co-Fe-B, b Co₂FeAl and c Co₂FeSi.

Supplementary Note 5. DIFFERENTIAL CONDUCTANCE

The differential conductance dI/dV in dependence of the applied bias voltage V reveals information on the energy landscape that the electrons experience when traveling between the two electrodes of a tunnel junction. Particularly the DOSs left and right of the tunnel barrier around the Fermi energy have a significant influence on the shape of the dI/dV vs. V curves. Brinkman has shown that for tunneling between two constant (flat) DOSs through a trapezoidal barrier, the dI/dV curve always exhibits a parabolic shape⁹. This description is no longer valid if the DOS possesses a gap. If the Fermi energy is scanned across a gap in the DOS by changing the bias voltage, the tunneling current will not significantly change although the voltage is increased. This is due to the lack of states in the gap. Only if the energy exceeds the gap energy and states are available, the current will increase again. In the dI/dV curve this can be recognized by a flat section around zero bias voltage leading to a deviation from the predicted parabolic shape.

For all MTJs investigated in this work, a gap or at least a pseudo gap can be found. In the Co-Fe-B/MgO/Co-Fe-B MTJs the gap is introduced by the coherent tunneling through the MgO barrier. In the Heusler compound based MTJs additionally a gap in the Heusler minority DOS is expected. Hence, a deviation from a perfect parabolic shape can be found in all dI/dV curves (Supplementary Figure 7). For a detailed explanation of the measurements at Co₂FeAl and Co-Fe-B and a comparison of the dI/dV curves to earlier measurements, please refer to Mann *et al.*¹⁰. For the Co₂FeSi MTJs the deviation from the parabolic shape is hardly visible. This might be due to several facts:



Supplementary Figure 8. Co₂FeAl based MTJs after dielectric breakdown. **a** Dependence of the Seebeck voltage for different laser powers, and **b** the resistance on the magnetic field. **c** Dependence of the Seebeck voltage in the P and AP state (left axis), and the effect ratio (right axis) on the laser power.

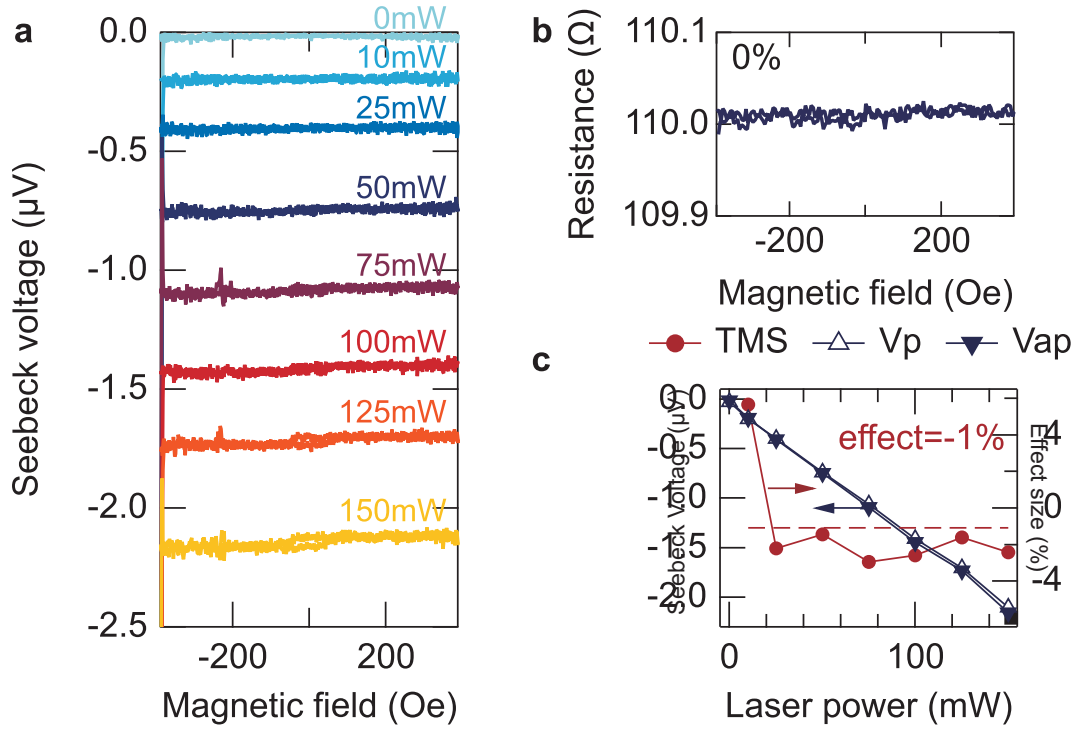
First, the IV-characteristics was obtained at room temperature. Second, the gap is not a real gap but a pseudo gap. Both circumstances lead to a less pronounced influence of the half-metallic DOS on the dI/dV characteristic. Third, the pseudo gap in the DOS is symmetric with respect to the Fermi energy, which leads to a symmetric dI/dV curve.

However, for a large TMS effect not only the presence of a gap in the DOS is of importance, also its position and the difference between the DOSs that contribute to the thermoelectric transport in the p and ap state have a significant impact. Since the tunneling current is represented by an integration of the DOS or the related transmission $T(E)$ over energy E (cf. Walter *et al.*⁴), the dI/dV curve cannot reveal the important features in the DOS that are necessary to gain a high TMS effect. Nevertheless, all curves show that the asymmetry of the transmission changes when the MTJ is switched from p to ap. This is a necessary ingredient to generate a high TMS effect.

Supplementary Note 6. CONTRIBUTIONS FROM THE LEADS: MTJS AFTER DIELECTRIC BREAKDOWN

To ensure that the Seebeck voltage is indeed generated by the temperature gradient across the MTJ and not, for example, in the leads, the junction is forced into a dielectric breakdown and the remaining Seebeck voltage is determined under unchanged irradiation conditions (Supplementary Figure 8). To break the 2 nm tunnel barrier, a bias voltage of 4 V is applied to the MTJ. The broken tunnel junction disables the spin-dependent tunneling across the barrier. Hence, after the breakdown of the barrier the TMR effect vanishes in both sample types, the Co₂FeSi and the Co₂FeAl based MTJs (Supplementary Figures 9 & 8). Simultaneously, the resistance drops from a few MΩ to a few hundred Ω, clearly indicating that the barrier has been destroyed by the voltage stress.

A similar behavior is found for the Seebeck voltage that exhibits almost no response to the external magnetic field. Only for higher laser powers, i.e., higher Seebeck voltages, a hysteresis loop is distinguished from the noise. The origin of the remaining switching might be due to magneto transport phenomena in the ferromagnetic Co₂FeSi bottom lead



Supplementary Figure 9. Co₂FeSi based MTJs after dielectric breakdown. **a** Dependence of the Seebeck voltage for different laser powers, and **b** the resistance on the magnetic field. **c** Dependence of the Seebeck voltage in the P and AP state (left axis), and the effect ratio (right axis) on the laser power.

or the shortened ferromagnetic electrodes in the Co₂FeAl based MTJs. For both MTJ types we emphasize that the shape of the Seebeck voltage versus magnetic field curves after breakdown of the junction are significantly different from the curves recorded at the same intact junctions. Since the MTJs reveal nearly no switching after the tunnel barrier is forced into a dielectric breakdown, it is guaranteed that the leads do not significantly contribute to the high TMS ratios obtained from the intact MTJs.

Moreover, the remaining Seebeck voltages of the broken MTJs are strongly reduced from several $-100 \mu\text{V}$ to a few μV . For the Co₂FeAl based MTJs that possess a TiN bottom lead free from ferromagnetic Heusler material, even the sign of the voltage is reversed. These remaining Seebeck voltages are probably generated by in-plane temperature differences in the bottom lead and not in the MTJs themselves. From this comparison of intact and broken MTJs, we conclude that the high Seebeck voltages and TMS ratios observed in the intact Heusler based MTJs are only generated due to the temperature difference across the MgO barrier.

Supplementary Note 7. COMSOL SIMULATIONS OF THE TEMPERATURES DURING HEATING

COMSOL Multiphysics finite element simulations are performed to determine the rise of the base temperature and the achieved temperature gradient over the MgO barrier, when the laser is applied to the top of the MTJ. The model we use is similar to the one of References^{4,6,7}, but the material parameters are adjusted according to Supplementary Table 2. For the simulations the MTJ sizes, the laser spot size and the laser power are chosen according to the values used in the experiments. Furthermore, the influence of the size of the laser spot on the temperature profile in the MTJs is investigated.

Supplementary Table 2. Material parameters for COMSOL simulations. If not specified otherwise, the values are taken from Refs.^{4,11–13}. The density of the Heusler compounds and the TiN layers are taken from XRR measurements. The thermal conductivities used in the simulations are printed in bold letters. Experimental thin film values are given if available.

Material	ρ ($10^3 \frac{\text{kg}}{\text{m}^3}$)	c_p ($\frac{\text{J}}{\text{kg}\cdot\text{K}}$)	$\kappa_{\text{bulk}} / \kappa_{\text{thin}}^{\text{exp}} (\frac{\text{W}}{\text{m}\cdot\text{K}})$
Au	19.32	128	320.0 / $70^{14} - 170^{15}$
Cr	7.15	449	94.0
Ru	12.37	238	117.0
Ta	16.65	140	57.0
Ta ₂ O ₅	8.27	306	0.2
Ni ₈₀ Fe ₂₀	8.7	460	19.0
Ir-Mn	10.18	69.7	6.0
Co-Fe-B	8.22	440	86.7
MgO	3.58	935	48.0 / 4.0 ¹⁶
SiO ₂	2.20	1052	1.4
Si	2.33	700	150.0
SiN	3.11	700	35.9
Co ₂ FeAl	6.8	424 ¹⁷	20 ^{18,19}
Co ₂ FeSi	7.2	424 ¹⁷	20 ^{18,19}
TiN	5.45	604 ²⁰	28.8 [?]

A. Heusler compound MTJs

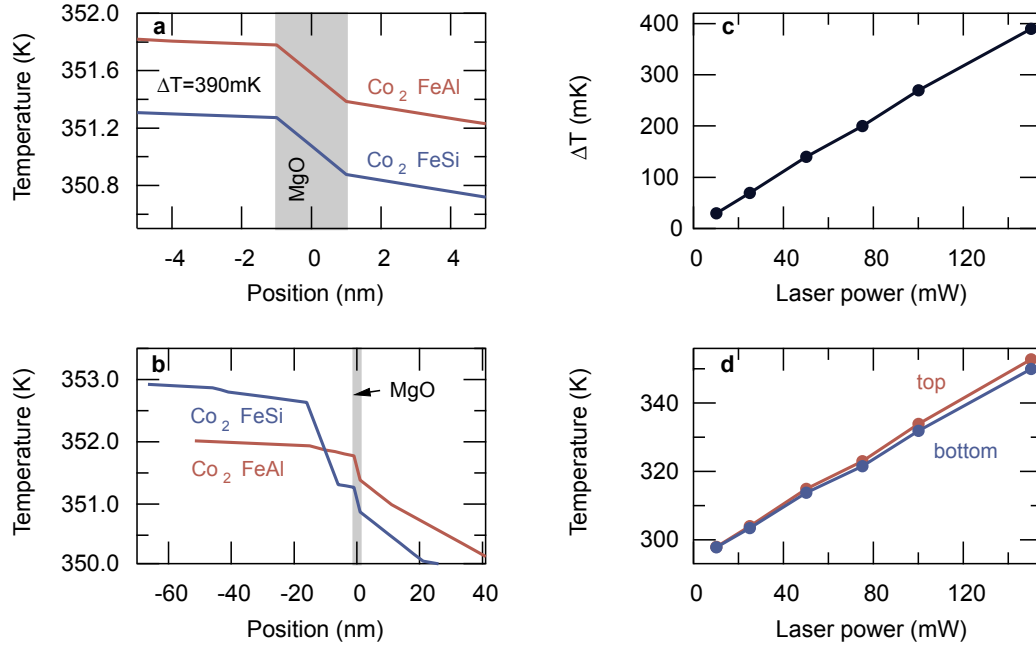
For the simulations of the temperature evolution upon heating in the Heusler compound based MTJs, a round MTJ of $3 \mu\text{m}$ in diameter is assumed. The laser spot is modeled as a Gaussian beam with a beam waist of $5 \mu\text{m}$. This value equals the experimentally determined beam diameter of $10 \mu\text{m}$. For the laser with a power of 150 mW, a power of 120 mW is measured at the position of the sample. Hence, this value is used in the simulations.

Supplementary Figure 10 displays the results of the COMSOL simulations for the Co₂FeAl and Co₂FeSi based MTJs. In Supplementary Figure 10a it can be seen that a temperature gradient is generated across the barrier of the MTJ, pointing from the bottom Heusler electrode (lower temperature) to the top electrode. The gradient across the insulating barrier is much steeper than the gradient generated in the metallic electrodes. This gradient over the barrier is the driving force for the Seebeck induced tunneling of electrons across the electrodes.

Hence, this gradient is used to calculate the Seebeck coefficients from the experimentally determined Seebeck voltages, which is in accordance with other TMS experiments performed by Walter *et al.*⁴ and Liebing *et al.*^{5,11}. The obtained gradients amount to a ΔT of 390 mK for the laser set to a power of 150 mW for both Heusler based MTJ types.

However, if the temperature change at all interfaces, i.e., over all layers of the MTJ (Supplementary Figure 10b), is considered, a second much larger gradient is observed in the Co₂FeSi based MTJs. This gradient is attributed to the Mn-Ir pinning layer. Mn-Ir has a much lower heat conductivity than the surrounding layers (cf. Supplementary Table 2), and hence, supports the generation of a temperature gradient. For the Co₂FeAl based MTJs that do not contain an Mn-Ir layer, no second gradient, that is equally steep as the gradient over the MgO barrier, is observed. The large second gradient in the Co₂FeSi based MTJs makes it necessary to check if the determined voltage indeed is mostly generated by the temperature gradient across the MgO barrier, and not by the second gradient in the samples. This is done by breaking the MgO barrier and determining the remaining Seebeck voltage, as discussed in the main text and in detail in Supplementary Note 6.

For the Co₂FeAl based MTJs simulations with different laser powers are performed (Supplementary Figures 10c,d). The generated temperature gradients rise linearly with the laser power and range between 30 mK for the laser set to 10 mW and nearly 400 mK for the laser set to 150 mW. Also, the base temperatures for different laser powers rise linearly from room temperature to approximately 350 K at 150 mW laser power. Since the temperature increases linearly with the applied laser power, a linear increase of the Seebeck voltage with laser power is expected. However, due to the simultaneous rise of the base temperature, it is possible to observe the temperature dependence of the Seebeck coefficients. This dependence might lead to a deviation of the Seebeck voltage from the expected ideal linear behavior.



Supplementary Figure 10. Simulated temperature gradients in the Heusler based MTJs. **a** ΔT across the 2 nm MgO barrier at 150 mW laser power. **b** Temperature evolution over the whole layer stacks. **c** Dependence of ΔT in the Co_2FeAl based MTJs on the applied laser power. **d** Increase of the base temperature \bar{T} with laser power for the Co_2FeAl based MTJs.

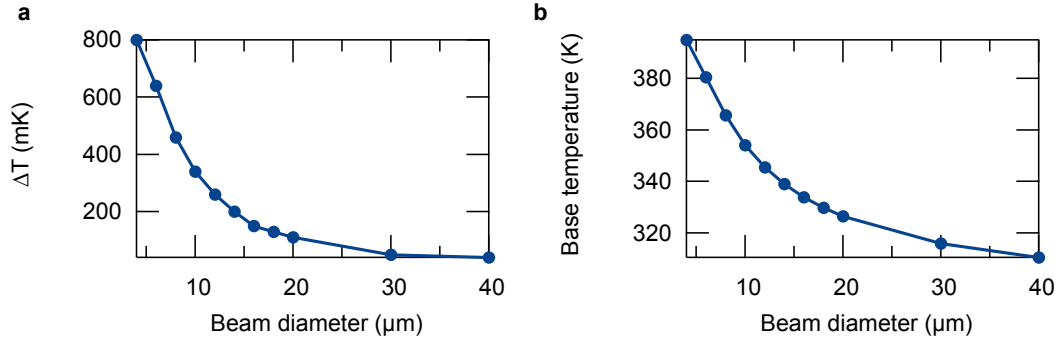
B. Dependence on laser spot diameter

For the Co_2FeAl based MTJs simulations of the temperatures with different sizes of the laser spot have been conducted (Supplementary Figure 11). The smallest diameter is chosen to be $4\ \mu\text{m}$ and the largest to be $40\ \mu\text{m}$. Within this range, a significant drop of the temperature difference across the MgO barrier from $\Delta T = 800\ \text{mK}$ for the smallest beam size to $50\ \text{mK}$ for the largest beam is obtained. Simultaneously, the base temperature decreases from $390\ \text{K}$ to $310\ \text{K}$.

These results reveal how drastically the size of the laser spot influences the Seebeck effect measurements. Hence, the beam size has to be carefully checked before or after each measurement.

SUPPLEMENTARY REFERENCES

- ¹Niesen, A. *et al.* Titanium nitride as a seed layer for Heusler compounds. *J. Appl. Phys.* **118**, 243904 (2015).
- ²Sterwerf, C., Meinert, M., Schmalhorst, J.-M. & Reiss, G. High TMR Ratio in Co_2FeSi and Fe_2CoSi Based Magnetic Tunnel Junctions. *IEEE Trans. Magn.* **49**, 4386-4389 (2013).
- ³Kato, A. & Tamari, N. Crystal growth of titanium nitride by chemical vapor deposition. *J. Cryst. Growth* **29**, 55-60 (1975).
- ⁴Walter, M. *et al.* Seebeck effect in magnetic tunnel junctions. *Nat. Mater.* **10**, 742-746 (2011).
- ⁵Liebing, N. *et al.* Tunneling Magnetothermopower in Magnetic Tunnel Junction Nanopillars. *Phys. Rev. Lett.* **107**, 177201 (2011).
- ⁶Boehnke, A. *et al.* Time-resolved measurement of the tunnel magneto-Seebeck effect in a single magnetic tunnel junction. *Rev. Sci. Instrum.* **84**, 063905 (2013).
- ⁷Boehnke, A. *et al.* On/off switching of bit readout in bias-enhanced tunnel magneto-Seebeck effect. *Sci. Rep.* **5**, 8945 (2015).
- ⁸Czerner, M., Bachmann, M. & Heiliger, C. Spin caloritronics in magnetic tunnel junctions: Ab initio studies. *Phys. Rev. B* **83**, 132405 (2011).
- ⁹Brinkman, W. F., Dynes, R. C. & Rowell, J. M. Tunneling Conductance of Asymmetrical Barriers. *J. Appl. Phys.* **41**, 1915-1921 (1970).
- ¹⁰Mann, A. *et al.* Insights into Ultrafast Demagnetization in Pseudogap Half-Metals. *Phys. Rev. X* **2**, 041008 (2012).



Supplementary Figure 11. Dependence of the temperatures on the beam size in the Co₂FeAl based MTJs. a The temperature difference across the MgO barrier. **b** The base temperature in the center of the MgO barrier. The simulations are performed for the laser set to a power of 150 mW.

- ¹¹Liebing, N. *et al.* Determination of spin-dependent Seebeck coefficients of CoFeB/MgO/CoFeB magnetic tunnel junction nanopillars. *J. Appl. Phys.* **111**, 07C520 (2012).
- ¹²Papuso, C., Sousa, R., Herault, J. Prejbeanu, I. L. & Dieny, B. Probing fast heating in magnetic tunnel junction structures with exchange bias. *New J. Phys.* **10**, 103006 (2008).
- ¹³Beecher, C., Dinwiddie, R. B., Abeel, A. M. & Lowden R. A. The thermal conductivity of silicon nitride with molybdenum disilicide additions (ed Tong, T. W.) (Technomic Publishing Company, 1994).
- ¹⁴Zink, B. L., Revaz, B., Cherry, J. J. & Hellman, F. Measurement of thermal conductivity of thin films with a Si-N membrane-based microcalorimeter. *Rev. Sci. Instrum.* **76**, 24901 (2005).
- ¹⁵Zhang, Q. G., Cao, B. Y., Zhang, X., Fujii, M. & Takahashi, K. Influence of grain boundary scattering on the electrical and thermal conductivities of polycrystalline gold nanofilms. *Phys. Rev. B* **74**, 134109 (2006).
- ¹⁶Lee, S. M., Cahill, D. G. & Allen, T. H. Thermal conductivity of sputtered oxide films. *Phys. Rev. B* **52**, 253-257 (1995).
- ¹⁷Bentouaf, A. & Hassan, F. E. H. Structural, electronic, magnetic and thermodynamic properties of full Heusler compound Co₂VSi: Ab initio study. *J. Magn. Magn. Mater.* **381**, 65-69 (2015).
- ¹⁸Shiomi, J., Esfarjani, K. & Chen, G. Thermal conductivity of half-Heusler compounds from first-principles calculations. *Phys. Rev. B* **84**, 104302 (2011).
- ¹⁹Lue, C. S. & Kuo, Y.-K. Thermoelectric properties of the semimetallic Heusler compounds Fe_{2x}V_{1+x}M (M=Al, Ga). *Phys. Rev. B* **66**, 085121 (2002).
- ²⁰Chase Jr., M. W. *NIST-JANAF Thermochemical Tables, Fourth Edition. J. Phys. Chem. Ref. Data, Monograph* **9**, 1-1951 (1998).

5.4 Comparison of laser induced and intrinsic tunnel magneto-Seebeck effect in CoFeB/MgAl₂O₄ and CoFeB/MgO magnetic tunnel junctions (Thesis article IV)

PHYSICAL REVIEW B **93**, 224433 (2016)

Comparison of laser-induced and intrinsic tunnel magneto-Seebeck effect in CoFeB/MgAl₂O₄ and CoFeB/MgO magnetic tunnel junctions

Torsten Huebner,^{1,*} Alexander Boehnke,¹ Ulrike Martens,² Andy Thomas,³ Jan-Michael Schmalhorst,¹ Günter Reiss,¹ Markus Münzenberg,² and Timo Kuschel^{1,4}

¹*Center for Spinelectronic Materials and Devices, Department of Physics, Bielefeld University, Universitätsstraße 25, 33615 Bielefeld, Germany*

²*Institut für Physik, Greifswald University, Felix-Hausdorff-Strasse 6, 17489 Greifswald, Germany*

³*Leibniz Institute for Solid State and Materials Research Dresden (IFW Dresden), Institute for Metallic Materials, Helmholtzstrasse 20, 01069 Dresden, Germany*

⁴*Physics of Nanodevices, Zernike Institute for Advanced Materials, University of Groningen, Nijenborgh 4, 9747 AG Groningen, The Netherlands*

(Received 27 April 2016; revised manuscript received 14 June 2016; published 30 June 2016)

We present a comparison of the tunnel magneto-Seebeck effect for laser-induced and intrinsic heating. Therefore, Co₄₀Fe₄₀B₂₀/MgAl₂O₄ and Co₂₅Fe₅₅B₂₀/MgO magnetic tunnel junctions have been prepared. The TMS ratio of 3% in case of the MAO MTJ agrees well with ratios found for other barrier materials, while the TMS ratio of 23% of the MgO MTJ emphasizes the influence of the CoFe composition. We find results using the intrinsic method that differ in sign and magnitude in comparison to the results of the laser heating. The intrinsic contributions can alternatively be explained by the Brinkman model and the given junction properties. Especially, we are able to demonstrate that the symmetric contribution is solely influenced by the barrier asymmetry. Thus, we conclude that the symmetry analysis used for the intrinsic method is not suitable to unambiguously identify an intrinsic tunnel magneto-Seebeck effect.

DOI: 10.1103/PhysRevB.93.224433

I. INTRODUCTION

Spin caloritronics is a rising field of research seeking to combine spin, charge, and temperature driven currents to develop new and improved ways of data processing and storage. Especially, the usage of temperature driven spin-polarized currents has attracted a lot of attention in the past years, since it may offer a way to deal with rising heat dissipation in nanodevices [1].

Lately, significant progress has been made in controlling temperature differences in magnetic nanostructures over a small distance [2], enabling the discovery of, for example, the *tunnel magneto-Seebeck* (TMS) effect [3,4]. This effect occurs in *magnetic tunnel junctions* (MTJs) when a temperature difference is generated across the barrier. The TMS effect describes the change of the Seebeck coefficient (S_p and S_{ap}) of the MTJ between the state of parallel (p) and antiparallel (ap) relative magnetization orientation of the ferromagnetic electrodes. The effect ratio [5] can be expressed by

$$\text{TMS} = \frac{S_p - S_{ap}}{\min(|S_p|, |S_{ap}|)}. \quad (1)$$

Recently, the reciprocal effect, the magneto-Peltier effect, has also been reported for MTJs [6]. Today, different heating methods are established to generate a temperature difference inside the MTJ: indirect Joule [4,7,8], indirect Peltier [6], and laser-induced heating [3,9,10]. An additional method proposes to use the direct intrinsic Joule heating by the tunneling current. With this method, the temperature difference is created without additional external heating and, thus, the effect is called the *intrinsic* TMS effect [11,12].

In most cases CoFeB/MgO/CoFeB MTJs are used to study the TMS effect, because they are well known, easily prepared, and show large *tunnel magnetoresistance* (TMR) effects [13]. Using MgAl₂O₄ (MAO) as a barrier material theoretically retains the aforementioned properties of MgO (for example, the Δ_1 symmetry filter effect [14]) whereas the lattice mismatch with typical electrode materials decreases from about (3–5)% for MgO to about 1% for MAO [15]. In addition, MgAl₂O_x double-barrier MTJs show a long-range phase coherence using the resonant states of Fe quantum wells with up to 12-nm thickness [16]. Here, the structural flexibility of MgAl₂O_x ensures a vanishing mismatch between barrier and electrode, effectively enhancing quantum phenomena. Additionally, an improved bias voltage dependence was found with a barrier consisting of MAO [17]. A maximum TMR ratio of over 160%, a very low *resistance area product* (RA) of less than 5 $\Omega\mu\text{m}^2$, as well as magnetization switching by spin-transfer torque was achieved by depositing and oxidizing Mg/Mg-Al layers [18].

In this work, we study CoFeB/MAO and CoFeB/MgO MTJs and place emphasis on the comparison of laser-induced and intrinsic TMS. After a description of the sample preparation in Sec. II, the results of the TMR and laser-induced TMS measurements are presented in Sec. III, followed by COMSOL simulations of the temperature differences, the Brinkman model, and the results of the intrinsic TMS.

II. SAMPLE PREPARATION

The CoFeB/MAO and CoFeB/MgO layer stacks are deposited on MgO(001) substrates to prevent parasitic effects originating from semiconducting substrates as reported in Ref. [9]. The sequence of layers of the MAO MTJ consists of a bottom contact Ta 10/Ru 30/Ta 5/Ru 5, a pinned layer

*thuebner@physik.uni-bielefeld.de

MnIr 10/Co₄₀Fe₄₀B₂₀ 2.5, a tunnel barrier MAO 1.8, a free layer Co₄₀Fe₄₀B₂₀ 2.5, and a top contact Ta 5/Ru 30/Ta 5/Au 60 (numbers are thicknesses in nm). Except for MAO, all films are prepared by *dc* sputtering at a base pressure of less than 5×10^{-7} mbar in a Leybold Vakuum GmbH CLAB 600. MAO is *rf* sputtered from a composite target in the same chamber. After deposition, *ex situ* postannealing in a vacuum furnace is carried out at 350 °C for 1 h with a subsequent cooling process in a magnetic field of 0.7 T. Elliptical junctions of $24 \mu\text{m}^2$ are prepared by electron beam lithography and subsequent ion beam etching. Ta₂O₅ (120 nm) is sputtered next to the MTJs to serve as insulator. In addition, Au bond pads are placed on top and next to the MTJs to allow electrical contacting via Au bonds and optical access. The experimental details of the Co₂₅Fe₅₅B₂₀ 2.5/MgO 1.7/Co₂₅Fe₅₅B₂₀ 5.4 (numbers are thicknesses in nm) MTJ are described elsewhere [10]. To measure the TMS effect, an established setup with a modulated diode laser ($P_{\text{max}}=150$ mW, $\lambda = 637$ nm, $f = 177$ Hz) is used to generate the temperature difference across the junction (see Ref. [3] or [9] for details). At the same time, the setup is able to record TMR loops and I/V characteristics with a Keithley 2400 Sourceter.

III. RESULTS

A. TMR and laser-induced TMS

Figure 1(a) depicts the TMR and TMS minor loops for an MTJ with a nominal barrier thickness of 1.8 nm MAO. Both loops show identical switching behavior, allowing the identification of clear antiparallel and parallel states. With Eq. (1) and a laser power of 150 mW the TMS amounts to 3.3% while the TMR ratio is 34%. Altogether, the TMS (TMR) ratios are relatively constant with a variation of $\pm 0.25\%$ ($\pm 1\%$) between different junctions. For this, we measured the TMS (TMR) effect at more than five (10) junctions. A similar TMS ratio was found for Co₄₀Fe₄₀B₂₀/MgO MTJs [9]. The TMR ratio is comparable to similar studies using sputter deposition from a composite, stoichiometric MAO target [19].

In comparison, Fig. 1(b) displays the TMS and TMR results of the Co₂₅Fe₅₅B₂₀/MgO MTJ. It exhibits an almost rectangular switching behavior resulting in a TMS ratio of $(23 \pm 3)\%$ and a high TMR ratio of around 200% indicating very good stack quality. Since the TMS depends on the electronic band structure of the electrodes, both TMS ratios are in good agreement with theoretical predictions for different Co and Fe compositions [20,21] and experimental results of Co_xFe_y/MgO/Co_xFe_y MTJs in case of laser-induced heating [3].

Figure 1(c) shows the Seebeck voltages of the MTJ with MAO barrier in the parallel and antiparallel magnetization alignment and the corresponding TMS ratios for different laser powers. A barrier of 1.8-nm MAO results in an averaged (over all laser powers) TMS ratio of $(3.3 \pm 0.2)\%$. In accordance with previous experiments [3], a linear increase of the Seebeck voltages with increasing laser power is observed.

B. COMSOL simulations

Simulations are performed with COMSOL Multiphysics to estimate the temperature differences across the barriers

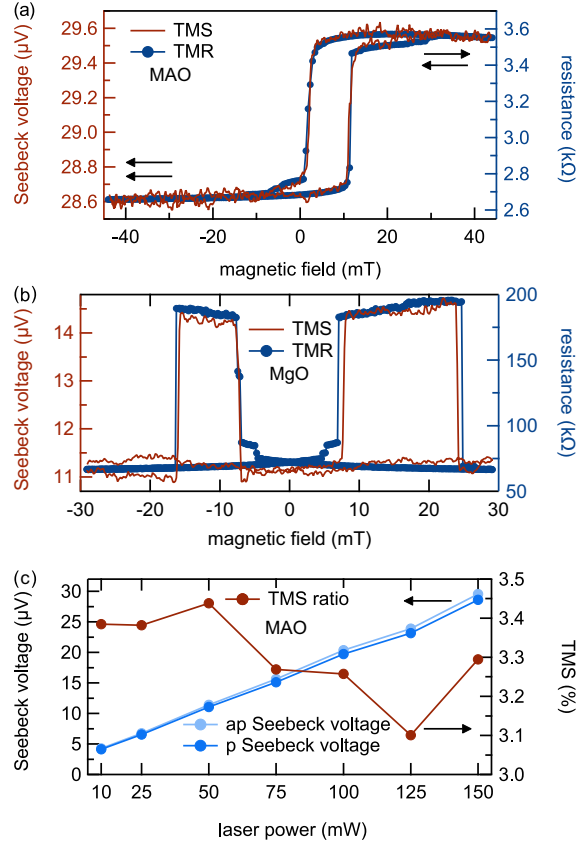


FIG. 1. (a) Typical TMS (measured with a laser power of 150 mW) and TMR minor loop of a junction with an area of $24 \mu\text{m}^2$ and a nominal MAO thickness of 1.8 nm. (b) TMS (150 mW) and TMR major loops of a CoFeB/MgO MTJ with a junction size of $2 \mu\text{m}^2$ and a nominal MgO thickness of 1.7 nm. (c) Antiparallel (light blue) and parallel (dark blue) Seebeck voltages for an MTJ with an MAO thickness of 1.8 nm increase linearly with the laser power, while the TMS ratio (red) is constant ($3.3 \pm 0.2\%$).

and to calculate the Seebeck coefficients. A crucial point within these simulations is the thermal conductivity of thin films as reported in Refs. [22,23]. For the MTJ with MgO barrier, a value of $\Delta T = 11$ mK was found for a laser power of 150 mW [10] resulting in Seebeck coefficients of $S_p = (-1010 \pm 20) \frac{\mu\text{V}}{\text{K}}$ and $S_{\text{ap}} = (-1320 \pm 20) \frac{\mu\text{V}}{\text{K}}$. The values used for the simulation of the MTJ with MAO barrier are given in Table I and the results are shown in Fig. 2. Since the thermal conductivity decreases for thin films in comparison to its bulk value and a similar behavior for thin MgO films is observed in Ref. [22], we assume a thermal conductivity of $(2.3 \pm 2) \frac{\text{W}}{\text{mK}}$ for MAO, which is one-tenth of the bulk value. Please note that according to Ref. [23] the thermal conductivity is very sensitive to the imbalance of phonon and electron temperature at nanomagnetic interfaces, which is why we use a large error range for the thermal conductivity of MAO. With the aforementioned assumption and an applied laser power of 150 mW, the temperature difference across

TABLE I. COMSOL simulation parameter values of thermal conductivity κ , density ρ , and heat capacity C_p . If not stated otherwise, the values of Walter *et al.* [3] are taken. Numbers in rounded brackets are bulk values.

Material	$\kappa \left(\frac{\text{W}}{\text{m K}} \right)$	$\rho \left(\frac{\text{kg}}{\text{m}^3} \right)$	$C_p \left(\frac{\text{J}}{\text{K kg}} \right)$
Ta	57	16 650	140
Ta ₂ O ₅ ^{a,b}	0.2	8270	306
Au	320	19 320	128
Ru	117	12 370	238
MnIr ^c	6	10 181	316
CoFeB	87	8216	440
MAO ^{d,e,f}	2.3 ± 2 (22-24)	3650	815

^aReference [24].

^bReference [25].

^cReference [26].

^dReference [27].

^eReference [28].

^fReference [29].

the tunneling barrier varies between 100 and 1400 mK. The Seebeck coefficients of the MTJ are given by $S_{\text{ap,p}} = -\frac{V_{\text{ap,p}}}{\Delta T}$. Thus, we get $S_{\text{ap}}^{1.8} \approx -160 \frac{\mu\text{V}}{\text{K}}$ and $S_{\text{p}}^{1.8} \approx -150 \frac{\mu\text{V}}{\text{K}}$. With respect to the uncertainty of the thermal conductivity of MAO, an error of $\pm 140 \frac{\mu\text{V}}{\text{K}}$ is calculated.

C. Brinkman model

Directly after the TMS measurements, I/V characteristics are recorded at the same junctions. The voltage-dependent current density between two electrodes separated by a thin insulating layer is described by Brinkman's model [30], which is based on the generalized Simmons' model [31]. Regarding the relatively low TMR ratio of the MAO MTJ, the presence of a symmetry filter effect can be excluded, which is a basic requirement for the validity of both models. This effect and the accompanying coherent tunnel process is responsible for the high TMR in the CoFeB/MgO MTJs, therefore excluding them from being taken into account within the subsequent Brinkman evaluation. Also, band structure effects caused, for example, by ferromagnetic half-metals are not included

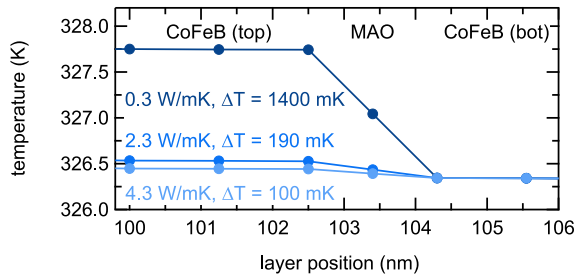


FIG. 2. COMSOL simulation of the temperature profile across the tunnel barrier with an applied laser power of 150 mW (120 mW at the sample as deduced from calibration measurements) for different thermal conductivities of MAO. The layer position of 0 nm corresponds to the top of the stack.

in both models. Thus, we focus on the MAO MTJ for the Brinkman evaluation. Within his model, Simmons assumes the potential of the barrier to be symmetric. In order to account for asymmetric barriers, Brinkman replaces the symmetric barrier potential by a trapezoidal barrier potential. The current density (in A/cm²) is then given by

$$J(V) = 3.16 \cdot 10^{10} \frac{\varphi^{\frac{1}{2}}}{d} \exp(-1.025 \varphi^{\frac{1}{2}} d) \cdot \left[V - \frac{A_0 \Delta \varphi}{32 \varphi^{\frac{3}{2}}} e V^2 + \frac{3 A_0^2}{128 \varphi} e^2 V^3 \right], \quad (2)$$

with $A_0 = \frac{4d\sqrt{2m_{\text{eff}}}}{3\hbar}$. φ is the barrier height (in V), d is the thickness of the barrier (in Å), $\Delta \varphi$ is the barrier asymmetry (in V), e is the elementary charge, \hbar is the reduced Planck constant, and m_{eff} is the effective electron mass. Brinkman states that in the case of $\Delta \varphi/\varphi < 1$ and $d > 10 \text{ Å}$ the error of this solution amounts to $\leq 10 \%$. The characteristic values of the barrier (height, thickness, and asymmetry) are obtained with

$$\begin{aligned} \varphi^2 &= \frac{e^2 C}{32 A} \ln^2 \left(\frac{h^3}{\sqrt{2} \pi e^3 m_{\text{eff}}} \sqrt{A C} \right), \\ d &= -\frac{\hbar}{\sqrt{8 \varphi m_{\text{eff}}}} \ln \left(\frac{h^3}{\sqrt{2} \pi e^3 m_{\text{eff}}} \sqrt{A C} \right), \\ \Delta \varphi &= -\frac{12 \hbar}{e \sqrt{2 m_{\text{eff}}}} \frac{\varphi^{\frac{3}{2}} B}{d C}, \end{aligned} \quad (3)$$

where A , B , and C are the parameters of a second-order polynomial fit to the differential conductance given by $dJ/dV = AV^2 + BV + C$.

Figure 3 shows the results with both dJ/dV curve and Brinkman fit for the antiparallel and parallel magnetization alignment. Using the Brinkman model, the barrier height φ , the barrier asymmetry $\Delta \varphi$, and the barrier thickness d are calculated (results are listed in Fig. 3). In the antiparallel case, the change of base temperature of the whole film stack induces a resistance change that is much larger than for the parallel case, which is why the Brinkman fit is not able to cover all features. Still, a good estimation of the barrier parameters is obtained, if compared to the results of the parallel case. It is noteworthy that the theoretically predicted value of the

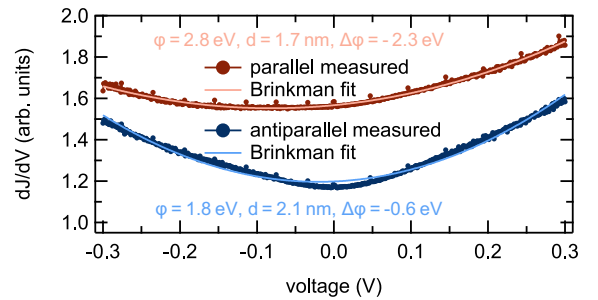


FIG. 3. dJ/dV curves (dark) with corresponding Brinkman fits (light) in the antiparallel (blue) and parallel (red) case. In addition, the resulting values for the barrier height φ , the barrier thickness d , and the barrier asymmetry $\Delta \varphi$ are shown.

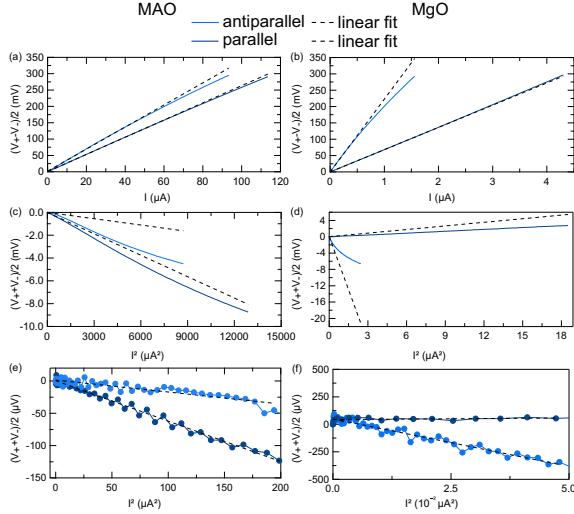


FIG. 4. (a) and (b) Antisymmetric contribution of the V/I characteristics. The dashed black lines are linear fits and illustrate the nonlinearity of the experimental data. (c) and (d) Linear fits to the symmetric contributions that are performed within (e) and (f) the small, and then extended to (c) and (d) the whole range.

effective electron mass of $m_{\text{eff}} = 0.422 m_e$ [14] results in a barrier thickness of $d = 1.7$ nm for the parallel case matching the nominal value of 1.8 nm within the 10% error range of the Brinkman model.

D. Intrinsic TMS and Brinkman model

Zhang, Teixeira *et al.* [11,12] measured V/I characteristics of CoFeB/MgO MTJs and derived “intrinsic” Seebeck coefficients via the slope of the symmetric contribution $[(V_+ + V_-)/2]$, where the temperature difference is generated by the Joule heating of the tunnel current. Within this model, the slope of the antisymmetric contribution $[(V_+ - V_-)/2]$ is directly correlated with the stack resistance. They neglect the general nonlinearity of tunnel processes and the accompanying dependence of the resistance on the voltage. In order to probe the validity of this intrinsic method, we now compare the results of the laser-induced TMS with the intrinsic TMS.

TABLE II. Results of the intrinsic symmetry evaluation. The resistances R extracted from the TMR loops are given as a comparison to the resistances from the antisymmetric contributions. A satisfying agreement between the two methods is achieved within the measurement uncertainty. Additionally, the large difference of the resistances between the MTJ with MAO and MgO barrier is also found in the slope of the symmetric contributions. After rounding to two significant digits, no difference remains in the α parameter for the parallel and antiparallel states of both MTJs.

Sample [state]	Antisymmetric slope (k Ω)	R from TMR (k Ω)	Symmetric slope (V/A ²)	α (K/A ²)
MAO [p]	2.6 ± 0.1	2.7 ± 0.1	$-6.3 \cdot 10^5 \pm 10^4$	$5.4 \cdot 10^{14}$
MAO [ap]	3.4 ± 0.1	3.6 ± 0.1	$-1.8 \cdot 10^5 \pm 10^4$	$5.4 \cdot 10^{14}$
MgO [p]	68 ± 2	66 ± 2	$2.9 \cdot 10^8 \pm 2.5 \cdot 10^8$	$1.2 \cdot 10^{15}$
MgO [ap]	223 ± 10	195 ± 20	$-8.6 \cdot 10^9 \pm 3 \cdot 10^8$	$1.2 \cdot 10^{15}$

Figures 4(a) and 4(b) depict the antisymmetric contributions of the V/I characteristics for both MAO and MgO barrier MTJs. They show a linear increase which diminishes for high currents and both magnetization alignments. This deviation from a purely linear behavior is caused by the changing resistance of the junction due to the induced base temperature changes with increased currents. Thus, additional terms of odd power are present in the I/V data and picked up by the asymmetry evaluation. The deviation from the linear behavior is more prominent in the antiparallel case. In case of the symmetric parts we find, except for the MgO MTJ in the parallel state, negative, nonlinear contributions [cf. Figs. 4(c) and 4(d)]. Therefore, only the first part of the curves is fitted to extract the Seebeck coefficients via the method of the intrinsic TMS [cf. Figs. 4(e) and 4(f)].

In addition to and to follow the method proposed by Zhang, Teixeira *et al.* [11,12], we need to calculate $\sum_j \eta_j R_j R_{\kappa_j}$, where η_j is the thermal asymmetric parameter obtained via $\eta_j = \frac{\nabla T \kappa_j \sigma_j}{J^2 d_j^2}$, R_j is the resistance, and $R_{\kappa_j} = \frac{d}{\kappa_j A}$ is the heat resistance. ∇T refers to the temperature gradient across the barrier, κ to the thermal conductivity, A to the area of the junction, σ to the electric conductivity, and J to the current density given by $J = I/A$ (I , current; A , area). The index j identifies each individual layer. Since the stacks show resistances of several k Ω originating mostly from the MAO and MgO barrier, we neglect the influences of other layers and assume $\sum_j \eta_j R_j R_{\kappa_j} = \eta_{\text{MAO/MgO}} R_{\text{MAO/MgO}} R_{\kappa_{\text{MAO/MgO}}} = \alpha$ with $R_{\text{MAO/MgO}} = R$ the resistance of the stack. From the TMR measurements we obtain $R_{\text{ap}} (R_{\text{p}}) = 3.6$ k Ω (2.7 k Ω) for the MAO barrier and $R_{\text{ap}} (R_{\text{p}}) = 195$ k Ω (66 k Ω) for the MgO barrier.

With these values and the thickness of the barrier, the area of the junction and the thermal conductivity of MAO and MgO mentioned in Sec. III B, $\sigma_{\text{MAO/MgO}}$ and $R_{\kappa_{\text{MAO/MgO}}}$ are calculated. Additionally, we take a mean current resulting from the I/V curves of 50 μA for the MAO barrier and 1 μA for the MgO barrier and, furthermore, assume a temperature gradient of 25 $\frac{\text{mK}}{\text{nm}}$ for MAO and 1 $\frac{\text{mK}}{\text{nm}}$ for MgO (please note Teixeira *et al.* used a temperature gradient of 75–195 $\frac{\text{mK}}{\text{nm}}$ generated by a current of 0.4 mA). Thus, we get values for the symmetric slope as well as for the α parameter, which are summarized in Table II and which allow one to directly compare the results of the intrinsic TMS with the results of the laser-induced TMS (cf. Table III).

TABLE III. Results of the intrinsic TMS evaluation. The results of the laser-induced TMS are given as a direct comparison. The error ranges of the intrinsic Seebeck coefficients result from the inaccuracy of the linear fits to the symmetric contributions.

	$S_p \left(\frac{\mu V}{K} \right)$	$S_{ap} \left(\frac{\mu V}{K} \right)$	TMS (%)
MAO MTJ			
Intrinsic	$-1.2 \cdot 10^{-3} \pm 10^{-4}$	$-3 \cdot 10^{-4} \pm 10^{-4}$	-75 ± 10
Laser	-150 ± 140	-160 ± 140	3.3 ± 0.2
MgO MTJ			
Intrinsic	0.3 ± 0.2	-7.5 ± 0.2	104 ± 3
Laser	-1010 ± 20	-1320 ± 20	23 ± 3

Clearly, the obtained values for the intrinsic Seebeck coefficients do not match with the results of the laser-induced TMS, neither for the MAO nor for the MgO barrier. Furthermore, the intrinsic TMS ratios do not coincide with the results of the laser-induced TMS ratios. Please note that changing the aforementioned assumptions only results in different values for the intrinsic Seebeck coefficients. However, the sign of the intrinsic TMS ratio is dominated by the slope of the symmetric contribution. Accordingly, in our case, S_p will always be larger than S_{ap} for the MTJ with MAO barrier, thus, resulting in a negative TMS ratio. In addition, the Seebeck coefficients obtained from the intrinsic method of the MTJ with MgO barrier show a different sign that is not observed with the laser-induced TMS. These findings directly contradict the results of the laser-induced TMS. Therefore, we are not able to identify any reasonable contribution of the intrinsic TMS which would be comparable to the more clear laser-induced TMS.

However, the Brinkman model offers an alternative way to explain the occurring antisymmetric and symmetric contributions in case of the MAO MTJ. We focus on the parallel case where a good agreement between data and model is obtained (cf. Fig. 3). Now, the symmetry evaluation is performed with simulated I/V curves based on the Brinkman model with different values for the barrier asymmetry $\Delta\phi$. Figure 5 shows the results of the symmetry evaluation of the original data, its corresponding Brinkman fit, a reversed barrier asymmetry, and a vanishing barrier asymmetry. Obviously, the barrier asymmetry plays a vital role for the symmetric contribution of the V/I curve.

Please note that a symmetric barrier shows no symmetric contribution in the VI curve, making the identification of an intrinsic TMS impossible. In contrast, the asymmetric contributions are the same for different values of the barrier asymmetry. Thus, the symmetric contribution of the V/I curve in the parallel case is very well described by the Brinkman model even without any assumptions of temperature differences.

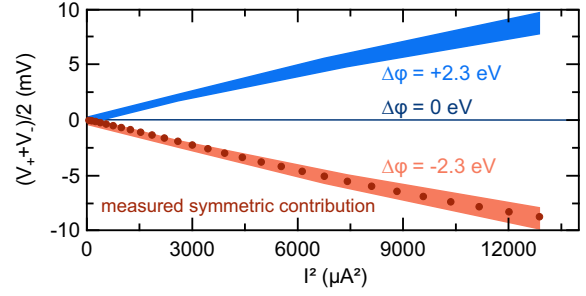


FIG. 5. Original symmetric contribution of the MAO MTJ in the parallel case (dark red), corresponding Brinkman fit ($\Delta\phi = -2.3$ eV) (light red), simulated barrier asymmetry of $\Delta\phi = +2.3$ eV (light blue), and $\Delta\phi = 0$ eV (dark blue). For the sake of clarity, only one in 10 data points of the original data is shown. The colored areas represent the typical error range of the Brinkman model of 10%.

IV. CONCLUSION

We have investigated the TMS effect of $\text{Co}_{40}\text{Fe}_{40}\text{B}_{20}/\text{MAO}$ and $\text{Co}_{25}\text{Fe}_{55}\text{B}_{20}/\text{MgO}$ MTJs with laser-induced heating. In case of a barrier consisting of MAO, the TMS ratio of about 3% as well as the Seebeck coefficients are consistent with findings of other groups who used similar materials. The results of the MgO-based MTJs show large TMR ratios of up to 200% and TMS ratios of around 20%. This TMS ratio is directly related to the different CoFeB composition. In addition, we have studied the symmetry of I/V characteristics within the framework of the intrinsic TMS proposed by Zhang, Teixeira *et al.* Both, antisymmetric and symmetric contributions, revealed deviations from the expected linear behavior suggested by the model of the intrinsic TMS. Our findings show that it is not possible to consistently compare the results of laser-induced and intrinsic TMS. Nevertheless, the Brinkman model offers an alternative way to explain the occurring features if no Δ_1 symmetry filter effect is present, giving a consistent explanation for the observed symmetric contribution. In particular, we found that the symmetric I/V contribution in the parallel case is solely influenced by the barrier asymmetry. Thus, we conclude that the symmetry analysis is not suitable to unambiguously identify an intrinsic TMS.

ACKNOWLEDGMENTS

The authors gratefully acknowledge financial support from the Deutsche Forschungsgemeinschaft (DFG) within the priority program Spin Caloric Transport (SPP 1538). They further thank Christian Heiliger from the University of Gießen for theoretical input.

- [1] G. E. Bauer, E. Saitoh, and B. J. van Wees, *Nature Mater.* **11**, 391 (2012).
 [2] R. Venkatasubramanian, E. Siivola, T. Colpitts, and B. O'Quinn, *Nature* (London) **413**, 597 (2001).

- [3] M. Walter, J. Walowski, V. Zbarsky, M. Münzenberg, M. Schäfers, D. Ebke, G. Reiss, A. Thomas, P. Peretzki, M. Seibt, J. S. Moodera, M. Czerner, M. Bachmann, and C. Heiliger, *Nature Mater.* **10**, 742 (2011).

- [4] N. Liebing, S. Serrano-Guisan, K. Rott, G. Reiss, J. Langer, B. Ocker, and H. W. Schumacher, *Phys. Rev. Lett.* **107**, 177201 (2011).
- [5] M. Czerner, M. Bachmann, and C. Heiliger, *Phys. Rev. B* **83**, 132405 (2011).
- [6] J. Shan, F. K. Dejene, J. C. Leutenantsmeyer, J. Flipse, M. Münzenberg, and B. J. van Wees, *Phys. Rev. B* **92**, 020414(R) (2015).
- [7] N. Liebing, S. Serrano-Guisan, K. Rott, G. Reiss, J. Langer, B. Ocker, and H. W. Schumacher, *J. Appl. Phys.* **111**, 07C520 (2012).
- [8] N. Liebing, S. Serrano-Guisan, P. Krzysteczko, K. Rott, G. Reiss, J. Langer, B. Ocker, and H. W. Schumacher, *Appl. Phys. Lett.* **102**, 242413 (2013).
- [9] A. Boehnke, M. Walter, N. Roschwesky, T. Eggebrecht, V. Drewello, K. Rott, M. Münzenberg, A. Thomas, and G. Reiss, *Rev. Sci. Instrum.* **84**, 063905 (2013).
- [10] A. Boehnke, M. Milnikel, M. von der Ehe, C. Franz, V. Zbarsky, M. Czerner, K. Rott, A. Thomas, C. Heiliger, G. Reiss, and M. Münzenberg, *Sci. Rep.* **5**, 8945 (2015).
- [11] Z. H. Zhang, Y. S. Gui, L. Fu, X. L. Fan, J. W. Cao, D. S. Xue, P. P. Freitas, D. Houssameddine, S. Hemour, K. Wu, and C.-M. Hu, *Phys. Rev. Lett.* **109**, 037206 (2012).
- [12] J. M. Teixeira, J. D. Costa, J. Ventura, M. P. Fernandez-Garcia, J. Azevedo, J. P. Araujo, J. B. Sousa, P. Wisnikowski, S. Cardoso, and P. P. Freitas, *Appl. Phys. Lett.* **102**, 212413 (2013).
- [13] V. Drewello, M. Schäfers, O. Schebaum, A. A. Khan, J. Münchenberger, J. Schmalhorst, G. Reiss, and A. Thomas, *Phys. Rev. B* **79**, 174417 (2009).
- [14] J. Zhang, X. G. Zhang, and X. F. Han, *Appl. Phys. Lett.* **100**, 222401 (2012).
- [15] Y. Miura, S. Muramoto, K. Abe, and M. Shirai, *Phys. Rev. B* **86**, 024426 (2012).
- [16] B. S. Tao, H. X. Yang, Y. L. Zuo, X. Devaux, G. Lengaigne, M. Hehn, D. Lacour, S. Andrieu, M. Chshiev, T. Hauet, F. Montaigne, S. Mangin, X. F. Han, and Y. Lu, *Phys. Rev. Lett.* **115**, 157204 (2015).
- [17] H. Sukegawa, H. Xiu, T. Ohkubo, T. Furubayashi, T. Niizeki, W. Wang, S. Kasai, S. Mitani, K. Inomata, and K. Hono, *Appl. Phys. Lett.* **96**, 212505 (2010).
- [18] H. Sukegawa, S. Mitani, T. Ohkubo, K. Inomata, and K. Hono, *Appl. Phys. Lett.* **103**, 142409 (2013).
- [19] B. Tao, D. Li, H. Liu, H. Wei, J.-F. Feng, S. Wang, and X. Han, *IEEE Trans. Magn.* **50**, 4401004 (2014).
- [20] E. A. Stern, *Phys. Rev.* **157**, 544 (1967).
- [21] C. Heiliger, C. Franz, and M. Czerner, *Phys. Rev. B* **87**, 224412 (2013).
- [22] S.-M. Lee, D. G. Cahill, and T. H. Allen, *Phys. Rev. B* **52**, 253 (1995).
- [23] J. Zhang, M. Bachman, M. Czerner, and C. Heiliger, *Phys. Rev. Lett.* **115**, 037203 (2015).
- [24] Z. L. Wu, M. Reichling, X.-Q. Hu, K. Balasubramanian, and K. H. Guenther, *Appl. Opt.* **32**, 5660 (1993).
- [25] K. T. Jacob, C. Shekhar, and Y. Waseda, *J. Chem. Thermodynamics* **41**, 748 (2009).
- [26] C. Papusoi, R. Sousa, J. Herault, I. L. Prejbanu, and B. Dieny, *New J. Phys.* **10**, 103006 (2008).
- [27] G. A. Slack, *Phys. Rev.* **126**, 427 (1962).
- [28] St. Burghartz and B. Schulz, *J. Nucl. Mater.* **212-215**, 1065 (1994).
- [29] S. Klemme and M. Ahrens, *Phys. Chem. Miner.* **34**, 59 (2006).
- [30] W. F. Brinkman, R. C. Dynes, and J. M. Rowell, *J. Appl. Phys.* **41**, 1915 (1970).
- [31] J. G. Simmons, *J. Appl. Phys.* **34**, 1793 (1963).

5.5 Enhancement of thermovoltage and tunnel magneto-Seebeck effect in CoFeB based magnetic tunnel junctions by variation of the MgAl_2O_4 and MgO barrier thickness (Thesis article V)

PHYSICAL REVIEW B **96**, 214435 (2017)**Enhancement of thermovoltage and tunnel magneto-Seebeck effect in CoFeB-based magnetic tunnel junctions by variation of the MgAl₂O₄ and MgO barrier thickness**Torsten Huebner,^{1,*} Ulrike Martens,² Jakob Walowski,² Alexander Boehnke,¹ Jan Krieft,¹ Christian Heiliger,³ Andy Thomas,⁴ Günter Reiss,¹ Timo Kuschel,^{1,5} and Markus Münzenberg²¹*Center for Spinelectronic Materials and Devices, Department of Physics, Bielefeld University, Universitätsstraße 25, 33615 Bielefeld, Germany*²*Institut für Physik, Greifswald University, Felix-Hausdorff-Strasse 6, 17489 Greifswald, Germany*³*Institut für Theoretische Physik, Justus Liebig University Giessen, Heinrich-Buff-Ring 16, 35392 Giessen, Germany*⁴*Leibniz Institute for Solid State and Materials Research Dresden (IFW Dresden), Institute for Metallic Materials, Helmholtzstrasse 20, 01069 Dresden, Germany*⁵*Physics of Nanodevices, Zernike Institute for Advanced Materials, University of Groningen, Nijenborgh 4, 9747 AG Groningen, The Netherlands*

(Received 22 June 2017; revised manuscript received 16 October 2017; published 26 December 2017)

We investigate the influence of the barrier thickness of Co₄₀Fe₄₀B₂₀-based magnetic tunnel junctions (MTJs) on the laser-induced tunnel magneto-Seebeck (TMS) effect. Varying the barrier thickness from 1 to 3 nm, we find a distinct maximum in the TMS effect for a 2.6-nm barrier thickness. This maximum is measured independently for two barrier materials, namely, MgAl₂O₄ (MAO) and MgO. Additionally, samples with a MAO barrier exhibit a high thermovoltage of more than 350 μ V in comparison to 90 μ V for the MTJs with a MgO barrier when heated with the maximum laser power of 150 mW. Our results allow for the fabrication of improved stacks when dealing with temperature differences across MTJs for future applications in spin caloritronics, the emerging research field that combines spintronics and thermoelectrics.

DOI: [10.1103/PhysRevB.96.214435](https://doi.org/10.1103/PhysRevB.96.214435)**I. INTRODUCTION**

In recent years, the combination of the spintronic *magnetic tunnel junction* (MTJ) and a temperature gradient were studied intensively [1–17]. Since these experiments combine spin, charge, and heat-driven currents, they are prominent examples for the emerging topic of spin caloritronics [18], which might provide a possibility to utilize the otherwise wasted heat in today's memory and sensing applications. To achieve this goal, an extensive knowledge about the involved thermal processes in nanostructures is key.

At first, the *tunnel magneto-Seebeck* (TMS) effect was predicted [1] and measured with two different techniques, laser induced [2] and extrinsically heated with a nanostructured heater line [3]. Later on, the experimentally even more challenging *tunnel magneto-Peltier effect*, which is reciprocal to the TMS effect, was observed as well [7]. Subsequent studies focused on the increase in effect sizes, film quality, and the overcoming of experimental challenges.

In particular, a giant TMS ratio of -3000% was found when applying an additional bias voltage across the MTJ [8], and a significant improvement of the TMS ratio was obtained with the usage of half-metallic electrodes from ferromagnetic Heusler compounds, such as Co₂FeAl or Co₂FeSi [9], and parasitic effects originating from semiconducting substrates were clarified [10]. Additionally, in a preceding publication [11], we compared the laser-induced TMS with the method of the intrinsic TMS, which uses a symmetry analysis of the tunneling current with respect to the applied voltage. The model of Brinkman *et al.* [19] offered an alternative way to explain the symmetric contribution previously associated with

the intrinsic TMS. Thus, we concluded that it is not possible to explicitly observe an intrinsic TMS.

Up to now, theoretical works focused only on six or ten atomic layers, respectively, of barrier thickness and on the electrode/barrier interface, which hugely influences not only the tunnel magnetoresistance (TMR), but also the TMS effect [20,21]. Fe-Co/MgO is used often as a model system within these studies due to the large computational effort that is necessary, e.g., to model the TMS for materials with a more complex crystal structure. Furthermore, Fe-Co/MgO exhibits coherent tunneling of the electrons via Δ_1 states and, thus, ensures high-TMR ratios needed for applications. A combination of an additionally applied temperature gradient and the continuing improvement of Seebeck voltages and TMS ratios will support the development of green energy-efficient waste heat recovery devices. In addition, the in-depth understanding of connections among spin, charge, and heat currents in MTJs will pave the way towards related spin caloritronic effects, such as the thermal spin-transfer torque [22–26].

Previous TMS measurements concentrated on the established MTJ system of Co-Fe(CoFeB)/MgO with a standard barrier thickness of around 2 nm. Therefore, we investigate the system of CoFeB and MgAl₂O₄ (MAO) with different barrier thicknesses and junction sizes in order to maximize the TMS effect. Theoretically, MAO exhibits an advantageous lattice mismatch (1%) with standard ferromagnetic electrodes, such as Fe, CoFe, or CoFeB when compared to MgO [(3–5)%] [27]. As a barrier, MAO also enables coherent tunneling via the Δ_1 symmetry filter effect [28]. So far, experimental results of the TMR effect in MAO MTJs fall short in comparison to MgO MTJs [29–31], but, for example, magnetization switching by *spin-transfer torque* has been demonstrated [32]. Additionally, by growing MAO barriers via *molecular*

*thuebner@physik.uni-bielefeld.de

TABLE I. Overview of different nominal barrier thicknesses of each series.

Series	Nominal barrier thickness (nm)
I (MAO)	1.0 1.4 1.6 1.8 ^a 2.0 ^a 2.2 2.6 3.0
II (MgO)	1.2 1.5 1.8 1.9 2.0 2.3 2.6 2.9

^aSamples were prepared independently of the rest of the series.

beam epitaxy, MgAl₂O_x double-barrier MTJs exhibit almost no lattice mismatch between electrode and barrier showing pronounced resonant tunneling features in quantum well structures [33]. As a direct comparison with recent experiments and theoretical predictions, we compare our results for MAO barriers with CoFeB/MgO MTJs.

This paper is organized as follows: Sec. II starts with the sample deposition and preparation, followed by Sec. III, which is split into three subsections. Here, Sec. III A deals with the results of the TMR and TMS measurements, Sec. III B deals with the results of the I/V curves, and Sec. III C deals with the thermovoltage and COMSOL evaluation. Section IV concludes this paper.

II. SAMPLE DEPOSITION AND PREPARATION

We prepared different sample series in order to give a detailed overview concerning reproducibility and comparability. The MAO and MgO MTJs are sputtered in a Leybold Vakuum GmbH CLAB 600 cluster tool at a base pressure of less than 5×10^{-7} mbar. This system allows the deposition of several samples without exposing them to ambient conditions in between sputtering processes. The whole stack of all series is composed of a bottom contact of Ta 10/Ru 30/Ta 5/Ru 5, a tunnel junction of Mn₈₃Ir₁₇ 10/Co₄₀Fe₄₀B₂₀ 2.5/barrier/Co₄₀Fe₄₀B₂₀ 2.5, and a top contact of Ta 5/Ru 30/Ta 5/Au 60 (the numbers are nominal thicknesses in nanometers). The resulting sample series are summarized in Table I. Two samples of series I are prepared independently of the rest of the series.

To achieve the exchange biasing of the ferromagnetic electrode by MnIr, the stacks are postannealed at 350 °C for 1 h, followed by cooling in a magnetic field of 0.7 T. *Electron-beam lithography* and *ion-beam etching* are used to pattern elliptical junctions of 0.5π , 2π , and $6\pi \mu\text{m}^2$ with the major axis being twice as large as the minor axis. Ta₂O₅ (120 nm) is used as insulating material between individual MTJs, and Au bond pads serve as electrical contacts and heat absorbers.

In order to measure the TMR effect and I/V characteristics, a *Keithley 2400 Sourcemeter* is used. For the generation of the thermovoltage, a modulated diode laser with a wavelength of 637 nm is focused via a confocal microscope onto the MTJ and generates a heat difference across the MTJ since the substrate of the sample acts as a heat sink. A frequency of 177 Hz, serving as a reference for the detection of the thermovoltage via a lock-in amplifier, and the maximum laser power of 150 mW is used. The size of the laser spot is freely adjustable by moving the sample in the direction of the beam, which has been studied intensively by Martens *et al.* [12]. Furthermore, a thorough description of the setup to measure laser-induced

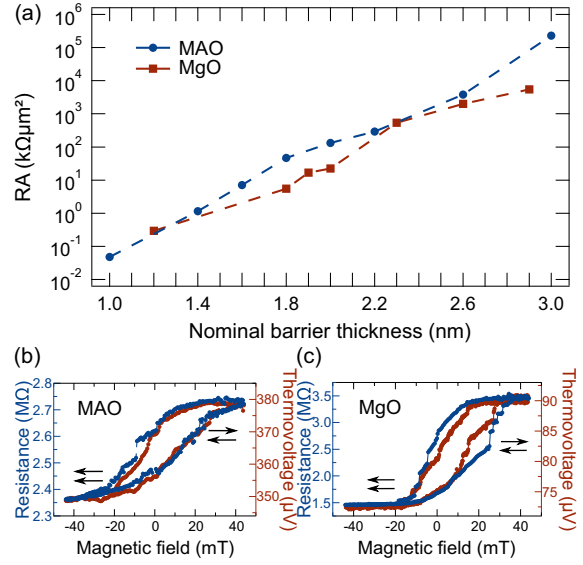


FIG. 1. (a) Averaged RA products for the MAO MTJs (the blue circles) and the MgO MTJs (the red squares) in the parallel state. (b) and (c) Exemplary minor loops with the highest switching ratios of the samples with MAO and MgO barriers, respectively. Both loops are measured at the smallest junction area of $0.5\pi \mu\text{m}^2$.

thermovoltages and TMS effects in MTJs is given by Boehnke *et al.* [10].

III. RESULTS

A. TMR and TMS results

Figure 1(a) shows the resistance area (RA) products of both series depending on the nominal barrier thicknesses in the parallel magnetization alignment. Please note that the error bars of the RA product are too small to be seen, indicating an overall homogenous sample quality of all series. As expected, the RA product increases exponentially with increasing nominal barrier thickness. In addition, the RA products of the independently prepared samples within series I fit very well together. Thus, the independent deposition of the samples of series I allows a direct comparison of the MTJs.

Since the RA product is governed mostly by the barrier, it is noteworthy that the different barrier materials lead to comparable RA values between the series. Two minor loops of the samples with the highest TMS ratios are shown in Figs. 1(b) and 1(c). Here, the nominal barrier thickness is 2.6 nm, and the junction size is $0.5\pi \mu\text{m}^2$ in both cases. Despite the high resistance resulting from the thick barrier of 2.6 nm, both MTJs show parallel and antiparallel states with the same switching behavior for TMS and TMR measurements. The extracted TMS (TMR) ratio amounts to 8% (18%) for MAO, whereas it is 28% (130%) for MgO. The sample with the MAO barrier shows a very high thermovoltage of around $375 \mu\text{V}$ in contrast to around $80 \mu\text{V}$ in the case of a MgO barrier when using a laser power of 150 mW. In addition, the minor loops presented in Figs. 1(b) and 1(c) exhibit a different squareness in contrast to samples with thinner barriers (cf. minor loops with a barrier

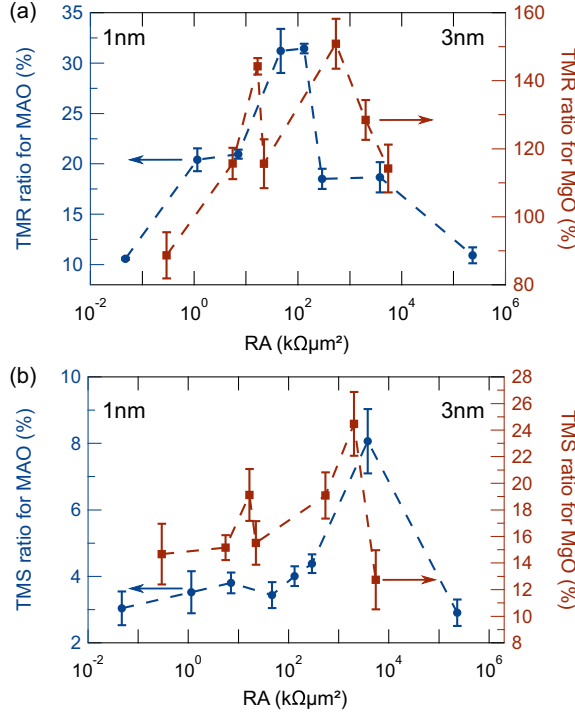


FIG. 2. (a) Averaged TMR ratios of all measured elements with resulting error bars versus RA: MAO (the left axis, blue circles) and MgO (the right axis, red squares). (b) Averaged TMS ratios of all measured elements with resulting error bars versus RA: MAO (the left axis, blue circles) and MgO (the right axis, red squares).

of 1.8-nm MAO in Ref. [11]). We attribute this difference to a change in the interlayer exchange coupling in line with results presented in Ref. [34].

Figure 2(a) summarizes the results of the TMR measurements of series I and II depending on the RA product. For each barrier thickness several elements as well as different element areas are measured and averaged. First, both barrier materials show TMR maximum values (MAO: 30%, MgO: 150%) around a nominal barrier thickness of 2 nm ($\text{RA}_{\text{MAO}} \approx 100 \text{ k}\Omega\mu\text{m}^2$, $\text{RA}_{\text{MgO}} \approx 1000 \text{ k}\Omega\mu\text{m}^2$). Second, the series with the MgO barrier exhibits a second peak of the TMR for a barrier thickness of 1.9 nm ($\text{RA} = 10 \text{ k}\Omega\mu\text{m}^2$). This peak might be related directly to the slightly increased RA product [cf. Fig. 1(a)] in this region.

The dependence of the TMS ratio on the barrier thickness of both series is shown in Fig. 2(b). Thin barriers of MAO exhibit a gradual increase in TMS ratios from 3% to 4%, whereas a distinct maximum is observed for a nominal barrier thickness of 2.6 nm. Here, the TMS ratio doubles to 8%. Furthermore, the TMS ratio of the MTJs with the MgO barrier shows a similar behavior. It rises from 14% to 19% in the case of thin barriers and shoots up to almost 28% for a nominal barrier thickness of 2.6 nm. In between, a local maximum is observable that directly corresponds to the position of the local TMR maximum. The errors of the TMR and the TMS ratios result from averaging over all measured elements.

Theoretically, since the TMS ratio depends on the asymmetry of the transmission function around the Fermi energy and the TMR ratio depends on the absolute number of states, a direct correlation between TMR and TMS ratios is not expected [1,21,35]. This statement is supported by the first measurements of Co_2FeSi - and Co_2FeAl -based MTJs and corresponding theoretical considerations by Boehnke *et al.* [9]. For both barrier materials, the TMS peak is located around the same value of RA of some $10^3 \text{ k}\Omega\mu\text{m}^2$ s, which corresponds to a nominal barrier thickness of 2.6 nm. Also, the TMS ratios of the samples prepared separately correspond well to the results of the rest of series I. Thus, we expect a similar asymmetry of the transmission function of these samples.

In contrast to our experiments, theoretical calculations predict an increasing TMS ratio when going down from ten monolayers (MLs) (2%) to six monolayers (10%) of MgO [21] (1 ML $\approx 2.1 \text{ \AA}$). A reason for these opposite results might be a different interface structure of the electrode and the barrier, which is assumed to be ordered perfectly in the calculations. Czerner and Heiliger [20] find the TMS to be very sensitive to the interface termination of the magnetic material and the barrier.

B. I/V measurements

Figures 3(a) and 3(b) show the dJ/dV (recalculated from I/V measurements) curves that are measured at the same elements as in Figs. 1(b) and 1(c). Although the curves look similar in the case of a MTJ with a MAO barrier, they look very different in the case of the MTJ with the MgO barrier. This difference is due to the coherent tunneling of MgO-based MTJs: The parallel curve is almost linear, whereas the antiparallel curve exhibits a pronounced kink around a bias voltage of 0 V. Since the MAO MTJs exhibit a rather low TMR, no Δ_1 symmetry filter effect and, thus, no coherent tunneling are present in the MTJs with the MAO barrier.

In order to further analyze the MTJs with the MAO barrier, we use the model of Brinkman *et al.* [19], which allows us to calculate the barrier height ϕ , the barrier asymmetry $\Delta\phi$, and the barrier thickness d_B from the I/V measurements. A theoretical description of this model can be found in Ref. [19], whereas the experimental details are described in Ref. [11]. With this model, we are able to quantitatively compare the samples with different MAO barrier thicknesses. One drawback of the Brinkman model is its limitation to MTJ systems that do not show coherent tunneling. In addition, it is not able to explain features resulting from density of states related effects, such as half-metallic ferromagnetism. Thus, it is not possible to extract physically reasonable barrier parameters of the MTJs with a MgO barrier because of the coherent tunneling resulting from the Δ_1 symmetry filter effect.

Figure 3(c) depicts the relative deviation of the calculated Brinkman barrier thickness (d_B) from the nominal barrier thickness (d_N). With respect to the error range of the Brinkman model of 10% (as stated by Brinkman *et al.* [19] in their original work, marked by the gray area), most of the elements are very close to the nominal barrier thickness. Except for the sample with a MAO barrier thickness of 1.4 nm, this deviation does not exceed 15%. An additional requirement of the Brinkman model to be applicable is $d_N > 1.0 \text{ nm}$. Apparently,

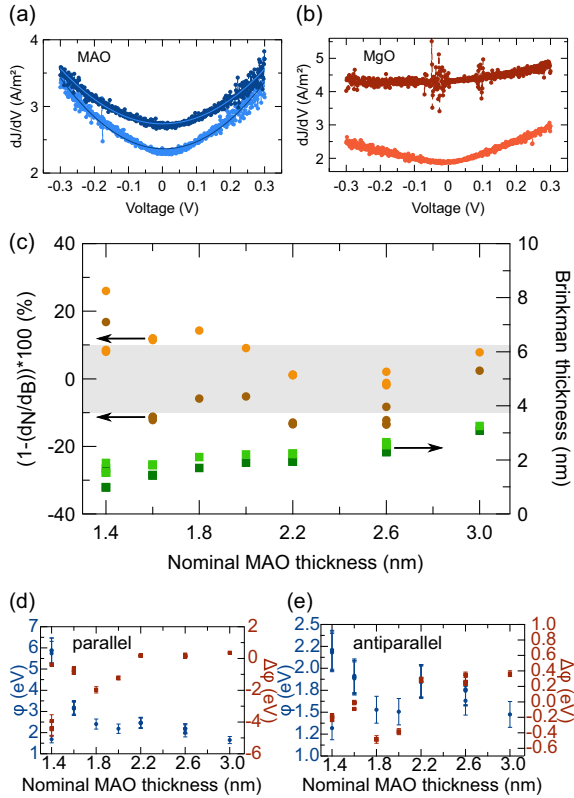


FIG. 3. (a) dJ/dV data of the MTJ with a MAO barrier (2.6 nm, $0.5\pi \mu\text{m}^2$) with the Brinkman fits that are used to extract barrier parameters (dark: parallel, light: antiparallel). (b) dJ/dV data of the MTJ with a MgO barrier (2.6 nm, $0.5\pi \mu\text{m}^2$) (dark: parallel, light: antiparallel). (c) Relative deviation of the nominal barrier thickness (d_N) and the calculated Brinkman barrier thickness (d_B). Dark (light) orange represents the results of the parallel (antiparallel) state. Please note that several element sizes are depicted that are partially overlapping in order to demonstrate the consistency of the method. The green squares are the extracted Brinkman thicknesses for each nominal MAO barrier thickness (dark: parallel, light: antiparallel). The gray area represents the typical error range of the Brinkman model of 10%. (d) and (e) Barrier height ϕ (blue circles) and asymmetry $\Delta\phi$ (red squares) values for all measured elements and barrier thicknesses in the (d) parallel and (e) antiparallel states.

the nominal barrier thickness of 1.4 nm is too close to this limit, resulting in huge variations of the Brinkman barrier parameters. Since all other Brinkman barrier thicknesses are very close to the nominal thickness, and the RA values of the MAO- and MgO-based MTJs are also very close, we assume that the nominal barrier thicknesses of both series are close to the real thickness, which is important for future theoretical and experimental works.

In general, the calculated Brinkman barrier thicknesses depicted by the green squares in Fig. 3(c) are larger in the antiparallel (light) than in the parallel state (dark). For the barrier height and the barrier asymmetry in Figs. 3(d) and 3(e), we find a reversed behavior. Here, the parallel values [Fig. 3(d)]

are generally larger than the antiparallel ones [Fig. 3(e)]. Again, the results of the sample with a barrier thickness of 1.4-nm MAO show a huge variation, whereas the results of all other samples are very consistent, even between different junction sizes. Excluding the results of the sample with a MAO barrier of 1.4 nm, the barrier height decreases from 3 to 1.7 eV (1.9 to 1.5 eV) in the parallel (antiparallel) state.

Additionally, the barrier asymmetry increases from -1 to 0.5 eV in the parallel state, whereas it increases from -0.1 to 0.4 eV in the antiparallel state. Overall, the calculated values of the samples that have been prepared independently from the rest of the series (1.8 and 2.0 nm) show almost no deviation from the general trend in the case of the barrier height. However, the values of the barrier asymmetry are different for the independently prepared samples. A possible explanation for this difference might be the deposition process, which plays a vital role for the barrier asymmetry. Nevertheless, since the TMS ratios agree very well, the geometric barrier asymmetry seems to have no significant influence on the asymmetry of the transmission function.

C. Thermovoltages and Seebeck coefficients

In order to investigate the high thermovoltages of the sample with the MAO barrier, Fig. 4(a) depicts the thermovoltage depending on the MTJ area of the sample with a nominal MAO barrier thickness of 2.6 nm. Furthermore, the remaining thermovoltage after a dielectric breakdown of the junction is shown [see the inset of Fig. 4(a)]. With this measurement, it is possible to deduce the contribution of the intact tunneling barrier. The dielectric breakdown of the barrier is confirmed via an additional TMR measurement after applying 3 V to the junction. During the breakdown, the resistance changes from the $M\Omega$ to the Ω range. After the breakdown, both the TMR and the TMS do not show any effect of magnetization switching [compare the inset of Fig. 4(a) to the minor loop shown in Fig. 1(b)].

Clearly, around 70% of the absolute thermovoltage is caused by the intact tunneling barrier in the case of small MTJ areas. This contribution decreases to 32% for larger MTJ areas. Since the laser has a spot size of $11 \mu\text{m}^2$ when focused onto the MTJ [12], one possible explanation for the decrease is the occurrence of nonhomogenous heating. Thus, additional lateral heat flows emerge, effectively lowering the temperature difference across the barrier and, ultimately, the measured thermovoltage. The regime of homogenous heating is indicated by the gray shaded area in Fig. 4(a), which represents the laser spot size. In future experiments, intermediate MTJ sizes could offer a more detailed insight into the processes of nonhomogenous heating and in-plane temperature differences. With additional in-plane temperature differences, Nernst effects and additional magnetothermopower contributions become possible, which are not taken into account in the current TMS experiments.

Figure 4(b) sums up the absolute thermovoltages in dependence of the RA product. Here, a laser power of 150 mW is applied to MTJs with an area of $6\pi \mu\text{m}^2$. In the case of MAO, a drop of about $20 \mu\text{V}$ in the absolute thermovoltage is measured for barrier thicknesses of 1.8 and 2.0 nm, which correspond to the samples that were prepared separately from the rest of the series. Since the RA products, the barrier heights and the

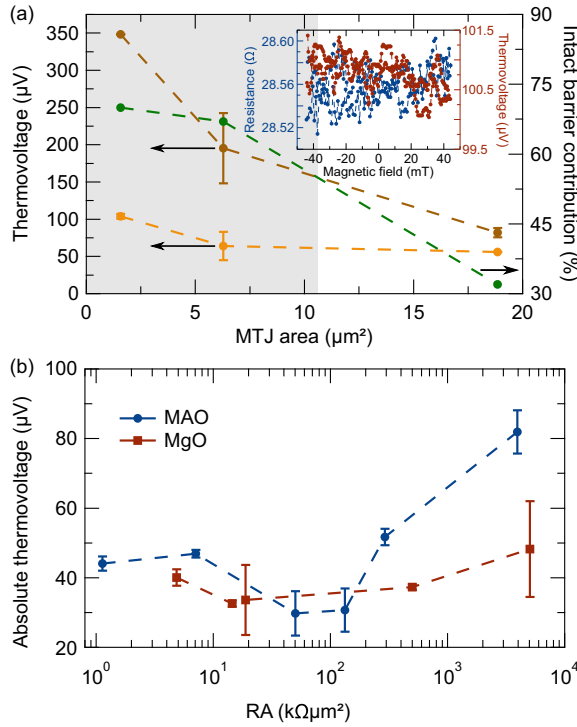


FIG. 4. (a) Absolute thermovoltage (dark orange) and thermovoltage after dielectric breakdown (light orange) depending on the MTJ area of the sample with a nominal barrier thickness of 2.6-nm MAO. The inset shows TMR and TMS measurements after applying 3 V to the junction and confirms the dielectric breakdown. Also, the contribution of the intact barrier to the absolute thermovoltage is shown (green) as well as the regime of homogenous heating (gray shaded area). (b) Measured absolute thermovoltages with a laser power of 150 mW of the MTJs with an area of $6\pi \mu\text{m}^2$ depending on the RA product of all series.

Brinkman barrier thicknesses of series I are in good agreement with each other, the only difference is the barrier asymmetry. All other MTJs with MAO barriers show a thermovoltage that is consistently larger by a factor of up to 2 in comparison with the MTJs with MgO barriers.

In general, an increasing barrier thickness results in an increased temperature difference and, ultimately, in an increased measured thermovoltage. The difference in the MTJs with MAO barrier thicknesses of 1.8 and 2.0 nm in comparison to the rest of the series is explainable by the addition of an automated sample stage controller. Reference [12] found that a difference in the z position of $1 \mu\text{m}$ can influence the measured thermovoltage by as much as 20% (indicated by the larger error bars of the samples with 1.8 and 2 nm of MAO). Martens *et al.* [12] also describe the automated sample stage in more detail. Excluding the two samples with MAO barriers, the difference between series I and series II is explainable by the different thermal conductivities of thin MAO and MgO films resulting in different temperature differences across the barrier and, thus, different thermovoltages.

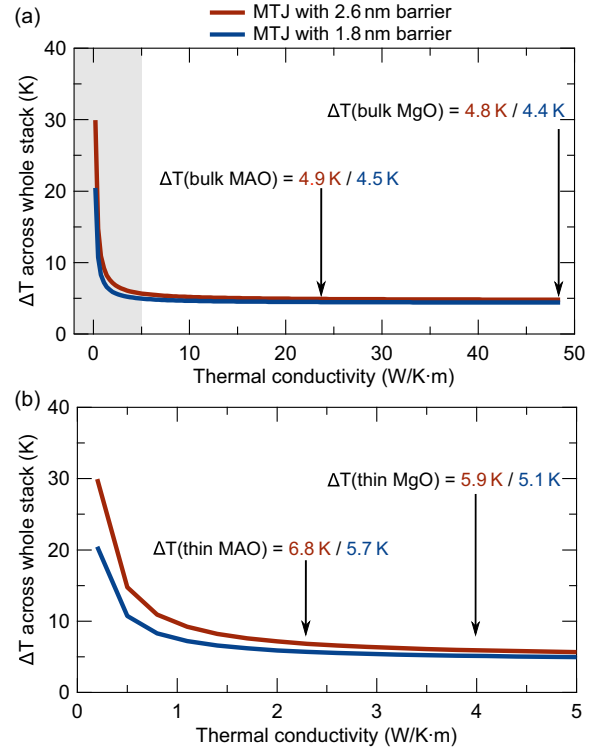


FIG. 5. (a) Dependence of the temperature difference across the whole stack on the thermal conductivity of the barrier including both bulk values of MAO and MgO for barrier thicknesses of 1.8 and 2.6 nm (laser power is 114 mW, deduced from calibration measurements). The thin-film regime is highlighted by the gray shaded area. (b) The thin-film regime with both MAO and MgO values for the two barrier thicknesses.

Bulk MAO has a thermal conductivity of $23 \text{ W K}^{-1} \text{ m}^{-1}$ [36], whereas bulk MgO has a thermal conductivity of $48 \text{ W K}^{-1} \text{ m}^{-1}$ [37]. In Ref. [37] the thermal conductivity of thin MgO films also is determined experimentally to be $4 \text{ W K}^{-1} \text{ m}^{-1}$. Taking the same reduction factor for thin MAO films, resulting in a thermal conductivity of $2.3 \text{ W K}^{-1} \text{ m}^{-1}$, a COMSOL simulation offers insight into the actual temperature difference across the whole stack.

Figure 5(a) displays the result of this simulation for the interesting range of thermal conductivity and two barrier thicknesses. Accordingly, the thin-film regime is shown in Fig. 5(b). Since the area of the MTJs ($1.6 \mu\text{m}^2$) is smaller than the area of the focused laser beam ($11 \mu\text{m}^2$), the MTJs are heated homogeneously. The temperature differences become very large in comparison to the values of preceding publications [2] (here, the laser spot area was usually around $240 \mu\text{m}^2$) since most of the laser-beam energy is absorbed directly above the MTJ instead of a larger area of the Au bond pad. A systematic study of the influence of the laser spot size can be found in Ref. [12]. Of course, with the lack of actual measurements of the thermal conductivity of thin insulating films, COMSOL simulations offer only limited insight into the

actual thermal distribution inside a MTJ. Hence, there is an ongoing discussion about the actual thermal conductivity of thin insulating films [13,15,38].

With the simulated temperature differences, the Seebeck coefficients for the MAO and the MgO MTJs with the highest TMS ratios are calculated (via $TMS = \frac{S_p - S_{ap}}{\min(|S_p|, |S_{ap}|)}$) to be $S_p = -51$ and $S_{ap} = -56$ $\mu\text{V/K}$ for MAO and $S_p = -12$ and $S_{ap} = -15$ $\mu\text{V/K}$ for MgO, which is in good agreement with previous results [2,8–11].

IV. CONCLUSION

We have studied the dependence of the laser-induced TMS effect on the barrier thickness of MAO and MgO MTJs and found a distinct maximum of the TMS ratio in the case of thick barriers (nominal barrier thickness of 2.6 nm) for both materials. The TMS ratio increased from (3 to 4)% to 8% for MTJs with the MAO barriers, whereas the TMS ratio for MTJs with the MgO barrier increased from around 15% to 28%. We found no experimental evidence of enhanced interface effects, which could explain the predicted increase in the TMS effect in the case of thin barriers. The Brinkman model offered detailed insight into the barrier heights and asymmetries of the MTJs with MAO barriers. A changing barrier asymmetry did not influence the TMS ratio, and thus the asymmetry of the transmission function, which we attribute to the Brinkman barrier asymmetry being a geometric parameter, whereas the transmission function of the MTJ depends on the energy. In addition, the extracted Brinkman barrier thicknesses provided a convenient way to compare samples with different nominal barrier thicknesses.

Furthermore, we measured very high thermovoltages of more than 350 μV at the smallest MTJs of 0.5π μm^2 with a MAO barrier, in contrast to 90 μV for MTJs with barriers of MgO. This difference also is reflected in the dependence of the thermovoltage on the barrier thickness. Here, MAO barriers show a thermovoltage that is larger by a factor of 2 in comparison with MgO barriers. Additionally, the MTJ with the MAO barrier exhibits Seebeck coefficients that are three times as large as for MTJs with the MgO barriers ($S_{p,MAO} = -59$ $\mu\text{V/K}$ versus $S_{p,MgO} = -18$ $\mu\text{V/K}$) taking the reduced thermal conductivity of thin insulating films into account. A thorough investigation of the contribution of the remaining thermovoltage to the absolute thermovoltage after dielectrically breaking the barriers revealed a significant deviation in case of nonhomogenous heating. Although 70% of the absolute thermovoltages are attributed to the barrier of small MTJs, this contribution decreases to $\approx 30\%$ in the case of MTJ areas larger than the laser spot size. Thus, the effect of nonhomogenous heating and potential lateral heat flows needs to be addressed in future experiments. Overall, we conclude that MAO is generally preferable as a barrier material when generating thermovoltages in MTJs. Still, further effort is needed to determine the real thermal conductivities of thin insulating films.

ACKNOWLEDGMENTS

The authors gratefully acknowledge financial support from the Deutsche Forschungsgemeinschaft (DFG) within the priority program Spin Caloric Transport (SPP 1538, MU 1780/8-2, KU 3271/1-1, RE 1052/24-2, HE 5922/4-2, TH 1399/4-2).

- [1] M. Czerner, M. Bachmann, and C. Heiliger, *Phys. Rev. B* **83**, 132405 (2011).
- [2] M. Walter, J. Walowski, V. Zbarsky, M. Münzenberg, M. Schäfers, D. Ebke, G. Reiss, A. Thomas, P. Peretzki, M. Seibt, J. S. Moodera, M. Czerner, M. Bachmann, and C. Heiliger, *Nat. Mater.* **10**, 742 (2011).
- [3] N. Liebing, S. Serrano-Guisan, K. Rott, G. Reiss, J. Langer, B. Ocker, and H. W. Schumacher, *Phys. Rev. Lett.* **107**, 177201 (2011).
- [4] N. Liebing, S. Serrano-Guisan, K. Rott, G. Reiss, J. Langer, B. Ocker, and H. W. Schumacher, *J. Appl. Phys.* **111**, 07C520 (2012).
- [5] N. Liebing, S. Serrano-Guisan, P. Krzysteczko, K. Rott, G. Reiss, J. Langer, B. Ocker, and H. W. Schumacher, *Appl. Phys. Lett.* **102**, 242413 (2013).
- [6] N. Liebing, S. Serrano-Guisan, K. Rott, G. Reiss, and H. W. Schumacher, *J. Magn. Magn. Mater.* **400**, 154 (2016).
- [7] J. Shan, F. K. Dejene, J. C. Leutenantsmeyer, J. Flipse, M. Münzenberg, and B. J. van Wees, *Phys. Rev. B* **92**, 020414(R) (2015).
- [8] A. Boehnke, M. Milnikel, M. von der Ede, C. Franz, V. Zbarsky, M. Czerner, K. Rott, A. Thomas, C. Heiliger, G. Reiss, and M. Münzenberg, *Sci. Rep.* **5**, 8945 (2015).
- [9] A. Boehnke, U. Martens, C. Sterwerf, A. Niesen, T. Huebner, M. von der Ede, M. Meinert, T. Kuschel, A. Thomas, C. Heiliger, M. Münzenberg, and G. Reiss, *Nat. Commun.* **8**, 1626 (2017).
- [10] A. Boehnke, M. Walter, N. Roschwesky, T. Eggebrecht, V. Drewello, K. Rott, M. Münzenberg, A. Thomas, and G. Reiss, *Rev. Sci. Instrum.* **84**, 063905 (2013).
- [11] T. Huebner, A. Boehnke, U. Martens, A. Thomas, J.-M. Schmalhorst, G. Reiss, M. Münzenberg, and T. Kuschel, *Phys. Rev. B* **93**, 224433 (2016).
- [12] U. Martens, J. Walowski, T. Schumann, M. Mansurova, A. Boehnke, T. Huebner, G. Reiss, A. Thomas, and M. Münzenberg, *J. Phys. D: Appl. Phys.* **50**, 144003 (2017).
- [13] T. Böhnert, R. Dutra, R. L. Sommer, E. Paz, S. Serrano-Guisan, R. Ferreira, and P. P. Freitas, *Phys. Rev. B* **95**, 104441 (2017).
- [14] T. Böhnert, S. Serrano-Guisan, E. Paz, B. Lacoste, R. Ferreira, and P. P. Freitas, *J. Phys.: Condens. Matter* **29**, 185303 (2017).
- [15] H. F. Yang, X. K. Hu, N. Liebing, T. Böhnert, J. D. Costa, M. Tarequzzaman, R. Ferreira, S. Sievers, M. Bieler, and H. W. Schumacher, *Appl. Phys. Lett.* **110**, 232403 (2017).
- [16] C. Lopez-Monis, A. Matos-Abiague, and J. Fabian, *Phys. Rev. B* **89**, 054419 (2014).
- [17] C. Lopez-Monis, A. Matos-Abiague, and J. Fabian, *Phys. Rev. B* **90**, 174426 (2014).

- [18] G. E. Bauer, E. Saitoh, and B. J. van Wees, *Nat. Mater.* **11**, 391 (2012).
- [19] W. F. Brinkman, R. C. Dynes, and J. M. Rowell, *J. Appl. Phys.* **41**, 1915 (1970).
- [20] M. Czerner and C. Heiliger, *J. Appl. Phys.* **111**, 07C511 (2012).
- [21] C. Heiliger, C. Franz, and M. Czerner, *Phys. Rev. B* **87**, 224412 (2013).
- [22] M. Hatami, G. E. W. Bauer, Q. Zhang, and P. J. Kelly, *Phys. Rev. Lett.* **99**, 066603 (2007).
- [23] H. Yu, S. Granville, D. P. Yu, and J.-P. Ansermet, *Phys. Rev. Lett.* **104**, 146601 (2010).
- [24] E. Padron-Hernandez, A. Azevedo, and S. M. Rezende, *Phys. Rev. Lett.* **107**, 197203 (2011).
- [25] J. C. Leutenantsmeyer, M. Walter, V. Zbarsky, M. Münzenberg, R. Gareev, K. Rott, A. Thomas, G. Reiss, P. Peretzki, H. Schuhmann, M. Seibt, M. Czerner, and C. Heiliger, *SPIN* **03**, 1350002 (2013).
- [26] A. Pushp, T. Phung, C. Rettner, B. P. Hughes, S.-H. Yang, and S. S. P. Parkin, *Proc. Natl. Acad. Sci. USA* **112**, 6585 (2015).
- [27] Y. Miura, S. Muramoto, K. Abe, and M. Shirai, *Phys. Rev. B* **86**, 024426 (2012).
- [28] J. Zhang, X. G. Zhang, and X. F. Han, *Appl. Phys. Lett.* **100**, 222401 (2012).
- [29] H. Sukegawa, H. Xiu, T. Ohkubo, T. Furubayashi, T. Niizeki, W. Wang, S. Kasai, S. Mitani, K. Inomata, and K. Hono, *Appl. Phys. Lett.* **96**, 212505 (2010).
- [30] B. Tao, D. Li, H. Liu, H. Wei, J.-F. Feng, S. Wang, and X. Han, *IEEE Trans. Magn.* **50**, 4401004 (2014).
- [31] T. Scheike, H. Sukegawa, K. Inomata, T. Ohkubo, K. Hono, and S. Mitani, *Appl. Phys. Express* **9**, 053004 (2016).
- [32] H. Sukegawa, S. Mitani, T. Ohkubo, K. Inomata, and K. Hono, *Appl. Phys. Lett.* **103**, 142409 (2013).
- [33] B. S. Tao, H. X. Yang, Y. L. Zuo, X. Devaux, G. Lengaigne, M. Hehn, D. Lacour, S. Andrieu, M. Chshiev, T. Hauet, F. Montaigne, S. Mangin, X. F. Han, and Y. Lu, *Phys. Rev. Lett.* **115**, 157204 (2015).
- [34] T. Katayama and S. Yuasa, *Appl. Phys. Lett.* **89**, 112503 (2006).
- [35] B. Geisler and P. Kratzer, *Phys. Rev. B* **92**, 144418 (2015).
- [36] St. Burghartz and B. Schulz, *J. Nucl. Mater.* **212–215**, 1065 (1994).
- [37] S.-M. Lee, D. G. Cahill, and T. H. Allen, *Phys. Rev. B* **52**, 253 (1995).
- [38] J. Zhang, M. Bachman, M. Czerner, and C. Heiliger, *Phys. Rev. Lett.* **115**, 037203 (2015).

5.6 Efficient metallic spintronic emitters of ultrabroadband terahertz radiation (Thesis article VI)

Efficient metallic spintronic emitters of ultrabroadband terahertz radiation

T. Seifert¹, S. Jaiswal^{2,3}, U. Martens⁴, J. Hannegan⁵, L. Braun¹, P. Maldonado⁶, F. Freimuth⁷, A. Kronenberg², J. Henrizi², I. Radu⁸, E. Beaupaire⁹, Y. Mokrousov⁷, P. M. Oppeneer⁶, M. Jourdan², G. Jakob², D. Turchinovich¹⁰, L. M. Hayden⁵, M. Wolf¹, M. Münzenberg⁴, M. Kläui² and T. Kampfrath^{1*}

Terahertz electromagnetic radiation is extremely useful for numerous applications, including imaging and spectroscopy. It is thus highly desirable to have an efficient table-top emitter covering the 1–30 THz window that is driven by a low-cost, low-power femtosecond laser oscillator. So far, all solid-state emitters solely exploit physics related to the electron charge and deliver emission spectra with substantial gaps. Here, we take advantage of the electron spin to realize a conceptually new terahertz source that relies on three tailored fundamental spintronic and photonic phenomena in magnetic metal multilayers: ultrafast photoinduced spin currents, the inverse spin-Hall effect and a broadband Fabry-Pérot resonance. Guided by an analytical model, this spintronic route offers unique possibilities for systematic optimization. We find that a 5.8-nm-thick W/CoFeB/Pt trilayer generates ultrashort pulses fully covering the 1–30 THz range. Our novel source outperforms laser-oscillator-driven emitters such as ZnTe(110) crystals in terms of bandwidth, terahertz field amplitude, flexibility, scalability and cost.

The terahertz window, loosely defined as the frequency range 0.3–30 THz in the electromagnetic spectrum, is located between the realms of electronics and optics^{1,2}. As this region coincides with many fundamental resonances of materials, terahertz radiation enables very selective spectroscopic insights into all phases of matter with high temporal^{3,4} and spatial^{5–8} resolution. Consequently, numerous applications in basic research^{3,4}, imaging⁵ and quality control⁶ have emerged.

To fully exploit the potential of terahertz radiation, energy-efficient and low-cost sources of ultrashort terahertz pulses are required. Most broadband table-top emitters are driven by femtosecond laser pulses that generate the required terahertz charge current by appropriately mixing the various optical frequencies^{9,10}. Sources made from solids usually consist of semiconducting or insulating structures with naturally or artificially broken inversion symmetry. When the incident photon energy is below the semiconductor bandgap, optical rectification causes a charge displacement that follows the intensity envelope of the incident pump pulse^{9–17}. For above-bandgap excitation, the response is dominated by a photocurrent^{18–24} with a temporally step-like onset and, thus, a generally smaller bandwidth than optical rectification⁹. Apart from rare exceptions¹⁴, however, most semiconductors used are polar^{1,2,12,13,15–17,21,22} and strongly attenuate terahertz radiation around the optical phonon resonances, thereby preventing emission in the so-called reststrahlen band located between ~1 and 15 THz.

The most promising sources covering the full terahertz window so far are photocurrents in transient gas plasmas^{9,10,25–29}. The downside of this appealing approach is that the underlying ionization process usually requires amplified laser pulses with high threshold energies on the order of 0.1 mJ. Measurable terahertz waveforms

can be obtained with pump-pulse energies down to ~1 μJ (ref. 29), which are, however still two to three orders of magnitude larger than those provided by low-cost femtosecond laser oscillators.

Metals are another promising material class for realizing terahertz sources³⁰, because they exhibit a pump absorptivity largely independent of wavelength³¹, short electron lifetimes of ~10 to 50 fs (ref. 32; implying broadband photocurrents), a featureless terahertz refractive index³³ (favouring gap-free emission) and large heat conductivity (for efficient removal of excess heat). In addition, metal thin-film stacks (heterostructures) are well established, simple and cheap to fabricate. Recent works have indeed demonstrated terahertz emitters based on metal structures^{34–37}. However, the bandwidth did not exceed 3 THz, and terahertz field amplitudes competitive with those of ZnTe emitters were obtained only in conjunction with amplified laser pulses^{36,37}. Consequently, the full potential of metal-based terahertz emitters is far from being realized.

At this point, it is important to acknowledge that all previously demonstrated terahertz emitters have taken advantage exclusively of the charge but not the spin of the electron. On the other hand, very recent tremendous progress in the fields of spintronics^{38–41} and femtomagnetism^{42,43} has shown that the electron spin offers entirely new possibilities for the generation of transient currents in metals. In fact, spin-to-charge conversion has been revealed lately as a new pathway to ultrafast photocurrents^{44,45}.

In this Article, we exploit the unique spintronic and photonic properties of ultrathin metal films to realize a terahertz emitter driven by ~1 nJ laser pulses from a compact, high-repetition-rate femtosecond laser oscillator. The new source combines various benefits in one device: large bandwidth, large terahertz field

¹Department of Physical Chemistry, Fritz Haber Institute of the Max Planck Society, 14195 Berlin, Germany. ²Institute of Physics, Johannes Gutenberg University, 55128 Mainz, Germany. ³Singulus Technologies AG, 63796 Kahl am Main, Germany. ⁴Institute of Physics, Ernst Moritz Arndt University, 17489 Greifswald, Germany. ⁵Department of Physics, University of Maryland Baltimore County, Baltimore, Maryland 21250, USA. ⁶Department of Physics and Astronomy, Uppsala University, SE-75120 Uppsala, Sweden. ⁷Peter Grünberg Institute and Institute for Advanced Simulation, Forschungszentrum Jülich and JARA, 52425 Jülich, Germany. ⁸Institute for Optics and Atomic Physics, Technical University Berlin and Helmholtz-Zentrum Berlin für Materialien und Energie, 12489 Berlin, Germany. ⁹Institut de Physique et Chimie des Matériaux de Strasbourg, 67200 Strasbourg, France. ¹⁰Max Planck Institute for Polymer Research, 55128 Mainz, Germany. *e-mail: kampfrath@fhi-berlin.mpg.de

ARTICLES

NATURE PHOTONICS DOI: 10.1038/NPHOTON.2016.91

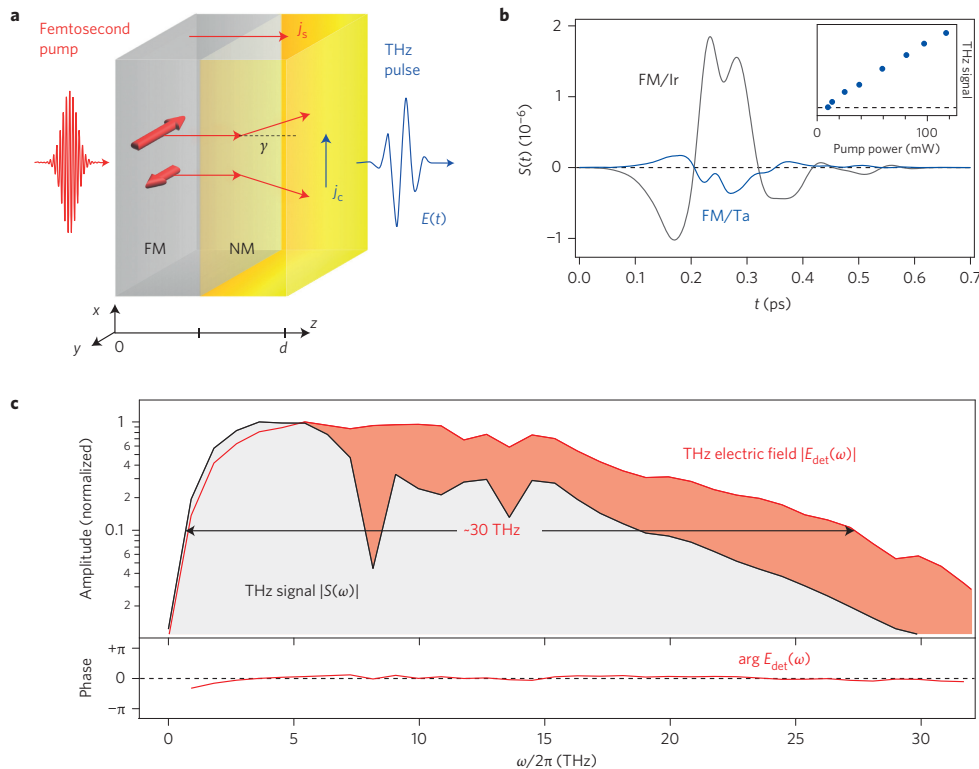


Figure 1 | Metallic spintronic terahertz emitter. **a**, Principle of operation. A femtosecond laser pulse excites electrons in the metal stack, thereby changing their band velocity and launching a current along the z direction. Because in the FM layer the mobility of spin-up (majority) electrons is significantly higher than that of spin-down (minority) electrons, the z current is spin-polarized. In the NM layer, spin-orbit interaction deflects spin-up and spin-down electrons in opposite directions and transforms the spin current j_s into an ultrafast transverse charge current $j_c = \gamma j_s$, leading to the emission of a terahertz electromagnetic transient. **b**, Typical electrooptic signal $S(t)$ of terahertz pulses obtained from photoexcited Ta- and Ir-capped $\text{Co}_{20}\text{Fe}_{60}\text{B}_{20}$ thin films and detected by a 50- μm -thick GaP crystal. Inset: Terahertz signal amplitude as a function of incident pump power. **c**, Fourier spectra of terahertz signal $S(t)$ and the extracted transient terahertz electric field $E_{\text{det}}(t)$ incident on the electrooptic detector. Both spectra are normalized to peak amplitude 1. The double-headed arrow illustrates the ~ 30 THz large bandwidth of the emitter. The flat spectral phase indicates that the terahertz pulse is Fourier-limited.

amplitude at low pump power, easy operation, scalability and low cost. This achievement becomes possible because our widely tunable approach provides access to a large set of spintronic metals and geometrical parameters for optimization.

Spintronic terahertz emitter

Figure 1a illustrates the basic principle of our spintronic terahertz emitter, with a bilayer structure consisting of ferromagnetic (FM) and nonferromagnetic (NM) metal thin films⁴⁴. The FM layer is magnetized in-plane, antiparallel to the y axis. An incident femtosecond laser pulse excites electrons in the metals to states above the Fermi energy, thereby changing their band velocity and scattering rate. Because the FM and NM layers have different transport properties, a net current along the z axis is launched. In addition, because the product of the density, band velocity and lifetime of spin-up (majority) electrons in FM metals (such as Fe, Co and Ni) is significantly higher than that of the spin-down (minority) electrons^{32,46}, the z current is strongly spin-polarized⁴².

On entering the NM layer, spin-orbit coupling deflects spin-up and spin-down electrons in opposite directions^{38–41} by a mean angle γ (Fig. 1a). This inverse spin-Hall effect (ISHE) converts the longitudinal (z -directed) spin current density j_s into an ultrafast transverse (x -directed) charge current density $j_c = \gamma j_s$, thereby acting as a source of terahertz radiation (Fig. 1a).

In our experiment, the metal stack was excited by femtosecond pulses from a Ti:sapphire laser oscillator (duration 10 fs, centre wavelength 800 nm, pulse energy 2.5 nJ, repetition rate 80 MHz). The transient electric field of the emitted terahertz pulse was measured by electrooptic sampling^{1,2,47} in suitable materials (see Methods). We started with bilayers consisting of FM $\text{Co}_{20}\text{Fe}_{60}\text{B}_{20}$ (thickness of 3 nm) capped by either NM Ta or Ir (3 nm) (see Methods). Typical terahertz electrooptic signals $S(t)$ obtained from these samples magnetized along the y axis (Fig. 1a) are presented in Fig. 1b.

Consistent with the generation mechanism outlined above⁴⁴, the emitted radiation has the following properties (Supplementary Fig. 4). It is linearly polarized, with the electric-field direction perpendicular to the sample magnetization, but it is independent of the pump polarization. The spin current and thus the terahertz field are reversed entirely, either when the external saturating magnetic field of 10 mT is reversed or when the two metallic films are grown in reverse order on the substrate. Finally, the terahertz signal amplitude grows linearly with the pump power (Fig. 1b, inset). Therefore, signal saturation due to pump-induced sample demagnetization is negligible here, consistent with the estimate that ultrafast magnetization quenching is less than 1% at the maximum pump fluence used⁴⁴.

Fourier-transforming the time-domain signals $S(t)$ yields the spectral amplitude $|S(\omega)|$ versus frequency $\omega/2\pi$. A typical spectrum

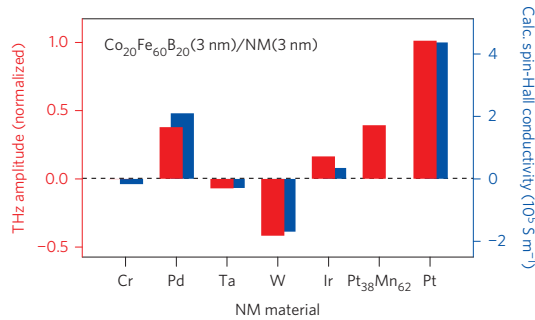


Figure 2 | Impact of the NM material. Terahertz signal amplitude (r.m.s.) as a function of the NM material used for the $\text{Co}_{20}\text{Fe}_{60}\text{B}_{20}(3\text{ nm})/\text{NM}(3\text{ nm})$ stack (red bars). For comparison, *ab initio* calculated values of the spin-Hall conductivity are also shown (blue bars), except for $\text{Pt}_{38}\text{Mn}_{62}$. A Cr cap layer leads to a nearly vanishing terahertz signal.

is shown in Fig. 1c. It covers a large bandwidth from ~ 1 to 18 THz. Note that spectral features such as the dip at 8 THz arise from the 50- μm -thick GaP electrooptic sensor and not from the emitter^{44,47}. By deconvoluting the detector response function from the signal $S(t)$, we obtain the terahertz electric field $E_{\text{det}}(t)$ directly in front of the detection crystal (see Methods). Strikingly, the field spectrum $|E_{\text{det}}(\omega)|$ (Fig. 1c) is remarkably smooth and extends from 1 to nearly 30 THz full-width at 10% amplitude maximum, without any gaps. In addition, the spectral phase of the transient field is flat (Fig. 1c), demonstrating that the terahertz pulse is Fourier-limited.

Although its bandwidth is already remarkably large, the $\text{Co}_{20}\text{Fe}_{60}\text{B}_{20}/\text{Ta}$ bilayer (Fig. 1b) generates a terahertz peak signal that is about two orders of magnitude smaller than that obtained from a standard emitter in linear terahertz spectroscopy⁹, a 1-mm-thick ZnTe(110) crystal (Fig. 4a). To boost the emitted terahertz field, we need to understand the key factors that determine it. The amplitude of the x -polarized terahertz field (Fig. 1a) directly behind the multilayer is given by (see Methods)

$$E(\omega) = Z(\omega)e \int_0^d dz \gamma(z)j_s(z, \omega) \quad (1)$$

where d is the film thickness, and e is the elementary charge. According to this generalized Ohm's law, the emitted field $E(\omega)$ equals the total charge current $-efdz \gamma_j$, times an impedance $-Z(\omega)$, which quantifies how efficiently a current is converted into

electromagnetic radiation. Here, $1/Z$ can be interpreted as the effective conductance of a parallel connection of all metal layers shunted by the adjacent substrate and air half-spaces (see Methods).

Equation (1) readily shows that maximizing Z , γ and j_s will lead to maximum terahertz output of the emitter for a given pump power. The numerous sample parameters that can be tuned in such an optimization are the FM/NM materials and the geometry of the heterostructure.

Maximizing the terahertz output

We started by varying the NM material, which primarily affects the emitted terahertz field through the magnitude and sign of the spin-Hall angle γ (equation (1)). In particular, we considered such metals for which large γ values have been reported³⁹. Importantly, for all samples studied here, we found emitted terahertz waveforms and spectra with shapes that are very similar to those shown in Fig. 1b,c. It is therefore sufficient to quantify the strength of the emitted terahertz field by the root mean square (r.m.s.) of the terahertz signal $S(t)$. This quantity is displayed in Fig. 2 as a function of the NM metal in $\text{Co}_{20}\text{Fe}_{60}\text{B}_{20}(3\text{ nm})/\text{NM}(3\text{ nm})$ heterostructures.

Figure 2 clearly shows that the terahertz field amplitude and polarity depend drastically on the NM material chosen. For instance, Pt delivers a one order of magnitude larger amplitude than Ta and Ir. Interestingly, choosing W for the NM layer leads to a comparable magnitude as with Pd or Pt, but with opposite sign. The sign change is consistent with the findings in previous works³⁹ and is related to there being a half-filled electronic d shell in W but an almost full d shell in Pt (ref. 48). More generally, we find that the entire trend of terahertz amplitude versus NM material (Fig. 2) is in good semiquantitative agreement with the spin-Hall conductivities measured previously³⁹ and calculated by us (Fig. 2; see Methods). This observation provides further evidence for the transport scenario outlined in Fig. 1a and ref. 44.

In contrast to the NM material, the terahertz signal amplitude is found to change only relatively little when the FM material $\text{Co}_{20}\text{Fe}_{60}\text{B}_{20}$ is substituted by Fe, Co, Fe-Co alloys or $\text{Ni}_{81}\text{Fe}_{19}$ (Supplementary Section 1). In essence, varying the materials forming the FM/NM bilayers shows that the combination $\text{Co}_{40}\text{Fe}_{40}\text{B}_{20}/\text{Pt}$ provides the best terahertz-emission performance.

In the next optimization step, we varied the stack geometry and measured the terahertz emission as a function of total sample thickness d while keeping the FM and NM layers approximately equally thick. The experiment revealed a surprising dependence (Fig. 3a): the terahertz amplitude increases with decreasing emitter thickness d , peaks at $d = 4\text{ nm}$, and falls off rapidly at smaller d .

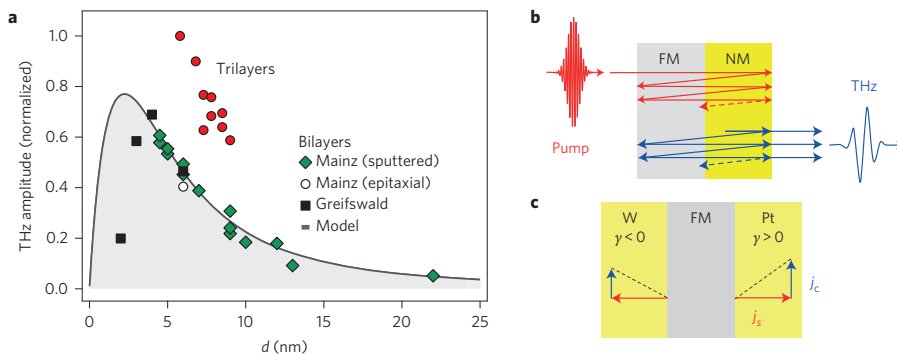


Figure 3 | Impact of stack geometry on emitter performance. **a**, Terahertz signal amplitude (r.m.s.) as a function of thickness d of the metal stack. Different symbols represent different sample fabrication schemes (see Methods). The solid line is a fit using a transport model (main text and Methods). **b**, Schematic of the thin-film Fabry-Pérot cavity that enhances both the incident pump and emitted terahertz radiation. **c**, Schematic of the trilayer emitter that converts the backward- and forward-flowing spin current j_s into a unidirectional charge current j_c with approximately equal efficiency.

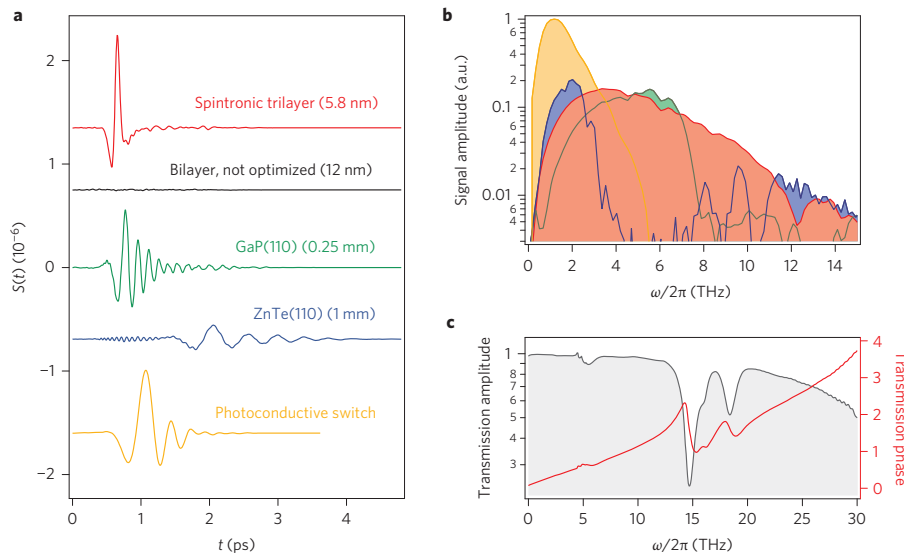


Figure 4 | Spintronic emitter performance and spectroscopic application. **a,b**, Terahertz signal waveforms (**a**) and resulting amplitude spectra (**b**) of the spintronic trilayer emitter in comparison to standard terahertz emitters as measured with a 70-μm-thick LAPC electrooptic sensor. Measurements were performed under identical conditions so that the output of all emitters can be compared directly. Deconvolution of the detector response function yields the transient terahertz electric fields, which are shown in Supplementary Fig. 1. **c**, Spectral amplitude and phase of the terahertz transmission of a 7.5-μm-thick PTFE thread-seal tape measured with our spintronic emitter using a 10-μm-thick ZnTe electrooptic sensor.

This behaviour is highly counterintuitive and in sharp contrast to most phase-matched frequency conversion schemes such as optical rectification and second-harmonic generation⁹. Indeed, equation (1) suggests that the terahertz field amplitude scales with metal thickness d . This trend, however, is overcompensated by a remarkable photonic effect: our metal thin film acts as a Fabry–Pérot cavity that resonantly enhances both pump and terahertz waves. As the cavity length d is much smaller than all wavelengths involved, all reflection echoes inside the film interfere constructively (Fig. 3b). The shorter the cavity, the more echoes occur before the light wave has decayed, resulting in even more enhancement. Below a critical thickness d_c , however, reflection losses at the cavity faces exceed attenuation in the metal bulk. The enhancement of the pump and terahertz electric field then saturates at $d < d_c$ and no longer compensates for the shrinking emitter volume. The emitted terahertz amplitude should first grow with decreasing d and, after reaching a maximum, decrease, in agreement with our experimental data (Fig. 3a).

A quantitative description of this behaviour is provided by equation (1) and a simple transport model for j_s (see Methods). The best fit (solid curve in Fig. 3a) is obtained when we assume that the spin-polarized carriers entering the Pt layer randomize their velocity over a length of 1 nm. In essence, Fig. 3a shows that the largest terahertz signal is provided by the 4-nm-thick $\text{Co}_{20}\text{Fe}_{60}\text{B}_{20}/\text{Pt}$ emitter, and this performance is very close to the absolute maximum predicted by our model.

Having identified the best bilayer emitter, we finally tailored the sequence of the spintronic metal layers. Figure 1a suggests that only the forward-propagating half of the photoinduced spin current travels into the NM layer where it is converted into a charge current. To also take advantage of the backward-flowing electrons, we introduced another NM layer on the left-hand side of the FM film (Fig. 3c). We chose $\text{W}/\text{Co}_{40}\text{Fe}_{40}\text{B}_{20}/\text{Pt}$, because W and Pt exhibit the largest spin-Hall angles γ , but with opposite sign (Fig. 2). Because of this unique possibility for spintronic engineering, the spin-Hall currents j_c in the W and Pt layer flow in the

same direction, radiate in phase and thus, again, boost the terahertz amplitude (Fig. 3c).

Indeed, as seen in Fig. 3a, the terahertz amplitude from each $\text{W}/\text{Co}_{40}\text{Fe}_{40}\text{B}_{20}/\text{Pt}$ trilayer is approximately twice as high as that from a bilayer counterpart with the same total thickness. In particular, the $\text{W}(2\text{ nm})/\text{Co}_{40}\text{Fe}_{40}\text{B}_{20}(1.8\text{ nm})/\text{Pt}(2\text{ nm})$ trilayer delivers a 40% higher terahertz amplitude than the best bilayer $\text{Co}_{20}\text{Fe}_{60}\text{B}_{20}(2\text{ nm})/\text{Pt}(2\text{ nm})$, even though the trilayer is ~50% thicker. This result indicates that the conversion of both forward and backward spin currents into terahertz radiation overcompensates the effect of the larger metal thickness.

Figure 3a concludes our model-guided optimization strategy and identifies the 5.8-nm-thick $\text{W}/\text{Co}_{40}\text{Fe}_{40}\text{B}_{20}/\text{Pt}$ trilayer as the best terahertz emitter out of the comprehensive set of more than 70 heterostructures studied here. With this extensive procedure, we have gone beyond all previous approaches for emitter design and have fully exploited the spintronic nature of our terahertz source. The evolution of our efforts is illustrated in Fig. 4a. The trilayer delivers a more than two orders of magnitude larger terahertz amplitude than $\text{Co}_{20}\text{Fe}_{60}\text{B}_{20}(10\text{ nm})/\text{Ta}(2\text{ nm})$, which is one of the bilayers we first investigated.

Performance test

To evaluate the performance of our trilayer emitter, we compared it to three state-of-the-art terahertz sources routinely used to cover the range from ~0.3 to 8 THz: the nonlinear optical crystals ZnTe(110) and GaP(110)^{1,9} and a high-performance photoconductive switch biased by interdigitated electrodes²² (see Methods). For all the emitters, terahertz emission was measured under identical conditions, and the terahertz signal amplitude was found to scale linearly with pump power. Consequently, a comparison of the terahertz spectral amplitudes provides a direct measure of how well each emitter performs at a given frequency. To directly identify spectral emission gaps, we chose a 70-μm-thick Lemke/amorphous polycarbonate (LAPC) electrooptic sensor¹⁴ that permits gap-free detection from ~0.3 to 15 THz (Supplementary Fig. 2).

Figure 4a,b displays terahertz waveforms $S(t)$ from all sources and the respective amplitude spectra. The resulting transient terahertz electric fields (see Methods) are shown in Supplementary Fig. 1. For ZnTe and GaP, the electrooptic signal $S(t)$ consists of slowly and quickly oscillating sections, which are, respectively, related to frequencies below and above the reststrahlen band of these crystals. Strong wave attenuation in the reststrahlen region⁴⁷ leads to considerable gaps from 3 to 10 THz and 7 to 13 THz in the ZnTe and GaP amplitude spectra $|S(\omega)|$, respectively (Fig. 4b). In contrast, the time-domain signal from the spintronic trilayer features a higher peak amplitude, is much shorter (Fig. 4a) and even Fourier-limited (Fig. 1c). Remarkably, the spectrum is gap-free and exceeds the spectral amplitude of the ZnTe and GaP crystals from 2.5 to 14 THz, except small frequency intervals around 6 and 12 THz where GaP and ZnTe, respectively, yield slightly more amplitude. We note that our trilayer emitter is characterized by an effective $\chi^{(2)}$ nonlinear optical coefficient that is five orders of magnitude larger than that of GaP (Supplementary Section 2). As revealed above, this coefficient is, however, confined to an only ~1-nm-thick layer at the FM/NM interfaces.

Although the photoconductive switch and the trilayer exhibit comparable terahertz signal amplitudes in the time domain (Fig. 4a), their performance is complementary in frequency space (Fig. 4b). In the case where exceptionally high amplitudes are required below 3 THz, the photoconductive switch is the source of choice. In contrast, the spintronic emitter provides more amplitude above 3 THz and exhibits a much wider bandwidth from 1 to 30 THz without a gap (Supplementary Fig. 1).

We routinely use our trilayer emitter to measure ultrabroadband terahertz transmission spectra. As an example, Fig. 4c displays the amplitude and phase of the complex-valued transmission of a 7.5- μm -thick polytetrafluoroethylene (PTFE, Teflon) sample, obtained using the trilayer emitter and a 10- μm -thick ZnTe(110) electrooptic sensor⁴⁷. Resonant features around 6, 15 and 18 THz are found, in excellent agreement with previous studies⁴⁹ using gas-plasma terahertz emitters that were, however, driven by five orders of magnitude more intense pump pulses. We finally note that such broadband and gapless terahertz spectroscopy would not be possible at all with standard solid-state emitters.

Conclusion

We have developed a conceptually new, high-performance and versatile terahertz source for broadband linear terahertz spectroscopy based on optically driven spin currents in ultrathin magnetic metal heterostructures. Our approach unifies the benefits of different emitter types in one device: it approaches the bandwidth of the much more expensive gas-plasma spectroscopy systems and delivers short, Fourier-limited pulses covering the full range from 1 to 30 THz without a gap. As with often-used optical-rectification crystals, our heterostructure is robust, passive, easy to use (in transmission mode under normal incidence) and driven by a low-cost, compact femtosecond laser oscillator. At the same time, the terahertz field amplitude emitted exceeds that of standard emitters such as ZnTe, GaP and a biased photoconductive switch. Similar to such switches, the direction and amplitude of the emitted terahertz field can be modulated easily by applying an oscillating magnetic field with small amplitude below 10 mT. In addition to these benefits, the broadband optical absorption of metals implies that the spintronic terahertz source can be driven by any laser oscillator, virtually independent of its output wavelength.

We emphasize that the fabrication of our emitter is inexpensive, straightforward and scalable, without involving any lithography steps. Fabrication costs are dominated by the substrate price, and we are able to deposit homogeneous layers on substrates with diameters as large as 20 cm (see Methods). Preliminary tests show that driving such large-area trilayers with intense laser pulses easily

yields terahertz pulses with peak fields of several 100 kV cm⁻¹, which exceed those obtained with more strongly pumped large-area ZnTe emitters⁵⁰. Therefore, spintronic terahertz sources exhibit a high potential for enabling nonlinear optical studies^{51,52} in the difficult to access region between 5 and 10 THz. More generally, our results highlight metallic magnetic multilayers as a new and very promising class of high-performance and broadband terahertz emitters. Finally, this work is an example of a rapid translation of recently discovered fundamental physical effects into useful technology that can straightforwardly be employed by the broad femtosecond-laser community.

Methods

Methods and any associated references are available in the [online version of the paper](#).

Received 18 September 2015; accepted 8 April 2016;
published online 23 May 2016

References

1. Ferguson, B. & Zhang, X. Materials for terahertz science and technology. *Nature Mater.* **1**, 26–33 (2002).
2. Tonouchi, M. Cutting-edge terahertz technology. *Nature Photon.* **1**, 97–105 (2007).
3. Ulbricht, R., Hendry, E., Shan, J., Heinz, T. & Bonn, M. Carrier dynamics in semiconductors studied with time-resolved terahertz spectroscopy. *Rev. Mod. Phys.* **83**, 543–586 (2011).
4. Kampfrath, T., Tanaka, K. & Nelson, K. Resonant and nonresonant control over matter and light by intense terahertz transients. *Nature Photon.* **7**, 680–690 (2013).
5. Chan, W., Deibel, J. & Mittleman, D. Imaging with terahertz radiation. *Rep. Prog. Phys.* **70**, 1325–1379 (2007).
6. Cocker, T. L. *et al.* An ultrafast terahertz scanning tunnelling microscope. *Nature Photon.* **7**, 620–625 (2013).
7. Sano, Y. *et al.* Imaging molecular adsorption and desorption dynamics on graphene using terahertz emission spectroscopy. *Sci. Rep.* **4**, 6046 (2014).
8. Zeitler, J. *et al.* Terahertz pulsed spectroscopy and imaging in the pharmaceutical setting—a review. *J. Pharm. Pharmacol.* **59**, 209–223 (2007).
9. Reimann, K. Table-top sources of ultrashort THz pulses. *Rep. Prog. Phys.* **70**, 1597–1632 (2007).
10. Blanchard, F. *et al.* Generation of intense terahertz radiation via optical methods. *IEEE J. Sel. Top. Quantum Electron.* **17**, 5–16 (2011).
11. Rice, A. *et al.* Terahertz optical rectification from (110) zinc-blende crystals. *Appl. Phys. Lett.* **64**, 1324–1326 (1994).
12. Kaindl, R., Eickemeyer, F., Woerner, M. & Elsaesser, T. Broadband phase-matched difference frequency mixing of femtosecond pulses in GaSe: experiment and theory. *Appl. Phys. Lett.* **75**, 1060–1062 (1999).
13. Huber, R., Brodschelm, A., Tauser, F. & Leitenstorfer, A. Generation and field-resolved detection of femtosecond electromagnetic pulses tunable up to 41 THz. *Appl. Phys. Lett.* **76**, 3191–3193 (2000).
14. Zheng, X., Sinyukov, A. & Hayden, L. M. Broadband and gap-free response of a terahertz system based on a poled polymer emitter–sensor pair. *Appl. Phys. Lett.* **87**, 081115 (2005).
15. Zheng, X., McLaughlin, C. V., Cunningham, P. & Hayden, L. M. Organic broadband terahertz sources and sensors. *J. Nanoelectron. Optoelectron.* **2**, 58–76 (2007).
16. Brunner, F. *et al.* A hydrogen-bonded organic nonlinear optical crystal for high-efficiency terahertz generation and detection. *Opt. Express* **16**, 16496–16508 (2008).
17. Katayama, I. *et al.* Ultrabroadband terahertz generation using 4-*N,N*-dimethylamino-4'-*N*-methyl-stilbazolium tosylate single crystals. *Appl. Phys. Lett.* **97**, 021105 (2010).
18. Shan, J. & Heinz, T. F. in *Ultrafast Dynamical Processes in Semiconductors* (ed. Tsien, K.-T.) 1–56 (Springer, 2004).
19. Apostolopoulos, V. & Barnes, M. THz emitters based on the photo-Dember effect. *J. Phys. D* **47**, 374002 (2014).
20. Klatt, G. *et al.* Terahertz emission from lateral photo-Dember currents. *Opt. Express* **18**, 4939–4947 (2010).
21. Shen, Y., Upadhy, P., Linfield, E., Beere, H. & Davies, A. Ultrabroadband terahertz radiation from low-temperature-grown GaAs photoconductive emitters. *Appl. Phys. Lett.* **83**, 3117–3119 (2003).
22. Winnerl, S. Scalable microstructured photoconductive terahertz emitters. *J. Infrared Millim. Terahertz Waves* **33**, 431–454 (2012).
23. Hale, P. *et al.* 20 THz broadband generation using semi-insulating GaAs interdigitated photoconductive antennas. *Opt. Express* **22**, 26358–26364 (2014).

ARTICLES

NATURE PHOTONICS DOI: 10.1038/NPHOTON.2016.91

24. Berry, C., Wang, N., Hashemi, M., Unlu, M. & Jarrahi, M. Significant performance enhancement in photoconductive terahertz optoelectronics by incorporating plasmonic contact electrodes. *Nature Commun.* **4**, 1622 (2013).
25. Thomson, M. D., Kref, M., Löffler, T. & Roskos, H. G. Broadband THz emission from gas plasmas induced by femtosecond optical pulses: from fundamentals to applications. *Laser Photon. Rev.* **1**, 349–368 (2007).
26. Kim, K., Glowina, J., Taylor, A. J. & Rodriguez, G. High-power broadband terahertz generation via two-color photoionization in gases. *IEEE J. Quantum Electron.* **48**, 797–805 (2012).
27. Lu, X. & Zhang, X. C. Investigation of ultra-broadband terahertz time-domain spectroscopy with terahertz wave gas photonics. *Front. Optoelectron.* **7**, 121–155 (2013).
28. Bartel, T., Gaal, P., Reimann, K., Woerner, M. & Elsaesser, T. Generation of single-cycle THz transients with high electric-field amplitudes. *Opt. Lett.* **30**, 2805–2807 (2005).
29. Buccheri, F. & Zhang, X. C. Terahertz emission from laser-induced microplasma in ambient air. *Optica* **2**, 366–369 (2015).
30. Ramanandan, G., Ramakrishnan, G., Kumar, N., Adam, A. & Planken, P. Emission of terahertz pulses from nanostructured metal surfaces. *J. Phys. D* **47**, 374003 (2014).
31. Zhang, L. *et al.* High-power THz to IR emission by femtosecond laser irradiation of random 2D metallic nanostructures. *Sci. Rep.* **5**, 12536 (2015).
32. Zhukov, V., Chulkov, E. & Echenique, P. Lifetimes and inelastic mean free path of low-energy excited electrons in Fe, Ni, Pt, and Au: *ab initio* GW + T calculations. *Phys. Rev. B* **73**, 125105 (2006).
33. Laman, N. & Grischkowsky, D. Terahertz conductivity of thin metal films. *Appl. Phys. Lett.* **93**, 051105 (2008).
34. Ramakrishnan, G. & Planken, P. Percolation-enhanced generation of terahertz pulses by optical rectification on ultrathin gold films. *Opt. Lett.* **36**, 2572–2574 (2011).
35. Polyushkin, D., Hendry, E., Stone, E. & Barnes, W. THz generation from plasmonic nanoparticle arrays. *Nano Lett.* **11**, 4718–4724 (2011).
36. Kadlec, F., Kuzel, P. & Coutaz, J. Study of terahertz radiation generated by optical rectification on thin gold films. *Opt. Lett.* **30**, 1402–1404 (2005).
37. Welsh, G. H., Hunt, N. T. & Wynne, K. Terahertz-pulse emission through laser excitation of surface plasmons in a metal grating. *Phys. Rev. Lett.* **98**, 026803 (2007).
38. Saitoh, E., Ueda, M., Miyajima, H. & Tatara, G. Conversion of spin current into charge current at room temperature: inverse spin-Hall effect. *Appl. Phys. Lett.* **88**, 182509 (2006).
39. Hoffmann, A. Spin Hall effects in metals. *IEEE Trans. Magn.* **49**, 5172–5193 (2013).
40. Sinova, J. *et al.* Spin Hall effects. *Rev. Mod. Phys.* **87**, 1213–1260 (2015).
41. Wei, D. *et al.* Spin Hall voltages from a.c. and d.c. spin currents. *Nature Commun.* **5**, 3768 (2014).
42. Battiato, M., Carva, K. & Oppeneer, P. M. Superdiffusive spin transport as a mechanism of ultrafast demagnetization. *Phys. Rev. Lett.* **105**, 027203 (2010).
43. Melnikov, A. *et al.* Ultrafast transport of laser-excited spin polarized carriers in Au/Fe/MgO(001). *Phys. Rev. Lett.* **107**, 076601 (2011).
44. Kampfrath, T. *et al.* Terahertz spin current pulses controlled by magnetic heterostructures. *Nature Nanotech.* **8**, 256–260 (2013).
45. Héroux, J. B., Ino, Y., Kuwata-Gonokami, M., Hashimoto, Y. & Katsumoto, S. Terahertz radiation emission from GaMnAs. *Appl. Phys. Lett.* **88**, 221110 (2006).
46. Jin, Z. *et al.* Accessing the fundamentals of magnetotransport in metals with terahertz probes. *Nature Phys.* **11**, 761–766 (2015).
47. Leitenstorfer, A., Hunsche, S., Shah, J., Nuss, M. & Knox, W. Detectors and sources for ultrabroadband electro-optic sampling: experiment and theory. *Appl. Phys. Lett.* **74**, 1516–1518 (1999).
48. Kontani, H., Tanaka, T., Hirashima, D., Yamada, K. & Inoue, J. Giant orbital Hall effect in transition metals: origin of large spin and anomalous Hall effects. *Phys. Rev. Lett.* **102**, 016601 (2009).
49. D'Angelo, F., Mics, Z., Bonn, M. & Turchinovich, D. Ultra-broadband THz time-domain spectroscopy of common polymers using THz air photonics. *Opt. Express* **22**, 12475–12485 (2014).
50. Blanchard, F. *et al.* Generation of 1.5 μ J single-cycle terahertz pulses by optical rectification from a large aperture ZnTe crystal. *Opt. Express* **15**, 13212–13220 (2007).
51. Liu, M. *et al.* Terahertz-field-induced insulator-to-metal transition in vanadium dioxide metamaterial. *Nature* **487**, 345–348 (2012).
52. Vicario, C. *et al.* Off-resonant magnetization dynamics phase-locked to an intense phase-stable terahertz transient. *Nature Photon.* **7**, 720–723 (2013).

Acknowledgements

The authors thank S. Winnerl for providing a TeraSED3 emitter and for stimulating discussions. The authors acknowledge the German Science Foundation for funding through SPP 1538/SpinCaT (Berlin, Greifswald, Jülich and Mainz groups) and through SFB TRR 173/Spin+X (Mainz group). The European Union is acknowledged for funding through ERC H2020 CoG project TERAMAG/grant no. 681917 (T.K.), FP7 project CRONOS/grant no. 280879 (T.K. and M.W.), FP7 Marie Curie ITN WALL project/grant no. 608031 (J.S., G.J. and M.K.), Career Integration Grant LIGHTER/grant no. 334324 (D.T.) and FP7 project FemtoSpin/grant no. 281043 (P.M. and P.M.O.). The authors are grateful for support from the Max Planck Society (T.K. and D.T.), the Swedish Research Council, the Röntgen-Ångström Cluster, and the K. and A. Wallenberg Foundation (P.M. and P.M.O.), the Samsung SGMI programme, the EFRE Program of the state of Rhineland Palatinate, TT-DINEMA, the Excellence Graduate School MAINZ (GSC 266) and the state research centre CINEMA (Mainz group). F.F. and Y.M. acknowledge Jülich Supercomputing Centre for computing time.

Author contributions

T.K. and T.S. conceived the experiments. T.K. and I.R. carried out preliminary measurements. S.J., U.M., A.K., J.He., E.B., M.J., G.J., M.M. and M.K. fabricated the spintronic emitters and optimized the fabrication process. L.B., T.S. and T.K. built the terahertz emission set-up. J.Ha. and L.M.H. fabricated the LAPC electrooptic detectors. T.S. performed the terahertz experiments and optical sample characterization. T.S. and T.K. analysed experimental data with contributions from D.T. and M.K. T.K. and T.S. developed the analytical terahertz-emitter model with contributions from F.F. and Y.M. F.F. and Y.M. calculated spin-Hall conductivities. P.M. and P.M.O. conducted calculations of the ultrafast spin transport. T.K., T.S., D.T., M.W. and M.K. co-wrote the paper. All authors contributed to discussing the results and writing the paper.

Additional information

Supplementary information is available in the [online version of the paper](https://www.nature.com/reprints). Reprints and permissions information is available online at www.nature.com/reprints. Correspondence and requests for materials should be addressed to T.K.

Competing financial interests

The authors declare no competing financial interests.

Methods

Sample fabrication. The magnetic heterostructures were grown on glass, sapphire or MgO substrates. Most of the samples from the Mainz group were fabricated using an Ar sputter deposition tool (Singulus Rotaris) with targets of 100 mm diameter. Typically, the Ar pressure range was 2×10^{-3} mbar to 4×10^{-3} mbar, the power used was 800 W, and the deposition rates were 1.2 \AA s^{-1} for the ferromagnetic (FM) layer and 2.1 \AA s^{-1} for the nonferromagnetic (NM) layer. Before deposition, a short plasma etch was performed to remove organic contaminants from the substrate surface. The epitaxial Fe(100) thin film (thickness 3 nm) was prepared by radiofrequency-sputtering on a MgO(100) substrate at room temperature. After confirmation of the epitaxial growth by reflection high-energy electron diffraction, an epitaxial Pt(100) layer (3 nm) was d.c. sputtered on top.

The $\text{Co}_{20}\text{Fe}_{60}\text{B}_{20}$ films from the Greifswald group were prepared by magnetron sputtering, and the NM metal films were grown by electron-beam evaporation under ultrahigh-vacuum conditions (base pressure of 5×10^{-10} mbar) using *in situ* transfer. Composition analysis of the films yielded a Co/Fe ratio of 1/2.1, and characterization by transmission electron microscopy revealed smooth $\text{Co}_{20}\text{Fe}_{60}\text{B}_{20}$ film surfaces below the atomic monolayer limit.

The samples exhibited typical thin-film properties⁵³, in-plane magnetic anisotropy and a nearly rectangular hysteresis curve with a coercive field well below 10 mT.

Sample optical properties. To further characterize the heterostructures, optical reflectance and transmittance were measured using the pump beam of the terahertz emission set-up (see next subsection for details). Our data (Supplementary Fig. 3) show that the multilayers absorb about 50% of the incident laser power, largely independent of the total metal thickness. The measured values of reflectance and transmittance agree excellently with calculations based on a transfer-matrix formalism⁵⁴ and literature data for the optical constants of the materials involved^{55,56}. Such good agreement is indicative of an optically homogeneous and flat metal film, as expected from the optimized film deposition.

The terahertz conductivity of the Pt and FM films was measured by terahertz transmission spectroscopy⁵⁷. We obtained values of $\sigma = (6.5 \pm 0.11) \times 10^5 \text{ S m}^{-1}$ for $\text{Co}_{40}\text{Fe}_{40}\text{B}_{20}$ and $(2.9 \pm 0.11) \times 10^6 \text{ S m}^{-1}$ for Pt, approximately independent of the terahertz frequency due to the high Drude scattering rate, which is on the order of 50 THz.

Terahertz emission set-up. In the optical experiment (Fig. 1a), the sample was kept in an external saturating magnetic field of 10 mT, and was excited by linearly polarized laser pulses (duration 10 fs, centre wavelength 800 nm, energy 2.5 nJ) from a Ti:sapphire laser oscillator (repetition rate 80 MHz) under normal incidence from the substrate side (beam diameter at sample 50 μm full-width at half-maximum of the intensity). The terahertz electric field was detected by electrooptic sampling^{1,2,47}, with probe pulses (0.6 nJ, 10 fs) from the same laser co-propagating with the terahertz field through an electrooptic crystal. The resulting signal $S(t)$ equals twice the terahertz-field-induced probe ellipticity, where t is the delay between the terahertz and probe pulse. Depending on the signal strength, duration and bandwidth required, we used various electrooptic materials: ZnTe(110) (thickness of 10 μm and 1 mm)⁴⁷, GaP(110) (50 and 250 μm)⁴⁷ and the poled-polymer guest-host system Lemke/amorphous polycarbonate (LAPC)¹⁴ (70 μm).

In the performance evaluation, the spintronic trilayer and reference emitters (Fig. 4a) were operated under identical pump-beam and detection conditions. The terahertz amplitude obtained from the commercially available photoconductive switch (TeraSED3, based on interdigitated electrodes on a semi-insulating GaAs substrate²²) was maximized by setting the d.c. bias voltage to 12 V (20% above the maximum value recommended by the technical specifications). All measurements were performed at room temperature in a N_2 atmosphere.

Signal deconvolution. To extract the terahertz electric field E_{det} incident onto the detector from the terahertz signal S measured by electrooptic sampling, we note that these waveforms are connected by the convolution

$$S(t) = (h * E_{\text{det}})(t) \quad (2)$$

The detector response function h depends on the parameters of the electrooptic crystal and the sampling pulse used^{47,58,59}. For the calculation of h , the optical constants are taken from refs 47,60 and 61. Supplementary Fig. 2 shows the spectral amplitude and phase of the calculated $h(\omega)$ for the detectors used in this work. By equidistant sampling of the measured $S(t)$ and the calculated $h(t)$, equation (2) can be rewritten as an overdetermined matrix equation and numerically solved for $E_{\text{det}}(t)$. Example traces of the absolute electric field are displayed in Supplementary Fig. 1a.

Derivation of equation (1). To derive a relationship between the emitted terahertz electric field and its source current, we note that within our sample the beam diameter is much larger than the sample thickness ($d \approx 10 \text{ nm}$). Plane-wave propagation along the z axis (Fig. 1a) is therefore assumed. The charge current density $-e\mathbf{j}_c$ resulting from the laser-driven spin current density $(\hbar/2)\mathbf{j}_s$ and the inverse spin-Hall effect generates an electromagnetic wave with an electric field

$E(z, t)$ polarized along the x axis (Fig. 1a). In the frequency domain, the dynamics of E are governed by the wave equation⁶²

$$[\partial_z^2 + k^2(z, \omega)]E(z, \omega) = Q(z, \omega) = -eZ_0 \omega \mathbf{j}_c(z, \omega)/ic \quad (3)$$

where c is the vacuum speed of light and $Z_0 = 377 \Omega$ is the vacuum impedance. The terahertz wavevector $k(z, \omega)$ is given by $k^2 = k_0^2 + \Delta(k^2)$ where $k_0 = n\omega/c$ refers to the system without a metal film, for which the refractive index $n(z, \omega)$ equals $n_1(\omega)$ for the substrate half-space ($z < 0$) and $n_2 \approx 1$ for the air half-space ($z > 0$). When metal films are deposited on the substrate, the wavevector landscape $k_0^2(z, \omega)$ changes by $\Delta(k^2) = iZ_0\sigma\omega/c$ where $\sigma(z, \omega)$ is the conductivity distribution of the metal stack. We omit the ω dependence in the notation for brevity and rewrite equation (3) as an integral equation

$$E(z) = \int dz' [Q(z') - \Delta(k^2)(z')E(z')] G_0(z, z') \quad (4)$$

where $G_0(z, z')$ is the Green's function of the system without metal films ($k = k_0$) (ref. 62). When both source point z' and observation point z are on the air side ($z, z' > 0$), one has $G_0(z, z') = (e^{ik_0|z-z'|}/2ik_0) \cdot (1 + r_{21}e^{2ik_0|z|})$ with $k_2 = n_2\omega/c$. The term with the Fresnel coefficient $r_{21} = (n_2 - n_1)/(n_2 + n_1)$ accounts for wave reflection at the air-substrate interface at $z = 0$.

Because the film is much thinner than the wavelength and attenuation length of the terahertz wave, we approximate all phase factors by 1 and assume the electric field E is constant throughout the metal multilayer (quasistatic approximation). As a consequence, both E and $G_0 \approx (c/i\omega)/(n_1 + n_2)$ can be moved in front of the integral of equation (4) and we obtain equation (1) of the main text in which the impedance is given by

$$\frac{1}{Z(\omega)} = \frac{n_1(\omega) + n_2(\omega)}{Z_0} + \int_0^d dz \sigma(z, \omega) \quad (5)$$

When the sheet conductance $\int dz \sigma$ of the metal stack is much larger than the shunt conductance $(n_1 + n_2)/Z_0$ of the two adjacent half-spaces, equation (1) turns into the familiar form of Ohm's law⁴⁴. Note that our derivation accounts for the propagation of the terahertz radiation inside the sample (including all reflection echoes) and the irradiation into free space (Fig. 3b). It is, however, restricted to the thin-film limit.

Model for metal-thickness dependence of terahertz emission. To model the terahertz emission amplitude of a FM/NM bilayer, we make use of equations (1) and (5) and assume that $\text{FM} = \text{Co}_{20}\text{Fe}_{60}\text{B}_{20}$ and $\text{NM} = \text{Pt}$. The impedance of the bilayer (equation (5)) is determined by the measured terahertz conductivities of the materials involved (see section 'Sample optical properties').

Equation (1) requires knowledge of the charge current density $\mathbf{j}_c(z) = \gamma(z)\mathbf{j}_s(z)$. To model the spatial structure of \mathbf{j}_c , we neglect the spin-Hall angle γ in the FM layer and determine the spin current density \mathbf{j}_s in the NM layer by considering the following simplified scenario. After excitation by the pump pulse, spin-polarized hot electrons from the FM layer enter the NM layer in which they first propagate ballistically away from the FM/NM interface (Fig. 1a). However, once an electron undergoes scattering, its velocity is randomized such that its contribution to the ultrafast photocurrent, and thus the terahertz signal, becomes negligible. To account for such velocity relaxation, we assume that the density of ballistic electrons behind the FM/NM interface decreases according to $e^{-(z-d_{\text{NM}})/\lambda_{\text{rel}}}$. Here, λ_{rel} can be considered as a hot-electron velocity relaxation length, and d_{FM} is the thickness of the FM layer. We furthermore assume that the electrons undergo perfect reflection at the NM/air and NM/FM interface.

As shown in ref. 63, these assumptions imply a spatial dependence of the ballistic spin current density inside the NM layer ($d_{\text{FM}} < z < d = d_{\text{FM}} + d_{\text{NM}}$) according to

$$\mathbf{j}_s(z) = \mathbf{j}_s(d_{\text{FM}}) \frac{\sinh[(z - d_{\text{FM}})/\lambda_{\text{rel}}]}{\sinh(d_{\text{NM}}/\lambda_{\text{rel}})} \quad (6)$$

where $\mathbf{j}_s(d_{\text{FM}})$ is the spin current density directly after the FM layer. Finally, the linear fluence dependence of the emitted terahertz field (Fig. 1b) indicates that the spin current is proportional to the energy density deposited by the pump pulse. Therefore, one has $\mathbf{j}_s(d_{\text{FM}}) \propto A/d$ where A is the absorbed fraction of the incident pump power (Supplementary Fig. 3). Inserting equation (6) and all other assumptions into equations (1) and (5), we obtain

$$E(d) \propto \gamma_{\text{NM}} \lambda_{\text{rel}} \frac{A}{d} \frac{\tanh(d_{\text{NM}}/2\lambda_{\text{rel}})}{n_1 + n_2 + Z_0 \int_0^d dz \sigma(z)} \quad (7)$$

with λ_{rel} and a global amplitude factor being the only free parameters.

The choice $\lambda_{\text{rel}} = 1 \text{ nm}$ yields the best fit to the measured thickness dependence of the emitted terahertz amplitude, including the existence of a maximum (Supplementary Fig. 6). The discrepancy for $d < 4 \text{ nm}$ (Fig. 3a) is most probably due to shortcomings of our simplified transport model and due to changes in the magnetic properties (such as the Curie temperature) of the sample when approaching small thicknesses d . For $d > 25 \text{ nm}$, we do not expect additional

ARTICLES

NATURE PHOTONICS DOI: 10.1038/NPHOTON.2016.91

Fabry–Pérot resonances for the pump beam because the decay length of the pump intensity (~ 15 nm) is much shorter than the wavelength (~ 300 nm) of the pump radiation inside the metal film.

Ab initio calculations of the spin-Hall effect. The spin-Hall conductivity (Fig. 2) was calculated using the Kubo formula within density-functional theory using the full-potential linearized augmented plane-wave (FLAPW) program FLEUR (<http://www.flapw.de>). We employed the generalized gradient approximation of the exchange correlation potential, a plane-wave cutoff at a wavevector of 85 nm^{-1} and experimental lattice constants (2.91, 3.892, 3.302, 3.166, 3.8402 and 3.926 \AA for Cr, Pd, Ta, W, Ir and Pt, respectively). Further details on the computation are given in ref. 64.

References

53. Boule, O., Malinowski, G. & Kläui, M. Current-induced domain wall motion in nanoscale ferromagnetic elements. *Mater. Sci. Eng. R* **72**, 159–187 (2011).
54. Yeh, P. *Optical Waves in Layered Media* (Wiley, 2005).
55. Liang, X., Xu, X., Zheng, R., Lum, Z. & Qiu, J. Optical constant of CoFeB thin film measured with the interference enhancement method. *Appl. Opt.* **54**, 1557–1563 (2015).
56. Ordal, M., Bell, R., Alexander, R. Jr, Newquist, L. & Querry, M. Optical properties of Al, Fe, Ti, Ta, W, and Mo at submillimeter wavelengths. *Appl. Opt.* **27**, 1203–1209 (1988).
57. Nuss, M. C. & Orenstein, J. in *Millimeter and Submillimeter Wave Spectroscopy of Solids* (ed. Gruener, G.) Ch. 2 (Springer, 1998).
58. Kampfrath, T., Nötzel, J. & Wolf, M. Sampling of broadband terahertz pulses with thick electrooptic crystals. *Appl. Phys. Lett.* **90**, 231113 (2007).
59. Gallot, G. & Grischkowsky, D. Electro-optic detection of terahertz radiation. *J. Opt. Soc. Am. B* **16**, 1204–1212 (1999).
60. Dietze, D., Unterrainer, K. & Darmo, J. Dynamically phase-matched terahertz generation. *Opt. Lett.* **37**, 1047–1049 (2012).
61. Zheng, X., McLaughlin, C., Leahy-Hoppa, M., Sinyukov, A. & Hayden, L. Modeling a broadband terahertz system based on an electro-optic polymer emitter-sensor pair. *J. Opt. Soc. Am. B* **23**, 1338–1347 (2006).
62. Mills, D. L. *Nonlinear Optics: Basic Concepts* (Springer, 1991).
63. Mosendz, O. *et al.* Quantifying spin Hall angles from spin pumping: experiments and theory. *Phys. Rev. Lett.* **104**, 046601 (2010).
64. Freimuth, F., Blügel, S. & Mokrousov, Y. Anisotropic spin Hall effect from first principles. *Phys. Rev. Lett.* **105**, 246602 (2010).

Efficient metallic spintronic emitters of ultrabroadband terahertz radiation

T. Seifert, S. Jaiswal, U. Martens, J. Hannegan, L. Braun, P. Maldonado, F. Freimuth, A. Kronenberg, J. Henrizi, I. Radu, E. Beaupaire, Y. Mokrousov, P.M. Oppeneer, M. Jourdan, G. Jakob, D. Turchinovich, L.M. Hayden, M. Wolf, M. Münzenberg, M. Kläui, T. Kampfrath

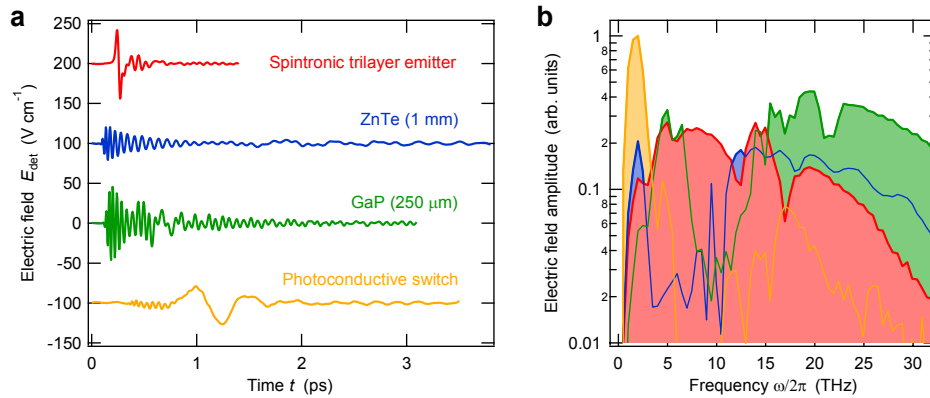


Figure S1 | THz electric field emitted by the spintronic source and other emitters. **a**, Transient THz electric field E_{det} incident on the electrooptic detection crystal following emission by four THz emitters: the spintronic trilayer emitter W(2 nm)/Co₄₀Fe₄₀B₂₀(1.8 nm)/Pt(2 nm), the (110)-oriented nonlinear-optical crystals ZnTe (thickness 1 mm) and GaP (250 μm), and a photoconductive switch. **b**, Corresponding field amplitudes obtained by Fourier transformation of the data of panel **a**. All emitters are driven by pump pulses (duration 10 fs, energy 2.5 nJ, centre wavelength 800 nm) from a Ti:sapphire laser oscillator (repetition rate 80 MHz). The THz signals are measured with a 1 mm thick ZnTe(110) electrooptic crystal. See the main text and Methods for more details.

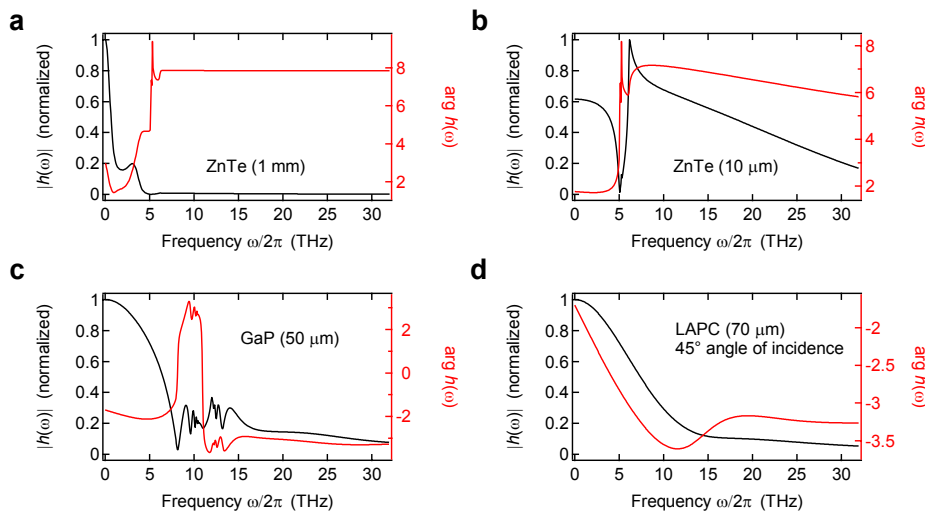


Figure S2 | Detector response. Spectral amplitude and phase of the calculated response functions $h(\omega)$ of the electrooptic detectors used in this work (see Methods): **a**, 10 μm ZnTe(110) on an inactive ZnTe(001) substrate, **b**, 1 mm ZnTe(110), **c**, 50 μm GaP(110) and **d**, 70 μm Lemke/amorphous polycarbonate (LAPC) under 45° angle of incidence. The amplitude maxima are normalized to 1.

SUPPLEMENTARY INFORMATION

DOI: 10.1038/NPHOTON.2016.91

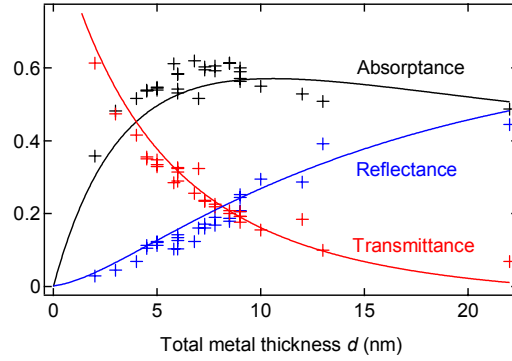


Figure S3 | Optical properties of the metal heterostructures. Reflectance, transmittance and resulting absorptance A of metal stacks as a function of metal thickness d , measured by using the optical pump beam of the THz emission setup. The solid lines show calculations (see Methods).

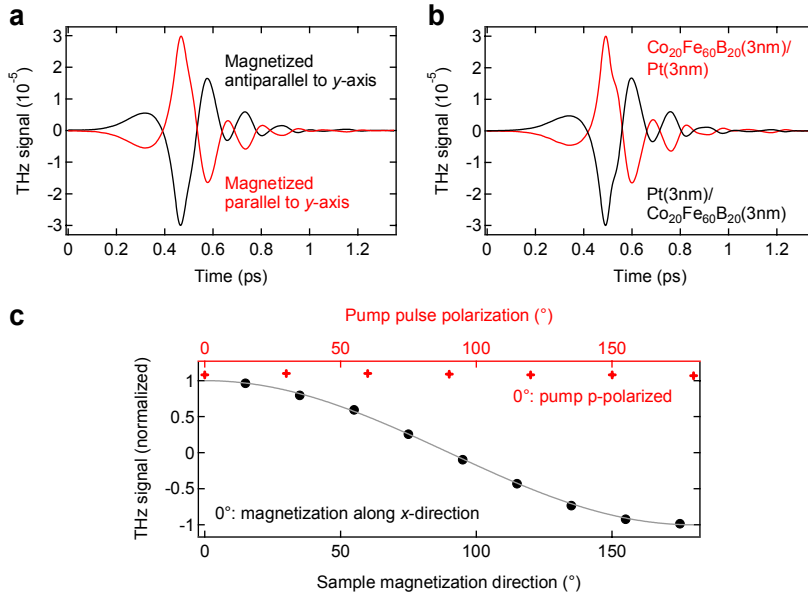


Figure S4 | Symmetry properties of the emitted THz radiation. **a**, THz signal for the FM layer magnetization parallel and antiparallel to the y -axis (see Fig. 1a main text). **b**, THz signal obtained for an FM/NM bilayer and its NM/FM counterpart having reversed layer stacking (see labels for sample details). **c**, THz signal amplitude as a function of the orientation of the linear pump polarization (red crosses) and as a function of the direction of the sample magnetization (black circles). For the latter measurement, a THz wire-grid polarizer was placed before the detection to block the x -polarized THz field component (see Fig. 1a main text). The grey solid line is the cosine of the angle between the polarizer wires and the sample magnetization.

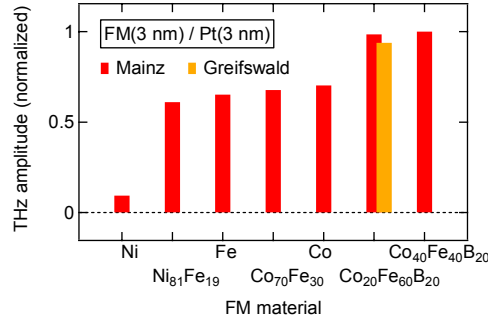


Figure S5 | Impact of the FM material. THz signal amplitude (RMS) of a FM(3 nm)/Pt(3 nm) heterostructure as a function of the FM material chosen. Different colours indicate different labs for sample fabrication (see Methods).

S1. Variation of the FM material. To study the impact of the FM material on THz emission, we consider FM(3 nm)/Pt(3 nm) heterostructures with the FM metals Fe, Co, Ni and their binary alloys. Results are displayed in Fig. 2b and show that all materials provide similar THz output, except Ni, which yields less than 20% of the maximum THz amplitude. The reason for this behaviour is not yet understood but may be related to the fact that the Curie temperature of Ni (627 K) is considerably lower than that of all other FM materials (>1000 K).

S2. Estimate of the quadratic nonlinear susceptibility. The amplitude of the THz pulses emitted from the spintronic THz emitter (STE) grows linearly with the pump fluence (Fig. 1b main text). Therefore, optically induced THz emission from the STE can be described phenomenologically as a $\chi^{(2)}$ -type nonlinear-optical process in which the pump field E_p induces an electric dipole density (polarization)¹

$$P^{(2)}(\omega) = \frac{\chi^{(2)}(\omega)}{Z_0 c} \int_{\omega_p > \omega > 0} d\omega_p E_p(\omega_p) E_p^*(\omega_p - \omega) = \frac{\chi^{(2)}(\omega)}{Z_0 c} F(\omega) \quad (S1)$$

at the difference frequency ω of all pump-frequency pairs ω_p and $\omega_p - \omega$. In writing Eq. (S1), we have assumed that the quadratic response function $\chi^{(2)}$ is independent of the pump frequency and abbreviated the integral by $F(\omega)$. In general, the dependence of $\chi^{(2)}$ on THz frequency ω makes the response non-instantaneous, that is, longer than the driving optical pump pulse. Since $-i\omega P^{(2)}(\omega)$ equals the charge-current density $-ej_c(\omega)$, we use Eqs. (1) and (5) of the main text to rewrite the THz electric field directly after the STE as

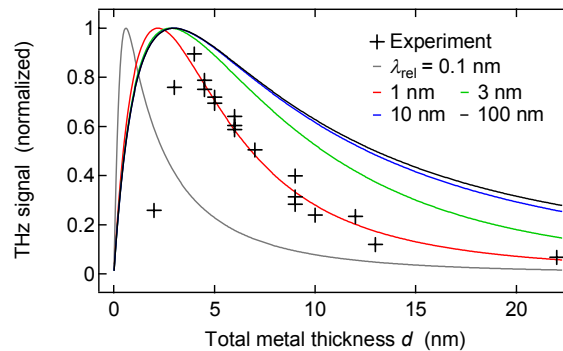


Figure S6 | Thickness dependence of THz emission. Normalized measured (crosses) and modelled (solid lines) THz signal amplitude as a function of total metal thickness d . Calculations are shown for 5 different values of the hot-electron velocity relaxation length λ_{rel} .

SUPPLEMENTARY INFORMATION

DOI: 10.1038/NPHOTON.2016.91

$$E(\omega) = \frac{1}{n_1(\omega) + n_2(\omega) + Z_0 \int_0^d dz \sigma(\omega)} \cdot \frac{i\omega F(\omega)}{c} \cdot \int_0^d dz \chi^{(2)}(\omega). \quad (\text{S2})$$

To estimate the $\chi^{(2)}$ magnitude of our STE, we compare the THz amplitude generated by the STE to that of a suitable reference emitter. We choose a 50 μm thick GaP(110) crystal because the magnitude ($5.4 \times 10^{-11} \text{ m V}^{-1}$) of its only nonvanishing $\chi^{(2)}$ tensor element is well known². In addition, THz-wave generation is still phase-matched at this thickness. According to Ref. 3, the THz amplitude directly after the GaP is given by a formula analogous to Eq. (S2),

$$E_{\text{GaP}}(\omega) = \frac{\exp[in_{\text{GaP}}(\omega)\omega d/c]}{n_2(\omega) + n_{\text{GaP}}(\omega)} \cdot \frac{i\omega F_{\text{GaP}}(\omega)}{c} \cdot d_{\text{GaP}} \chi_{\text{GaP}}^{(2)}(\omega). \quad (\text{S3})$$

Here, d_{GaP} is the GaP thickness, and n_{GaP} is the refractive index of GaP. As with Eq. (S2), n_2 is the refractive index of air.

In our experiment, we find that the peak electrooptic signal (Fig. 4a main text) and the THz field amplitude (Fig. S1a) of the STE are comparable to those of GaP. Consequently, we have $|E| \sim |E_{\text{GaP}}|$. Similarly, the first and second term of Eq. (S2) have the same order of magnitude as their GaP counterparts in Eq. (S3). Therefore, the ratio of the nonlinear-optical coefficients is roughly given by

$$|\chi^{(2)}/\chi_{\text{GaP}}^{(2)}| \sim d_{\text{GaP}}/d_{\text{eff}}, \quad (\text{S4})$$

that is, by the ratio of the GaP thickness ($d_{\text{GaP}} = 50 \mu\text{m}$) and the effective thickness d_{eff} of the STE region in which the THz charge current is generated. Since $d_{\text{eff}} \sim \lambda_{\text{rel}} \sim 1 \text{ nm}$ (see main text and Methods), the $\chi^{(2)}$ coefficient of the STE is nearly 5 orders of magnitude larger than that of GaP, yet located in a sheet of only $\sim 1 \text{ nm}$ thickness at the FM/NM interface.

References

- ¹ Mills, D.L. *Nonlinear optics: Basic concepts* (Springer, 1991).
- ² Leitenstorfer, A., Hunsche, S., Shah, J., Nuss, M. & Knox, W. Detectors and sources for ultrabroadband electro-optic sampling: Experiment and theory. *Appl. Phys. Lett.* **74**, 1516-1518 (1999).
- ³ Kaindl, R.A. *et al.* Broadband phase-matched difference frequency mixing of femtosecond pulses in GaSe: Experiment and theory. *Appl. Phys. Lett.* **75**, 1060-1062 (1999).